INFN

Istituto Nazionale di Fisica Nucleare

BriXSinO

Technical Design Report

This document, and the project envisioned herein, are dedicated to the memory of three great scholars and teachers, whose personal and scientific heritage for LASA and most of the authors are unforgettable and unvaluable: Francesco Resmini, Claudio Birattari and Rodolfo Bonifacio.

Authors

Alberto Bacci, Michele Bertucci, Angelo Bosotti, Francesco Broggi, Mauro Citterio, Illya Drebot, Marco Giammarchi, Dario Giannotti, Dario Giove, Stefano Latorre, Chiara Meroni, Paolo Michelato, Laura Monaco, Rocco Paparella, Francesco Prelz, Marcello Rossetti Conti, Andrea R. Rossi, Luca Serafini, Daniele Sertore, Marco Statera, Verardo Torri
INFN - Milano, Via Celoria 16 - 20133 Milano & INFN - LASA, Via Fratelli Cervi 201 - 20090 Segrate

Simone Cialdi, Michele Opromolla, Bruno Paroli, Vittoria Petrillo, Lucio Rossi, Massimo Sorbi, Edoardo Suerra
Università degli Studi di Milano & INFN - Milano, Via Celoria 16 - 20133 Milano

Maria Pia Abbracchio, Samuele Altilia, Stefano Capra, Daniele Cipriani, Cristina Lenardi, Carlo Pagani
Università degli Studi di Milano, Via Festa del Perdono 7 - 20122 Milano & Università degli Studi di Milano, Dip. Fisica, Via Celoria 16 - 20133 Milano

Antonello Andreone, Can Koral, Zahra Mazaheri, Giovanni Mettivier, Gian Paolo Papari, Bruno Piccirillo, Andrea Rubano, Paolo Russo
Università di Napoli "Federico" & INFN - Napoli, Complesso Universitario di Monte S. Angelo ed. 6, via Cinthia - 80126 Napoli

Riccardo Calandrino, Antonella del Vecchio
Istituto di Ricovero e Cura a Carattere Scientifico Ospedale San Raffaele, Via Olgettina 60 - 20132 Milano

Francesco Canella, Rafael Ferragut, Ezio Puppin
Politecnico di Milano, P.le Leonardo da Vinci 32 - 20133 Milano & INFN - Milano, Via Celoria 16 - 20133 Milano

Paolo Cardarelli
INFN - Ferrara, via Giuseppe Saragat 1 - 44122 Ferrara

Adolfo Esposito
INFN - Laboratori Nazionali di Frascati, Via Enrico Fermi 54 - 00044 Frascati

Gianluca Galzerano
CNR - Istituto di Fotonica e Nanotecnologie, P.le Leonardo da Vinci 32 - 20133 Milano & INFN - Milano, Via Celoria 16 - 20133 Milano

Maria Rosaria Masullo, Andrea Passarelli
INFN - Napoli, Complesso Universitario di Monte S. Angelo ed. 6, via Cinthia - 80126 Napoli

Domenico Paparo
CNR - Istituto di Scienze Applicate e Sistemi Intelligenti, Via Campi Flegrei, 34 - 80078 Pozzuoli (NA)

Gianfranco Paternò, Angelo Taibi
Università degli Studi di Ferrara & INFN - Ferrara, via Giuseppe Saragat 1 - 44122 Ferrara

Marcel Ruijter, Sanae Samsam
Università degli Studi di Roma "La Sapienza", Piazzale Aldo Moro, 5 - 00185 Roma & INFN - Milano, Via Celoria 16 - 20133 Milano

Alberto Torresin
Polo Ospedaliero, DGWelfare, Regione Lombardia & Università degli Studi di Milano, Dip. Fisica, Via Celoria 16 - 20133 Milano

Angelo Vanzulli
Università degli Studi di Milano, Dip. Oncologia e Emato-oncologia, Via Festa del Perdono 7 - 20122 Milano & ASST Grande Ospedale Metropolitano Niguarda, Piazza Ospedale Maggiore, 3 - 20162 Milano

Foreword

BriXSinO is a demonstrator of a new acceleration mechanism - two way in the same Linac (à la MariX), pursuing at the same time research of beam and machine operation in E.R.L. (Energy Recovery Linac) mode, following the original Maury Tigner's configuration of opposite way, dog-bone recirculation. BriXSinO's mission is the demonstration of high peak and average brightness beam generation, acceleration and manipulation with large energy sustainability, as requested by the high intensity frontier. Energy sustainability implies developing accelerators with large efficiency in transforming AC power into electron beam power: most Linacs do not overcome a few percent in efficiency - BriXSinO aims at achieving efficiencies larger than 20%. Besides such a primary mission, that is in the mainstream of future strategies for large scale particle accelerators, BriXSinO will offer unique radiation beams to users of X-Rays and THz, thanks to the very large expected electron beam power/brightness.

Due to constraints in the footprint available at LASA's site, and budget/resources limitations typical of a demonstrator, BriXSinO will be restricted to modest beam energy, below 50 MeV in ERL mode, and 90 MeV in two-way mode, a minimum requirement in order to conceive a machine set-up composed of multiple accelerating sections, operated with Super-conducting CW RF cavities, within a configuration capable to effectively test two-way and E.R.L. operation modes.

Nevertheless, the beam power achieved is expected to reach up to 250 kW, carried by a CW 5 mA - 50 MeV electron beam, that is recirculated by a proper arc-shaped beam transport line, and decelerated through the main SC Linac back down to the injector beam energy, at about 5 MeV. The challenge is to generate, accelerate, manipulate, characterize, deliver to users and recover back such a large beam power, at the same time reaching the high phase space density (i.e. peak brightness) requested by the Compton source and the THz FEL operation. Such a task implies reaching normalized transverse emittances below 1 mm – mrad, together with energy spreads below 0.1%, and time and pointing stabilities typical of high brightness Linacs. These are in fact minimum requirements on beam quality requested to drive either I.C.S. (Inverse Comtpon Scattering sources) or Free Electron Lasers (FEL): the great advantage of ERLs, compared to storage rings, is the full accessibility to beam phase space for experiments, married to beam power levels typical of storage rings, that are not achievable in standard Linacs.

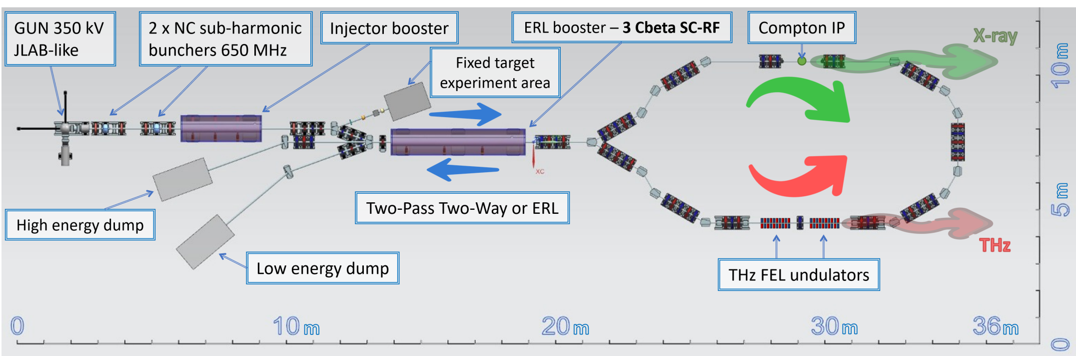

Figure 1: BriXSinO's functional schematics.

BriXSinO's electron accelerator would not reach his missions without a photonic machine based on a very high phase-stability laser system, capable to pump the optical Fabry-Pérot cavity of the Compton source and, at the same time, drive the injector photo-cathodes with CW beams with up to 100 MHz rep rate. An ultra-stable kW-class fiber laser is the core of the photonic machine, to drive the Fabry-Pérot cavities up to MW-class stored power level and 10 mA-class electron beams delivered by photo-cathodes. The integration between the two - electron and the photonic - machines is essential in BriXSinO.

Phase stabilities performances up to the level of the laser optical carrier will allow full synchronization of the electron beam with radiation beams delivered to users. This would allow experiments with fully synchronized mono-chromatic X-Rays from the Compton source with THz beams from the Free Electron Laser oscillator.

Dual color X-Rays up to 35 keV are also planned to be generated in the Compton source by a system of twin shiftable Fabry-Pérot optical cavities, that was conceived, developed and successfully tested for the first time in the context of the R&D activity associated to the preparation of this TDR. This innovative and new technique will allow two and three-dimensional breast radiography by exploiting dual-energy flashes and K-edge subtraction or speckle-based Phase Contrast Imaging.

Fully coherent kW-class THz beams generated by the FEL oscillator cavity will also be available, opening a new unexplored range of user experiments with imaging methods from 6 to 30 THz, with applications to medical imaging, molecular spectroscopy and remote mesoscopic morphological characterization of materials. The peculiarity of having two synchronized radiation sources at two widely different wavelengths (THz and X-Rays) allows extremely interesting and advanced pump and probe experiments: simultaneous operation of the Compton source and the THz FEL is a unique capability of BriXSinO's recirculation arc and BriXSinO's dog-bone ERL operation mode.

Last but not least, a dedicated fixed target beam line, carrying an intense beam of up to 10 MeV energy and up to 5 mA average current, will enable experiments in the flash-therapy domain, as well as new positron source investigations in conjunction with QUPLAS experiments and scientific case, aiming at generate ultra-intense very collimated beams of positrons to conduct fundamental research also with positronium.

BriXSinO Executive Summary

Introduction

Particle Accelerators are characterized by very low energy sustainability, mainly due to their low efficiency in transforming alternating electrical (AC) into particle beam power.

The increasing and irreversible requests of complete financial and energetic autonomy of Research Infrastructures with reduced environmental impact drive the research communities at conceiving a long term strategy with the purpose of developing sustainable accelerators for the frontiers of the High Energy Physics (HEP) and of the future applied researches.

Energy Recovery Linacs (ERLs) [1] promise to be a keystone for future sustainable accelerators. Their characteristic is indeed to be a good compromise between the full availability coupled with total waste of the beam of Linacs and the highly reduced beam availability paired to beam saving typical of the storage ring case. ERLs provide users/experiments full access and availability to the beam phase space quality/density and contained access to beam energy and particles. This reasonable balancing between use of the beam and beam power waste/dissipation is attractive not only to users oriented to radiation experiments, i.e. Free Electron Lasers (FEL), Inverse Compton Scattering (ICS), and synchrotron radiation, but also in the HEP scenario, as extensively discussed in Ref. [2].

The main perspectives of ERLs include: to provide nearly linac quality/brightness beam at nearly storage ring beam powers, to mitigate intractable, namely expensive, environmental/safety concerns since the beam can be dumped at low energy, to consider higher power applications than would otherwise be unaffordable, looking at GW class beams.

Main ERL paradigms worldwide are BNL-ERL [3] and CBETA [4]. BNL-ERL, now under commissioning at the Collider Accelerator Department at Brookhaven National Laboratory, is aimed at 500 mA at 20 MeV. A superconducting laser photocathode RF gun is powered by a 1 MW CW klystron and equipped with a load-lock system for the insertion of high quantum efficiency photocathodes, providing high brightness electron beams at unprecedented average power. The objectives are halo generation and control, Higher-order mode issues, coherent emissions for the beam and high brightness/high power beam generation and preservation. CBETA, commissioned since 2019, will serve as prototype of the fixed field alternating gradient-ERL concept. The design incorporates several highly innovative concepts and could achieve higher performance at lower cost.

The facility presented here, named BriXSinO [5], is inspired, on reduced scale, by the same philosophy of other more ambitious and expensive projects grown up around the MariX concept [6–11]. Researchers from INFN LASA, with their knowledge of Superconducting technology, and from the Università degli Studi of Milan, expert in radiation, are the core of a cooperation collecting people from other INFN groups, INFN-Ferrara, INFN-Napoli, LNF, Universities as Naple, Ferrara, Politecnico of Milan, Institutions as the CNR and Hospitals like San Raffaele. The shared aim is to develop at the INFN LASA laboratory in Segrate, close to Milan, a test-facility that would enable addressing the physics and technology challenges posed by the ERL generation. The location foreseen for the infrastructure is shown in Figure 2. A geological survey commissioned to a specialized company didn't report any particular problematic.

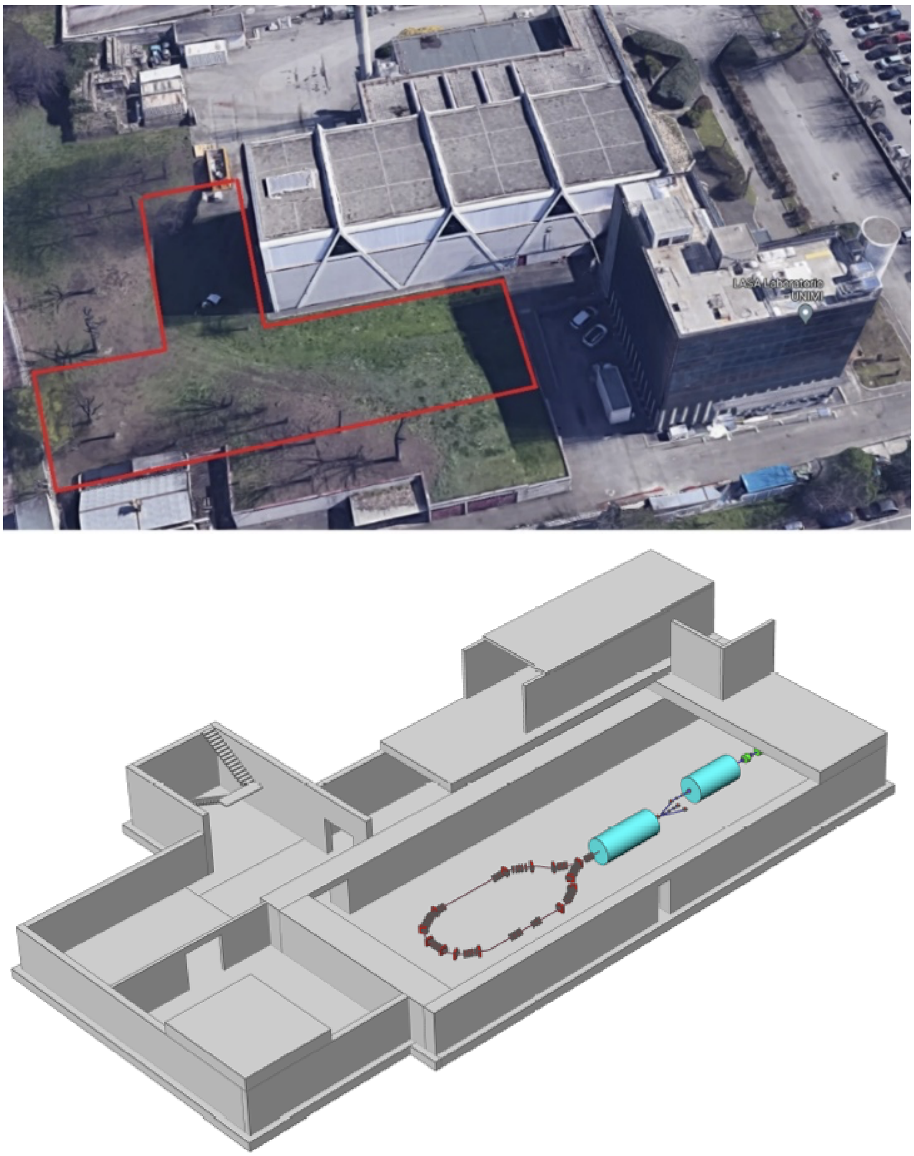

Figure 2: LASA aerial view and rendering of the building.

Sustainability, as scientific concept, is the Leitmotiv of the study; sustainability, as habit of life, is and will be systematically practiced throughout the project, by reusing instrumentation already present, recycling the materials, exploiting the disused spaces, taking advantage of all kinds of synergies, organizing all the documentation electronically, encouraging remote control and online meetings for limiting travels, thus leveling prices and impact at minimum in all phases.

A newly conceived scheme of ERL with counter propagating beams is proposed in BriXSinO: 5 mA of average electron beam current in CW mode with a time structure organized in a regular repetition rate up to 100 MHz, i.e. bunch spacing 10 ns. The users will be therefore allowed to exploit at will the beam quality and phase space, saving at the same time large part of the electron beam kinetic energy for recovery the beam power via deceleration in the same Superconducting (SC) Linac. It is similar in parameters and dimensions to a storage ring, with the very much larger recovery of the 225 kW beam power (>90%). Moreover, the electron bunches in BriXSinO travel through the full orbit back-and-forth just one time, while, conversely, in a storage ring electrons travel over many turns (namely > 10^{10}) so their phase space quality must be very carefully preserved to avoid instabilities that may seriously impact the storage ring life-time.

Its unique features will enable at LASA, in the close proximity of both Universities with deep knowledges of physics foundations and Hospitals of excellence, new promising synergies between fundamental physics oriented research and high social impact applications.

The importance of BriXSinO at INFN LASA is then twofold. From one hand, it will act as test facility for fundamental questions and strategies of Dynamics and Energetic by hosting experiments for maximizing the energy sustainability and minimizing the AC power consumption.

From the other hand, it will work as user facility by providing large quality THz and X-Rays emission from its high brightness accelerated electron beam, enabling important and advanced applications as described in details in Ref. [12]. In synthesis, the X-Rays produced at BriXSinO will allow two and three-dimensional breast radiography by exploiting dual-energy flashes and Kedge subtraction or speckle-based Phase Contrast Imaging. The Hospital San Raffaele, adjacent to LASA, could profit immediately by these studies. Characterization of materials could be done by wide X-Ray scattering (WAXS) and small angle X-Ray scattering (SAXS). All these techniques, from advanced X-Ray imaging to material discrimination, can be effectively translated for the non-destructive testing of industrial or Cultural Heritage samples. The THz source can extend imaging methods to the unexplored range from 6 to 30 THz, with applications to medical imaging, molecular spectroscopy and remote mesoscopic morphological characterization of materials. It can provide full extended images based on interferometric systems and improve sensitivity of imaging tools by introducing explicit control and handling methods on wavefront shape, polarization and orbital momentum of the THz probe beam, both in the preparation and detection stages. The peculiarity of having two synchronized radiation sources at two widely different wavelengths (THz and X-Rays) allows extremely interesting and advanced pump and probe experiments. The project has already collected large appreciation, lot of consents and wide interest in the Scientific National and International Communities; many papers, specifically on BriXSinO, have been published [12–15] or are actually submitted [15] and it has been invited, as oral presentation, to the next IPAC Conference 2022 at Bangkok.

BriXSinO structure and parameters

Figure 3 shows a schematic layout of BriXSinO. From the left side, the injector generates electron bunches through a DC gun. Downstream the gun, the bunches are first compressed with two RF sub harmonic bunchers (650 MHz), then boosted by three 2-cell SC cavities at the energy of about 4.5 MeV, and finally injected into the ERL superconducting Module through a low energy dogleg. The possibility to extend the injector maximum energy up to 10 MeV has been also considered. In the middle region, the ERL Superconducting Modules (and/or two-way linac) are present. The beam here passes in both directions, either with opposite phase for ERL working mode, or in the two-pass two-way acceleration mode [16]. At the right end there is the arc, designed in such a

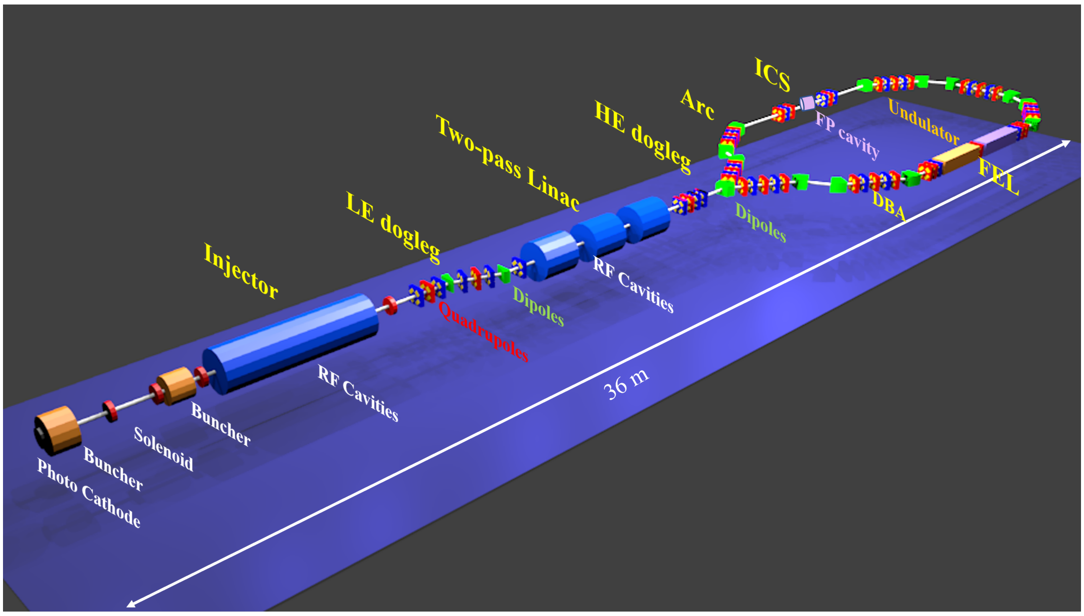

Figure 3: BriXSinO general layout. From left: injector with DC gun, bunchers and radiofrequency cavities. Low-energy (LE) dogleg with quadrupoles in red and dipoles in green. Two-way (or ERL zone) SC linac that can be operated in the two-pass two-way acceleration or ERL mode. High-energy (HE) dogleg. Recirculating loop (Arc), made by Double Bend Achromats (DBA), hosting the light sources and bringing back the beam to the two-way zone. On left branch of the arc: Fabry-Pérot (FP) cavity with Inverse Compton Scattering (ICS) source. On right branch of he arc: Free-Electron Laser (FEL).

way to bring back the beam to the Superconducting modules. The arc lattice is constituted by 7 DBA (Double Bend Achromat). In the straight parts, it will host two experimental areas devoted to ICS and THz FEL without any additional magnetic elements. BriXSinO's beams travel the cavity sequence twice, back and forth, and in different phase conditions. BriXSinO can therefore operates in two different working modes. The first is the ERL working mode: an ad hoc path length adjustment system synchronizes the coming back beam with the decelerating RF wave crest: the electron beam is decelerated giving up its energy to the cavity radiofrequency. The second working mode is the two-pass two-way acceleration mode fundamental for operation à la MariX [16]. The beam is re-injected in the linac by the arc transport line, where the beam can be also compressed avoiding emittance dilution [17]. This novel working mode, that will be tested in BriXSinO for the first time, permits to save precious space while improving the efficiency by doubling the energy exchange in the linac. All start-to-end beam dynamics simulations have been done by using the codes ASTRA [18] and Elegant [19] coupled with the genetic algorithm GIOTTO [20]. BriXSinO's beams will possess similar levels of high brightness as other (non-ERL) Linacs, enough to drive FELs and/or ICS, i.e. rms transverse normalized emittances in the µm range and relative energy spreads in the 10^3 range. A list of BriXSinO's electron beam characteristics, summarized in Tables 1 and 2, emphasizes different cases of operations, namely the ERL operation to demonstrate the two-way acceleration foreseen in MariX (Table 1), the application to drive ICS at very large photon flux (10^{12} photons/s) (Table 2, second column) and a kW-class THz FEL (Table 2, third column). A further operation mode for BriXSinO is the use of its injector for fixed target experiments performed with maximum electron energy of 10 MeV and 5 mA average current. The availability of such a high intensity beam (50 kW) enables both experiments of flash therapy tests using electrons, with a capability to irradiate samples with a delivered total charge in a 200 ms time interval up to 1 mC, as

Table 1: Electron beam parameters at diagnostic station after 2-way acceleration (a la MariX).

Parameter	**Value**
Energy (MeV)	< 80
Bunch charge (pC)	50 - 200
Repetition rate (GHz for CW operation)	0.9286
Average Current (mA)	< 5
Beam power @ dump (W)	400
$\varepsilon_{n,x,y}$ (mm − mrad)	1.0
Energy spread (%)	< 0.2
Bunch separation (μs)	> 1
Beam energy fluctuation (%)	< 0.2
Pointing jitter (μm)	50

well as converting the electron beam into bremsstrahlung photons with energy peaked at 7 - 8 MeV at an impressive flux of 10^{16} photons/s (i.e. up to 30 kW X-Ray beam).

Radiation sources driven by BriXSinO electron beam

BriXSinO will host in the zero dispersion zones of the arc two radiation sources: an Inverse Compton Source (ICS), named Sors and one THz Free-Electron Laser Oscillator, named TerRa. The inverse Compton scattering source Sors is based on the interaction between the electrons arriving at the interaction points (IP) and the laser pulse. Sors is placed in the clockwise direction of electron beam between two DBAs. The IP occupies a asymmetrical region between the focusing and the defocusing triplets as compromise between the short focal length needed to the electrons to be focused in the transverse dimension up to 35 μm and the size of the optical table hosting the double Fabry-Pérot Optical Cavity needed for producing two color X-Rays shown in Figures 4 and 5.

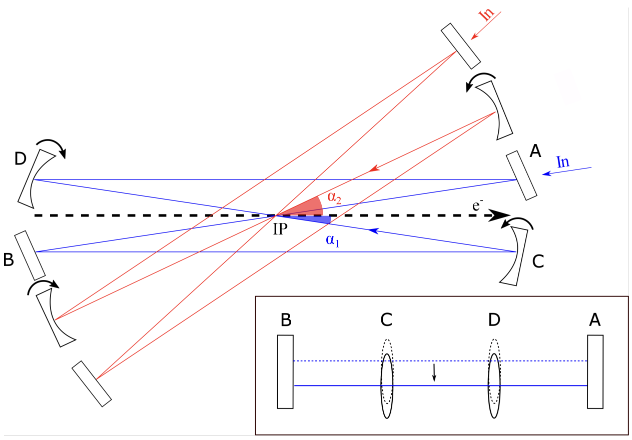

Figure 4: Two color cavity: the photons stored in the cavities will collide with the electron bunches at the same interaction point (IP) but with two different angles: α_1 (blue) and α_2 (red).

The Compton photon energy can be tuned from 16 keV to 45 keV by varying the electron energy from 30 to 50 MeV. The Compton emission has been simulated using the MonteCarlo code

Table 2: BriXSinO's electron beam main parameters: Electron beam parameters at Compton Interaction Point for I.C.S., and at THz FEL *Maximum (CW, ca. 92.86 - 0.9286 MHz, **after ERL.

Parameter	**ICS**	**FEL**
Energy (MeV)	22 - 45	22 - 45
Bunch charge (pC)	50 - 200	50 - 100
Repetition rate (GHz)*	0.9286	0.4643
Average Current (mA)	< 5	< 5
Peak Current (A)	-	8 - 12
Nominal beam power (kW)	< 225	< 225
Beam energy @ dump (MeV)	4.5	4.5
Beam power @ dump** (kW)	< 22.5	< 22.5
Bunch length (rms, mm)	2.2	< 1
$\varepsilon_{n,x,y}$ (mm – mrad)	1 - 3	1 - 3
Slice Emittance (mm – mrad)	-	1.2 - 1.7
Energy spread (rms, %)	0.5 - 1.5	0.1
Slice Energy spread (%)	-	0.05
Focal spot size (rms, μm)	30 - 60	100
Bunch separation (ns)	10 - 1000	10 - 20
Beam energy fluctuation (rms, %)	< 0.1	< 0.01
Time arrival jitter (fs)	< 150	<50
Pointing jitter (μm)	10	20

CAIN [21]. Two color radiation, widely required by imaging applications, can be obtained by using two different laser pulses impinging on the same electron beam at different angles, thus exciting different frequencies [13]. The potentialities of such source can be improved by using different polarizations of the initial laser pulses or by producing a temporal sequence of two X-Ray pulses with different colors. Figures 6 and 7 presents the spectra of the single and two color radiation.

To produce the dual-color beam we need two Fabry-Pérot cavities oriented differently. An electron beam at 43 MeV can produce two colors at 31.8 and 34 keV, surrounding the iodine K-edge (33.17 keV), colliding with the laser at angles 7° and 30°. The two cavities have the same geometry and are formed by 4 mirrors, 2 curved/2 flat, in the near-confocal configuration [14]. With a finesse of about 5000 it is possible to reach a power of about 200 kW by entering with 100 W. The X-Ray radiation will be delivered to users by means of beamlines equipped with instruments and detectors common to any user requirements including beam stoppers, precollimation, luminometers, filtration, collimation, beam intensity monitor. Two experimental stations are foreseen: the first one (EXPS1) will be equipped with calibrated diffraction wires for Quantitative Inline Phase Contrast Imaging and for Fresnel Diffraction Interferometry. Calibrated silica nanoparticles will be used for 2D transverse coherence mapping with the Heterodyne Near Field Scattering (HNFS) technique, which provides resolutions in the micrometric range compatible with the expected coherence areas. EXPS1 will additionally provide quasi-real-time monitoring of the coherence properties of the radiation for phase contrast imaging applications, enabling to assess the stability or degradation of parameters over time. EXPS2 will be equipped with a beam profile monitor consisting of a low-

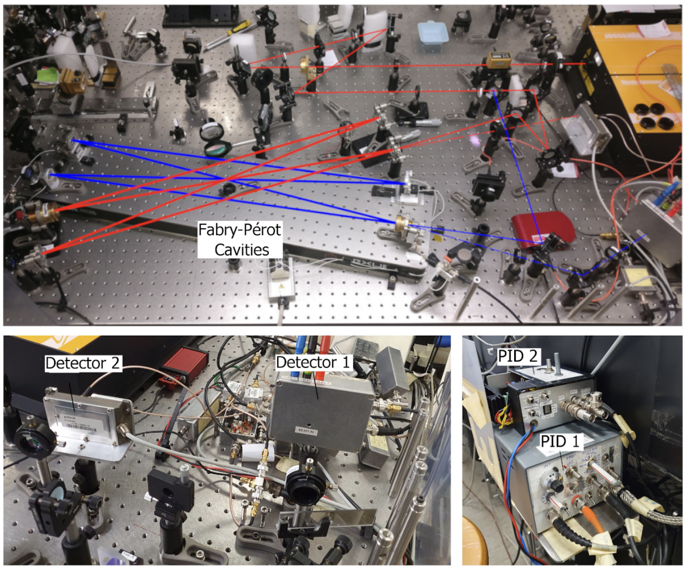

Figure 5: Two color cavity: photo.

Table 3: Laser parameters.

Laser parameter	**ICS**
Pulse energy (mJ)	2.7
Wavelength (nm)	1030
Pulse length (ps)	1.5
Repetition rate (MHz)	1300/14
Focal spot size (x,rms,µm)	90
Focal spot size (y,rms,µm)	80
Laser parameter a_0	3.3×10^{-3}
Collision angle (°)	7
Collision angle for two colors (°)	30

noise high-resolution cooled digital camera coupled to a high resolution crystal type scintillators to efficiently convert the 9 - 37 keV photon energy into visible light.

The other zero dispersion region of the arc is occupied by undulators and THz cavity of the Free-electron Laser Oscillator TerRa [15]. The two undulator sections have variable gaps, linear polarization, peak magnetic field of about 1 T, periods of 4.5 and 3.5 cm respectively and length of 1.75 m. The optical cavity embedding the undulators is composed by metal-coated (gold on copper) mirrors with a total reflectivity of the order of 97% , with length is L_c = 12.92 m and round trip of 25.84 m. The code GENESIS 1.3 [22] has been used, coupled to a tool for the evaluation through the Huygens integral of the radiation round trip transport taking into account the details of the whole optical line [8], to evaluate the radiation power.

Using an electron beam energy E = 40 MeV, the undulators both tuned at λ = 20 µm, mirror loss of 1.5%, extraction at 4%, energy jitters of 0.3%, pointing instability of 100 µm, intra-cavity energy level of one-few hundreds µJ, leading to 3 - 17 µJ of extra-cavity energy and 0.15 - 0.7 kW of output average power can be obtained. The radiation parameters are summarized in Table 5. Figure 8 shows the temporal and spectral distribution of the intra-cavity radiation in single color

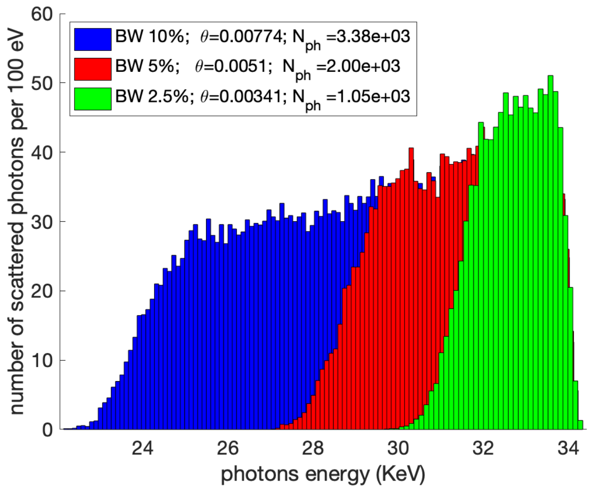

Figure 6: Spectrum of the X-Ray: distribution of the scattered photon number as a function of the photon energy for different bandwidth values.

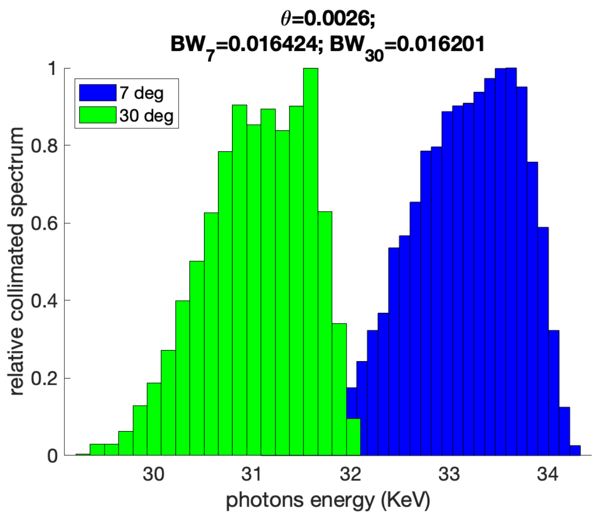

Figure 7: Spectrum of the two color X radiation vs photon energy.

operation.

Tuning the two undulator modules at different wavelengths enables the generation of two THz color [23]. The two produced colors are separated in spectrum, but temporally almost synchronized and exhibit extremely interesting characteristics for experimental applications. The intra-cavity energy reaches levels of 50 - 500 µJ, delivering therefore to the users 1 - 100 µJ (0.06 - 1 kW of average power in each color). Figure 9 shows the temporal and spectral distributions at the end of the undulator line. The spectrum is characterized by two narrow and quite clean spikes, tunable and well separated. As all two color sources based on FELs, the frequency tuning can be operated either by changing the magnetic field of the undulators (an operation that requires small adjustments in few minutes) or by choosing a different electron beam working point. The THz radiation is then delivered to users. Advanced diagnostics have been grouped and connected into a common Geometric Phase Enhanced Short T-waves (GEST) Platform. It includes a Geometric Phase-based Beam Shaper, a FullStokes Imaging Geometric Phase Polarimeter, a Polarized Sagnac Interferometer, a Geometric Phase Shearing Interferometer and a TeraHertz

Table 4: Radiation parameters, (*) 1/(m^{3}bw%)

γ-Ray parameter	1	2
Mean photon energy (keV)	32.68	29.34
Bandwidth rms (keV)	0.8	2.9
Bandwidth FWHM (keV)	2.3	9.3
Collimation angle (mrad)	3.35	7.70
Nominal photons per shot	10^4	10^4
Collimated photons per shot	10^3	3×10^3
Rms size(μm)	47	37
Rms divergence (mrad)	2.3	4.8
Pulse length (ps)	3.26	3.26
Peak brilliance (*) ($\times10^{13}$)	3.0	0.6

Table 5: Characteristics of the radiation at λ = 20 μm and λ = 35 μm. IC: intra-cavity, EC: extra-cavity. Mirror Losses= 2×1.5%. Extraction 4%. Repetition rate= 46.4 MHz.

Wavelength(μm)	20	20	35	35
Undulator length (m)	1.75	4	1.75	4
Single shot IC energy(μJ)	84	420	250	420
Single shot EC energy(μJ)	3.35	16.8	10.0	16.8
Average power(kW)	0.15	0.78	0.47	1.16
Bandwidth (%)	0.65	2.5	1.85	4.2
Size(mm)	2.0	2.6	2.4	2.8
Divergence(mrad)	2.8	4	4.2	5.0
Pulse rms length (μm)	635	830	749	1000

Hyper-Raman spectroscopy system. A microbolometric camera array is planned to be used as image detector. Options for reflection measurements have been also considered.

The ongoing R&D activities

The activities have involved a total of 40 researchers, PhD students, technicians, organized in Working Groups, with a regular exchange of information via group meetings and seminars. The pandemic problems during 2020 and 2021 have in general slowed the activities and compromised some connected experiments like for instance ACTIS. The research and development activities on BriXSinO have included detailed start-to-end simulations of all aspects of the project. Extended beam dynamics simulations have been performed using code ASTRA [18] to investigate the optimum electron bunch size and its dependence on the laser spot size at the photocathode, the complete control of emittance and energy spread, the precision in the re-injection of the beam inside the linac. The code GIOTTO [20] was used to drive the scan and the statistics and to optimize the beam both in the interaction point of the ICS and at the entrance of the TeraHertz undulator. The problems connected to the travel of the beam in the arc have also been analyzed. A novel numerical tool named HOMEN, developed ad hoc, has been devoted to the study of the effect of

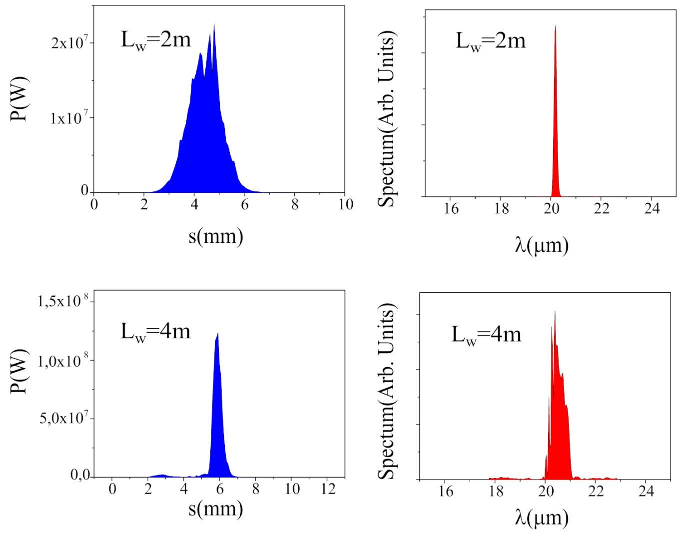

Figure 8: Radiation power P(W) vs coordinate z(mm) on the left and spectral distributions in arbitrary units vs λ(μm) on the right for $\lambda = 20$ μm. $L_w = 1.75$ m in the upper line, $L_w = 4$ m in the lower one.

the high order modes (HOMs) in the accelerator superconductive cavities, an open problem that could affect the performances of BriXSinO and, in general, of ERLs. Preliminary simulations of a single 1.3 GHz SW 7-cell cavity module show that, by injecting 3×10^6 bunches, each with a 50 pC charge, and initial energy $E = 10$ MeV, HOMs give an energy oscillation due to the injection phase which is different from bunch to bunch because their frequencies are not multiple of the machine repetition rate. These oscillations are small and induce an additional relative energy spread of about 2.5×10^{-3}. We expect that a variation of this magnitude will not introduce major effects on the quality of the radiation produced by either BriXSinO light sources. The next phase foresees to extend the analysis to the ERL working mode by injecting the returning beam from the arc compressor in a decelerating RF phase. The ICS both in the single color and in the dual color mode has been simulated by using CAIN [21] and ComptonCross [24]. Single color and dual color operations are foreseen also for the THz FEL [23].

The R&D activities are not limited only to theoretical and numerical analyses, but concern also an intense experimental program, focused on the Fabry-Pérot cavity and the photocathode.

Their main objectives are to test the high Finesse Fabry-Pérot (FP) optical cavity, the amplification system and the lines for the RF-Guns (harmonic + temporal and spatial shaping + spatial stabilization) and to prove the possibility of using a Cs_2Te photocathode at 100 MHz repetition rate and high average current (mAs scale).

Regarding the activity on the Fabry-Pérot cavity [14], the laser oscillator is a commercial mode-locked Yb-laser model Orange from the Menlo Company, holding an internal amplification system supporting an output of 10 W and several actuators. The light is centered at the wavelength of 1035 nm with a spectral width of 13 nm with repetition rate from 92.696 to 93.02 MHz. The laser system needs one amplification systems for the cavities and one for the photocathodes. The two FP cavity are stabilized with respect to the external laser by exploiting the Pound-Drever-Hall (PDH) technique. The nominal finesse of the cavities has been measured by amplitude modulation as about 5100, so it can get 200 - kW300 with an input signal of about 100 W. The two cavities for two-color operation have been built with the design scheme presented in Figure 4 and 5. The switch between the two energies by swapping the interaction laser is performed by rotating the curved mirrors of two opposite angles to translate the optical plane vertically. This technique allows us to shift the focus of the cavity by about 120 μm in 50 ms while keeping the cavity stabilized. The

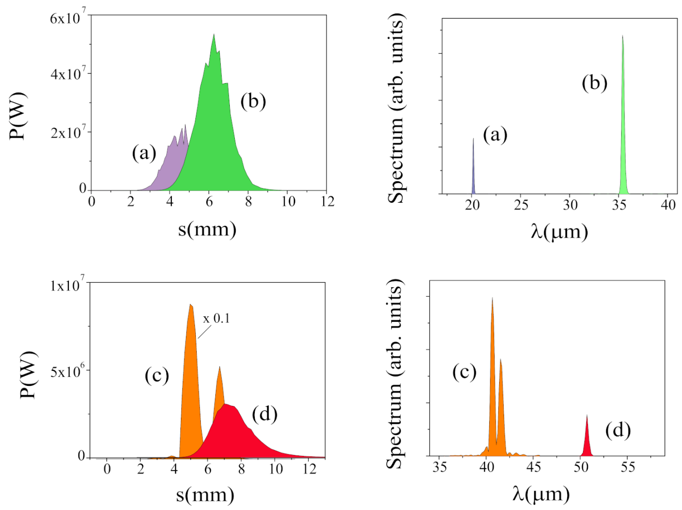

Figure 9: Two color radiation. Top line: power distribution P(W) vs coordinate z(mm) on the left and spectral amplitude (arbitrary units) vs λ(μm) on the right for (a) E = 40 MeV λ = 20 μm; (b) E = 40 MeV, λ = 35 μm; Bottom line: the same as in top line for (c) E = 25 MeV, λ = 40 μm; (d) E = 25 MeV λ= 50 μm.

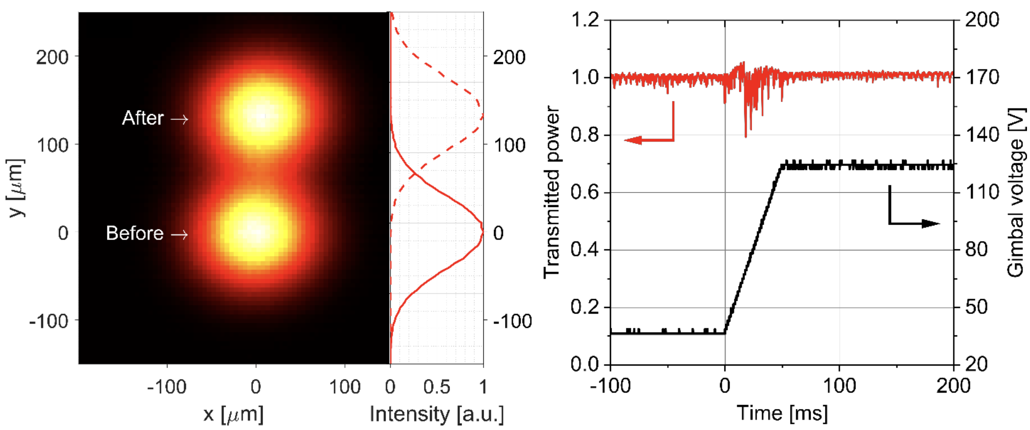

Figure 10: Radiation spot.

image of the focus before and after the movement are shown in Figure 10. Figure 11 shows the pre-amplifier.

The next steps of BriXSinO's R&D will be the construction and testing of the line for RF-guns at the LASA laboratory and the high power amplification test RF-Guns Line. The first amplification stage has been achieved up to 100 W. The high repetition operation mode is the basic operation mode of BriXSinO and the qualification of the Cs_2Te photocathodes at 100 MHz is a key passage. The main components of the test bench in installation at INFN LASA are: a DC gun to sustain 100 kV with a dedicated UHV beamline with diagnostic insertions; high voltage and high power components, in particular a 150 kV (at 3 mA) power supply; different photoemissive materials produced in the photocathode laboratory at LASA; a high repetition rate laser able to provide different pulse energies as well as different repetition rates. The state of the laboratory is documented in Figure 12.

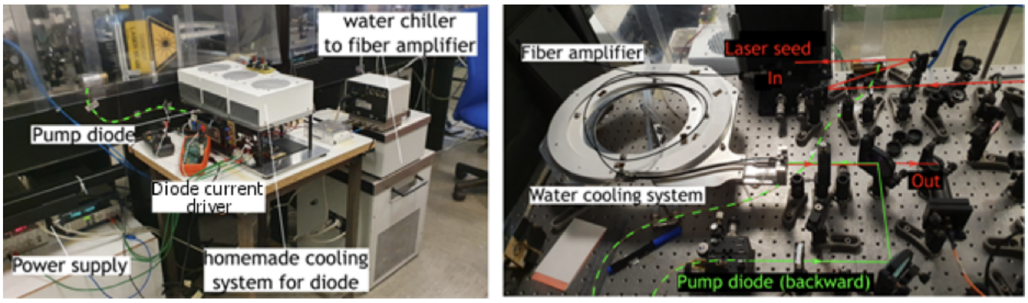

Figure 11: Preamplifier system. The preamplifier is pumped forward by a 976 nm Photontec (M976) laser diode, which supplies a maximum power of 60 W. Both pump light and seed pulses are coupled to the fiber thanks to a Pump Combiner from AFR Company.

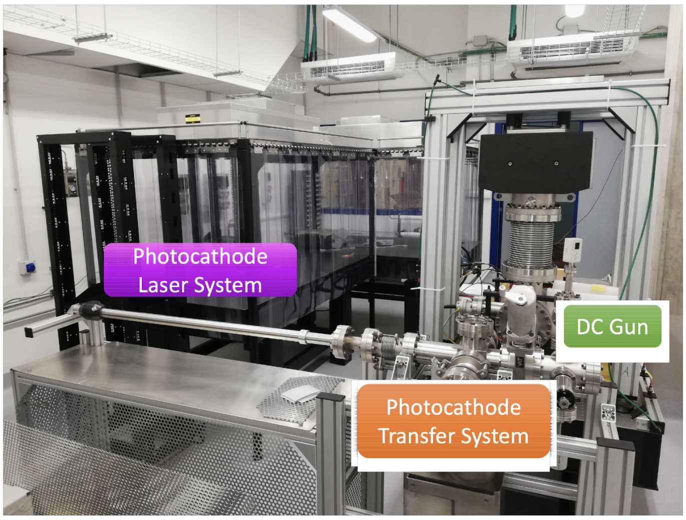

Figure 12: LASA laser laboratory: DC gun; 150 kV (at 3 mA) power supply; high repetition rate laser.

Timetable and costs

The tentative and preliminary timetable of the project is illustrated in Figure 13. Construction/acquisition and commissioning and operation in R&D and test-mode will overlap for a period of 3 years. All costs from the project preparation to the commissioning phase (i.e. prior to the start of operation) are summed up in order to determine the total project cost (TPC). The contributes to the TPC are summarized in VI (on the price basis of the year 2021) and are: the acquisition and/or development of main instrumentation parts as described in the previous chapters; the cost for commissioning the facility with beams; an additional personnel cost (not included in the TPC) covering allowances for personnel moving to work at LASA; the cost for personnel overheads related to management and support. Note that recurrent costs during the construction phase (electricity, water and Helium) are not included in the TPC since they have been assumed to be covered by the LASA operation budget free of charge to the BriXSinO project. The same applies to the cryogenic plant. The costs related to a dedicated building have been evaluated but they are not included in the TPC, leaving this as a possible option compared to others that involve different reconfigurations of the LASA laboratory. As part of the construction cost evaluation, every item in the budget list is estimated within an expected lowest and highest price range based on the current knowledge about the component or system. Using these price ranges, a statistical probability distribution of the project construction cost can be derived. The estimated prices were chosen such that the estimated construction cost is in the centre of this probability distribution, i.e. at 50% probability.

Table 6: Project cost.

Project preparation (before formal approval)	0.4 M€
Project construction	9.3 M€
Collaborations/Travels	0.9 M€
Personnel overhead	0.3 M€
Total construction cost	**10.9 M€**
Machine commissioning (ERL operation)	0.2 M€
Experimental areas	2.9 M€
Machine commissioning (experimental areas)	0.3 M€
Total project cost	**14.3 M€**
Research Grants	0.5 M€
Dedicated building	∼8 M€

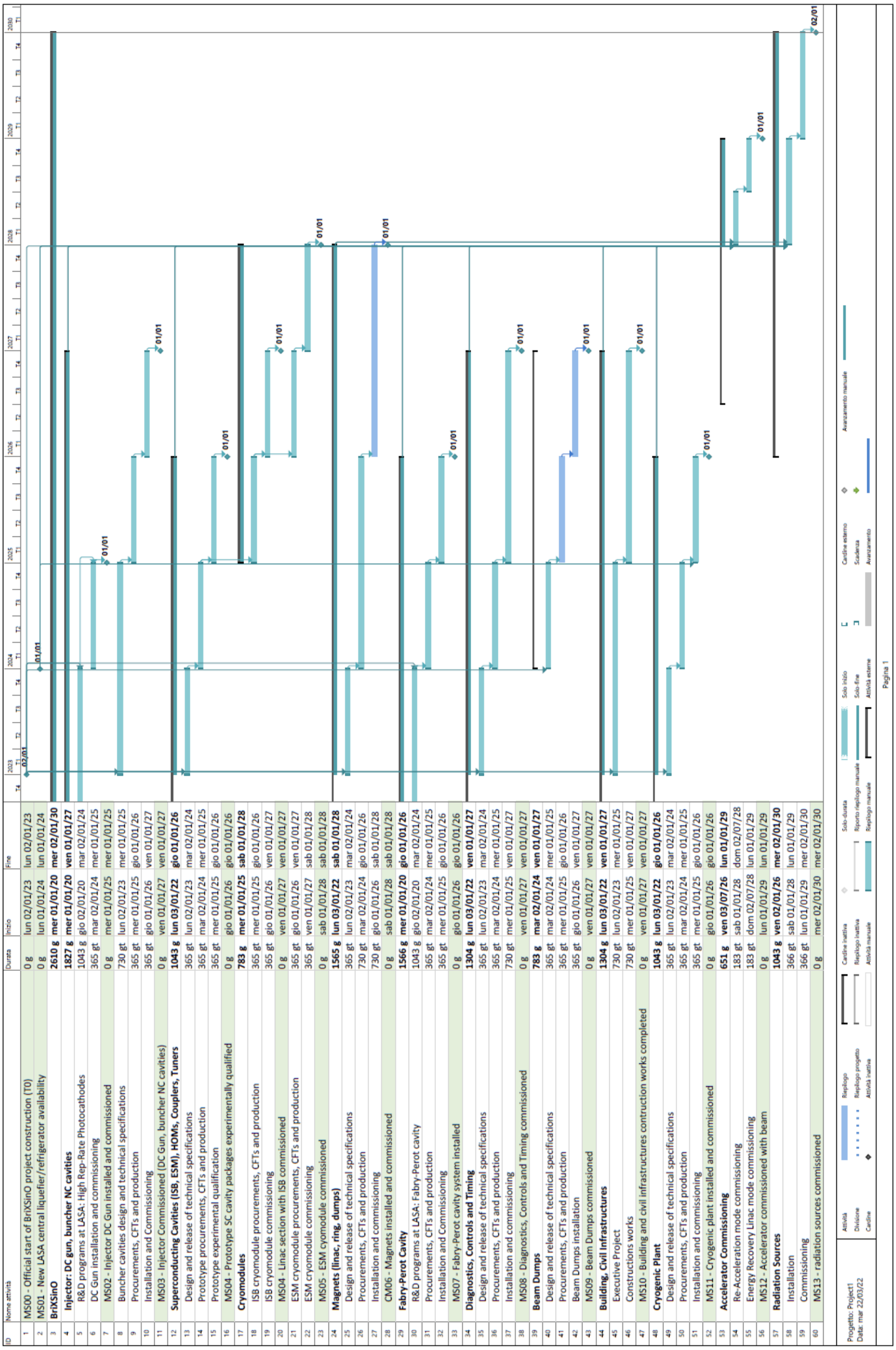

Figure 13: Tentative timetable of the project.

Bibliography

[1] M. Tigner. “A possible apparatus for electron clashing-beam experiments”. In: *Il Nuovo Cimento (1955-1965)* 37.3 (1965), pp. 1228–1231.

[2] CERN. *European Strategy for Particle Physics*. `https://europeanstrategyupdate.web.cern.ch/welcome`. Accessed: 2021-11-09.

[3] I. Ben-Zvi. “The 300 mA Srf Erl”. In: *AIP Conference Proceedings*. Vol. 1563. 1. American Institute of Physics. 2013, pp. 13–19.

[4] R.J. Michnoff et al. *CBETA-Novel Superconducting ERL*. Tech. rep. SLAC National Accelerator Lab., Menlo Park, CA (United States), 2019.

[5] L. Setafini. *BriXSinO Conceptual Design Report*. In preparation. 2022.

[6] L. Serafini et al. “MariX, an advanced MHz-class repetition rate X-Ray source for linear regime time-resolved spectroscopy and photon scattering”. In: *Nuclear Instruments and Methods in Physics Research Section A: Accelerators, Spectrometers, Detectors and Associated Equipment* 930 (2019), pp. 167–172.

[7] P Cardarelli et al. “BriXS, a new X-ray inverse Compton source for medical applications”. In: *Physica Medica* 77 (2020), pp. 127–137.

[8] V. Petrillo et al. “Coherent, high repetition rate tender X-ray free-electron laser seeded by an extreme ultra-violet free-electron laser oscillator”. In: *New Journal of Physics* 22.7 (2020), p. 073058.

[9] M. Opromolla et al. “High Repetition Rate and Coherent Free-Electron Laser Oscillator in the Tender X-ray Range Tailored for Linear Spectroscopy”. In: *Applied Sciences* 11.13 (2021), p. 5892.

[10] N.S. Mirian et al. “High-repetition rate and coherent free-electron laser in the tender x rays based on the echo-enabled harmonic generation of an ultraviolet oscillator pulse”. In: *Physical Review Accelerators and Beams* 24.5 (2021), p. 050702.

[11] C. Curatolo and L. Serafini. “Electrons and X-rays to Muon Pairs (EXMP)”. In: *Applied Sciences* 12.6 (2022), p. 3149.

[12] C. Koral et al. “Multi-Pass Free Electron Laser Assisted Spectral and Imaging Applications in the Terahertz/Far-IR Range Using the Future Superconducting Electron Source BriXSinO”. In: *Frontiers in Physics* (2022), p. 127.

[13] I. Drebot, V. Petrillo, and L. Serafini. “Two-colour X-gamma ray inverse Compton backscattering source”. In: *EPL (Europhysics Letters)* 120.1 (2017), p. 14002.

[14] E. Suerra et al. “A new method for spatial mode shifting of stabilized optical cavities for the generation of dual-color X-rays”. In: *Nuclear Instruments and Methods in Physics Research Section A: Accelerators, Spectrometers, Detectors and Associated Equipment* 1019 (2021), p. 165852.

[15] V. Petrillo. *High brilliance Free-Electron Laser Oscillator operating at multi-MegaHertz repetition rate in the short TeraHertz emission range*. 2022.

[16] A. Bacci et al. “Two-pass two-way acceleration in a superconducting continuous wave linac to drive low jitter x-ray free electron lasers”. In: *Physical Review Accelerators and Beams* 22.11 (2019), p. 111304.

[17] M Rossetti Conti et al. "Optimization of the arc compressor performance in the MariX free electron laser". In: *Journal of Physics: Conference Series*. Vol. 1596. 1. IOP Publishing. 2020, p. 012035.

[18] K. Flöttmann et al. *ASTRA: A space charge tracking algorithm*. 2011.

[19] M. Borland. *ELEGANT: A flexible SDDS-compliant code for accelerator simulation*. Tech. rep. LS-287. https://www.osti.gov/biblio/761286. Argonne National Lab., IL (US), Aug. 2000.

[20] A. Bacci, V. Petrillo, and M. Rossetti Conti. "GIOTTO: A genetic code for demanding beam-dynamics optimizations". In: *Proceedings of the 7th International Particle Accelerator Conference (IPAC 2016), Busan, Korea*. 2016, pp. 8–13.

[21] K. Yokoya. *User manual of CAIN, version 2.40*. 2009.

[22] S. Reiche. "GENESIS 1.3: a fully 3D time-dependent FEL simulation code". In: *Nuclear Instruments and Methods in Physics Research Section A: Accelerators, Spectrometers, Detectors and Associated Equipment* 429.1-3 (1999), pp. 243–248.

[23] Michele Opromolla and Vittoria Petrillo. "Two-Color TeraHertz Radiation by a Multi-Pass FEL Oscillator". In: *Applied Sciences* 11.14 (2021), p. 6495.

[24] V. Petrillo et al. "Photon flux and spectrum of γ-rays Compton sources". In: *Nuclear Instruments and Methods in Physics Research Section A: Accelerators, Spectrometers, Detectors and Associated Equipment* 693 (2012), pp. 109–116.

Contents

I The Machine 43

1 Introduction 45
1.1 Sustainability of electron accelerators: BriXSinO's way 45
1.2 Interest and Strategy for ERL in Italy and International Scenario 48
1.3 The Challenges of High Power/High Brightness Electron Beams 54
1.4 BriXSinO general layout 57

2 BriXSinO Beam Dynamics and Simulations 59
2.1 BriXSinO Beam Dynamics peculiar aspects 59
2.2 HOM evolution trough HOMEN model 67
2.3 Wakefield and HOM evaluation inside the ESM region 69

3 An Injector for 5 mA - 100 MHz electron beam 73
3.1 The DC gun with focusing solenoids 74
3.2 The 650 MHz sub-harmonic Bunchers 75
3.3 The transport optics 76
3.4 Injector Superconducting Booster (ISB) 77
3.5 Dogleg and matching section into the main ERL SC accelerating module. 78

4 The ERL Main SC-Linac 81
4.1 Cryomodule and SC Cavities 81
4.2 Power coupler 83

4.3 Frequency tuner 85
4.4 HOM absorber 85
4.5 Control system (Low level RF - LLRF) 86
4.6 SC cavity construction and characterization 87

5 Low Phase Noise Laser System 89

6 Compton Source: high flux X-Ray with F-P cavities 93
6.1 "Sors" Inverse Compton scattering X-Ray source 93
6.2 Fabry-Pérot cavities 96

7 High Power kW-class THz Free Electron Laser 101
7.1 The TeraHertz FEL Source TerRa@BriXSinO 101

8 Diagnostics, Timing Controls 107
8.1 Beam diagnostics 107
8.2 Timing & Synchronisation 109
8.3 Integrated Control System 110

9 Cryogenics 113
9.1 Overview and constraints 113
9.2 Superconducting cavity cryomodules 113
9.3 Cryogenic heat-loads 115
9.4 BriXSinO cryogenic plant scheme 116
9.5 BriXSinO operational workload for the LASA plant 117

10 Magnets 121
10.1 General Remarks 121
10.2 The injector optics 122
10.3 The arc optics 126
10.4 The dump optics 129
10.5 Undulator 129
10.6 Powering 129

11 Vacuum system, chambers 135
11.1 The beam line vacuum system 135
11.2 The insulating vacuum system 138
11.3 The RF coupler vacuum 138
11.4 Particle free operations 139
11.5 Vacuum security 139

12 Ancillary Plants 143
12.1 The electrical and thermal plants 143

13 Radio-Protection 149
13.1 Introduction 149
13.2 Shielding outlines 149
13.3 Shielding Design Criteria 150
13.4 The operational radiation safety program 153
13.5 Interlock design and feature 153

14 The Site and the Infrastructure Systems 157
14.1 The underground building 157
14.2 The buildings above ground 160

15 Cost Evaluation and Risks 163

16 Time Schedule (Detailed Tech. Design, Acquisition, Install., Commiss.) 169

II Users Experiments 173

17 X-Ray Advanced Imaging and Medical Applications 175
17.1 Monochromatic high-resolution X-Ray imaging system 176
17.2 2D and 3D Breast Imaging 176
17.3 Photon Counting pixel detector characterization 177
17.4 Dual-energy and K-edge subtraction imaging 178
17.5 Speckle-based Phase Contrast Imaging 180
17.6 Small-angle X-Ray scattering 181
17.7 Non-destructive Testing for Cultural Heritage and industrial samples 181

18 X-Ray Beam Lines and Experimental Stations 185
18.1 Beam stopper and beam shutter 186
18.2 Luminometer and beam intensity monitor 186
18.3 Filtration 186
18.4 Collimation 187
18.5 X-Ray transport to the experimental area 187
18.6 Experimental stations 187

19 THz Applications with kW-class beams 191
19.1 Introduction 191
19.2 Imaging for photoelastic processes in biomedicine 193
19.3 Hybrid approaches using X-Ray and metamaterial research for sensing in biology 193
19.4 Hyperspectral Imaging and THz thermometry 194

19.5 Geometric phase based shearography for stress tests on composite structures and surface profilometry 195
19.6 THz Hyper-Raman spectroscopy with twisted light for chiral agents' detection 196
19.7 Remote detection of inhomogeneities, form and stress birefringence in bulk materials based on GEST platform 197

20 THz Beam Lines and Experimental Stations 203
20.1 Introduction 203
20.2 Geometric Phase Optical Elements 203
20.3 Design of the optical layout of GEST platform 204

21 Applications of Electron Beams on Target 211
21.1 Introduction 211
21.2 Low energy electrons in Therapy 212
21.3 Ultrahigh dose rate X-Ray generation 212
21.4 A proposal for a dedicated experimental area 213

22 QUPLAS: fundamental research opportunities at BriXSinO 217
22.1 (QUantum interferometry and gravitation with Positrons and LASers) 217
22.2 Introduction 217
22.3 Towards Positronium Quantum Interferometry 218
22.4 QUPLAS and BriXSinO: the positron beam 218
22.5 Conclusion 219

III Appendices 221

23 Reports on ongoing R&D activity 223
23.1 The purpose of the R&D program 223
23.2 Laser System 223
23.3 The photocathode stress test 233
23.4 First results with HOMEN 237

24 Geologic survey 243

25 BriXSinO CAD pictures 253

List of Figures

1.1 ERL Landscape. 52
1.2 Brightness vs photon energy landscape. 53
1.3 BriXSinO general layout 57

2.1 Injector blocks schema sketch 61
2.2 Beam parameters 62
2.3 Dispersion plot 63
2.4 Simulation results 63
2.5 BriXSinO arc design. 64
2.6 One BriXSinO's DBA with its relative platform 65
2.7 Arc Twiss parametrs 66
2.8 Normalized emittance and transverse beam size 66
2.9 Beam path to FEL IP 67
2.10 CST electromagnetic model 69
2.11 Beam spectrum 70
2.12 Impedance real part 70
2.13 Modules impedance 71

3.1 Scheme of the "inverted insulator" 74
3.2 Scheme of the buncher cavities 77
3.3 IBS cryomodule schematic view 77
3.4 CBETA IBS SC cavity antenna power coupler 79
3.5 BriXSinO IBS SC cavity RF power scheme 79
3.6 Dogleg and matching section sketch 79

4.1 Layout of the ERL Superconducting Linac Module 82
4.2 RF forward power vs. beam current 84
4.3 Modified TTF III power coupler 84
4.4 ERL RF power distribution scheme. 84
4.5 CBETA ERL frequency tuner 85

4.6 HOM beamline absorber . . . 86
4.7 ERL LLRF scheme. . . . 87

5.1 Layout of the optical tables. . . . 90

6.1 Inverse Compton scattering IP. . . . 93
6.2 Geometry of the scattering process. . . . 94
6.3 Spectra of scattered photons. . . . 95
6.4 Number of scattered photons . . . 95
6.5 Spot size of scattered radiation . . . 96
6.6 Two color spectrum and energy angular distribution . . . 96
6.7 Layout of Fabry-Pérot cavities . . . 98

7.1 Radiation wavelength vs electron energy . . . 102
7.2 The undulator TU&IO at BriXSinO . . . 102

8.1 Three-tier Integrated Control System . . . 111

9.1 Schematic representation of technical interfaces . . . 114
9.2 Schematic cryogenic loops scheme . . . 115
9.3 Schematic layout of the BriXSinO cryogenic plant. . . . 117
9.4 BriXSinO requirements vs commercially available refrigerators . . . 119

10.1 BriXSinO general layout . . . 121
10.2 Injector blocks schema sketch . . . 122
10.3 Cross section of the AC1 solenoid . . . 123
10.4 BriXSinO injector dipole . . . 124
10.5 BriXSinO injector quadrupole . . . 125
10.6 BriXSinO arc layout . . . 126
10.7 BriXSinO arc dipole . . . 127
10.8 BriXSinO high energy dipole . . . 128
10.9 BriXSinO dump quadrupole . . . 131
10.10 THz radiation at 45 MeV . . . 132
10.11 THz radiation at 30 MeV . . . 132

11.1 the SAES Getters NEXTorr®pump. . . . 137
11.2 SIP ion pumps . . . 138
11.3 Layout of Slow pumping . . . 139
11.4 Layout of the BriXSinO vacuum system . . . 140

13.1 Typical shield behind high energy beam dump . . . 153

14.1 LASA location. . . . 158
14.2 LASA Aerial picture. . . . 159

15.1 Breakdown of the total project costs . . . 164

16.1 Proposal for BriXSinO timeplan . . . 170

17.1 Images of microcalcifications . . . 177
17.2 Linear attenuation coefficient . . . 179
17.3 Schematic of an X-Ray speckle imaging experiment. . . . 180

18.1 Sketch of the ICS X-Ray beamline . . . 185
18.2 Plot of Helium gas and dry air transmission . . . 187
18.3 View of the experimental hall . . . 188

18.4 Concept design of the experimental stations 189

19.1 Optical layout of the THz spectrometer 195
19.2 Details of the spectroscopy area 196
19.3 THYR Spectroscopy scheme 198

20.1 Working principle of a GPOE 204
20.2 Block diagram sketch of the platform GEST 205
20.3 Internal optical layout of GPBS 207
20.4 Internal optical layout of FSIGPP 207
20.5 Internal optical layout of PSID 208
20.6 Internal optical layout of GPSI 209

21.1 Scheme of the beamline for FLASH-RT 213
21.2 Scheme of the simulation setup for heatload 214
21.3 Coronal slice of the energy deposit in the W/Cu materials. 214
21.4 Radiative losses vs. collisional losses in a W target 215
21.5 Air kerma rate over photon energy. 215

23.1 Measured repetition rate as function of the motor step position. 224
23.2 Setup of the repetition rate stabilization system. 225
23.3 Amplification system scheme. 225
23.4 Pre-amplifier system assemble in laboratory. 226
23.5 Pre-amplifier stage output power plotted versus the pump power. . . 226
23.6 High-power amplifier stage with homemade cooled system. 227
23.7 Optical cavities with their active stabilization system. 228
23.8 Power spectral density of the optical cavity. 228
23.9 Scheme of the imaging system for cavity foci. 229
23.10 Shift of focus position 229
23.11 Photocathode laser layout 230
23.12 Laser line for the test of photocathodes 230
23.13 Impulse selection representation via BBO-Pockels Cell. 231
23.14 3D model of the optical table, view 1 232
23.15 3D model of the optical table, view 2 232
23.16 Sketch of the test bench at LASA. 233
23.17 Actual status of the laser lab at LASA. 234
23.18 Overview of the HV DC gun 235
23.19 Details of the HV DC gun 236
23.20 The LASA production systems 237
23.21 The LASA transport box (suitcase) 237
23.22 Typical spectral response of a Cs_2Te photocathode. 238
23.23 Expected performance for the Photocathode Stress Test 239
23.24 Beam dynamics simulation for stress test 239
23.25 HOM studies 240
23.26 First resonant monopole 241
23.27 Oscillation of the stored energy 241

25.1 BriXSinO axonometric projection. 253
25.2 BriXSinO top view. 254

List of Tables

1.1 A Comparison concerning efficiency and sustainability 47
1.2 BriXSinO's electron beam main parameters 49
1.3 Electron beam parameters at injection into THz-FEL undulator 50
1.4 Electron beam parameters after 2-way acceleration 51
1.5 Electron beam for fixed target experiments 51
1.6 Summary of most common used photocathodes 55

2.1 Laser pulse shape data 61
2.2 Best bunchers working parameters 61
2.3 Beam parameters at the injector exit 62
2.4 DBA quadrupoles parameters. 66
2.5 Beam parameters at ICS and FEL IPs 67

3.1 Request for Injector Beam generation. 73
3.2 DC Gun reference parameters. 75
3.3 Buncher cavities parameters. 76
3.4 Power requirements for the two buncher cavities. 76
3.5 BriXSinO ISB cavity parameters. 78
3.6 RF power requirements for ISB 79

4.1 BriXSinO ERL cavity main parameters 83
4.2 RF power requirements for two different energy recovery efficiencies. . 85

5.1 Harmonics parameters 91
5.2 Cavity parameters 91

6.1 Parameters of start to end simulations 97

7.1 PM: permanent magnets, VG: variable gaps, LP: linear polarization . . 103
7.2 Intra-cavity radiation vs undulator length and current 104
7.3 Intra-cavity radiation vs emittance and current 104
7.4 Properties of the intra-cavity (IC) and extra-cavity (EC) radiation 105

7.5 Intra-cavity radiation vs energy spread 105

8.1 Main measured quantities. 107

9.1 Electromagnetic parameters for BriXSinO SC cavities. 115
9.2 Expected cryogenic heat-loads 116
9.3 $2\,\mathrm{K}$ circuits expected requirements 118
9.4 $4.5\,\mathrm{K}$ circuits expected requirements 118

10.1 BriXSinO optics. 122
10.2 The solenoid main parameters. 123

11.1 BriXSinO vacuum systems 136

15.1 Contributions to the total project cost. 164
15.2 Relation between the WP groups and the chapters in this report . . . 164
15.3 Risks assessment and mitigation. 165

16.1 BriXSinO's milestones 171

21.1 Electron beam parameters for fixed target experiments 211

23.1 $2\,\mathrm{K}$ circuits expected requirements 224

The Machine

1 Introduction 45

2 BriXSinO Beam Dynamics and Simulations 59

3 An Injector for 5 mA - 100 MHz electron beam 73

4 The ERL Main SC-Linac 81

5 Low Phase Noise Laser System 89

6 Compton Source: high flux X-Ray with F-P cavities 93

7 High Power kW-class THz Free Electron Laser 101

8 Diagnostics, Timing Controls 107

9 Cryogenics 113

10 Magnets 121

11 Vacuum system, chambers 135

12 Ancillary Plants 143

13 Radio-Protection 149

14 The Site and the Infrastructure Systems 157

15 Cost Evaluation and Risks 163

16 Time Schedule (Detailed Tech. Design, Acquisition, Install., Commiss.) 169

1. Introduction

1.1 Sustainability of electron accelerators: BriXSinO's way

Particle Accelerators are well known to be a class of devices characterized by very low *energy sustainability*, mainly due to their low efficiency to transform AC electrical power into particle beam power, that is a primary figure of merit concerning experiments and/or applications performed with accelerated particles.

Part of the reason for such a low efficiency comes from the need to perform an extremely large frequency up-conversion in the oscillating electro-magnetic fields responsible for accelerating the beam, typically from the 50-60 Hz of the AC power network up to the multi-GHz range of Radio-Frequency (RF), or the THz range of plasma/optical waves, at a level of peak power exceeding tens of MW to a few PW, and average power from hundreds of kW up to tens of MW. The low efficiency in transferring part of the electro-magnetic energy stored in the accelerating field (associated to either RF waves or plasma waves) into the kinetic energy of the accelerated particle beam, is another reason of such an insuccess of particle accelerators on the *road toward high efficiency and large sustainability*.

However, being particle accelerators well recognized as one of the best tool of discovery in the history of human kind, such a poor score in achieving good efficiencies and large energy sustainability has been quite neglected so far, or in best case considered as a minor issue.

An increasing awareness in the particle accelerator community, in particular that involved in developing particle accelerators for scientific research, about an *increasing and irreversible request of sustainability* coming from society at large, is raising consensus in deploying more and more resources to developing more sustainable accelerators for the future scenarios in the High Energy Physics (HEP) frontiers as well as in the applied research frontiers. After LHC power bill, with an AC power consumption of 120 MW, and having in mind the foreseen FCC power consumption of 580 MW, the HEP community is perfectly aware that a change in strategy has to be conceived for the long-term future. An *increase in global sustainability* (energy and financial - the two are inherently connected) is becoming a must.

Restricting the discussion to Electron Accelerators, novel techniques have been seriously investigated and pursued in the last decade, giving rise to a *new generation of accelerators*, named

E.R.L. (Energy Recovery Linacs), that although still in its infancy, holds a strong promise to be the paved road toward the future of sustainable accelerators. Its acronym by itself clearly points out the concept of energy recovery opposed to energy waste - it looks as the right way to go.

BriXSinO, as described in this document, aims at developing at INFN LASA laboratory a test-facility that would enable addressing the physics and technology challenges posed by the ERL generation, hoping to make in a short-to-mid term scenario a *significant advance in the National and INFN contest*.

As for all electron accelerators, radiation emission from the (high brightness) accelerated electron beam is typically an opportunity as well as an issue. The opportunity consists in enabling applications with the emitted bright synchrotron radiation beams - this is the case for accelerators devoted to applied research and/or the medical field - while the issue deals with very large electron accelerators serving HEP experiments (typically colliders), where the loss (waste) of energy due to synchrotron radiation emission seriously limits the feasibility as well the sustainability of these large machines at the energy frontier (e.g. LEP, LHC, FCC-ee, etc).

The development of BriXSinO's test facility at LASA aims at investigating both domains, the one where best efficiency in accelerating a high power electron beam is pursued, and the one where very high flux radiation beams (in THz spectral range and in X-Rays) are made available to medical applications and applied research in general, with an *overarching mission* dealing with maximizing the beam power available to users and experiments for the minimum AC power consumption, in other words the *maximum energy sustainability*.

In order to better underline the key factors of energy sustainability in particle accelerators we list in the following Table a few paradigmatic examples of different types of electron accelerators, trying to cover almost all the available technologies in the zoology of electron accelerators. Ranging from plasma-based accelerators to Superconducting Linacs, to Storage Rings. For sake of comparison and for a broader overview, we listed also some paradigmatic cases of proton machines, like LHC and the 590 MeV PSI Cyclotron.

The main figures of merit derived in the Table are i) the *beam-to-plug efficiency*, *i.e.* the ratio between the absolute beam power generated and the total AC power consumption needed to run the machine and its ancillary plants. And ii) the so-called "*true efficiency*" , that is defined as the ratio between the *available beam power* and the total AC power consumption. Available beam power is a concept involving the amount of beam that can be wasted by any user of the accelerator, actually by all users simultaneously performing experiments with the beam: a user can waste beam either by intercepting particles in the beam and making them disappear (as for experiments at a collider) or by decreasing the beam kinetic energy by making its particles radiate e.m. fields.

The input data listed in the Table 1.1, used to evaluate beam-to-plug and true efficiencies, are the maximum energy of the accelerated electrons, the average current (i.e. the total amount of bunch charge accelerated in a second), the beam power (being a product of these first two quantities), the AC power consumption (setting the annual power bill of the machine): the ratio between these two last quantities represents the b-t-p efficiency. In the column before the last one we list the beam availability as defined above: this quantity is needed to compute the true efficiency as the ratio between the available beam power and the AC power consumption.

Why do we need to refer to true efficiency instead of b-t-p efficiency? Clearly because not all accelerators are configured and operated so to let users "burn" completely the beam: typically only Linacs are meant to deliver the beam to users and let them waste it completely (to a beam dump or to an equivalent fixed target experiment). Linacs grant full access to beam, while storage rings almost no access: ERLs *allow full access to beam phase space but very limited access to beam energy/power*.

As a matter of fact, accelerators based on ERL schemes want to recover most of the beam power so to decrease the AC power bill, so that only a small fraction of the beam power is available to users, while accelerators based on storage rings are severely limited in the amount of beam that can

Table 1.1: A Comparison concerning efficiency and sustainability among Plasma Linacs (a), RT-Linacs (b), SC-RF Linacs (c), ERLs (d), Storage Rings (e), High power Cyclotrons (f). (*limited by beam dump **power emitted in synchrotron radiation *** 10 h life-time (360 MJ / 36,000 s))

ACCELERATOR	Energy Energy	Average current	Beam power	AC power	Efficiency b-t-p	Beam availability (beam power)	True efficiency
EuPRAXIA@SPARC_LAB (a)	5 GeV	0.3 nA	1.5 W	2 MW	7.5×10^{-7}	100% (1.5 W)	7.5×10^{-7}
BELLA (a)	7.8 GeV	5 pA	40 mW	200 kW	2.0×10^{-7}	100% (40 mW)	2.0×10^{-7}
STAR (b)	150 MeV	100 nA	15 W	400 kW	3.8×10^{-5}	100% (15 W)	3.8×10^{-5}
MariX (c)	3.8 GeV	50 µA	190 kW	17 MW	1.1%	100% (190 kW)	1.1%
Euro XFEL (c)	19 GeV	32 µA	608 kW	17.8 MW	3.4%	100% (608 kW)	3.4%
BriXSinO (d)	45 MeV	5 mA	225 kW	450 kW	50%	10% (22 kW)*	4.9%
Elettra (e)	2 GeV	310 mA	620 MW	4.0 MW	n.a.	0.015% (90 kW)**	2.3%
LHC (e)	7 TeV	540 mA	3.8 TW	120 MW	n.a.	3.2×10^{-9} (10 kW)***	$\sim 10^{-4}$
PSI Cyclotron (f)	590 MeV	2.4 mA	1.4 MW	10 MW	14%	100% (1.4 MW)	14%

be wasted, just because they cannot afford a life-time as short as a few turns of the ring (otherwise they wouldn't be called "storage rings"!). The beam power listed in case of storage rings looks enormous, but one has to consider that this is not active power, but purely reactive power, therefore not available to be dissipated.

The first four examples (EuPRAXIA, BELLA, STAR and MariX) are Linacs, BriXSinO is an Energy Recovery Linac, Elettra a storage ring operated as a light source, and just for reference we report also LHC numbers and features, since it represents the case of a storage ring for protons where the amount of available beam to experiments is really very small - it is the fraction of protons disappearing due to collisions. Not surprisingly, the case of high power cyclotron (590 MeV PSI Cyclotron) achieves the best performance in terms of efficiency in the global scenario of particle accelerators. Cyclotrons are quite simple and compact machines (for the delivered proton energy) that allow the user to completely burn the CW beam (similarly to Linacs, true efficiency is in this case equal to b-t-p efficiency).

Concerning electron accelerators, *Linacs are very poor in sustainability performances*, storage rings are doing quite better, the real way to go is ERL: nevertheless, LED performances (almost 85% efficiency), a paradigmatic example of a significant break-through in energy sustainability, looks like an unreachable goal.

Main characteristic of ERLs is to be a good compromise between beam full availability married to full waste, the Linac case, and highly reduced beam availability married to beam saving, the storage ring case.

Energy Recovery Linacs give users/experiments full access and availability to the beam phase space quality/density, but very limited access to beam energy and particles. This is a reasonable compromise between use of the beam and beam power waste/dissipation. The ERL compromise is attractive not only to users looking for radiation oriented experiments, i.e. those experiments that use the e.m. radiation generated in various forms by the electron beam, like Free Electron Lasers (FEL), Inverse Compton Scattering (ICS), and synchrotron radiation, but also in the HEP scenario, as extensively discussed in ref. [1] concerning CERC, Perle, ERLC and EXMP.

As clearly pointed out in the table, Linacs based on Room Temperature RF and plasma waves exhibit very poor efficiencies ($< 10^{-4}$), either because most of the AC power is dissipated into heat, and because the beam is completely wasted without any recovery. Superconducting Linacs like MariX have a quite better efficiency, although we should note that the value listed (1.1%) is evaluated considering the full availability of the electron beam, that is generally not used in Linacs driving FELs (users are interested only in radiation beams).

The light source case based on storage ring, represented by Elettra in Table 1, clearly shows that the amount of available power to users (90 kW is the synchrotron radiation power emitted by Elettra) is a very small fraction of the beam power, bringing in any case the true efficiency at a much larger value than Linacs (2.3%). The case of LHC is very peculiar but quite interesting as a reference comparison: this is a storage ring of protons where the beam power is lost either by emitting synchrotron radiation (accounting for about 6 kW) and by loosing protons in collisions (those necessary to generate Higgs bosons and a wealth of other elementary particles of the SM zoology). At the end only 10 kW of LHC beam power is available to users and/or "dissipated", bringing to a very modest true efficiency of about 10^{-4}, slightly better than Linacs.

Instead, BriXSinO's way to high sustainability addresses the challenge by applying a newly conceived scheme of ERL with counter-propagating beams: 5 mA of average electron beam current in CW mode with a time structure (regular repetition rate up to 100 MHz, *i.e.* bunch spacing 10 ns) at all similar to that of a storage ring, but with very large recovery of the 225 kW beam power (>90%). BriXSinO's users will be allowed to use at will the beam quality and phase space, *i.e.* with significant degradation of emittance and energy spread of the beam due to the impact of FEL emission or Compton backscattering, saving at the same time large part of the electron beam kinetic energy for the recovery of the beam power via deceleration in the same SC Linac. As a matter of fact, the electron bunches in a ERL like BriXSinO are traveling through the full orbit back-and-forth just one time, so even a serious degradation of phase space quality may be acceptable for just taking back the beam to the deceleration through the Linac, necessary to recover its energy. Instead, electrons in a storage ring must travel over many turns (>10^{10}) so their phase space quality must be very carefully preserved to avoid instabilities that may seriously impact the storage ring life-time.

Needless to say, BriXSinO's beams will be characterized by similar levels of high brightness as other (non-ERL) Linacs, large enough to drive FELs and/or ICS, *i.e.* rms transverse normalized emittances in the µm range and relative energy spreads in the 10^{-3} range.

BriXSinO could be the Italian test facility for ERL-based HEP machines, like EXMP [2], a new paradigm of muon collider based on electron-photon primary collisions, conceived and designed at Milan-LASA as a HEP oriented opportunity for BriXSinO. Indeed, in EXMP it is of crucial relevance the generation, acceleration and energy recovery of high brightness large power electron beams, which have to drive also high powerX-Ray FELs to provide the photon beams for collisions. This is a perfect combination of technological and physics issues to be addressed by a test facility oriented to ERL, FELs and radiation sources in general.

A list of BriXSinO's electron beam characteristics are listed in Table 1.2, emphasizing 3 cases of operations, namely the ERL operation to drive ICS at very large photon flux (10^{12} photons/s), the ERL operation to drive a kW-class THz FEL, and the MariX-like operation of *two-way acceleration*. Experiments with THz FEL and ICS are described further on in Chapter 17 and 19.

A further operation mode for BriXSinO that is conceived and illustrated in this document is the use of BriXSinO's injector for fixed target experiments, performed with maximum electron energy of 10 MeV and 2.5 mA average current (see Table 1.5). The availability of such a high intensity beam (50 kW) enables both experiments of flash therapy tests using electrons, with a capability to irradiate samples with a delivered total charge in a 200 ms time interval up to 1 mC, as well as converting the electron beam into bremsstrahlung photons with energy peaked at 7-8 MeV at an impressive flux of 10^{16} photons/s (*i.e.* up to 30 kW X-Ray beam!). These experiments will be illustrated in Chapter 21.

1.2 Interest and Strategy for ERL in Italy and International Scenario

Energy recovery as a concept dates to as early as 1965 [3]. As with many innovative accelerator ideas the practical realization of the concept took many decades to materialize.

An almost unknown contribution to this idea was due in 1977 by a 25 MeV electron double-pass Linac (named reflexotron) built and tested in a medical-therapy configuration at Chalk River Labs

Table 1.2: BriXSinO's electron beam main parameters: Electron beam parameters at Compton Interaction Point for I.C.S.

Energy (MeV)	22 - 45
Bunch charge (pC)	50 - 200
Repetition rate (MHz) (CW operation, ca. 92.86 – 0.9286 MHz)	1300./14, down to 0.9286
Average Current (mA)	< 5
Nominal beam power (kW)	< 225
Beam energy @ dump (MeV)	4.5
Beam power @ dump (kW, after ERL)	< 22.5
Bunch length (rms, mm)	2.2
$\varepsilon_{nx,y}$ (mm – mrad)	1.0 – 3.0
Bunch Energy spread (rms, %)	0.5 – 1.5
Focal spot size (rms, µm)	30 - 60
Bunch separation (ns)	10 – 1000
Beam energy fluctuation (rms)	< 0.1 %
Time arrival jitter (fs)	< 150.
Pointing jitter (µm)	10.

[3]. The first appearance was through demonstration experiments conducted initially at the SCA FEL machine at Stanford [4] and MIT-Bates [5]. However, the real impact on accelerator developments was the operation at Jefferson Lab of DEMO-FEL [6]. This inspired various groups throughout the world to explore the potential of energy recovery for various applications, including pushing the boundaries of existing technology to deliver highly advanced light sources encompassing both FELs and spontaneous sources.

1.2.1 Energy Recovery Linac basic idea

In an energy recovery linac (ERL), in its most basic configuration, electrons are generated in a high brightness electron source, accelerated through the linac, and transported by a magnetic arc lattice to the point of their end use, which could be a photon generating device (a wiggler or an undulator) if the ERL is used as a light source, or the interaction region with protons or ions if the ERL is used either for the electron cooling of high energy ion beams, or to provide the electrons in an electron-ion collider. After they are used, the electrons are transported back to the entrance of the linac 180° out of phase for deceleration and energy recovery and they are dumped at an energy close to their injection energy. ERLs can be compared and contrasted with the two traditional types of accelerators, storage rings and linacs.

1.2.2 Energy Recovery Linac Rationale

The characteristics of synchrotron radiation beams are ultimately limited by the properties of the electron or positron beams used to produce the SR. These limits are well understood for storage rings and the ultimate characteristics obtainable with storage rings are within sight of those now obtained with the best third-generation machines. The principal limitations are on the bunch length, cross-sectional distribution, and the vertical and horizontal emittances. Most typically, the bunches are several tens of ps long, and have horizontal emittances and sizes which are considerably larger than in the vertical direction. The emittances ultimately limit the brilliance of the SR, which, in

Table 1.3: Electron beam parameters at injection into THz-FEL undulator

Energy (MeV)	22 - 45
Bunch charge (pC)	50 - 100
Repetition rate (MHz) (CW operation, ca. 92.86 – 46 MHz)	1300./14 or 1300./28
Average Current (mA)	5
Nominal beam power (kW)	< 225
Beam energy @ dump (MeV)	4.5
Beam power @ dump (kW, after ERL)	< 22.5
Peak Current (A)	8 - 12
$\varepsilon_{nx,y}$ $(mm-mrad)$	1.5
energy spread (%)	0.1
slice $\varepsilon_{nx,y}$ $(mm-mrad)$	1.2 – 1.7
slice energy spread (%)	0.05
Bunch separation (ns)	10 - 20
Beam energy fluctuation (%)	< 0.05
Time arrival jitter (fs)	< 50.
Pointing jitter (μm)	20.

turn constrains the transverse coherence; the source size and shape constrains the micro-X-Ray beams possible; and the bunch length limits the ability to produce intense sub-ps X-Ray pulses. The combination of transverse and longitudinal emittances also constrains the degeneracy factor, i.e., the number of photons in each quantum mode. Many applications have been suggested which would benefit from higher brilliance, smaller source size, and shorter pulses than are feasible with storage rings.

In storage rings, the emittance and bunch length are established by a dynamic radiation equilibrium, the minimum value of which is controlled, for a given focusing lattice, by the beam energy: the higher the energy, the larger the emittance.

By contrast, the beam emittance and bunch length in a well-designed linac are controlled entirely by the particle source preceding the linac. Today's electron sources have inherent six-dimensional emittances less than those achievable in SR-controlled storage rings, making higher brilliance possible with linac drivers. Therefore, the proposed XFELs, which require very low emittance, are all based on linacs.

The drawback is that it takes a lot of power to accelerate the high-current electron beam needed to produce high X-Ray flux. A 100 mA beam at 7 GeV, typical of the APS, carries 700 MW of power, which is the output of a large electrical generating station. A continuously operating high-current linac may be prohibitively expensive to operate if the electron-beam energy is discarded. In a storage ring, using the same electrons repeatedly circumvents this continual power need, so the kinetic energy of the initial acceleration is not wasted.

The alternative to storage rings and to simplified schemes based on linacs may be found using an approach that looks at energy as the main resource. Linacs operate by maintaining a resonant electro- magnetic field to exert a unidirectional force on a charged particle. Whether a linac accelerates or decelerates electrons depends on the position of the electrons relative to the phase

Table 1.4: Electron beam parameters at diagnostic station after 2-way acceleration (a la MariX)

Energy (MeV)	< 80
Bunch charge (pC)	50 - 20
Repetition rate (MHz for CW operation)	0.9286
Average Current (μA)	5
Beam power @ dump (W)	400
$\varepsilon_{nx,y}$ (mm – mrad)	1.0
energy spread (%)	< 0.2
Bunch separation (μs)	> 1
Beam energy fluctuation (%)	< 0.2
Pointing jitter (μm)	50.

Table 1.5: Electron beam for fixed target experiments

Energy (MeV)	< 10
Bunch charge (pC)	25 - 50
Repetition rate (MHz for CW operation)	< 92.86
Average Current (mA)	2.5 - 5
Beam power @ dump (kW)	< 50

of the electromagnetic field. When a linac is used as a decelerator, the particle kinetic energy is transferred into the resonant electromagnetic field, which can then be used to accelerate other electrons. An energy recovery linac is characterized by high average beam power (multi GeV @ some 100 mA) for single pass experiments, excellent beam parameters, high flexibility, multi user facility. Thus, the primary distinction between a storage ring and an ERL is that the ERL is designed to recycle the electron energy rather than the electrons themselves.

The central role played by energy in such an approach leads to consider superconducting linacs as the ideal solution, to minimize wall losses and obtain high efficiency, thanks to their Q values of the order of 10^{10}. Moreover, in RT linacs CW high current operation mode is hampered by limited HOM damping capabilities. SC RF allows to build ERL "compact" (high gradient) machines for high current CW operation (large aperture, strong HOM damping). Considering SC as an envisaged technology for ERL linac designs, we must carefully analyze the fact that wall plug power balance moves from RF to cryogenics. Existing advanced cryogenics knowledge and plants constitute facilitator elements in the proposal of a new facility.

1.2.3 Existing ERL facilities and open challenges

The picture below summarizes the status of ERL facilities in the world ranging from the ones that have ceased operations, up to operative and in progress projects.

It is noticeable that the current situation cover a range of beam current up to 30 mA and energies up to tens of MeV. Higher energies up to 10-100 GeV are due to proposed facilities devoted to ERL-based energy frontier collider projects and proposals [7].

The number of operative facilities and ongoing projects is quite low but still shows a great interest in the field, both from the experimental point of view of the obtainable radiations and in the progress in accelerator technology.

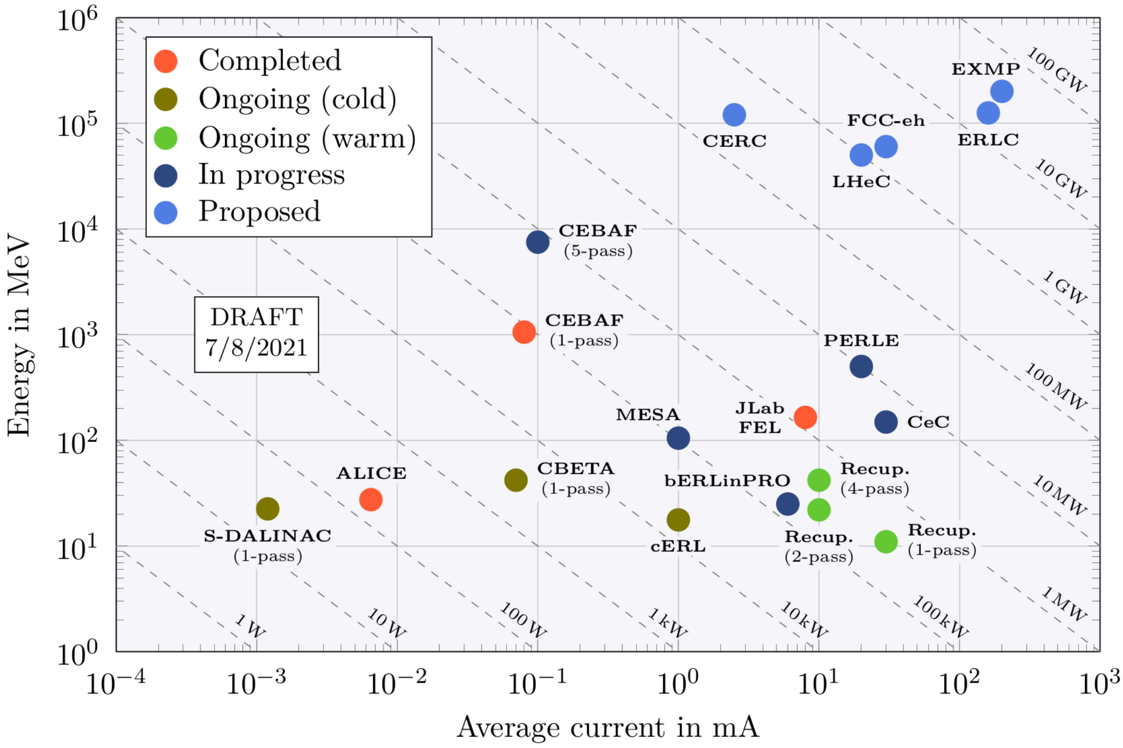

Figure 1.1: ERL Landscape.

The main challenges in accelerator technology are related to all the different areas involved in ERL designs:

- Beam generation: the current target value of CW beams with currents of the order of 100 mA and optimum beam emittance of the order of few microns may be obtainable using different technologies ranging from DC guns up to RF guns, both as RT machines or superconducting ones. Although a DC gun seems the most probable solution for today projects because of the maturity of its development, there are still significant challenges in achieving the high voltages required for low emittance, and developing a practical cathode system that will reliably deliver 100 mA.
- Acceleration: superconducting RF technology for electron linacs may be considered mature, looking at the considerable amount of efforts applied over recent years, for example towards accelerators suitable for a future linear collider. Nevertheless, most of these development have been devoted to the achievement of high gradients in pulsed systems with low currents beams. The requirement for the ERL main accelerator is for CW operation and demands the use of efficient (high Q), controllable cavities, with designs which minimize HOMs and extract their power efficiently.
- Electron Beam Transport: the high quality beams generated and accelerated must be transported to the source points without significant degradation of the transverse emittance. The longitudinal properties of the beam have to be manipulated to produce highly-compressed beams, capable of producing sub-picosecond sources and driving the user experiments. At low energies, space charge presents a challenge. The beam transport also must be designed to minimize the disruption by instabilities such as CSR through the arcs and wake field effects in the linacs and in the space reserved for the experiments.
- Diagnostics: the success of ERLS facilities will require advanced diagnostics and the development of tuning procedures which can use those diagnostics to achieve and maintain

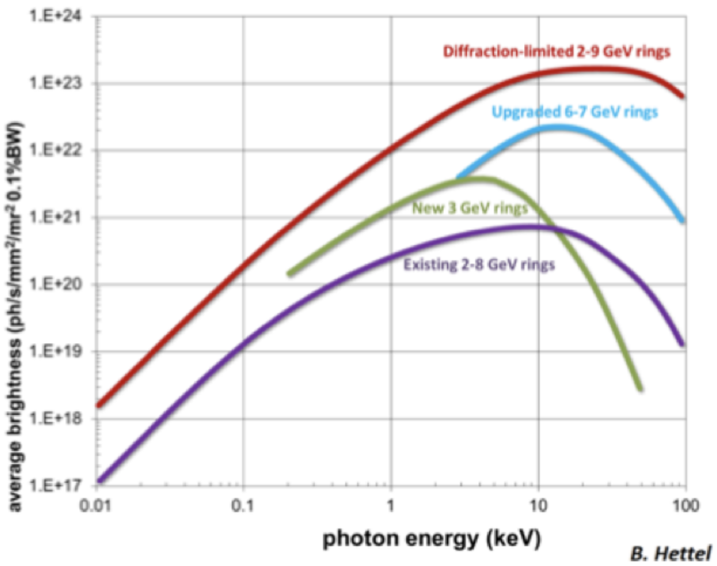

Figure 1.2: Brightness vs photon energy landscape.

the demanding operating performance.

Many groups are active in developing different approaches to the areas above discussed and collaborations between these groups are underway to facilitate the establishment of new ERL facilities and to advance and expand in a reasonable time interval the possibilities offered by these machines.

The above discussions about the ERL scheme may be summarized as the follows:

- Provide (nearly) linac quality/brightness beam at (nearly) storage ring beam powers
- Mitigate intractable (i.e. expensive) environmental/safety concerns since we may dump the beam at low energy
- Allow to consider higher power applications than would otherwise be unaffordable, looking at GW class beams.

In just a statement we can say that "ERLs apply wherever a beam with simultaneous high quality and high average power is needed"

Considering this statement and looking at the existing and operative facilities, we may analyze the panorama of ERL applications. Most of them are related to new opportunities in FEL radiation applications.

Free electron lasers offer simultaneous transverse and longitudinal coherence and peak brightness approaching 10 orders of magnitude improved with respect to spontaneous SR sources. This makes them very attractive for chemistry, biology, drug development, materials development etc. To date however, FELs are limited in AVERAGE brightness with respect to "4$^{\text{th}}$ generation" spontaneous SR sources. Indeed, the lasing process is too good at extracting power from the electron beam and putting it into the radiation, so the spent beam is too "screwed up" to store in a storage ring.

Applications of ERL-FELs to the "real world" are still in its infancy. Some examples are shown below:

JLAB FEL (1995-2013) 10 kW IR-FEL, 1 kW UV-FEL, broadband THz

- Discoveries in material synthesis using the FEL has led to the founding BNNT LLC in 2010, which specializes in Boron Nitride Nanotube synthesis.
- BNNT materials particularly useful for aerospace construction where enhanced radiation shielding needed – e.g. interplanetary spacecraft.

Daresbury ALICE (2005-2017)

- Multiyear user program on esophageal cancer diagnosis technique
- The challenge was to identify patients with Barrett's oesophagus who will develop esophageal cancer – present diagnosis method subjective – leads to false positives

NovoFEL (2003-present)

- THz & IR for biological research

KEK CERL (2010-present)

- In process of converting to FEL research for lithography industry

Recently an exciting proposal for the use of high current electron beams arises in Europe and may represent the first industrial use of a high power superconducting linear accelerator. In 2016, a project launched by the Dutch company ASML, a world leading manufacturer of lithography systems, received the National Icon award of the Netherlands for a novel concept to produce molybdenum 99 (^{99}Mo), the world's most used medical isotope which is an important tool in medical diagnostics and cancer treatment. The new production method suggested by ASML is based on an electron accelerator and could become a good alternative to the current way of production in only a few remaining old nuclear reactors, which also produces high-level radioactive waste and, due to the age of the reactors, does not have a long-term perspective.

MeV photons are predominantly produced by linac accelerated electrons impinging on target and the process involved is bremsstrahlung. This will result in a white source, broadband dominated by low energy photons with high energy cutoff. A tunable and monochromatic / monoenergetic / narrowband source of MeV photons with high flux would allow the "photonics" paradigm of atomic physics enabled by solid state lasers from 1960s to be translated to the nuclear regime. The inverse Compton scattering (ICS) of electrons on external (laser) photons is the solution to this expectative, due to energy-angle correlation combined with collimation. ICS sources may take advantage of ERL schemes because after the energy recovery the energy spread caused by the ICS can be reset and the low emittance beam can be recovered.

Photons from 1 to 300 MeV may be obtained with different foreseen applications in detection of clandestine nuclear materials, defects in fuel assemblies, nuclear decommissioning. Isotopic transmutation at industrially relevant quantities without need for chemical partition.

1.3 The Challenges of High Power/High Brightness Electron Beams

High-brightness electron beam source development is a critical element in the path to the success of upcoming projects, such as linac-based light sources and industrial-scale UV lasers.

Disparate needs are driving injector design in several different directions; for instance, high beam powers for IR and UV FELs, low transverse emittances for linac-based X-Ray light sources, and emittance aspect-ratio control for linear colliders.

High-brightness electron gun development can be broadly categorized into different distinct categories. Injectors for national facility-scale linac-based light sources represent one broad category. This includes both X-Ray free-electron lasers and energy-recovery linacs; the main differences lie in the required beam repetition rates, as the desirable single-bunch characteristics are quite similar. Second, there is presently strong interest in the use of small energy-recovery linacs to provide beams for high- power IR and UV free-electron lasers. The injectors for this category of devices generally have (relatively) relaxed transverse emittance requirements, strong longitudinal emittance requirements, and very high ($\sim$ 1 A) average beam current requirements. Finally, electron beam sources for next-generation linear colliders represent a combination of several fascinating challenges. The ability to produce a "flat" beam with a high transverse emittance ratio could at worst reduce the requirements on the e- linac damping ring, and at best eliminate the need for one altogether.

There are elements common to most of these areas of application, however, which must be addressed regardless of the final application. These include:

- Increasing the duty factor, for higher average performance figures.
- Improving the beam quality, for higher single-bunch performance figures.
- Improving the techniques used to build the guns, e.g., for improved symmetrization, cooling (for NC guns), or power-feed capabilities (for SRF guns).
- Increasing the operational reliability of the entire injector system, including drive laser and RF systems.
- Improving the fundamental electron source, e.g., cathodes and cathode research.
- Improving the basic tools (theory and simulation) used to understand and design injectors.

Of these, perhaps the cathode research and development is the most critical common element. All of the injector Technology, Components, Subsystems Particle Sources, Injectors categories require high-performance cathodes in one sense or another. Sensitive improvements in lifetime, robustness, quantum efficiency, and thermal emittance are known requirements. Electron beam emission uniformity is known to be a critical factor in determining final beam quality; this is a topic that requires considerable further attention, both in terms of the type of cathode (especially high-quantum-efficiency materials) and in terms of uniformity evolution over time in an operational environment. At the same time, a corresponding effort is requested to the laser community in order to provide spatial and temporal profiles that maintain, and eventually improve, the beam performances as generated from the photocathodes

Table 1.6 summarizes the main features related to these scenarios.

Table 1.6: Summary of most common used photocathodes from ref. [8].

Cathode type	**Cathode**	**Typical wavelength & energy, λ_{opt} (nm), (eV)**	**Quantum efficiency (electrons per photon)**	**Vacuum for 1000 h (Torr)**
PEA: mono-alkali	Cs_2Te	211, 5.88	0.1	10^{-9}
		264, 4.70	-	-
		262, 4.73	-	-
	Cs_3Sb	432, 2.87	0.15	?
	K_3Sb	400, 3.10	0.07	?
	Na_3Sb	330, 3.76	0.02	?
	Li_3Sb	295, 4.20	0.0001	?
PEA: multi-alkali	Na_2KSb	330, 3.76	0.1	10^{-10}
	$(Cs)Na_3KSb$	390, 3.18	0.2	10^{-10}
	K_2CsSb	543, 2,28	0.1	10^{-10}
	$K_2CsSb(O)$	543, 2,28	0.1	10^{-10}
NEA	GaAs(Cs,F)	532, 2.33	0.1	?
		860, 1.44	0.1	?
	GaN(Cs)	260, 4.77	0.1	?
	GaAs(1-x)Px $x \sim 0.45$ (Cs,F)	532, 2.33	0.1	?
S-1	Ag-O-Cs	900, 1.38	0.01	?

1.3.1 Energy Recovery Linacs

Energy Recovery Linear Accelerators (ERL) require injectors which deliver periodic sequence of electron bunches with different parameter range:

- Bunch charge
- Bunch repetition rate
- Beam emittance
- Beam energy spread
- Bunch length

A common goal for all the sources for future ERLs is relatively High Average Current (up to 100s mA figure).

The minimum achievable emittance is limited by bunch charge and emission field on the photocathode and may be found as [9]:

$$I_{\max} = \frac{Q}{\tau} = I_0 \frac{\sqrt{2}}{9} \left(\frac{eE_{\mathrm{emit}} r}{mc^2} \right)^{\frac{3}{2}} \frac{\varepsilon}{r} \propto \sqrt{\frac{h\nu - \phi_{\mathrm{eff}}}{mc^2}} \Rightarrow \varepsilon \propto \frac{Q^{\frac{3}{2}}}{E_{\mathrm{emit}}}. \tag{1.1}$$

The emission field on the photocathode is related to the technology adopted for this component considering the requirement to handle CW operations. Possible injector technologies so far adopted in the ERL community in different projects may be summarized as:

- DC photoinjectors
- Normal Conductive RF photoinjectors with a frequency not higher than about 200 MHz
- Superconducting RF photoinjectors
- Thermionic injectors.

The charge delivered by the photoinjector is related mainly to:

- Photocathode material and its Quantum Efficiency (QE) and lifetime
- Laser pulse parameters on the cathode
- Laser pulse transport
- Minimum dark current which may be an issue for “green” photocathodes

The level of operational vacuum is a parameter of paramount relevance to provide acceptable photocathode lifetime for chosen photocathode and it has, in some cases, also forced the choice of the technology.

The characteristics of the laser pulse are mainly influenced by spatial and temporal laser profile (pulse length and, as result, power density). The laser pulse energy does not represent a problem for delivery by laser for "green" photocathodes but may be an issue for "UV" ones. The same applies for mirrors damage that may be involved in laser transport, due to high peak and average power density needed for high average current generation.

The requirements involved with photocathodes that are still under evaluation and study for medium-high current beam sources may be summarized as below: Preferable choice for ERLs

- Sb-based "green" photocathodes (preferable choice for ERLs) such as Cs_3Sb, Cs_2KSb, Na_2KSb, CsNaKSb and others
  - ○ Widely used in industry in PhotoMultiplierTube
  - ○ Enough robust for operation with high average current
  - ○ Laser systems are available
  - ○ Technology under development for accelerator applications
    - ◇ Optimization of deposition procedure to obtain high QE and robustness
    - ◇ Lifetime at high average current
    - ◇ Mean Transverse Energy
    - ◇ Operation at cryogenic temperature
- GaAs based photocathode for delivery of polarized electrons

- Very sensitive to operational vacuum and as result low charge lifetime in the range of 100's C
- Major efforts are concentrated on improving operational performance

- Cs_2Te photocathodes
  - Very robust. Operated at DESY FLASH for more than 2 years
  - High QE, but require UV laser which is still not available for 100 mA range

1.4 BriXSinO general layout

A schematic layout of BriXSinO, then discussed in detail in the next chapter on beam dynamics (BD), is presented into the Figure 1.3, that for sake of simplicity has been divided in three main parts:

1. The injector, where electron bunches are generated using a DC gun. Downstream the gun the bunches are compressed with two RF sub harmonic bunchers (650 MHz), then are boosted by three 2-cell SC cavities at the energy of ≈ 4.5 MeV, and finally injected into the ERL superconducting Module (ESM) through a low energy dogleg. We also considered the scientific case to extend the injector maximum energy up to 10 MeV.
2. The ESM (and/or two-way linac) zone, that is the region where the beam passes in both directions, in one case with opposite phase for ERL working mode, or in the other case for the so called two-pass two-way acceleration mode.
3. The arc, which has been designed to bring back the beam to the common ESM. The lattice considered the use of 7 DBA (Double Bend Achromat). Such an approach led us to the consideration that the lattice may host two experimental areas devoted to ICS and THz FEL, without any additional magnetic elements.

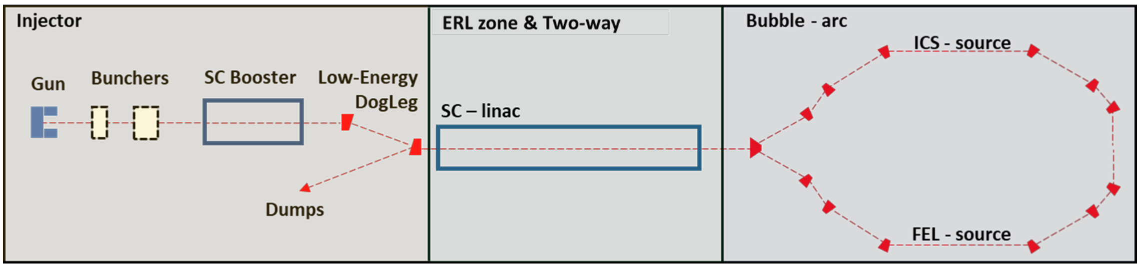

Figure 1.3: BriXSinO general layout. It is divided in tree main zone: the injection one up to the low-energy dogleg exit, the ERL zone (or two-way) that host the SC linac that can be operate in the two-pass two-way acceleration mode or ERL mode and the recirculating loop, that hosts the light source and bring backs the beam to the two-way zone.

BriXSinO can operate in two different working modes:

1. **The ERL mode**: because BriXSinO cavities see the same beam twice, one of the main goals will be to switch to the ERL working mode, allowing to operate with higher average current beams increasing the repetition rate. This task will be operated using an ad hoc path length adjustment system (for a more detailed discussion see) [10]), injecting the coming back beam on decelerating RF wave crest.
2. **The two-pass two-way acceleration mode**: where a beam accelerates two times inside the same linac, in the forward direction and then in the backward one. The beam is re-injected in the linac using the arc transport line, named recirculating loop (abbreviated with the name of arc), where eventually the beam can be compressed avoiding emittance dilution. This new working mode permits to save space improving the efficiency, doubling the energy exchange in the linac [11].

Bibliography

[1] CERN. *European Strategy for Particle Physics*. https://europeanstrategyupdate.web.cern.ch/welcome. Accessed: 2021-11-09. 2021.

[2] C. Curatolo and L. Serafini. "Electrons and X-rays to Muon Pairs (EXMP)". In: *Appl. Sci.* 12 (2022), p. 3149.

[3] M. Tigner. "A possible apparatus for electron clashing-beam experiments". In: *Il Nuovo Cimento (1955-1965)* 37.3 (1965), pp. 1228–1231.

[4] T.I. Smith et al. "Development of the SCA/FEL for use in biomedical and materials science experiments". In: *Nuclear Instruments and Methods in Physics Research Section A: Accelerators, Spectrometers, Detectors and Associated Equipment* 259.1-2 (1987), pp. 1–7.

[5] C.P. Sargent and J.B. Flanz. "RF system for a 1 gev pulse stretcher ring". In: *IEEE Transactions on Nuclear Science* 32.5 (1985), pp. 2614–2616.

[6] G.R. Neil et al. "Sustained kilowatt lasing in a free-electron laser with same-cell energy recovery". In: *Physical Review Letters* 84.4 (2000), p. 662.

[7] A. Hutton. *Energy Recovery Linac facilities*. https://indico.cern.ch/event/1040671/. Simposium on Energy Recovery Linacs. June 2021.

[8] D.H. Dowell et al. "Cathode R&D for future light sources". In: *Nuclear Instruments and Methods in Physics Research Section A: Accelerators, Spectrometers, Detectors and Associated Equipment* 622.3 (2010), pp. 685–697.

[9] D. Filippetto et al. "Maximum current density and beam brightness achievable by laser-driven electron sources". In: *Phys. Rev. ST Accel. Beams* 17 (2 Feb. 2014), p. 024201.

[10] M. Arnold et al. "First operation of the superconducting Darmstadt linear electron accelerator as an energy recovery linac". In: *Physical Review Accelerators and Beams* 23.2 (2020), p. 020101.

[11] A. Bacci et al. "Two-pass two-way acceleration in a superconducting continuous wave linac to drive low jitter x-ray free electron lasers". In: *Physical Review Accelerators and Beams* 22.11 (2019), p. 111304.

2. BriXSinO Beam Dynamics and Simulations

In this Chapter we present BriXSinO beam dynamics (BD) studies with a reference simulation.

Then, multi bunch operation typical issues are discussed, as the high order modes (HOM) effects on the BD.

The contribution of the dark current due to the cathode and RF cells has not been considered in the BD simulations since a first evaluation of its maximum value is below 1 nA.

All BD simulations here reported have been done using the Astra code [1], which considers full 3D space charge effects, and which can be driven by the optimization code GIOTTO [2] based on a genetic algorithm (GA). For the BriXSinO arc has been used the tracking code ELEGANT [3]. In the following we will report the rational of the BD approach and the main results obtained.

2.1 BriXSinO Beam Dynamics peculiar aspects

In an ERL to maximize the energy recovery from the beam, while minimizing the complexity and the environmental impact, it is necessary to set the injection energy E_0 at values of few MeV. A low injection energy together with the high efficiency of superconducting acceleration cavities makes ERLs economically sustainable, indeed particularly advantageous. Further a low injection and low dumping energy considering megawatt class electron beams strongly mitigate radiation and environmental issues, e.g., the use of electrons well below 10 - 14 MeV strongly reduces the nuclei activation in dump materials [4].

In the study here presented we set an ERL injection energy of ~4.5 MeV, which compared with other worldwide ERL projects (e.g. [5, 6]) is significantly low. Anyway, because BriXSinO is a flexible and modular machine, the injector booster has been designed to reach a maximum energy of 10 MeV on purpose to have the possibility to inject a straight beamline to explore high rep. rate electron beam experiments, with energies up to 10 MeV.

The reference simulation on which we are presenting the BD is based on a 100 pC bunch, a charge chosen ad hoc considering typical low beam energies that can be reached into DC guns and consequently the space-charge non liner effects that make more complex the BD. Further, 100 pC is a good charge value also considering the photo-cathode performances.

Understood the bunch charge of 100 pC and the benefits of a 4.5 MeV low energy beam injection, there is a drawback coming from space-charge effects resulting in a complex emittance compensation [4], both into the injector and into the dogleg (or merger in racetrack ERL).

To cope with a complex BD dominated by space-charge we present a BD solution based on the use of two sub-harmonic bunchers for the ballistic bunching and on the velocity bunching (VB) technique [7]. The rationale of the layout is the following: the sub-harmonic bunchers with a relative long RF bucket, that trap electron bunches from the DC gun 300 keV low energy, giving a chirp in energy for the ballistic bunching while performing acceleration. Between the two bunchers there is a quite long drift that can host diagnostic devices. After the first two compressions and accelerations, the beam is injected into a SC short booster (three cavities with 2-cell, @1.3 GHz) where the bunches are further compressed by the VB and accelerated at the injection energy of 4.5 MeV. Downstream the SC short booster the beam passes through a low energy dogleg to be injected in to the ERL line, then through a matching line it is injected into the arc. After the arc the beam passes a second time into the ERL for both operation modes; ERL or two-way acceleration. Then, it is transported to the dumps, the low energy one in case of the ERL operation mode or in the high energy one in case of two-way acceleration mode.

All the beam line knobs, also considering their relative positions, have been optimized by the GIOTTO code, which use has been mandatory to optimize the BD of the dispersed beam in the presence of space charge forces. The arc, differently from all the other BriXSinO regions has been optimized using the ELEGANT code and its optimization tools.

Below are some of the main advantages of the layout here proposed:

- The use of a 250-300 kV DC gun, today no longer a challenging or top expensive device. In the simulation here presented to be conservative we considered 250 kV.
- A beam line with different knobs, which permits the VB compression technique but at the same time the bunch energy spread compensation by playing with injection phases and acceleration gradients of the RF cavities. Further, a not too crowded beam line, which is valuable to place diagnostic devices.
- The use of a GA (like GIOTTO code) to optimize the BD, in particularly of the dogleg, a task made complicated by space charge nonlinear effects. Previous studies (e.g. [4]), reporting space charge effects in ERL mergers, show how it is needed to avoid strong focusing along the dogleg that results into an emittance degradation. To overcome these effects ad hoc dogleg configurations can be used, for example a promising one named “zigzag” schema [4]. Here we show how by using properly GIOTTO the space charge effects can be perfectly compensated by a proper beam line setting, both closing the dispersion and compensating the emittance in a space charge dominated doglegs.

The following reference simulation and BD study is divided in three main machine sections as shown previously in Figure 1.3: the injector, the ERL two-way linac and the recirculating arc.

2.1.1 The injector

The injector is based on a DC gun 300 keV class) operated at ~92.86 MHz rep. rate. The gun is driven by an Ytterbium laser extracting photo electrons from a Cs_2Te photocathode. The laser pulse shaping characteristics are resumed in Table 2.1.

Downstream the gun there is a 7 cm long solenoid for the emittance compensation. It is followed by two RF bunchers working a 650 MHz.

The beam bunchers perform simultaneously two functions, a first acceleration stage and a suitable compression. These are fundamental to dump the space-charge, to increase the beam peak current in view of experimental activities like the THz FEL source and to avoid the energy spread increase by RF curvature in the following booster modules. Both the solenoid and the RF bunchers are based on NC technologies.

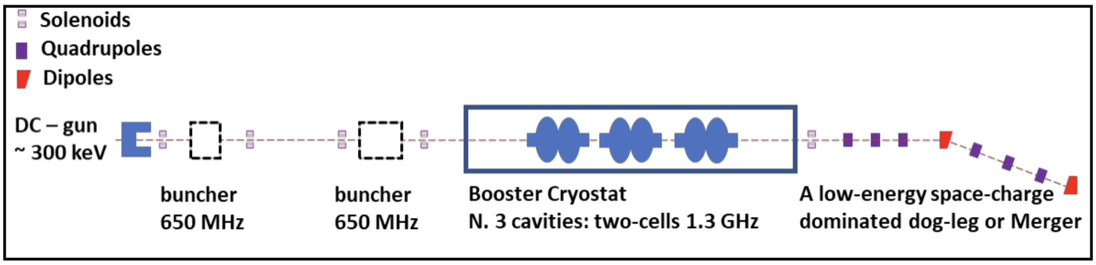

Figure 2.1: Injector blocks schema sketch: the DC-gun, the two sub harmonica bunchers, the cryostat booster carrying three 2-cells cavity and the low energy dogleg. The different lengths of the two bunchers is because of the different phase velocity.

Table 2.1: Laser pulse shape data at the gun photocathode.

Flat-top laser pulse (ps)	22.3
Rising time (ps)	1
σ_x transverse uniform (mm)	0.710
Extracted bunch charge (pC)	100

The bunchers frequency of 650 MHz, rather than 1.3 GHz (linac frequency), has been chosen for BD reasons; a longer RF bucket guarantees a more linear accelerating field that results in a more effective bunch longitudinal compression (ballistic bunching) and in a more linear spread correlation. The best working point for the two bunchers, obtained by using GIOTTO optimizing the emittance, the energy spread and the compression, before the bunch enters the dogleg, is reported in Table 2.2.

Table 2.2: Best bunchers working parameters, found using GIOTTO, minimizing the normalized bunch emittance, the energy spread and the bunch length.

	First buncher	**Second buncher**
RF phase velocity (normalized to c)	0.740	0.907
RF E_{peak} (MV/m)	3.4	3.4
Injection phase (°)	-30	-17

The injector beam energy of $\approx$ 4.5 MeV is reached thanks to three 2-cell SC cavities enclosed inside the dedicated cryomodule (see Section 9.2), device previously named SC short injector booster.

The injector main beam parameters, after an accurate optimization again done with GIOTTO, are shown in Fig. 2. The key parameters on which the optimization has been done are: laser spot size at the gun's cathode and its flattop time duration, first solenoid B_z intensity, RF peak field and injection phase of buncher-I, second and third solenoid B_z intensity, RF peak field and injection phase of buncher-II, fourth solenoid B_z intensity, RF peak field and injection phases of the 2-cell three accelerating SC cavities inside the short booster; i.e., to find the best injector setting GIOTTO moved 16 knobs.

The Figure 2.2 shows the optimum behavior of the normalized emittance, the envelope, the energy gain, the energy spread and the longitudinal compression of the 100 pC bunch. The emittance oscillations, resulting from space-charge effects, are very well controlled with the solenoids and

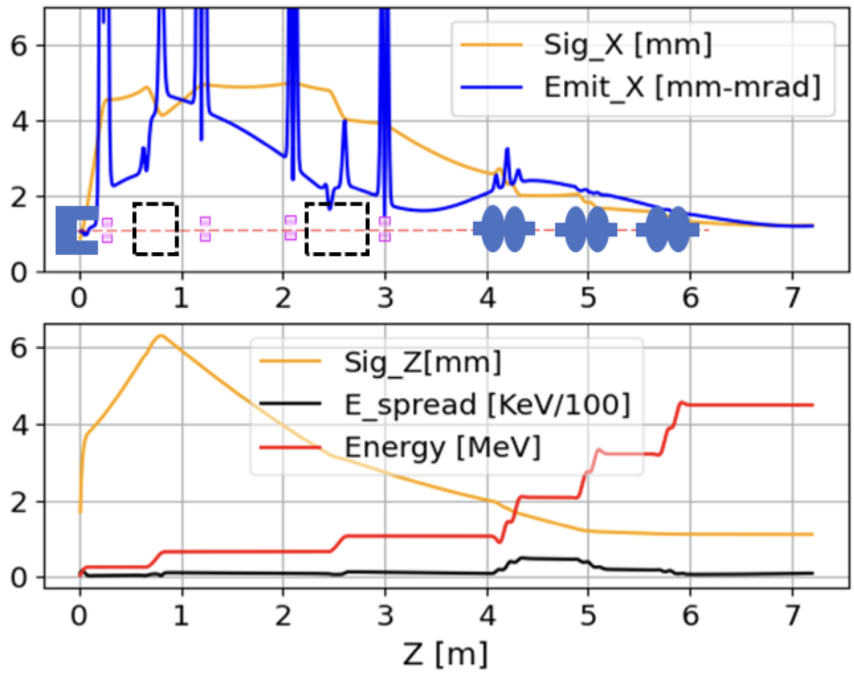

Figure 2.2: The upper plot reports the normalized emittance (in blue) and the transverse envelope (in yellow) for a cylindrical symmetry beam. Furthermore, the main active elements are shown to help the reader to see theirs effects on the BD. The lower plot shows three curves, the energy gain (in red), the bunch longitudinal compression (in yellow) and the energy spread (in black).

with the transverse focusing of accelerating cavities. The beam envelope before the dogleg of the order of 1 mm is compatible with the dogleg's matching line. The bunch undergoes a longitudinal compression of a factor of 6 with respect to its maximum length reached into the drift after the DC gun; the beam energy spread, brought back to its initial values after the acceleration, is remarkable. Table 2.3 reports the optimal beam parameters obtained at the injector exit.

Table 2.3: Beam parameters at the injector exit, before the bunch enters the low energy dogleg.

Beam Energy [MeV]	43
Bunch charge [pC]	100
Norm. emitt. $\varepsilon_{n,xy}$ [mm − mrad]	1.2
Focal spot size σ_{xy} [mm]	1.2
Energy spread σ_E [%]	0.19
Bunch length σ_z [mm]	1.1

Downstream the injector booster the beam enters the low beam energy dogleg (~4.5 MeV). As discussed above - to overcome the space charge detrimental effects and at the same time to close the beam dispersion opened into the dogleg - we used the GIOTTO code. In Figure 2.3 are shown the main curves characterizing the BD into the dogleg, which represent the GIOTTO solution, in particular: the normalized emittance on both the transverse planes show a mild increase of 0.4 mm − mrad (chromatic effects), the dispersion and its first derivative are perfectly closed. It is worth noting that at the dogleg exit the beam is almost restored in cylindrical symmetry. It is not necessary to show the main beam parameters at the end of the dogleg because they are quite the

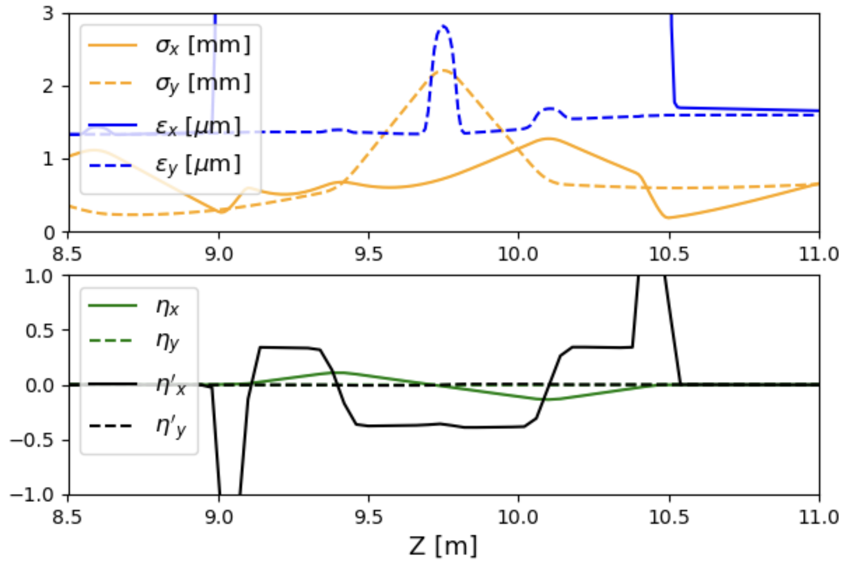

Figure 2.3: For both transversal dimensions, the upper plot shows the beam envelops and the beam normalized emittance. The lower plot shows the vertical and horizontal dispersion (η), together with first derivative dispersion (η').

same before entering the dogleg, except the mild emittance increase.

2.1.2 The ERL two-way main linac

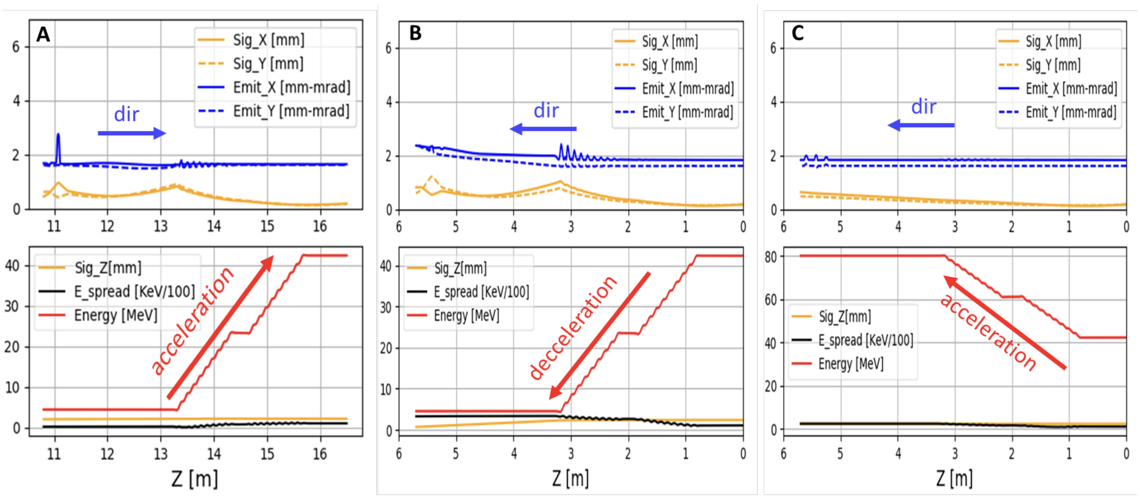

Figure 2.4: Simulation results of the main linac beam tracking (a case with a preliminary approach based on two SC 1.3 SW 7-cell cavities). Different working modes and beam directions are considered: plot A shows the beam acceleration after the low-energy dogleg, plot B shows the beam deceleration for the coming back beam (from the recirculation loop) and the plot C shows the second time beam acceleration (two-way two pass acceleration).

This machine region downstream the injector is essentially represented by the cryostat hosting the 1.3 GHz SW SC 7-cell cavities, presented into the Chapter 4. The simulations here reported highlight how in the forward and in the backward directions the BD preserves good beam qualities, considering both the ERL and the two-way two pass acceleration working modes. For the case of a cryostat hosting two 7-cell cavities, the Figure 2.4 shows in the plot (A) the direct acceleration operation mode, in the plot (B) the ERL operation mode (decelerating the beam) and in the plot C the two-way two pass acceleration mode. In the plots (A, B, C) for sake of clarity are also reported the beam directions. A more careful recent evaluation was carried out, pointing to the need of a cryostat hosting three 7-cell cavities instead of two, with the benefit to work at a lower accelerating gradient and to have an additional knob for the BD control.

Head-on scattering effects on counter-propagating bunches, characterizing this machine part, have not been considered a major issue because the BriXSinO maximum average currents of 5 mA, that gives limits to the single bunch charge or rep. rate; the effect scale with the bunch charge and number of interactions, the physical problem has been previously analyzed into MariX CDR [8, 9].

2.1.3 The BriXSinO Recirculating Loop

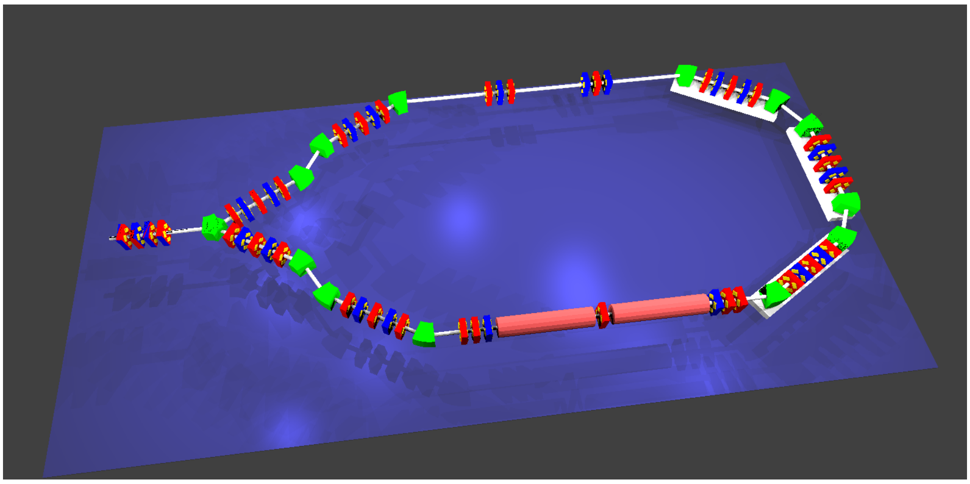

Figure 2.5: BriXSinO arc design.

The loop shown in Figure 2.5 is based on a peculiar single achromatic cell design, the BriXSinO's DBA (Double Bend Achromat). The choice of a single repeated element within the arc brings several ad- vantages: the use of common optics and engineering solutions and fewer beam dynamics issues to deal with.

The peculiarity of this DBA is that it has quadrupole optics within the dispersed area. This choice allows a linear arrangement of the cell elements (dipoles and quadrupoles) and therefore their installation on a single compact girder. The closed dispersion region has been reduced to a minimum compatibly with the presence of beam diagnostic stations.

The three DBAs used to U-turn the beam are arranged on three separate platforms (assembled on top of girders foreseeing the use of linear bearings) whose position can be adjusted along the longitudinal axis of the machine. These three movable DBA allows to easily change the beam path length up to a maximum of 120 mm (that is slightly higher than the required $\lambda/2$) that means a total longitudinal translation of the platforms of 60 mm with a solution that in terms of total devices displacements and its accuracy, weights and size, is similar to other project [10–12]. The estimated weight of a platform plus a DBA is of the order of 1200 kg that is compatible with mechanical solutions based on stepper motors remotely controlled, further the accuracy of the motion can be control in the way to cope with fine injection phase adjustment (i.e. 1-3 RF degrees). The peculiar DBA scheme with all the optics hosted on a single girder greatly simplifies this operation, a representative image of a platform and the relative DBA (magnets and the platform are not in scale) is shown in Figure 2.6.

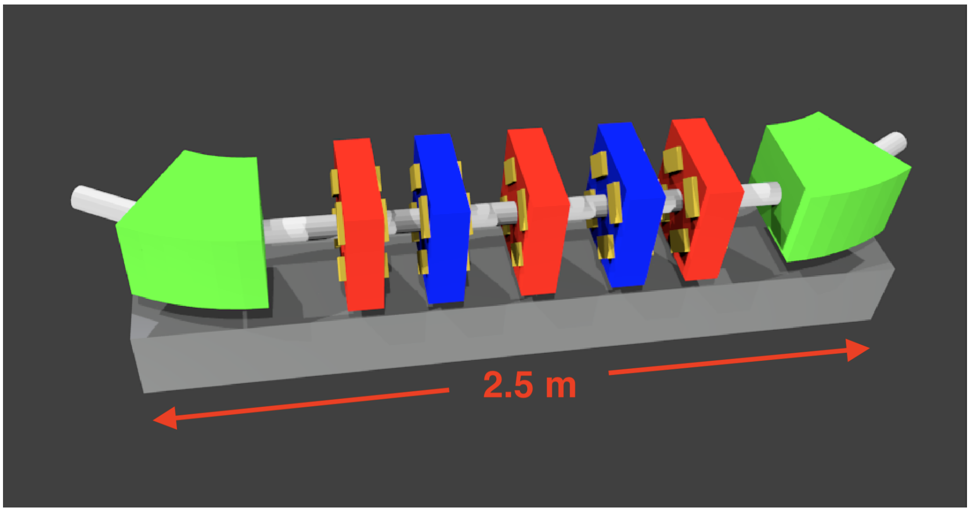

Figure 2.6: One BriXSinO's DBA with its relative platform. The platform and magnets 3D sketch are not in scale.

The BriXSinO recirculating loop abbreviated with the name of arc and hosting an Inverse Compton Source (ICS) and a THz FEL radiators (see Figure 2.5) is based on seven DBA and four quadrupoles after the ERL that represent the beam matching line to the arc itself. It follows a description of different arc areas:

- The four quadrupoles matching line downstream the ERL is thought to properly control beams traveling in both the directions backward and forward [13].
- The DBA works with two 30° dipoles and five quadrupoles into the dispersive regions. The whole DBA length is about 3.1 m long and the peculiar configuration of five quadrupoles into the dispersive region provides a very flexible tuning from the BD point of view, leaving fully available the non-dispersive region, of about 0.6 m long, for the installation of different diagnostic devices and equipment.
- The ICS (Inverse Compton Scattering) X-Ray source, named "Sors" is based on two quadrupoles triplets, the first to focus the beam on the Interaction Points (IP), the second to control its envelop after the IP. The two triplets are separated by a quite long distance of 1.5 m to host the Fabry-Pérot Optical Cavity. Since these two triples are in mirror symmetry (having an identical transport matrix) we are in the condition that if we provide a different focusing strength of electron beams at IP the out-coming beams will be restored to the matched parameters at the DBA entrance.
- The THz FEL radiator named "TerRa" is injected by a proper quadruples triplet, as at the radiators exit a triplet match the beam to the last two DBA's.

This simulation considers an electron beam at the energy of 43 MeV and the DBA is matched with the following parameters: $\beta_x = \beta_y$ and $\alpha_{x,y} = 0$. The DBA quadrupoles configuration is presented in Table 2.4

Table 2.4: DBA quadrupoles parameters.

QA1	K1=20.7
QA2	K1=-26.05
QA3	K1=27.10
QA4	K1=-26.05
QA5	K1=20.7

The beam parameters here presented have been optimized for the specific case of the ICS experiment (see relative chapter), considering a beam running in the clockwise arc direction. In Figure 2.7 and Figure 2.8 are shown the main optical functions and simulation results as computed by the ELEGANT code and tracking the whole beam.

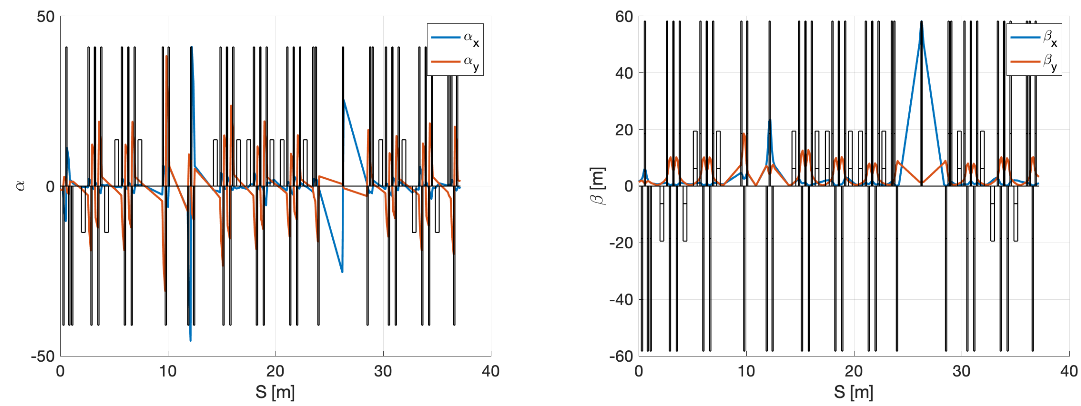

Figure 2.7: Arc Twiss parametrs

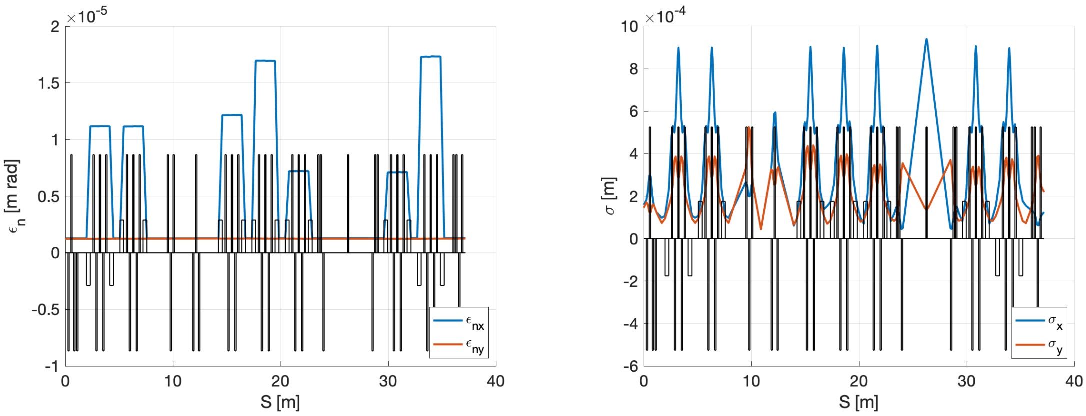

Figure 2.8: Normalized emittance (left) and transverse beam size (right).

The main electron bunch parameters at the ICS IP, related to this 43 MeV Working Point (WP) dedicated to the ICS experiment, are reported in Table 2.5.

BriXSinO WPs, considering the THz FEL case, can exploit the arc as a compressor in the same mode as in the MariX FEL [13, 14]. In this first reference simulation, with the scope to be conservative, we did not consider any bunch compression and we tracked the beam at the FEL matching line entrance with the only scope to preserve a good beam quality. The final beam

Table 2.5: Electron bunch main parameters at the ICS interaction point and at the FEL matching line.

Beam Energy [MeV]	43	
Bunch charge [pC]	100	
Norm. emitt. $\varepsilon_{n,xy}$ [mm − mrad]	1.6	
Energy spread σ_E [%]	0.2	
Bunch length σ_z [mm]	1.9	
	ICS	FEL
Focal spot size σ_x. σ_y [µm]	44.8, 43.6	109.0, 73.5

parameters reported in Table 2.5 are very similar to the ICS case, this because the DBA optical functions are the same. Since the FEL light emission phenomenon is related to the machine repetition rate it must highlighted that for 100 pC bunches the maximum acceptable repetition rate is 46.4 MHz (1/14 of 1.3 GHz); this is consequence of the machine maximum available current that is 5 mA. In Figure 2.9 is highlighted the simulated path up to the FEL source. For both the ICS and FEL working points, considering the emittance at 93% (i.e. cutting 7% on the halo), the normalized emittance values go down to ~1.2 mm − mrad on both the x and y planes.

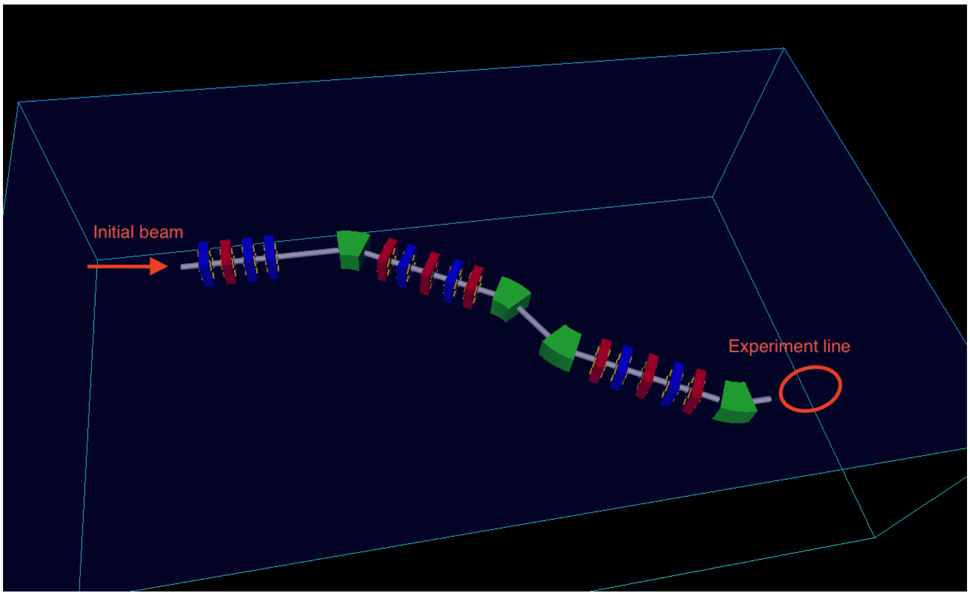

Figure 2.9: The beam path from the arc matching line up to the FEL radiator.

2.2 HOM evolution trough HOMEN model

In the course of BriXSinO study work, it was highlighted how crucial it is to investigate the possible effects on BD of HOMs on the electron beam especially considering the high repetition rate of the machine and the two-way circulation in the linac. Consequently, we have developed the *HOMEN* model (High Order Mode evolution based on ENergy budget) with the aim of simulating these effects.

The goal of this tool is to simulate the growth and effect of HOMs on the beam on very long time scales (tens of millions of bunches).

Once completed and optimized HOMEN will be of vital importance for several tasks:

- establishing the dumping strategy of the most damaging modes for the electron beam and BriXSinO light sources (exploiting HOM couplers).
- To study the filling-up phase of the ERL.
- be possibly integrated in the control system in order to facilitate the real time control of the beam.

We consider the electric field along the cavity axis as the sum of contributions from its modes:

$$E_{z,n}(z,t) = A_n(t) e_n(z) \sin(\omega_n t + \phi_{n,i}), \tag{2.1}$$

where the indices $n = \{1, \cdots, N_{\mathrm{RF}}\}$ represents the RF modes and $i = \{1, \cdots, N_b\}$ represents the bunch number in the sequence of e^- bunches composing the beam, $A_n(t)$ is the mode oscillation amplitude and $e_n(z)$ is the on-axis field distribution. It is important to keep in mind that we make use of the *Slowly Varying Envelope Approximation* (SVEA) i.e.

$$\frac{dA_n}{dt} \ll \omega_n A_n. \tag{2.2}$$

Writing the scaling relation $A_n = a\sqrt{U_n}$ between the stored energy in the n$^{\mathrm{th}}$ mode U_n and A_n after few passages we obtain the following relation:

$$\frac{dA_n}{dt} = \frac{A_n}{2U_n} \frac{dU_n}{dt}. \tag{2.3}$$

The variation of the stored energy in the n$^{\mathrm{th}}$ mode can be expressed as:

$$\frac{dU_n}{dt} = -\frac{\omega_n U_n}{Q_{L_n}} + \delta_{1,n} |P_{\mathrm{RF}}| - \frac{q_i V_{\mathrm{acc}_{i,n}}}{\tau_{\mathrm{cav}_i}} + \frac{q_i^2 k_{\mathrm{loss},n}}{\tau_{\mathrm{cav}_i}}. \tag{2.4}$$

The four factors in the sum represents the following quantities:

1. $-\frac{\omega_n U_n}{Q_{L_n}}$ is the power dissipated on the cavity walls for each mode; for the fundamental mode Q_{L_n} represents the Q-loaded factor, for $n > 1$ it represents the relative damped quality factors.
2. $\delta_{1,n} |P_{\mathrm{RF}}|$: power from RF source, the Dirac delta indicates that the RF source provides energy only to the fundamental mode.
3. $-\frac{q_i V_{\mathrm{acc}_{i,n}}}{\tau_{\mathrm{cav}_i}}$ is the energy exchanged with the beam.
4. $\frac{q_i^2 k_{\mathrm{loss},n}}{\tau_{\mathrm{cav}_i}}$: power lost by the beam stored in the HOM according to the proper $k_{\mathrm{loss},n}$ factor.

In Equation (2.4), τ_{cav} is the time of flight of the bunch through the cavity:

$$\tau_{\mathrm{cav}_i} = \frac{L_{\mathrm{cav}}}{\beta(t_{0,i})\, c} \tag{2.5}$$

and $V_{\mathrm{acc}_{i,n}}$ is the overall accelerating potential of the cavity.

These two equations are accompanied by the one describing the energy gain of the bunch after passing through the cavity:

$$\frac{d\gamma_i}{dt} = \frac{e}{m_0 c^2 \tau_{\mathrm{cav}_i}} \sum_{n=1}^{N_{\mathrm{RF}}} V_{\mathrm{acc}_{i,n}}. \tag{2.6}$$

The approach of our model is to integrate with a 4th order Runge-Kutta method the system of equations (2.3)-(2.6) with time step equal to τ_{cav_i}.

Finally, the overall accelerating potential of the cavity is calculated before each integration step according to the following relation:

$$
\begin{aligned}
V_{\mathrm{acc}_{i,n}} &= A_n\left(t_{0,i}\right)\int_0^{L_{\mathrm{cav}}} e_n(z)\sin\left(\frac{\omega_n z}{\beta\left(t_{0,i}\right)c}+\phi_{n,i}\right)dz \qquad (2.7)\\
\phi_{n,i} &= \phi_{n,1}+\frac{\omega_n(i-1)}{f_{\mathrm{rep}}}\\
t_{0,i} &= \frac{i-1}{f_{\mathrm{rep}}},
\end{aligned}
$$

with f_{rep} representing the repetition rate of the machine.

The calculation of the integral is time consuming if compared with the integration step calculation and risks to vanish the computational advantage given by this model.

To avoid this, we decided to pre-load tabulated values of the integral in (2.7) for a properly chosen set of values of the variables $\beta\left(t_{0,i}\right)$ and $\phi_{n,i}$; at each RK step a bi-cubic interpolation algorithm is applied in order to estimate faster all the desired integrals.

A set of initial conditions is required to conveniently set up the system at the beginning of the integration ($A_n(t=0)$, $U_n(t=0)$, $\phi_{n,1}$, $\gamma_i(t=0)$, $\beta_i(t=0)=\sqrt{1-\gamma_i^{-2}(t=0)}$, $z_i(t=0)$).

Results of numerical solution of the HOMEN model are reported in Appendix, Chapter 23.4.

2.3 Wakefield and HOM evaluation inside the ESM region

One of the major challenges for running large currents through the accelerating structure is the effect of strong higher-order modes (HOMs) in the cavities of the SC linac that can lead to beam breakup. We present the simulation results of HOM studies for the prototype 7-cell cavity model.

The study has been primarily performed on a zero-order model of a singular module of the 1.3 GHz 7-cell cavities, later called *module*, shown in Figure 2.10, resorting on CST wakefield solver of the Dassault Systèmes [15]

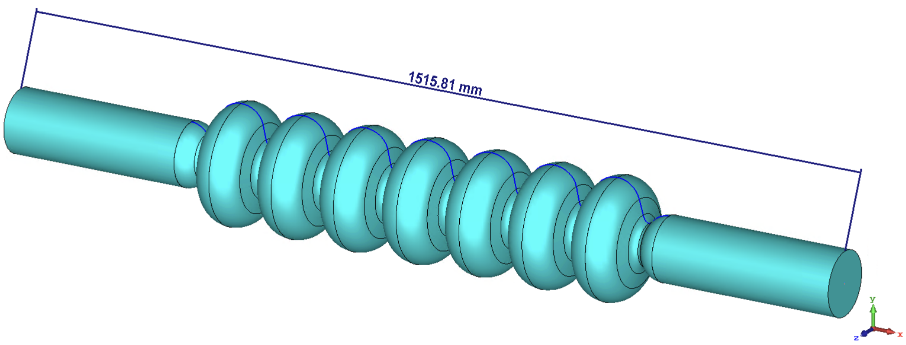

Figure 2.10: CST electromagnetic model of the 1.3 GHz SC SW 7-cell cavities.

The electromagnetic analysis of the resonating modes inside the module leads to five main peaks relative to the longitudinal impedance (1.3, 2.43, 3.84, 5.45 and 6.7 GHz), the order of magnitude of the Q-factors is 10^{10} considering the conductivity of a superconductor as boundary material of the structure. The modes higher then 1.3 GHz are over the beam pipe cut-off frequency. The R/Q are estimated to be 774 and 125 for the first and second mode respectively, in the approximation of closed resonating structure, that is strictly valid only below pipe cut-off frequency. Figure 2.11

shows the comparison between the beam spectrum, assuming Gaussian bunch profile for 2.2 mm bunch-length and 92.86 MHz repetition rate, and the real part of the longitudinal impedance to have a graphical estimation of the device power losses. The amplitude values of the impedance peaks are not entirely reliable because the simulated wakefield did not completely decay do the high conductivity of the boundaries.

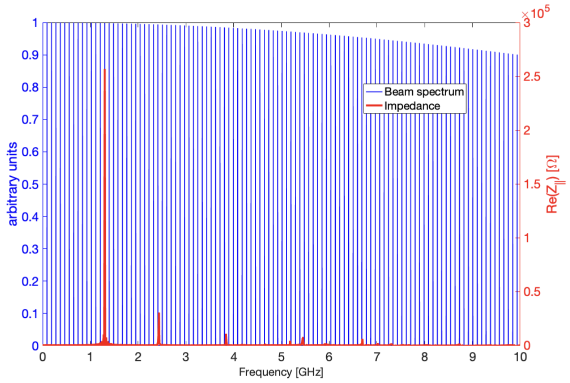

Figure 2.11: Beam spectrum, assuming Gaussian bunch profile for 2.2 mm bunch-length and 92.86 MHz repetition rate, compared with real part of the longitudinal impedance.

The longitudinal and transverse impedance are shown in Figure 2.12. The longitudinal main peaks are the same shown before plus one at 10.7 GHz, above that value there is a numerous number of peaks with lower amplitude values. In the transverse plane the peaks are at: 1.74, 2.56, 3.83, 4.25, 10.7, 13.26 and 18.27 GHz; going to higher frequencies the behavior shows other resonances at 23.90, 25.00, 26.46 and 29.07 GHz.

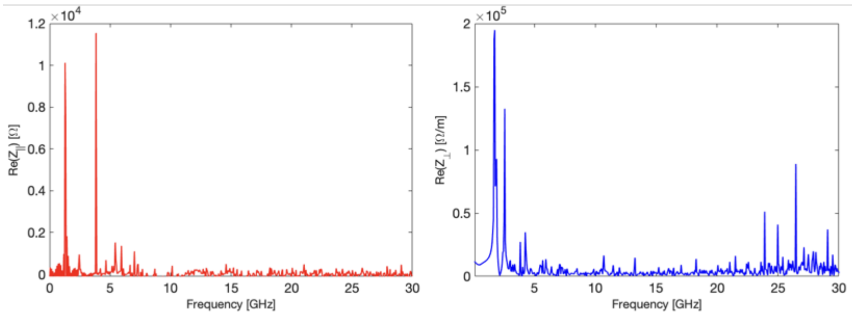

Figure 2.12: Real part of the longitudinal and transverse impedance up to 30 GHz.

From the longitudinal loss factor of one module, it is possible to calculate the average power transferred to the beam from the field excited by the beam itself. The result is a longitudinal loss factor of 3.5 V/pC per one-cavity section (10.5 V/pC for 3 modules) at the design bunch length of σ_z = 2.2 mm. The average monopole mode HOM power excited by the 5 mA, 100 pC beam is found to be 5 W for the entire structure.

An efficient damping of the HOMs in the superconducting cavities is essential in the case of high current linac, as in our case. The absorbing material suggested is the Silicon Carbide, SC-35® from Coorstek [16], whose properties are shown in [17]. The absorbing device, long 125 mm, has a hollow cylindrical shape and it is placed in the center of the connecting pipes, far from the cavity entrances to avoid any possible pollution during operation. Figure 2.13 shows the longitudinal impedance evaluated for the three modules simulation (blue line) compared with three times the single module one (green line) and for the three modules with Silicon Carbide (SiC) installed as HOM damper in the pipes (blue line). The presence of the SiC absorber does not affect the first three modes but it is effective on the modes that are fully resonating inside the connecting pipes (as shown in Figure 2.13 on the right).

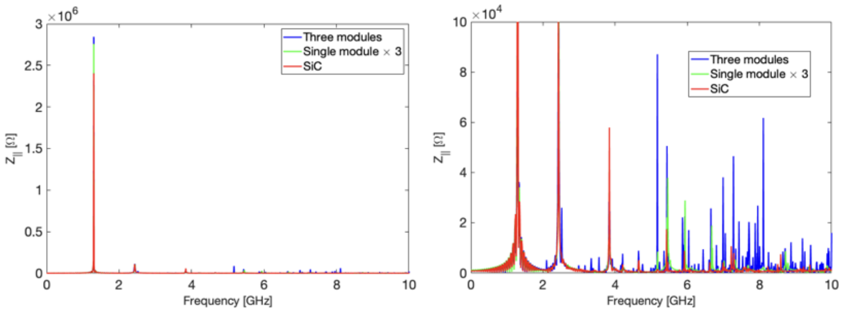

Figure 2.13: on the left, longitudinal impedance of three modules compared with three times the single module and the three modules with Silicon Carbide (SiC) installed as HOM damper in the pipes; on the right, enlarged view of the same parameter for the three cases.

Bibliography

[1] K. Flöttmann et al. *ASTRA: A space charge tracking algorithm*. 2011.

[2] A. Bacci, V. Petrillo, and M. Rossetti Conti. "GIOTTO: A genetic code for demanding beam-dynamics optimizations". In: *Proceedings of the 7th International Particle Accelerator Conference (IPAC 2016), Busan, Korea*. 2016, pp. 8–13.

[3] M Borland. *ELEGANT: A flexible SDDS-compliant code for accelerator simulation*. Tech. rep. LS-287. `https://www.osti.gov/biblio/761286`. Argonne National Lab., IL (US), Aug. 2000.

[4] V.N. Litvinenko, R. Hajima, and D. Kayran. "Merger designs for ERLs". In: *Nuclear Instruments and Methods in Physics Research Section A: Accelerators, Spectrometers, Detectors and Associated Equipment* 557.1 (2006), pp. 165–175.

[5] C. Gulliford et al. "Demonstration of low emittance in the Cornell energy recovery linac injector prototype". In: *Physical Review Special Topics-Accelerators and Beams* 16.7 (2013), p. 073401.

[6] M. Abo-Bakr and M. Arnold. "Working Group Summary: ERL Facilities". In: *Proc. ERL'19* (Berlin, Germany). ICFA Advanced Beam Dynamics Workshop on Energy Recovery Linacs 63. https://doi.org/10.18429/JACoW-ERL2019-FRCOYBS01. JACoW Publishing, Geneva, Switzerland, June 2020, pp. 171–176. ISBN: 978-3-95450-217-2. DOI: `10.18429/JACoW-ERL2019-FRCOYBS01`. URL: `http://jacow.org/erl2019/papers/frcoybs01.pdf`.

[7] M Ferrario et al. "Experimental demonstration of emittance compensation with velocity bunching". In: *Physical review letters* 104.5 (2010), p. 054801.

[8] L. Serafini et al. *MariX - Multi-disciplinary Advanced Research Infrastructure for the generation and application of X-Ray - CDR*. `http://www.marix.eu/`.

[9] P Cardarelli et al. "BriXS, a new X-ray inverse Compton source for medical applications". In: *Physica Medica* 77 (2020), pp. 127–137.

[10] M. Arnold et al. "First operation of the superconducting Darmstadt linear electron accelerator as an energy recovery linac". In: *Physical Review Accelerators and Beams* 23.2 (2020), p. 020101.

[11] F. Lemery et al. "Overview of the ARES Bunch Compressor at SINBAD". In: *10th Int. Particle Accelerator Conf.(IPAC'19), Melbourne, Australia*. 2019.

[12] H.L. Owen and P.H. Williams. "A modular path length corrector for recirculating linacs". In: *Nuclear Instruments and Methods in Physics Research Section A: Accelerators, Spectrometers, Detectors and Associated Equipment* 662.1 (2012), pp. 12–20.

[13] M Rossetti Conti et al. "Optimization of the arc compressor performance in the MariX free electron laser". In: *Journal of Physics: Conference Series*. Vol. 1596. 1. IOP Publishing. 2020, p. 012035.

[14] A. Bacci et al. "Two-pass two-way acceleration in a superconducting continuous wave linac to drive low jitter x-ray free electron lasers". In: *Physical Review Accelerators and Beams* 22.11 (2019), p. 111304.

[15] *CST Studio Suite - Getting started.*

[16] `www.coorstek.com`.

[17] R. Eichhorn et al. "Higher order mode absorbers for high current ERL applications". In: *Proc. Of the IPAC* (2014).

3. An Injector for 5 mA - 100 MHz electron beam

The BriXSinO injector aims to provide a high power and high brightness CW beam. The Injector has to provide different bunch charges at different repetition rate and energies, as presented in the introduction and summarized in Table 3.1.

Table 3.1: Request for Injector Beam generation.

Experiment	**Charge** (pC)	**Rep. rate** (MHz)	**Average current** (mA)
ICS	50 - 200	0.9286 - 92.85	5
THz FEL	50 - 100	46 - 92.86	5
2-way	5	1	0.005
Fixed Target	25 - 50	<92.86	<5

To achieve these parameters, we have done an extensive simulation activity as presented in the dedicated section to select optimal components and their characteristics to get the design goals.

Under these assumptions, the Injector is composed of different elements that can be grouped into the following sections:

- The DC gun with focusing solenoids.
- The two 650 MHz sub-harmonic bunchers.
- Transport optics.
- Injector Superconducting Booster.
- Dogleg and matching section into the main ERL SC accelerating module.

The general layout of the Injector is based on a laser-driven photoemission DC gun running at nearly 100 MHz where the electrons are accelerated at 300 keV. The long bunch so generated is compressed and further accelerated in two Normal Conducting (NC) buncher cavities, operated at 650 MHz with $\beta = 0.74$ and $\beta = 0.904$ to optimize the bunching and acceleration efficiency due to the non-relativistic properties of the beam. Finally, the electron bunch is accelerated in a

Superconducting Booster Cryomodule that hosts three 1.3 GHz two-cell Nb cavities operated at 2 K. The energy at the exit of the SC module is 5 MeV. Afterwards, a transport system consisting of a dogleg and a matching section brings the beam into the main ERL module. Hereafter, we will briefly describe the functional and operational aspect of each section of the injector.

3.1 The DC gun with focusing solenoids

For the components selection there has been a trade-off between parameters and cost in the choice of the electron source. We finally chose a DC gun because, in our operation parameter space (especially the very high rep rate), it provides a robust and already well-developed solutions with proven and well documented successful operations at even higher rep rate.

We are considering as reference for our design, the "inverted insulator" design developed at JLAB [1]. This DC gun assures stable operation with the parameters required by BriXSinO.

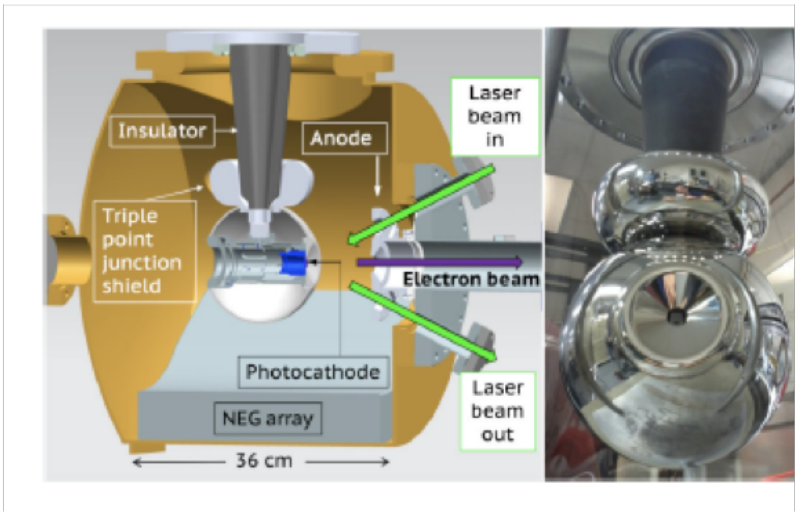

Figure 3.1: Scheme of the "inverted insulator" JLAB DC Gun with detailed view of the cathode and inner side of the insulator.

Based on the experience developed at LASA on Cs_2Te photocathodes, we have chosen this material as a baseline for the BriXSinO injector due to its robustness and stability as set by operation in user-facilities as FLASH and European-XFEL at DESY, to mention few. Nowadays about 150 Cs_2Te photocathodes have been deposited and used in High brightness guns and in user facilities [2], showing high stability and uniformity in term of Quantum Efficiency (QE), low dark current and long operative lifetime [3]. While this cathode has shown outstanding performance during operation up to 9 MHz in pulse mode and 1 MHz in CW mode, to assess the operation capability at the BriXSinO repetition rate a dedicated R&D activity is on-going to operate this photocathode at 100 MHz in a DC gun. This is clearly a challenge for the photocathode that needs to withstand high average current and, probably, ion back bombardments due to operation in a constant accelerating field. The availability at LASA of the expertise and of a dedicated deposition system together with the foreseen operational scheme of 1 week/month mitigate considerably the risk given by the BriXSinO photocathode operation regime. Furthermore, a new production system, in operation since July 2021 at LASA, is dedicated to the production of alkali antimonide photocathodes (KCsSb) sensitive to visible light that can be used in BriXSinO running with the 2^{nd} harmonic of the laser instead of the UV. The possible use of these photocathodes will be addressed when these films will be fully characterized.

The electron bunch is generated by a UV laser running at 258.75 nm by fourth harmonic generation from the mode locked Yb laser used also for the Inverted Compton Experiment. The expected pulse length on the photocathode is planned to be 20-30 ps to mitigate the space charge effect in the emission and acceleration process in the DC gun. For a detailed description of the photocathode laser system, refer to Chapter 5. The long bunch generated in the DC gun is focused by solenoids magnets before injection into the sub harmonic bunchers. The solenoids are clearly also a key parameter for achieving low emittance downstream in the Linac, by applying the beam emittance compensation scheme.

The reference parameters for the generation of the electron beam are summarized in Table 3.2.

Table 3.2: DC Gun reference parameters.

Cathode Material	Cs_2Te
Cathode QE (@ 257 nm) [%]	10
Drive Laser Wavelength [nm]	258.75
Drive laser pulse length [ps]	22.3
Drive laser pulse shape	Flat top (1 ps rise time)
Drive Laser spot size s [mm]	0.710
Drive laser spot shape	Uniform
Repetition rate [MHz]	92.857
DC Gun Voltage [kV]	300
Electron Energy [MeV]	0.3
Bunch charge [pC]	50
Average current [mA]	5
Normalized emittance at gun exit [mm – mrad]	1.2
Electron pulse length at gun exit [ps]	44

3.2 The 650 MHz sub-harmonic Bunchers

As mentioned before, the DC Gun generated electron bunches have long longitudinal profile to avoid emittance dilution but, to minimize nonlinear energy spreading due to RF waveform in the main superconducting Linac, bunches need to be compressed to shorter length after the gun and before entering the BriXSinO SC Booster. As the beam is still non-relativistic at this point, the simplest method of bunch compression is the velocity bunching for which we choose sub-harmonic bunching solution, employing two $\beta < 1$, 650 MHz spherical reentrant shape copper cavities. The beam energy before entering the first cavity is assumed to be 300 keV and 638 keV before entering the second.

The buncher cavity geometries have been designed using Superfish and CST simulation, using as a reference the cERL buncher cavity design [4]. Table 3.3 summarizes the main parameters for the two buncher cavities.

Unlike the superconducting section of the Injector (see 3.4), the beam loading of the buncher cavities is negligible, as the RF power is almost all dissipated in the cavity walls. The RF power coupler is a key element and the one proposed for the PIP-II project will be used as a reference [5]. The power budget to feed the buncher is reported in Table 3.4.

We have still to select the proper amplifier technology, though we are looking to the market of solid-state amplifiers (SSA) used for broadcasting, mainly for digital TV application. Nevertheless, the tube solution is also considered at this point of the project. In the table above we considered the

Table 3.3: Buncher cavities parameters.

	Buncher 1	**Buncher 2**
Resonant frequency (π-mode) (MHz)	650	
β (v/c)	0.74	0.906
Accelerating voltage (MV)	0.45	0.424
Beam phase (°)	-30	-17
Input beam energy (MeV)	0.3	0.638
Electric field amplitude (MV/m)	3.4	
Cell per cavity	1	
Active cavity length (m)	0.171	0.209
Cavity quality factor Q_0	3.2×10^4	3.67×10^4
Nominal external quality factor Q_{ext}	3.02×10^4	3.24×10^4
R/Q (Ω)	195.7	223
Cavity geometry factor G (Ω)	211	244.4
$E_{\text{peak}}/E_{\text{acc}}$	3.07	3.88
$B_{\text{peak}}/E_{\text{peak}}$ (mT/(MV/m))	0.96	0.96
$B_{\text{peak}}/E_{\text{acc}}$ (mT/(MV/m))	2.94	3.73

Table 3.4: Power requirements for the two buncher cavities.

	Buncher 1	**Buncher 2**
Nominal incident power (kW)	36.4	23.6
15% Margin (losses) (kW)	41.9	27.1
Power to beam (kW)	2.0	2.2
Efficiency (Solid State Amp.) (%)	40	
Plug Power @ nominal E_{acc} (kW)	104.5	67.7

SSA efficiency, being the worst-case scenario (klystron efficiency is > 50%) to determine the AC power required to operate the buncher amplifiers.

A scheme of the RF power system for the buncher cavity is shown in figure Figure 3.2.

3.3 The transport optics

The compressed and accelerated beam needs to be transported to the Injector Superconducting Booster (ISB) preserving the electron beam characteristics. Moreover, in this section we need also to fully characterize the beam parameter space. For this reason, the section in between the last buncher and the entrance of the ISB is equipped with different stations for diagnostic as presented in the dedicated section. The goal is to have here the full 6D-space characterization of the beam both for optimizing the previous section of the injector and for proper matching into the ISB.

A specific characteristic of this beam line is our requirements to have UHV vacuum level to protect the SC cavities and avoid any back-bombardments towards the sensitive cathode installed in the DC gun.

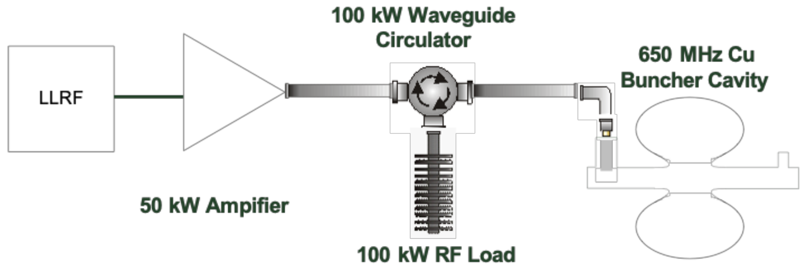

Figure 3.2: Scheme of the RF power chain for the buncher cavities.

3.4 Injector Superconducting Booster (ISB)

The Superconducting section of the Injector complex is a cryomodule (see Chapter 9 for details) that hosts three CBETA like 1.3 GHz 2 cell SC cavities [6] as shown in Figure 3.3, to boost the beam energy before entering the ERL section up to a maximum of 5 MeV.

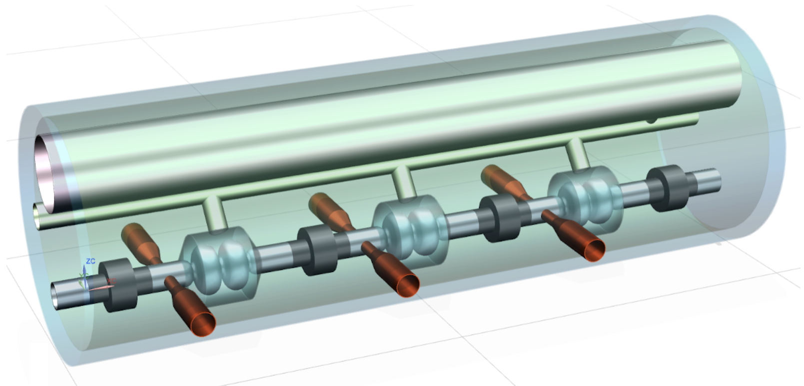

Figure 3.3: IBS cryomodule schematic view. Each cavity is powered by two couplers to minimize kick to beam. HOM absorbers are foreseen between cavities.

The Injector cavity main parameters are summarized in Table 3.5.

The loaded quality Factor Q_{L} is determined after the following equation:

$$Q_{\mathrm{L}} = \frac{E_{\mathrm{acc}}}{I_{\mathrm{beam}} \frac{R}{Q}}, \tag{3.1}$$

with $I_{\mathrm{beam}} = 5$ mA. To achieve a maximum $E_{\mathrm{acc}} = 7.5$ MV/m we need to feed the cavity with about 8.2 kW RF forward power. As in CBETA, injector cavity is equipped with two identical antenna type couplers symmetrically attached to the beam pipe of the cavity. This is a remedy to reduce the transverse kick to the beam [7]. Cavity geometry showing electric field lines and details of the coupling antennas of CBETA injector cavity are shown in Figure 3.4. The power coupler is the modified TTF III device [8].

The frequency tuner for the 2-cell injector cavities has been adopted from the INFN LASA blade tuner design. Short piezo-electric actuators have been integrated in the frequency tuner mechanism to allow for fast microphonics compensation [9].

The simplified injector power scheme is shown in Figure 3.5, were like in the ERL Linac a 10 kW commercial solid state amplifier solution has been chosen to power each cavity separately.

The BriXSinO Injector can also be used as a standalone accelerator to supply a 10 MeV beam for fixed target experiments such as cell irradiation experiments or Flash Therapy. Beyond the actual impact on heat-loads and related cryogenic budget, the accelerating gradient would be raised to 15 MV/m for these applications while keeping the beam power still below 25 kW.

Table 3.5: BriXSinO ISB cavity parameters.

Resonant frequency (π-mode) (GHz)	1.3
Accelerating voltage (MV)	1.64
Accelerating gradient E_{acc} (MV/m)	7.5
Cells per cavity	2
R/Q (Ω)	222
Cavity geometry factor G (Ω)	261
Cavity quality factor Q_0	2×10^{10}
Nominal external quality factor Q_{ext}	1.5×10^{6}
Cell-to-cell coupling (%)	0.7
$E_{\mathrm{peak}}/E_{\mathrm{acc}}$	1.94
$B_{\mathrm{peak}}/E_{\mathrm{acc}}$ (mT/(MV/m))	4.28
Small beam pipe diameter (mm)	78
Large beam pipe diameter (mm)	106
Inner iris diameter (mm)	70
Active cavity length (m)	0.218
Cavity length flange-to-flange (m)	0.536

Table 3.6 reports the RF and plug power needed for both ERL and fixed target injector setups.

3.5 Dogleg and matching section into the main ERL SC accelerating module.

The 5 MeV beam is finally transported to the ERL SC Module (ESM). To allow for beam dumping after its second way through ESM, a dogleg scheme is adopted. After the dogleg, a matching section is foreseen for proper injection of the beam into the accelerating module. The dogleg scheme is shown in Figure 3.6.

To allow also the low charge-high energy experiment, a straight line is foreseen after IBS and before the dogleg to extract the beam and transport to the experimental station.

The complicated beam dynamic solutions and challenges needed to include these different modes of operations are reported in the dedicated Chapter 2.

This section, as the transport line between the DC gun and IBS, is used for full beam characterization. For this reason, we plan here to have a diagnostic section for beam matching and dispersive sections for energy beam characterization. Being this line in between the two superconducting modules, it will be considered, from a cleaning and vacuum point of view, UHV-clean room preparation grade. This involves, as for the Injector transport line, the need for transportable clean room to allow for proper conditions for components installation.

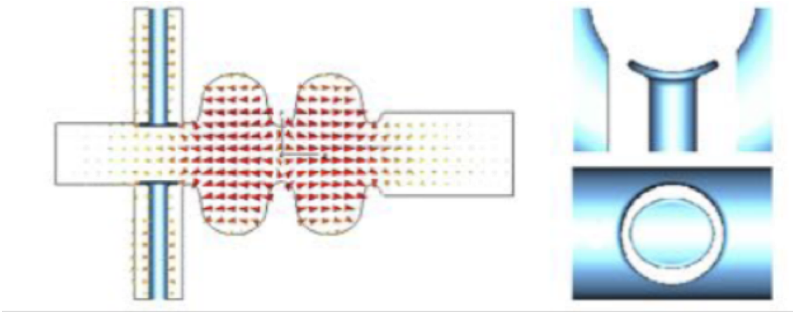

Figure 3.4: CBETA IBS SC cavity antenna power coupler. To compensate for coupler kicks, two symmetrical couplers are installed for each cavity. E-field profile is in the left picture, the right picture shows instead a detailed view on the antenna coupler optimized shape.

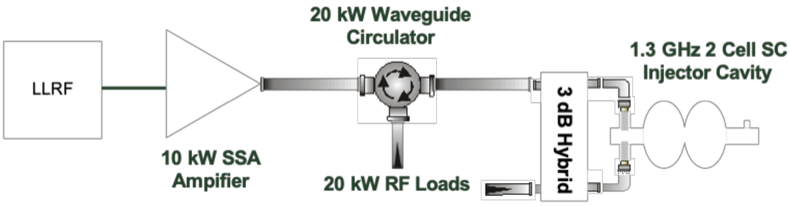

Figure 3.5: BriXSinO IBS SC cavity RF power scheme. A similar scheme is used for the ERL Cryomodule cavities.

Table 3.6: RF power requirements for two different mode operation of the Injector Superconducting Booster.

	High Charge Low Energy	**Low Charge High Energy**
Beam current I_{beam} (mA)	5	2.5
E_{acc} (MV/m)	7.5	15
Accelerating voltage V_{cav} (MV)	1.64	3.49
Nominal Incident Power P_{for} (kW)	8.2	8.2
Power from amplifier 15% loss (kW)	9.4	9.4
Power coupler Max Power P_{coupler} (kW)	5	5
Max energy gain (MeV)	5	10
#cav, # solid state amps (40% efficiency)	3	3
Plug Power @ nominal E_{acc}, P_{plug} (kW)	70.5	70.5

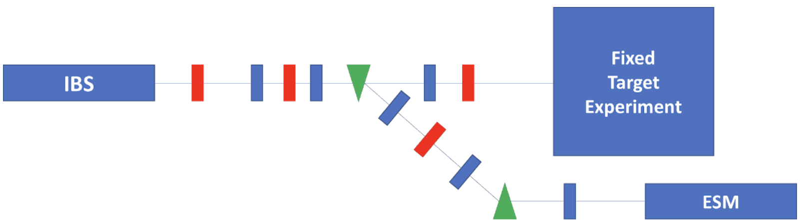

Figure 3.6: Dogleg and matching section sketch from IBS to ESM. The straight line for low-energy high energy experiments is shown too.

Bibliography

[1] C. Hernandez-Garcia et al. “Compact- 300 kV dc inverted insulator photogun with biased anode and alkali-antimonide photocathode”. In: *Physical Review Accelerators and Beams* 22.11 (2019), p. 113401.

[2] C. Pagani et al. “LASA Cs_2Te Photocathodes: The Electron Source for XFELs”. In: *Congress of the Department of Physics*. Springer. 2017, pp. 281–292.

[3] S. Lederer et al. “Update on the Photocathode Lifetime at FLASH and European XFEL”. In: *39th Int. Free Electron Laser Conf.(FEL’19), Hamburg, Germany*. 2019.

[4] T. Takahashi et al. “Development of a 1.3-GHz buncher cavity for the compact ERL”. In: *Proc. 5th Int. Particle Accelerator Conf.(IPAC2014)*. 2014, pp. 3866–3868.

[5] S. Kazakov et al. “Latest Progress in Designs and Testings of PIP-II Power Couplers”. In: *Proc. SRF’19* (Dresden, Germany). International Conference on RF Superconductivity 19. JACoW Publishing, Geneva, Switzerland, 2019, pp. 263–266. DOI: 10.18429/JACoW-SRF2019-MOP080.

[6] G. Hoffstaetter, D. Trbojevic, and C. Mayes. *CBETA Design Report*. Tech. rep. BNL-114549-2017-IR. Brookhaven National Lab.(BNL), Upton, NY (United States), 2017.

[7] V. Shemelin et al. “Dipole-mode-free and kick-free 2-cell cavity for the SC ERL injector”. In: *Proceedings of the 2003 Particle Accelerator Conference*. Vol. 3. IEEE. 2003, pp. 2059–2061.

[8] V.F. Khan et al. “High power rf input couplers and test stand for the bERLinPro project”. In: *Proc. IPAC’14* (2014), pp. 2487–2489.

[9] M. Liepe et al. “The Cornell ERL superconducting 2-cell injector cavity string and test cryomodule”. In: *2007 IEEE Particle Accelerator Conference (PAC)*. IEEE. 2007, pp. 2572–2574.

4. The ERL Main SC-Linac

The layout of the ERL Superconducting Module (ESM) follows the CBETA Main Linac Cryomodule [1] and is shown in Figure 4.1. It hosts three superconducting 7-cell cavities and has an overall length of 5 m, providing 40 MeV energy gain to the beam. As said in Section 2.1.2 this is the solution we arrived after the starting evaluation of a two-cavity cryostat. The cavity design, based on the CBETA ERL resonator, is characterized by a cell shape optimized to have a high beam-break-up (BBU) limit for the beam current. Also, with 5 mA beam current combined with the short bunch operation, an efficient damping of the Higher Order Modes (HOMs) is needed, leading to the installation of radiofrequency (RF) power absorbers between cavities. In the following the main part of the ESM will be described.

4.1 Cryomodule and SC Cavities

The cryomodule design has been guided by the ILC cryomodule while necessary modifications have been made to allow Continuous Wave (CW) operation, with correspondingly higher dynamic cryogenic loads. All components within the cryomodule will be suspended from the Helium Gas Return Pipe (HGRP).

The RF cavity operates in CW with resonant frequency f_0=1.3 GHz. The design accelerating gradient needed to achieve 40 MeV beam with I_{beam}=5 mA is 16.5 MV/m, with the intrinsic quality factor Q_0=2×10^{10}. Though this value is challenging, it is required minimize heat to be removed from cavity walls and thus the load for the cryogenic system. Table 4.1 shows the BriXSinO ERL cavity main parameters.

The loaded quality factor (Q_{L}) is determined by the residual detuning δf [2] (i.e. the residual difference between the generator frequency and the cavity resonant frequency) according to the relation

$$Q_{\text{L}} = \frac{f_0}{2\delta f}, \tag{4.1}$$

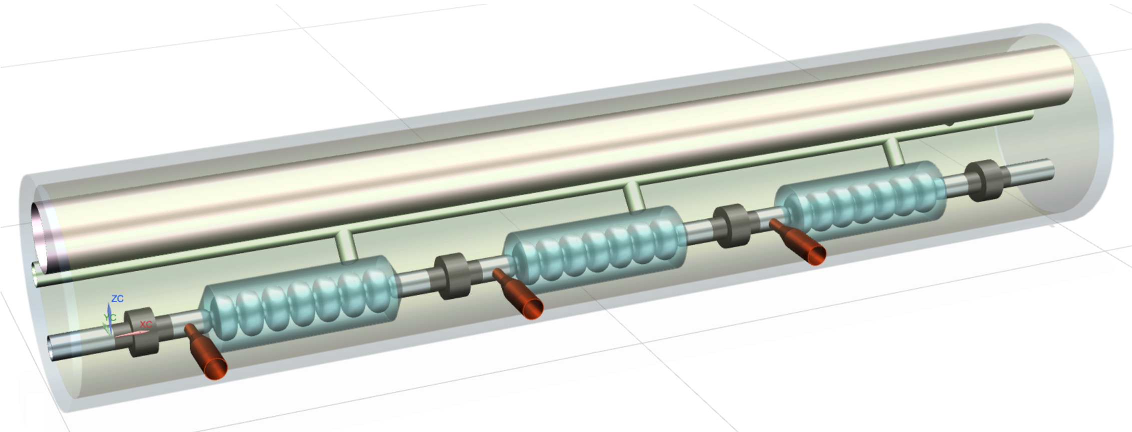

Figure 4.1: Layout of the ERL Superconducting Linac Module

where $\delta f = \delta f_D + \delta f_S$. The first term δf_D is the dynamic detuning due to microphonics and dynamic ponderomotive effects. The second term δf_S is the static detuning due to static Lorentz force detuning, mechanical tuners, etc.

If we conservatively assume $\delta f = 20$ Hz rms (almost double than CBETA) we get an optimal value of about 3.25×10^7. To determine the required amplifier output power [2], we can use the general expression for the forward RF power of a resonating cavity driven by a power source

$$P_f = \frac{(\beta+1)L}{4\beta Q_L \frac{r}{Q}} \left[(E_{acc} + I_{beam} r_L \cos\Psi_b)^2 + \left(2Q_L \frac{\delta f}{f_0} E_{acc} + I_{beam} r_L \sin\Psi_b \right)^2 \right] \tag{4.2}$$

where P_f is the RF forward power in [W], E_{acc} is the cavity accelerating gradient [V/m], (r/Q) is the shunt impedance per unit length, [Ω/m], $r_L = Q_L(r/Q)$ is the (coupled) shunt impedance per unit length [Ω/m], β is the cavity coupling factor ($\beta = (Q_0 - Q_L)/Q_L \gg 1$), I_{beam} is the magnitude of the vector sum of the beam currents in the cavity and Ψ_b is the phase of the vector sum of the currents ($\Psi_b = 0$ is defined as being the beam on crest).

Using the above equation we get $P_f \approx 3.6$ kW. After including a 15% power margin to cope with transmission losses about 4.1 kW forward power would be required for each cavity, but additional margin is required by the specific needs of operation in energy recovery mode. Since perfect energy recovery means perfect beam current cancellation, the recovery efficiency parameter is defined by the residual net beam current amplitude after cancellation. Figure 4.2 shows the minimal RF power requirements for different beam currents and recovery efficiencies.

For a technology demonstrator such as BriXSinO, the baseline choice of a 10 kW RF Solid State Amplifier (SSA), following CBETA choice [3], is therefore the result of a trade-off between the will to benefit from the ERL scheme by lowering RF amplifier capital cost and allow for not ideal recovery efficiency, anyhow restricted to not less than (90%).

The expected AC (plug) to RF efficiency for the SSAs is about 40% which results in AC plug power requirement of 30.7 kW for the 3 amplifiers needed for the full Linac, in case of full recovery. The RF and AC plug powers in case of perfect and 95% recovery efficiencies are shown in Table 4.2.

Each SSA unit will be cooled down by water (or other coolant like ethylene glycol) chillers working at 30 °C water temperature and a flux up to 30 L/min. The amplifier requested bandwidth is 1.3 GHz ± 20 MHz.

This configuration can also handle two-way acceleration with 5 μA beam current up to 80 MeV final energy.

Table 4.1: BriXSinO ERL cavity main parameters

Parameter	Value
Type of accelerating structure	Standing wave
Accelerating mode	TM_{010} π-mode
Fundamental frequency (MHz)	1300
Design gradient (MV/m)	16.5
Intrinsic quality factor Q_0	2×10^{10}
Loaded quality factor Q_{EXT}	3.25×10^7
Active length (m)	0.81
Cell to cell coupling (%)	2.2
Iris diameter (mm)	72
Beam tube diameter (mm)	110
R/Q (Ω)	774
Geometric factor G (Ω)	271
E_{peak}/E_{acc}	2.06
B_{peak}/E_{acc} (mT/MV/m)	4.196
$\Delta f/\Delta l$ (kHz/mm)	350
Lorentz force detuning constant (Hz(MV/m)^2)	1
Cavity bandwidth $\delta f = f/(2Q_{EXT})$ (Hz) HWHM	20
Total longitudinal loss factor $k_{\parallel}$ (V/pC), σ=2.2 mm	3.5

4.2 Power coupler

The main coupler needs to provide at least about 3.6 kW CW RF to the cavity for perfect ERL operation and 20 Hz detuning operation, but must withstand up to 10 kW CW to also allow not perfect ERL efficiency. As reported in the previous paragraph, the coupler external-Q is 3.25×10^7 (with the option to adjust it using a waveguide three-stub tuner) in order to minimize the RF power requirements taking into account the preview microphonics noise. The BERLinPro modified TTF III [4] power coupler is the suitable solution for our design: modifying the cooling of the coupler inner conductor, CW power capability has been raised from 5 kW to 10 kW. The coupler consists of a cold section mounted on the cavity in the clean-room and sealed by a 'cold' ceramic window, and a warm section incorporating a transition from the evacuated coaxial line to the air-filled waveguide. The warm coaxial line is sealed by a 'warm' ceramic window. Both windows are made of alumina ceramics and have anti-multipacting titanium nitride coating.

The scheme 10 kW SSA and TTF III power coupler is also previewed for three two cell CBETA cavities of BriXSinO Injector SC Booster (ISB), so that we can afford a single power coupler design for all SC cavities. The modified TTF III coupler installed on the 2-cells cavity of the BERLinPro booster is shown in Figure 4.3 as a reference.

The RF power distribution from the power amplifier to the resonator employs R12 (WR770) or R14 (WR650) standard waveguides. A conceptual diagram of the RF system is shown in Figure 4.4.

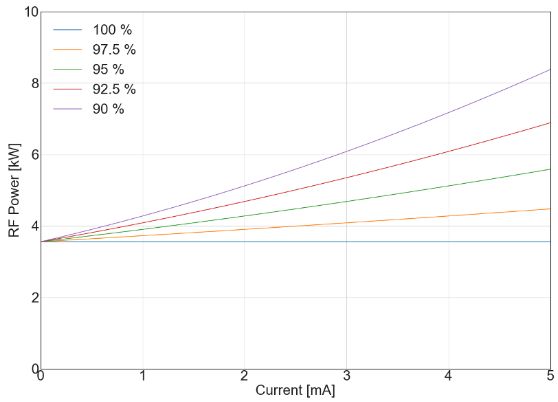

Figure 4.2: RF forward power vs. beam current at different recovery efficiencies. As visible, in the case of a perfect recovery (100%) only the nominal 3.6 kW would be required (without margins applied).

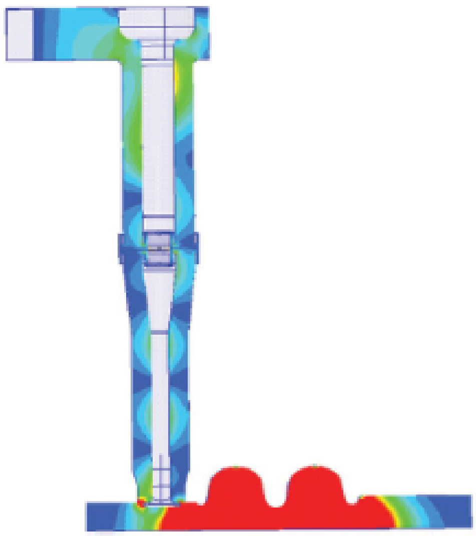

Figure 4.3: Geometry and EM field power density for a modified TTF III power coupler installed on BERLinPro booster cavity.

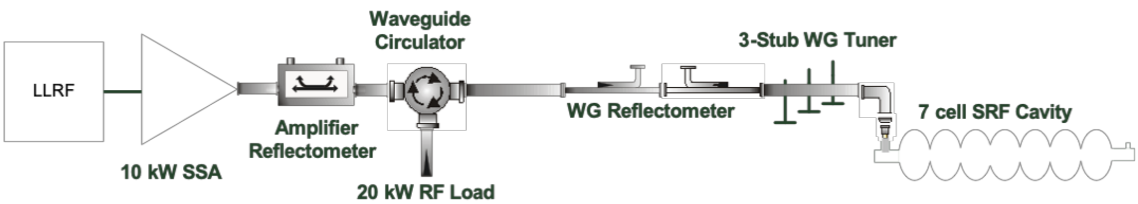

Figure 4.4: ERL RF power distribution scheme.

Table 4.2: RF power requirements for two different energy recovery efficiencies.

Recovery Efficiency	100%	95%
E_{acc} (MV/m)	16.5	16.5
Accelerating voltage V_{cav} (MV)	13.4	13.4
Nominal Incident Power P_{for} (kW)	3.6	5.3
Power from amplifier 15% loss (kW)	4.1	6.1
# cav, # solid state amps (40% efficiency)	3	3
Plug Power @ nominal E_{acc}, P_{plug} (kW)	30.7	45.7

4.3 Frequency tuner

The frequency tuner [5] has the twofold task of tuning the cavity at the proper frequency and of keeping it on resonance during operation. The first action is accomplished via slow mechanical deformations to the cavity. The fast compensation during operation is performed by a piezo-assisted mechanism allowing counteracting the Lorentz force detuning and microphonic noise. Currently at CBETA a lateral frequency tuner solution has been adopted, based on Saclay I tuner with a stepping motor drive for slow frequency adjustment (> 500 kHz tuning range) and piezo-electric actuators hosted in a proper frame for fast compensation (> 1 kHz tuning range) (Figure 4.5). In the search for optimized and homogeneous technical solutions, the possibility to use the same coaxial blade tuner in use for ISB cavities will be considered.

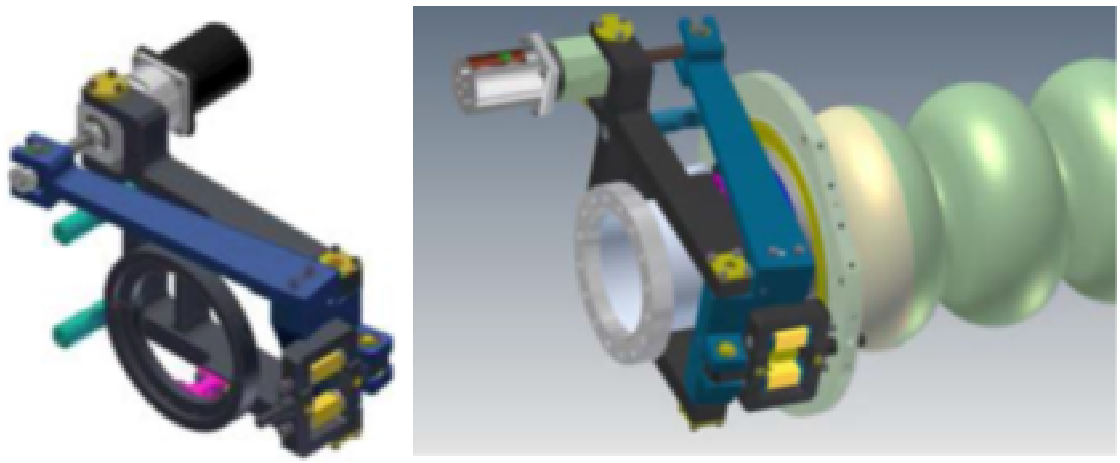

Figure 4.5: 3D view of the CBETA ERL Linac cavity frequency tuner.

4.4 HOM absorber

When a charge crosses a resonant structure, as an RF cavity, it excites the fundamental mode and Higher Order Modes (HOMs). The fields of these latter modes, when trapped inside the structures, can have consequences both for the extra RF power dissipated on the cavity walls and for the beam stability [6]. The HOMs are an issue for all CW machines and especially for ERLs which is strongly related to the bunch spectrum and the induced wake function. Besides being a problem for the beam stability, the HOM power is dissipated at cryogenic temperatures (at 4.5 K and 80 K) and hence it constitutes a major load to the cryogenic plant. A deep analysis of this topic has already been done in Chapter 2, Sections 2.2 and 2.3, using HOMEN and CST codes, so here we just put

Figure 4.6: HOM beamline absorber installed between two cavities (courtesy of Cornell).

as a reminder few relations that describe the HOM interactions with beam and the accelerating structures, in stationary working conditions.

The average monopole HOM power loss per cavity is proportional to its longitudinal loss factor $k_{\|}$, and is also proportional to the beam current I_{beam} times bunch charge Q_{bunch}, that is:

$$P_{\|} = k_{\|} Q_{\mathrm{bunch}} I_{\mathrm{beam}} \tag{4.3}$$

where the loss-factor $k_{\|}$ depends on cavity shape and bunch length and can be found in Table 4.1. From Section 2.3 we get that the average monopole mode HOM power excited by the 5 mA, 50 pC beam is found to be 2.5 W for the entire ERL Main Linac.

If a monopole mode is excited on resonance, the loss for this mode can be much higher:

$$P_{\mathrm{HOM}} = 2 Q_{\mathrm{L}} \frac{R}{Q} I_{\mathrm{beam}}^2 \tag{4.4}$$

proportional to Q_{L} and R/Q of the excited monopole mode. For high currents, this power can be very large, unless the mode is damped to a low quality factor.

Dipole modes can cause beam-break-up (BBU) instability, if not sufficiently damped. The BBU threshold is

$$I_{\mathrm{BBU}} \propto \frac{\omega}{\left(\frac{R}{Q}\right) Q} \tag{4.5}$$

so strong HOM damping is required to push the threshold above the operating beam current. As outlined in Chapter 2, the optimal solution for the HOM absorption is to install a broadband absorbing material cylinder [5], covering the HOM range up to 40 GHz, coaxially to the beam line and located in the beam tube sections between the cavities, with the beam passing on its axis. CBETA solution employs a SiC cylinder from CoorsTek (SC_35) which is shrink fit into a titanium cooling jacket and flange, as shown in Figure 4.6.

4.5 Control system (Low level RF - LLRF)

All ERLs require very stable RF fields [7], of the order of 10^{-4} in relative amplitude and below 0.1° in phase. This is challenging because the superconducting cavities in an ERL need to be

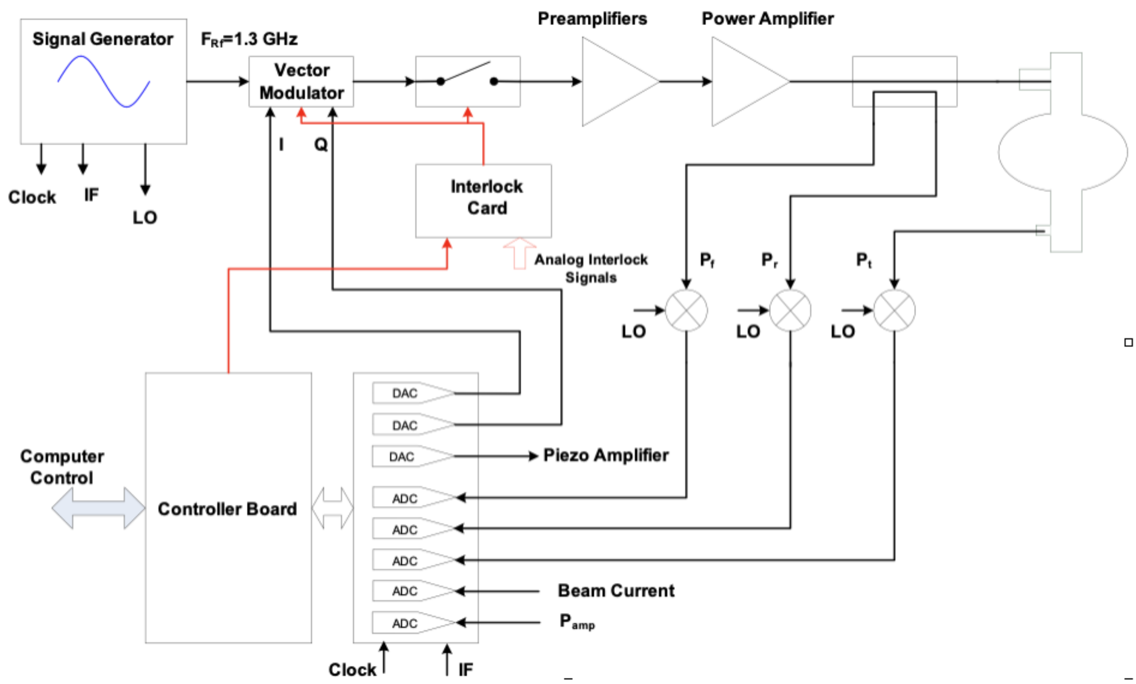

Figure 4.7: ERL LLRF scheme.

operated with a high loaded Q_L, of several 10^7 for efficient operation. The LLRF system must include low noise field I/Q detection, low latency field control, advanced feedforward-feedback cavity frequency control with a fast piezo-driven frequency tuner, and a state-machine for start-up and trip-recovery. Finally, since for beam acceleration, but above all for the feasibility of the ERL operation, the LLRF system must provide the monitoring of the beam (forward and backward) phases with respect to the RF field.

A general architecture scheme for a LLRF to be used for BriXSinO operation is shown in Figure 4.7.

Input signals are cavity input, reflected and transmitted powers, together with resonant frequency, beam current and power amplifier level. An interlock card processes alarm signals and switches the RF power off.

4.6 SC cavity construction and characterization

INFN LASA [8] has great experience in realizing accelerating structures involving industry, that in the last years led to the delivery of half of the 1.3 GHz 800 resonators to EXFEL and 38 cavities for the medium beta section of ESS. The construction process has many intermediate steps, from deep drawing of niobium sheets to form half-cells to the final resonator. After each construction step, components and full cavity must pass frequency, dimension and geometry controls. A rigid quality control protocol, based on the exchange and analysis of certificates during all the phases of cavity construction together with inspections of the companies facilities, successfully used during EXFEL and ESS cavity production, will be issued to be sure to fulfill all design specs during the resonator manufacturing.

Cavity qualification test is done at LASA vertical test facility, checking the resonator specs ($Q_0 \geq 2 \times 10^{10}$ @ $E_{acc} = 16.5\,\text{MV/m}$) with a power test at $T = 2\,\text{K}$ temperature.

Bibliography

[1] G. Hoffstaetter, D. Trbojevic, and C. Mayes. *CBETA Design Report*. Tech. rep. Brookhaven National Lab.(BNL), Upton, NY (United States), 2017.

[2] T. Powers and C. Tennant. *Implications of incomplete energy recovery in srf-based energy recovery linacs*. Tech. rep. Thomas Jefferson National Accelerator Facility, Newport News, VA, 2007.

[3] N. Banerjee et al. “RF Commissioning and Performance in the CBETA ERL”. In: *10th Int. Particle Accelerator Conf.(IPAC’19), Melbourne, Australia, 19-24 May 2019*. JACOW Publishing, Geneva, Switzerland. 2019, pp. 3003–3006.

[4] V.F. Khan et al. “High power rf input couplers and test stand for the bERLinPro project”. In: *Proc. IPAC’14* (2014), pp. 2487–2489.

[5] F. Furuta et al. “Performance of the Cornell Main Linac Prototype Cryomodule for the CBETA Project”. In: *North American Particle Accelerator Conf.(NAPAC’16), Chicago, IL, USA, October 9-14, 2016*. JACOW, Geneva, Switzerland. 2017, pp. 204–207.

[6] M. Liepe et al. “Conceptual layout of the cavity string of the Cornell ERL main linac cryomodule”. In: *power [MW]* 2.4 (2003), p. 6.

[7] M. Liepe and J. Knobloch. “Superconducting RF for energy-recovery linacs”. In: *Nuclear Instruments and Methods in Physics Research Section A: Accelerators, Spectrometers, Detectors and Associated Equipment* 557.1 (2006), pp. 354–369.

[8] P. Michelato et al. “Status of the ESS medium beta cavities at INFN-LASA”. In: *Proc. of the 10th Int. Part. Accel. Conf.(IPAC), Melbourne, Australia*. 2019, pp. 2211–2214.

5. Low Phase Noise Laser System

One of the fundamental elements in the BriXSinO machine is the optical system. The aims of the optical system are both pumping the two Fabry-Pérot (FP) cavities of the inverse Compton scattering (ICS) X-Ray source and exciting the photocathode for the generation of the electron bunches. Moreover, the laser oscillator will be used to carry the timing reference to all other BriXSinOcomponents. These goals will be performed on two optical tables, shown in Figure 5.1. On the first one, placed along the electrons pipeline, will be positioned the main oscillator, the fiber amplifier system and the two FP cavities. On the second, located near to the photocathode, will be the second fiber amplifier system, the Pockels cell and the process chain that treats the light pulses before they reach the photocathode. A small portion of the light coming from the primary oscillator on the first optical table will be brought to the second through an optical fiber.

The main oscillator, model Orange from the Menlo Company, is a 1035 nm mode-locked Yb-laser with the design 92.857 MHz repetition frequency. An internal amplification system guarantees a maximum output power of 10 W, with a spectral width of 13 nm and a pulse duration of 190 fs. The light pulses, outgoing the oscillator, are temporally stretched by a chirped volume Bragg gratings (CVBG) up to 440 ps with a spectral width of 2.8 nm, required for the amplification processes based on the well know chirped-pulse amplification (CPA) technique. The laser is then divided in two by a beam splitter (BS): a small portion (100 mW) is coupled in fiber and carried to the other optical table; the remaining power (about 2 W) instead goes to the amplification system of the FP cavities.

The strategy we intend to follow in BriXSinOwill be to use a FP cavity with a "low" Finesse but with high input power. The cavity will be easier to align and with better stability than a cavity with a "high" Finesse. Since the cavity gain will be in the thousands, to have cavity power in the hundreds of kW the amplification system has to bring the laser input power up to 100 W per cavity. Considering there are two cavities it will be necessary either an amplifier up to 200 W or two amplifiers of 100 W. The NKT aeroGAIN-BASE-1.2 fiber amplifier will perform this system. The fiber has a 10 μm signal core and is pumped by a 200 μm Yb-fiber diode at 976 nm. To avoid non-linear effects on the signal arriving at the very sensitive Fabry-Pérot cavities, the pump is injected to the fiber in the backward configuration. Furthermore, at the start and end of each

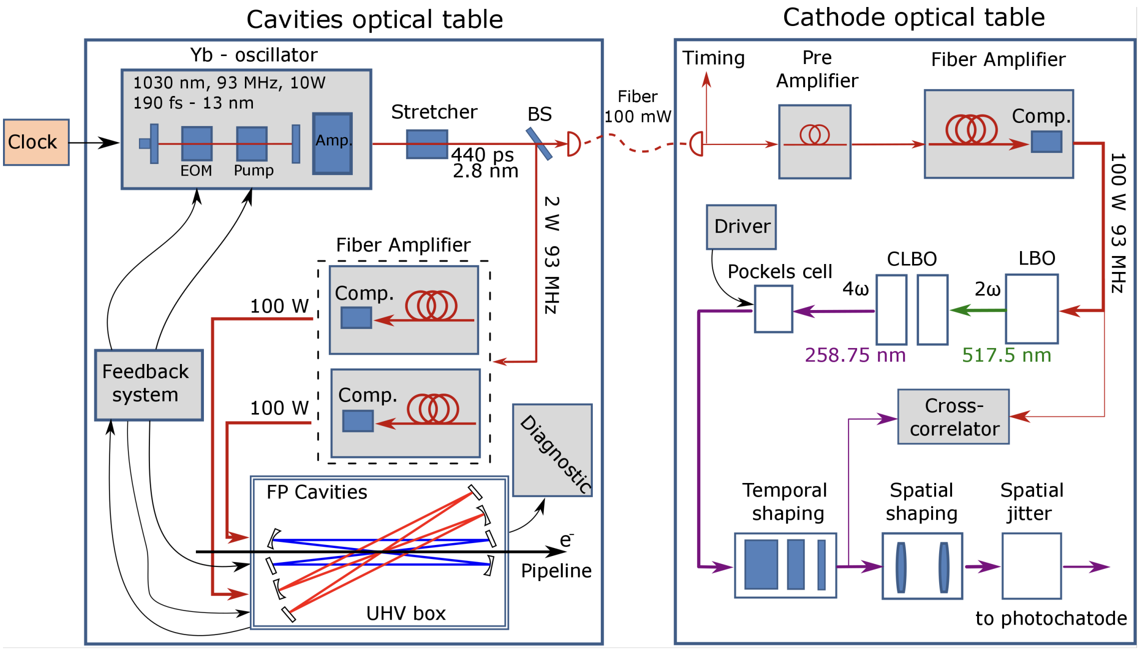

Figure 5.1: Layout of the optical tables.

amplification stage are needed Faraday isolators (FIs) to avoid self-lasing phenomena and to protect the oscillator from dangerous reflections.

Once out of the amplifier, the light reaches the FP cavities, which are located inside a UHV chamber. The cavities are formed by 4-mirrors each in the crossed configuration. Three mirrors are made by ultra-low expansion (ULE) material while the entrance mirror is made by sapphire. The cavities are undercoupled, and the Finesse will be about 5000, in order to reach a power around 200 kW. For a FP cavity to be in resonance with an oscillator laser is need a feedback system. The cavities stabilization system has to fulfill two tasks: lock the round trip path of the cavity to the repetition rate of the laser and keep the carrier-envelope-phase (CEP) of the oscillator stable. Both tasks occur using the so-called Pound – Drever – Hall (PDH) technique and the scheme will be shown in Chapter 23. About the cavities: one of the peculiarity of the BriXSinO ICS source will be producing a dual-color X-Ray beam with a high repetition rate. To obtain the two-color beam we need the two FP cavities to be oriented differently with respect to the electron beam. The photons store in the cavities will collide with the electron bunches at the same interaction point (IP) but with two different angles. The switch between the two energies can be made by swapping the interaction laser. The technique proposed for our source involves rotating the curved mirrors by two opposite angles to translate the optical plane vertically, and will be shown in the Appendix 23. The FP cavity table will be located inside the ICS room, which will be not accessible during machine operation. It will therefore be necessary that all the handlings are remotely controllable. Such movements will be necessary to align the cavity laser beam with the electron beam, to optimize the ICS process. Furthermore, the cavities will be monitored by an external diagnostic system, which takes part in the signal coming from the UHV box and allows to secure the laser in case of operating errors or loss of cavity stabilization.

About the second optical table, light arrives at low power thanks to an optical fiber. After that, the light is first pre-amplified up to about 2 W by a polarization-maintaining (PM) Yb-doped fiber, and then amplified up to 100 W by commercial SC-B high-power fiber amplifier, produced by the Alphanov Company. The amplifier is pumped forward by a 976 nm Photontec (M976) laser diode. Then, before reaching the photocathode, the light pulses have to be treated. Starting from the IR light at 1035 nm, the 4th harmonic (258.75 nm) is generated to obtain pluses suitable for the photoemission process. The task is performed using Lithium tri-borate (LiB_3O_5) and BBO (BaB_2O_4) crystals for the second and fourth harmonic generation, respectively.

Since one of the features of BriXSinO is recovering energy from the returning electron beam, the power that reaches the photocathodes must rise slowly without leaps. In conditions of energy recovery Linac (ERL) regime there cannot be a significant imbalance in the power of the input beam compared to the return one, otherwise, the RF guns are not able to provide such discrepancy. For this reason, the power of the laser beam arriving on the photocathodes must be raised slowly. Changing the repetition rate after the 4th harmonic generation ensures a smooth rise in power while keeping the energy per single pulse constant. This task is assigned to a Pockel cell, driven by a modulator.

Subsequently, the pulses undergo an intensity profile shaping both in temporal and spatial domain. The stacking method for the temporal shaping exploits birefringent crystals: using n crystals it is possible generate $2n$ pulses replicas with alternate polarizations. These replicas add together to give a rectangular temporal profile.

The so-called π-Shaper, based on the aspheric lens method, will be used instead for the spatial shaping. A typical scheme for a π-Shaper involving two aspherical lenses: the two lenses rearrange the Gaussian intensity distribution of the incoming pulse, in order to obtain a spatially rectangular profile.

The diagnostic on the temporal shape of the pulses is achieved by the cross-correlation between the 4^{th} harmonic signal and the IR one. Finally, a system provides the required spatial stabilization on the photocathode target.

The following tables show the parameters of the BriXSinO optical system.

Table 5.1: Harmonics parameters

Harmonic parameters		
	2^{nd} harmonic	**4^{th} harmonic**
Wavelength (nm)	517.5	258.75
Repetition rate (MHz)	92.857	92.857
Pulse duration (ps)	1.2	3
Power (W)	37	6
After shaping		
Shape		Rectangular
Dimension (mm)		0.5
Pulse duration (ps)		22
Rising time (ps)		1
Ripple (%)		10

Table 5.2: Cavity parameters

Free spectral range (MHz)	92.587
Input power (W)	100
Finesse	5000
Gain	2800
Mode width (kHz)	18

6. Compton Source: high flux X-Ray with F-P cavities

6.1 "Sors" Inverse Compton scattering X-Ray source

6.1.1 Inverse Compton scattering experimental line

The inverse Compton scattering experimental line is placed in the clockwise direction of electron beam in the zero dispersion interval between two DBAs. The interaction point (IP) region of the line is not equidistant from the two adjacent DBAs. It is in fact 0.75 m from the focusing triplet upstream the IP and 0.95 m to the defocusing triplet as shown in figure 6.1. This has been chosen as compromise between the short focal length needed to the electrons to be focused in the transverse dimension up to 35 μm and the size of optical table with installed the two Fabry-PérotOptical Cavity for producing two color X-Rays.

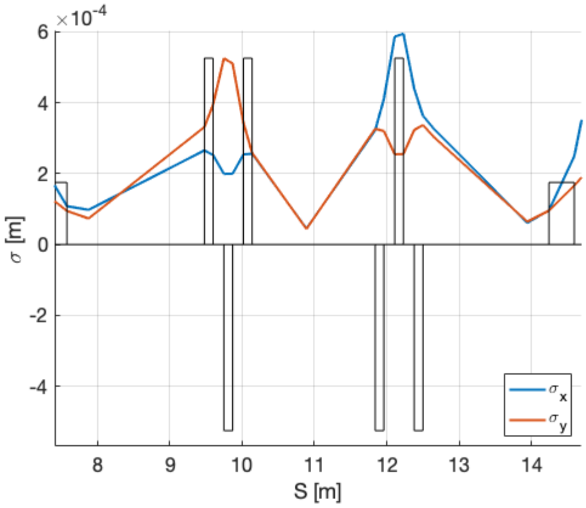

Figure 6.1: Inverse Compton scattering IP.

In Table 6.1 the parameters of the electron beam at IP as obtained by start to end simulation are presented.

6.1.2 Inverse Compton scattering theory

A schematic geometry of the Compton interaction is shown in Fig. 6.2. The electrons, arriving in the interaction points (IP) with energy E_0, interact with the laser pulse, whose photons have energy E_L. The interaction angle is α_0. The scattered photons acquire an energy

$$E_\mathrm{ph} = \frac{2E_\mathrm{L}\gamma^2(1+\cos\alpha_0)}{1+\gamma^2\theta^2}, \tag{6.1}$$

correlated with the emission angle θ, and they are spread in a cone with opening angle $\approx 1/\gamma$ around the direction of the electron motion, where γ is the electron Lorentz factor. The photon energy is maximum on axis ($\theta = 0$, Compton edge), while it decreases as the emission angle increases. This permits to control the relative bandwidth $\Delta E_\mathrm{ph}/E_\mathrm{ph}$ [1] [2] by means of irises.

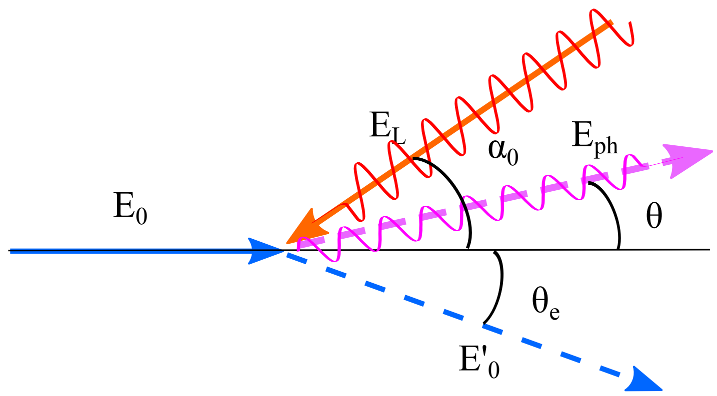

Figure 6.2: Geometry of the scattering process. The interaction angle between the incoming electron E_0 and the incoming photon is α_0. The emitted photon draws an angle θ with the incoming electron direction. E_0' is the electron energy after the scattering, θ_e is the electron scattering angle.

The total number of photons scattered in a single Compton process can be evaluated as:

$$N_\gamma = \frac{1}{2\pi\sqrt{\sigma_{Ly}^2+\sigma_y^2}}\frac{\sigma_{Th}N_LN_e}{\sqrt{\sigma_{Lx}^2+\sigma_x^2+(\sigma_{Lz}^2+\sigma_z^2)\tan\left(\frac{\alpha_0}{2}\right)^2}} \tag{6.2}$$

where N_L is the number of photons per laser pulse, N_e the number of electrons per bunch, σ_{Th} the total Thomson cross-section, $\sigma_{Lx,Ly} = w_{0x,y}/2$ the rms laser pulse spot sizes, $\sigma_{x,y}$ the rms electron bunch spot sizes, $\sigma_{Lz,z}$ the rms laser pulse and electron bunch length respectively and α_0 the interaction angle. The number of scattered photons inversely depends on a combination of the transverse and longitudinal r.m.s. sizes of the interacting bunches. A direct way to maximize the photon flux is then to focus as much as possible both electron and laser pulses at the IP and optimize their profile overlap.

The Compton photon energy can be tuned from16 keV to 45 keV by varying the electron energy value E_e from 30 to 50 MeV as shown in formula 6.1.

6.1.3 Inverse Compton scattering simulation

The first working point is the result of a full start-to-end simulation along all the BriXSinO electron beam line for electrons energy at IP E =43 MeV, from the photocathode to the radiation detector.

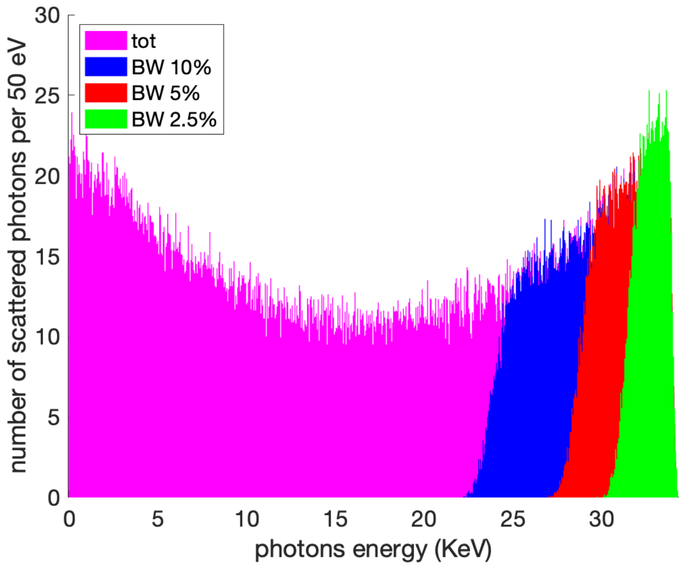

Figure 6.3: Spectra of scattered photons.

The electron bunch parameters at IP used in this simulation, as well as the laser and the radiation characteristics, are presented in the first seven lines of Table 6.1. The Compton emission has been simulated using the MonteCarlo code CAIN [3]. The distribution of the scattered photon total number is presented in Figure 6.3 as a function of the photon energy E_{ph} for different bandwidth values. The total number of emitted photons in the full solid angle attains 2.5×10^5 per shot.

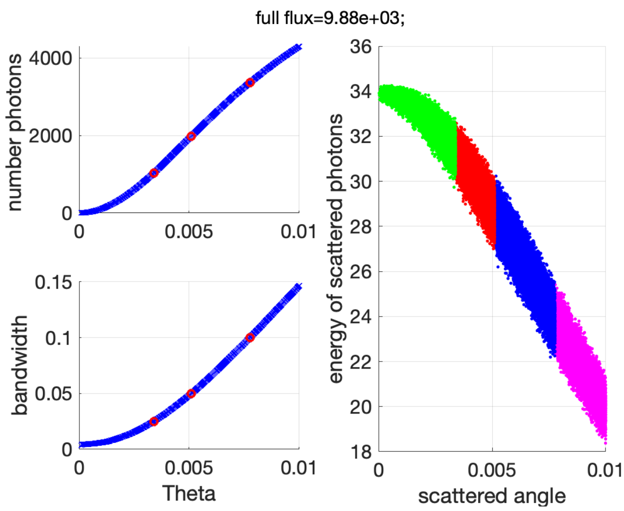

Figure 6.4: Number of scattered photons and their bandwidth as function of scattered angle (left). Energy angular distribution (right)

Due to the boosted nature of the Compton back scattering process, the radiation exhibits an energy-angle correlation (see formula 6.1) with the most energetic photons emitted on axis, while the outer regions are occupied by low energy photons as shown in figure 6.4. This feature makes possible to get monochromatic radiation by inserting irides or collimators along the path of the radiation, selecting therefore only the photons within a given collimation angle θ_{max}. Figure 6.5 presents the spot size of scattered radiation at 10 m, 15 m and 20 m.

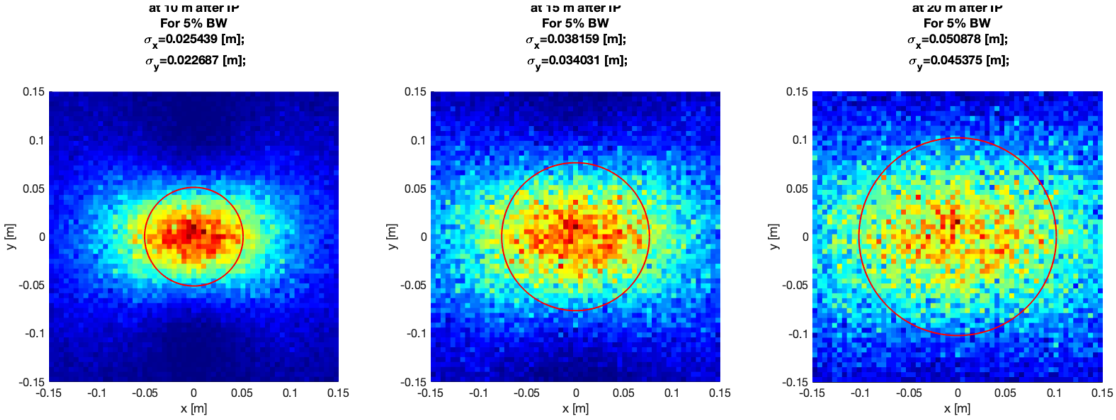

Figure 6.5: Spot size of scattered radiation at 10 m, 15 m and 20 m.

6.1.4 Two colour

As shown in formula 6.1 the energy of scattered photons depends also from initial collision angle α_0. This dependence can be used in the scheme consisting in the use of two laser pulses impinging on the same electron beam at two different angles, with frequencies given by formula 6.1. In papers [4] and [5] we have presented a new scheme to produce two color X-Rays based on compact Compton sources. The potentialities of scattered radiations can be improved by using a different polarization of the initial laser pulses. This scheme can be extended to the production of a sequence of two X-Ray pulses with different colors separated also in time. Figure 6.6 presents the spectra of the two radiations (left) and their energy-angular distributions.

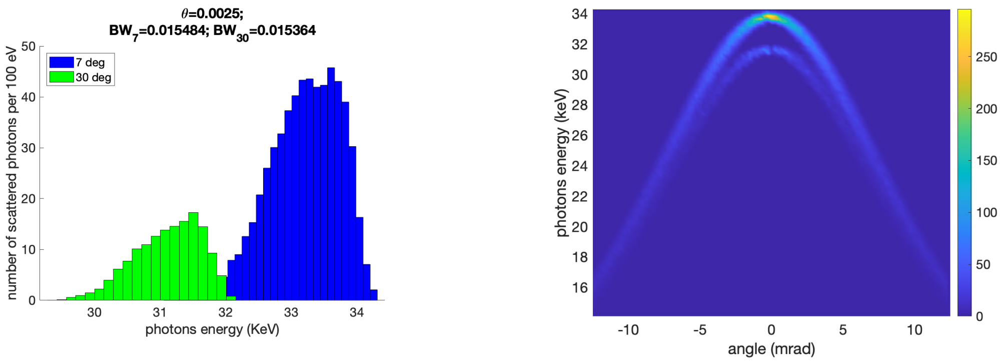

Figure 6.6: Two color spectrum (left) and energy angular distribution (right).

This is of paramount importance for adjusting the time needed by the detectors to record and load the two images at two different colors, that is mandatory for digital subtraction.

6.2 Fabry-Pérot cavities

The BriXSinO ICS source is designed with two Fabry-Pérot cavities to produce a high two-color X-Ray flux. The cavities share the same geometry and are formed by 4 mirrors, 2 curved-/2 flat, in the near-confocal configuration. The cavities are undercoupled, therefore for a finesse F the power inside them is given by:

Table 6.1: Parameters of start to end simulations. (1): brilliance peak: $\frac{N_{ph}}{(2\pi)^{5/2}\sigma_{\gamma x}\sigma_{\gamma y}\sigma_{\gamma X'}\sigma_{\gamma Y'}\sigma_z BW\%}$

Electron beam Parameters			
Electrons mean energy [MeV]	43		
Bunch charge [pC]	100		
Nominal normalized ε_{nx}, ε_{ny} [mm – mrad]	1.25, 1.25		
Nominal relative energy spread σ_e	2.1×10^{-3}		
Bunch length rms [µm]	1.94×10^{3}		
Focal spot size σ_x, σ_y µm	44.8, 43.6		
Laser Parameters			
Laser pulse energy (mJ)	2.7		
Laser wavelength (nm)	1030		
Laser pulse length [ps]	1.5		
Laser focal spot size w_0x RMS [µm]	90		
Laser focal spot size w_0y RMS [µm]	80		
Laser parameter $\alpha_0 = 6.8 * (\lambda_{las}/W0) * \sqrt{\frac{U_L(\mathrm{J})}{\sigma_t(\mathrm{ps})}}$	3.3×10^{-3}		
Collision angle [°]	7 (30 for 2d color)		
γ-ray Photon beam Parameters			
Bandwidth rms %	2.5	5	10
Bandwidth rms [keV]	0.8	1.57	2.9
FWHM [keV]	2.3	4.9	9.3
Collimation angle θ_{max} [mrad]	3.35	5.1	7.7
Peak spectrum [keV]	33.6	33.6	33.6
Mean spectrum [keV]	32.68	31.41	29.34
Nominal # photons per shot N_{Tot}	10^4		
Nominal # photons per shot after collimation N_{ph}	10^3	2×10^3	3.3×10^3
Source rms size $\sigma_{\gamma x}$, $\sigma_{\gamma y}$ [µm] at IP	47, 37		
Source rms $\sigma_{\gamma X'}$,$\sigma_{\gamma Y'}$ divergence [mrad]	1.67, 1.58	2.54, 2.27	3.8, 3
Source rms divergence θ_{RMS} [mrad]	2.3	3.4	4.8
Spot Size at 10 m [mm]	16.6 , 15.9	25.3, 22.7	38, 30
Rad. pulse length $\sigma_{\gamma z}$ [ps]	3.26		
brilliance peak(1)	3.3×10^{13}	1.5×10^{13}	6.2×10^{12}

$$P_{\mathrm{cav}} = \frac{2F}{\pi} P_{\mathrm{in}}. \tag{6.3}$$

With a finesse of 5000 and considering the further losses, it is possible to reach a power of about 200 kW by entering with 100 W.

The peculiarity of the BriXSinO ICS source will be producing a dual-color X-Ray beam with a high repetition rate. To achieve the dual-color beam we need two FP cavities oriented differently with respect to the electron beam.

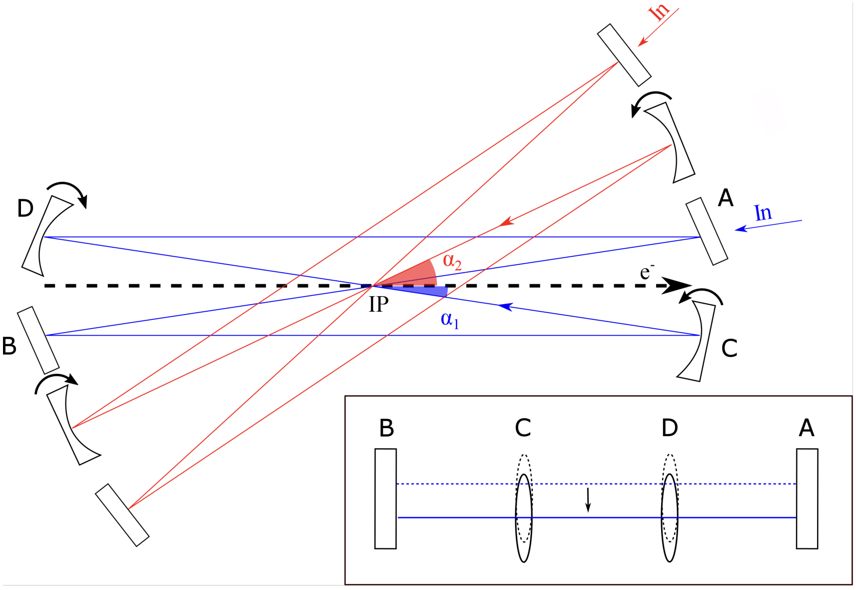

Figure 6.7: Layout of Fabry-Pérot cavities

The scheme is shown in Figure 6.7: the photons store in the cavities will collide with the electron bunches at the same interaction point (IP) but with two different angles: α_1 (blue) and α_2 (red). These angles α_i between the laser and the electron beam is related to the energy scattered photon energy, as for Eq. (6.1). If we consider only the horizontally scattered photons (θ= 0) and an electron beam at 43 MeV ($\gamma \, approx$ 84), the best solution to work around iodine K-edge (33.17 keV) is achieved for collision angles of α_1 = 7° and α_2 = 30°, corresponding to X-Rays energies of 34.0 keV and 31.8 keV, respectively.

The switch between the two energies can be made by swapping the interaction laser. The technique proposed for our source involves the translation of the optical plane vertically by rotating the curved mirrors. The curved mirrors will be equipped with piezoelectric mounting that allowing rotations around the vertical and horizontal axis. At the bottom of Figure 6.7 is displayed the equivalent scheme of the blue cavity as linear. The curved mirrors that rotate are represented by two lenses that undergo a linear displacement. This movement rigidly translates the optical axis and consequently the focus of the cavity. Our simulations have shown that is possible to shift the focus of the cavity by hundreds of μm while it is in actively stabilized resonance. Our measurements will be exposed in Appendix 23.

Parameter of the laser pulses at the focal point are reported in Table 6.1.

Bibliography

[1] N. Ranjan et al. "Simulation of inverse Compton scattering and its implications on the scattered linewidth". In: *Physical Review Accelerators and Beams* 21.3 (2018), p. 030701.

[2] C. Curatolo et al. "Analytical description of photon beam phase spaces in inverse Compton scattering sources". In: *Physical Review Accelerators and Beams* 20.8 (2017), p. 080701.

[3] K. Yokoya. *User manual of CAIN, version 2.40*. 2009.

[4] I. Drebot, V. Petrillo, and L. Serafini. "Two-colour X-gamma ray inverse Compton back-scattering source". In: *EPL (Europhysics Letters)* 120.1 (2017), p. 14002.

[5] I. Drebot et al. "Multi Colour X-Gamma Ray Inverse Compton Back-Scattering Source". In: *Proc. 9th International Particle Accelerator Conference (IPAC'18), Vancouver, BC, Canada, April 29-May 4, 2018* (Vancouver, BC, Canada). International Particle Accelerator Conference 9. JACoW Publishing, 2018, pp. 4196–4198. ISBN: 978-3-95450-184-7. DOI: `doi:10.18429/JACoW-IPAC2018-THPMF057`.

7. High Power kW-class THz Free Electron Laser

Terahertz (THz) radiation is a frontier area for researches in physics, chemistry, medicine, biological and material sciences [1]. The increasing number of advanced applications of THz waves in all these different fields demands versatile and tunable sources combining high-power and excellent output performances. Novel experiments and tests of interesting techniques to be performed at BriXSinO with THz radiation are discussed in details in this Report, Part II.

Mainly, IR, far-IR and THz FELs are designed to operate as oscillators, i.e., they are equipped with resonators confined by mirrors: mostly the mirrors are two, one of them highly reflective and the other one either translucent or containing out-coupling apertures for permitting the extraction of the radiation. Cavities with a larger number of mirrors have also been considered. Moreover, propagation can be in vacuum or in waveguide. An exhaustive comparative analysis of all TeraHertz FEL worldwide can be found in [2].

7.1 The TeraHertz FEL Source TerRa@BriXSinO

Due to the limited space allocated for the TeraHertz source in the facility bunker, to the high repetition rate and stability in energy provided by the Super Conduction (SC) accelerator, together with the low peak current of the electron beam, the FEL Oscillator concept is the only possible alternative fitting objectives, requirements and constraints of the BriXSinO project. The whole BriXSinO layout, comprehending the TeraHertz Radiation (TerRa) source in the bottom branch of the BriXSinO ring, can be found in Chapter 2.1.3.

7.1.1 The Undulator (TU&IO) and magnetic transfer lines

The scientific case of the Terahertz FEL source Terahertz Radiator (TerRa) indicates strong interest in radiation of wavelengths between 10 and 100 µm (3-30 THz). Figure 7.1 shows the radiation wavelengths allowed by undulator periods from 2.8 to 4 cm and by electron energies from 10 to 55 MeV according to the FEL resonance $\lambda = \lambda_w(1+a_w^2)/(2\gamma^2)$, indicating the possible accomplishments. To increase the radiation spectral domain, the undulator should have variable gaps.

The BriXSinO accelerator line delivers a 50-100 pC electron beam with energy between 22 to 45 MeV, as shown in Table 1.3. With those data, a subset of the reference wavelengths can be achieved using undulator periods from 2.8 to 4 cm.

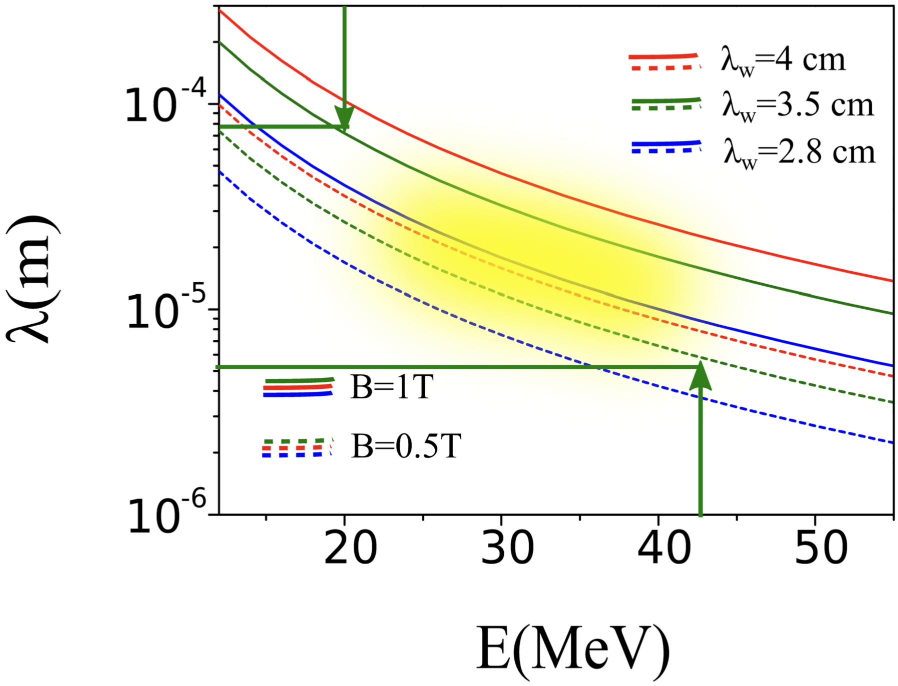

Figure 7.1: Radiation wavelength vs electron energy for λ_w=2.8,3.5,4 cm and $B = 1$ T and 0.5 T. In yellow the region of the scientific case.

The radiation in the TeraHertz range experiences a strong diffraction process, so short period undulators, with their tiny gaps, are not suitable to such a spectral range. The operation at THz wavelengths requires gaps at least of the order of 1 cm, for permitting the transport of a transversely large electron beam and containing the propagation of the highly diffracted radiation. At fixed period, increasing the gap by moving away the girders leads to lower the magnetic field, shifting in conditions of limited emission. For radiation with wavelengths larger than 25 µm, periods shorter than 3 cm require gaps smaller than 5-7 mm with the danger of interaction of electrons and photons with the wall. Periods larger than 3.7 cm, instead, do not permit the operation at wavelengths smaller than 30 µm.

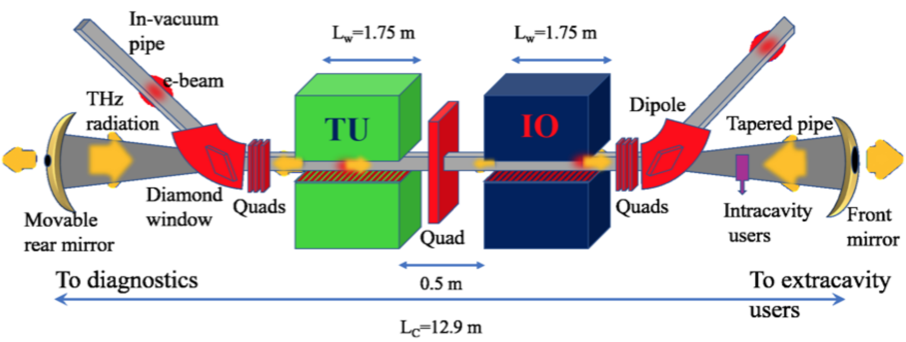

Figure 7.2: The undulator TU&IO at BriXSinO. The elements are not in scale.

The FEL Oscillator TerRa@BriXSinO source is conceived as composed by two undulator modules, separated by a drift where a quadrupole, phase shifters, diagnostics and correctors are allocated, and embedded into an optical cavity equipped with mirrors suitable to the considered

Table 7.1: PM: permanent magnets, VG: variable gaps, LP: linear polarization

Und.		TU	Und.		IO
PM	VG	LP	PM	VG	LP
λ_w	cm	3.5	λ_w	cm	3
B	T	0.5-1	B	T	0.5-1
λ	µm	5-50	λ	µm	3.5-35
gap	cm	1	gap	cm	0.9
$\sigma_{x,y}$	mm	0.15-0.3	$\sigma_{x,y}$	mm	0.15-0.3
L_w	m	1.75	L_w	m	1.75

frequency range. The undulator TU&IO, whose pictorial view is represented in Figure 7.2, is made by two undulator sections that could also be characterized by different periods: TU (Terahertz Undulator) and IO (Infrared Oscillator). They can work either tuned at the same wavelength or separately delivering different wavelengths. The line can be realized modularly, by commissioning previously the TU undulator section and then upgrading the device with the insertion of the IO second module.

Following what mentioned before, a period of 3.5 cm seems to be a good compromise for the TU undulator. The IO module, that should operate at shorter wavelengths, could be of a similar or slightly smaller period, for instance, 2.8-3 cm.

In Table 7.1 the main characteristics of the undulators are reported.

The coupling of the electron beam to the undulator is a fundamental step for allowing substantial radiation growths. The quadrupole allocated in the drift between the two modules facilitates the matching.

The non-magnetic stainless steel beam pipe could be constituted by sections of length about 2 m. The external sizes of the vacuum chamber should be of 10-12 mm within the gaps. The horizontal dimension of the pipe (orthogonal to the undulator magnetic field) should be larger (i.e., at least 4 cm) and could host some lateral mechanical support systems (high vacuum flanges at the end of any pipe section and electron position monitors). In-between the undulator sections there should be a diagnostic chamber with two independent vertical actuation systems (motorized linear stages) capable to host different optical systems (quads, phase shifters, BPM) so as to determine the position of the optics with a precision and repeatability of the order of 10-20 µm for preventing higher electron beam misalignment. Referring to [3], we can argue that permanent magnet undulators with H configuration, linear polarization and variable gaps are suitable for TerRa.

7.1.2 Cavity, Mirrors and radiation transfer lines

The cavity is of a symmetric near-concentric design with a round trip length of L_{rt}=25.8 m; the undulator can be supposed at the center of the cavity. L_{rt} must be a multiple of the distance D between two bunches (at 92.86 MHz, D=3.22 m). This value is helpful for allocating the 2+2 m undulator and diagnostics and for permitting the expansion of the MW-class intra-cavity radiation on the cavity mirrors, whose inter-distance, i.e. L_C = 12.9 m, is equal to four times the bunch separation. The cavity length of 12.9 m would allow the FEL oscillator to start up also when the repetition rate of the quasi-CW electron bunch is decreased, for diagnostic or operation motivations, from 92.86 MHz to 46.5, 23.2 and even 11.6 MHz. The radius of the 15 THz optical mode at the undulator center is about 2 mm. At this location the matched electron beam radius is about 0.2 mm, guaranteeing a good coupling between the electron bunch and the radiation in a large range. The Rayleigh length of a 20 µm wavelength pulse of radius 2 mm is 1.25 m. The radiation, downstream

Table 7.2: Intra-cavity radiation at λ=20 µm in µJ vs L_w (m) and I(A). Saturation is obtained after 100-1000 round trip cycles, i.e., in 1-10 µs, so each datum is the results of 1000-10000 time-dependent Genesis 1.3 runs. Emittance $\varepsilon = 2\,\mathrm{mm-mrad}$, $\Delta\gamma/\gamma = 2.5\times10^{-4}$.

L_w \ I	7.5 A	10 A	20 A	25 A	30 A
1.75 m	10^{-6}	4×10^{-6}	4×10^{-5}	79	270
2.5 m	10^{-6}	10^{-6}	120	175	245
3.5 m	220	355	980	1300	1700

Table 7.3: Intra-cavity radiation in uJ vs ε (mm − mrad) and I(A). L_w=4 m.

$\Delta\gamma/\gamma$	ε(mm − mrad) \ I(A)	5	7.5	10	12.5
2.5×10^{-4}	1.4	105	224	288	535
	2	100	220	355	560
10^{-3}	1.4	85	210	332	488
	2	79	171	296	381

the undulator, is Fourier transform limited and therefore diverges from 2 mm up to about 1.5 cm rms. A tapered pipe, in-vacuum or filled by a controlled atmosphere, connecting the exit of the bending dipole to the mirrors, with dimensions increasing from 1 cm to 15 cm, could avoid the air absorption of the THz radiation.

The cavity mirror radius of curvature is designed to be about 15-25 m, which results in a Rayleigh length in the desired range and a cavity stability parameter of about 0.95.

The water-cooled mirrors, made of copper and covered with gold, should present holes, with round-trip loss near 5%. The out-coupling holes also serve for alignment with a visible reference laser. A system of diamond windows separate the ultra-high vacuum part of the pipe inside the resonator, between the two dipoles, where electrons and radiation are superimposed, from the more moderate vacuum (or controlled atmosphere) of the tapered pipe which drives the radiation between the dipoles and the mirrors. Behind the front mirror, an additional iris and a normal-incidence quartz window can be installed. The radiation of the terahertz FEL, emitted through the mirror opening as a continuous train of pulses, is then transmitted through a dedicated optical beamline to the experimental hall. It could be useful to bore also the rear mirror, in order to put additional radiation diagnostics inside the bunker. An additional experimental station placed close to the exit of the undulator could permit intra-cavity experiments.

7.1.3 FEL working points and simulations

The numerical modeling of the TerRa source has been carried on by using the three-dimensional, time-dependent FEL code Genesis 1.3 [4]. Starting from the electron beam parameters listed in Table 2b, Part I, we have injected into the undulator a sequence of randomly prepared electron beams different one from each other both microscopically and macroscopically, in order to simulate the fluctuations of a bunch train. The study has been performed for radiation wavelengths between 20 and 50 µm. Each result is obtained by maximizing the output power as function of the delay time and cycling the radiation within the cavity, taking into account the details of the optical line that returns the radiation to the mouth of the undulator. Table 7.2 shows the intra-cavity radiation energy in µJ vs current I(A) and undulator length L_w(m) for the case $\Delta\gamma/\gamma$=2.5×10^{-4} and emittance 2 mm − mrad. The results indicate that a surely successful operation at the typical BriXSinO current

Table 7.4: Properties of the intra-cavity (IC) and extra-cavity (EC) THz radiation with different wavelengths.(*,**)This cases has been done with a peak value of current of (*) 15 A and (**) 20 A.

λ (µm)	20	30	35*	50**
Beam energy (MeV)	40	33.2	30	26
IC Energy (µJ)	355	300	952	560
EC energy (µJ)	17.7	15	46.6	16.8
EC average power kW	1.77	1.5	4.66	16.8
Peak power (MW)	250	100	250	100
bandwidth (%)	0.6	1.6	2.7	1.3
size (mm)	2.6	3.5	4.5	5
divergence (mrad)	4	5.5	2.3	5
time duration (mm)	0.5	1	4	4
time delay (mm)	2.2	3	3.5	8
coherence degree	1	0.9	0.8	0.5

values requires a net undulator length of the order of 3.5 m, meaning a total of 4 meters comprises the 0.5 m of empty space between the modules. Then, the parameter space (current vs emittance) has been sampled and the emission region individuated for two values of $\Delta\gamma/\gamma$.

Table 7.5: Intra-cavity radiation in uJ vs $\Delta\gamma/\gamma$ and Δx, L_w=4 m, ε=2 mm – mrad, I=10 A

$\Delta\gamma/\gamma \backslash \Delta x$	0 µm	30 µm	100 µm	170 µm
2.5×10^{-4}	355	302	283	260
10^{-3}	330	280	250	230
1.5×10^{-3}	321	253	190	180

In Table 7.3, the results of such study are reported. The process is characterized by thresholds dominated by current and emittance, and seems to be more sensible to current than emittance. Total mirror reflectivity along the whole cavity of 95% has been assumed. Losses accumulated downstream the exit of the cavity along the transfer line to users have not been accounted for. Due to the relatively large wavelength and to the scarce qualities of the beam, the slippage is huge. A slippage tight control is needed. It can be provided by a transfer line introducing about 2 ± 0.075 mm of delay in the round trip of the radiation. Table 7.4 reports the main properties of the radiation. Single shot power in time and spectrum vs wavelength appear to be single spiked with constant phase. Mirror losses < 5% produce intra-cavity single shot output radiation energy of 17.7 µJ, meaning 1770 W of average power at λ=20 µm. The combined effect of fluctuations in energy $\Delta\gamma/\gamma$ and in beam position Δx is shown in 7.5. Time energy jitters $\Delta\gamma/\gamma < 1.5\times10^{-3}$ and pointing instabilities producing transverse deviations $\Delta x < 170$ µm are tolerate.

Bibliography

[1] C. Koral et al. “Multi-Pass Free Electron Laser Assisted Spectral and Imaging Applications in the Terahertz/Far-IR Range Using the Future Superconducting Electron Source BriXSinO”. In: *Frontiers in Physics* (2022), p. 127.

[2] `hzdr.de/db/Cms?pNid=471`.

[3] J. Pflueger. “Undulator technology”. In: *CERN Yellow Reports: School Proceedings* 1 (2018), pp. 55–55.

[4] S. Reiche. “GENESIS 1.3: a fully 3D time-dependent FEL simulation code”. In: *Nuclear Instruments and Methods in Physics Research Section A: Accelerators, Spectrometers, Detectors and Associated Equipment* 429.1-3 (1999), pp. 243–248.

8. Diagnostics, Timing Controls

8.1 Beam diagnostics

The task of beam diagnostics and instrumentation is to support and aid as much as possible to reach the project goals, i.e. to demonstrate that an ERL is a valuable candidate for a future light sources in terms of stability and reliability. The beam characteristics detailed in the opening part of the present document call for tens of femtosecond precision in time structure and micrometer precision in beam position measurement. As a general principle, we plan to assemble the diagnostics complex for both the commissioning and operation phases by integrating commercially-available instrumentation wherever applicable, and to otherwise tap into larger laboratories expertise by establishing suitable scientific collaborations. The main measured quantities along with the foreseen instrumentation are summarized in the following table:

Table 8.1: Main measured quantities.

Quantity	**Instrumentation**
Emittance	OTR screens, quadrupole scans
Bunch length	Electro-optical devices, deflecting cavities, streak cameras
Compression	Pyro detectors
Bunch arrival time	Bunch arrival monitor
Transverse position	BPM
Transverse position and profile	OTR, YAG screens, wire scanners
Energy spread	Deflecting cavities
Charge	Integrating Current Transformers, BPM sum signals

Here's a list of coarse design considerations for the various classes of diagnostics devices:

8.1.1 Beam Position Monitors

The backbone of the diagnostics system is composed by a set of Beam position monitors (BPMs). The present design foresees 10 beam position monitors (BPM) evenly spread along the injector, around the loop (including the 2 experimental stations) and towards the beam dump. The monitors consist of either simple circular pick-up electrodes or strip line ensembles similar to the ones in use at STAR and developed for other electron machines in Italy.

We refer to these devices as "standard BPMs" (due to their moderate resolution). BPM electronics will follow the simplest possible design, with analog RF front-end modules (as appropriate for each pickup type), and a generic FPGA-based digital carrier board with ADCs mezzanine modules to be shared by all BPMs.

Particular care will be devoted to the BPMs installed close to the main accelerating structure where we need to determine the position of the two co-propagating beams with time displaced bunches. In this case a high bandwidth (up to 3 GHz) may be required and we will develop a special front end.

8.1.2 Beam Size Monitors

The preservation of the small emittance of the beam and the capability to detect its envelopes are part of the project's challenges. Therefore, up to 8 beam size monitors will be installed.

Screen monitors (SCM) with a fluorescent target and optical transition radiation (OTR) targets made of stainless steel will be used for transverse beam profile measurements. We plan to remove undesired coherent OTR (C-OTR) by using a YAG:Ce scintillation target exploiting the spatial property of OTR. Wire scanners (WS) are an alternative for the measurement of high current and energy beam profiles. WS are suited to provide fast scans, i.e. the wire will be driven through the beam during one pulse. Nevertheless, OTR-based systems have been considered as an option also in this area at least for commissioning purpose and in single-bunch operation.

8.1.3 Emittance Measurements

Emittance control is of paramount relevance in the proposed design. Special locations in non-dispersive sections have been foreseen downstream the injector and in the beamlines to measure the projected and if possible the slice emittance. The emittance measurements will be performed with the quadrupole scan method. The transverse beam size will be recorded on a screen monitor while scanning the excitation of a quadrupole magnet just upstream the screen. A set of four beam size measurements will be combined to determine the local Twiss parameters as well as the emittance. This will also allow controlling the optics and correcting its match to the following sections.

8.1.4 Bunch Length Measurements

In the proposed scheme the electron bunch length at the photocathode will be around 20 ps. As the bunch length varies along the accelerator components, appropriate methods of bunch length measurement should be selected.

Commercial streak cameras are useful instrument for the measurement of spatial-temporal structure of electron bunches longer than 200 fs. Synchrotron radiation or optical transition radiation can be used for a direct bunch length measurement using streak camera.

Autocorrelation of coherent synchrotron radiation (CSR) from a dipole magnet or coherent transition radiation (CTR) from a metal foil target can be used to improve the above reported temporal resolution limits. When the micro-bunching instability grows, the CSR or CTR amplitude increases quadratically in the spectrum with respect to the bunch charge. This feature can be exploited as an on-line bunch length monitoring-device during operation. For the time-domain sub-picosecond bunch length diagnostics, a transverse RF deflecting cavity may be used.

The bunch longitudinal structure can also be detected via more novel electro-optical (EO) bunch duration measurement technologies.

8.1.5 Charge Measurement

To ensure a transmission efficiency close to 100% the bunch charge has to be measured at various locations along the machine and well controlled for stable operation. An integrating current transformer can be used for bunch-by-bunch charge measurement. A Faraday cup as well as the beam-dump can be used for charge measurements in the low energy section of the machine. Commercially available integrating current transformers (e.g., Bergoz ICT) will be used in higher energy sections. Their accuracy in bunch-by-bunch charge measurement is few pC. Sum signals from some BPMs can be used, with appropriate calibrations, for non-critical applications. Another possibility are turbo integrating current transformers, which guarantee a measurements range between 50 fC and 300 pC.

8.1.6 Beam Energy and Energy Spread Measurements

In dispersive sections, the beam position along the path varies in proportion to the beam energy. Thus, the beam energy variation can be monitored with an OTR screen at the dispersive section. The slice energy spread is also very important, and can be measured by bending the RF-deflected bunch in the perpendicular direction with analyzing magnets. Separate beam analyzing stations will be installed for the beam energy and spread measurements.

8.1.7 Expected tolerances, resolution and precision

The performance expected for the instrumentation described so far may be estimated from the results obtained at major laboratories involved with similar projects summarized as follows:

- BPMs: 10 µm
- Screen monitors: 50 µm to ≈ 10 µm
- Electro-optical bunch length monitors: ≈ 150 fs
- CTR visible spectrum: ≈ 1 fs
- Integrating current transformers: ≈ 5 pC
- Turbo integrating current transformers: ≈ 50 fC
- Compression monitors: relative measurements only
- Bunch arrival time monitors: ≈ 10 fs
- Transverse deflecting structure: slices of ≈ 20 fs each. Sub fs operation requires higher voltages or longer structures (traveling wave)
- Timing and synchronization: fs up to hundreds of fs

8.2 Timing & Synchronisation

The precision for a timing and synchronization system, given the projected beam characteristics is still within the range of a conventional copper-based RF distribution. A commercial, high quality oscillator (Rohde+Schwarz or equivalent), aligned to GPS for absolute timing, can serve as the master clock.

This RF system will serve as a day zero solution and will provide a well understood and reliable solution for the first commissioning of the machine. The optical system clock can remain autonomous and locked in sync to the main RF.

As the project progresses the bunch length will be reduced to hundreds fs and a more precise synchronization system will be necessary. With the aim of understanding as much of the underlying physics of the machine as possible, a comprehensive diagnostic of the bunch parameters is essential.

Also, with respect to the use of the short pulses in a future experiment at the ERL, it is necessary to have knowledge of pulse length and arrival time at the experimental station.

To match these advancements and to study the possibilities offered by more flexible timing schemes we will evolve the timing system accordingly. As the copper-free operation of large accelerator has been proven in several installations around the world (e.g [1, 2]), leading to the commercialization of fully integrated “reference clock distribution systems” (with accuracies on the order of tens to hundreds of femtoseconds, stability over several days of operation, and typical jitters < 15 fs rms, [3]) we plan to explore, in a cost-reduction perspective for larger future systems, the adoption of such systems, as well as the adoption of standard, Ethernet-based protocols ([4]) for clock distribution where nanosecond-accuracy is sufficient.

A high precision optical synchronization system based on the foreseen existing oscillators for the laser systems may reach an accuracy in the order of a few tens femtoseconds. Utilizing electro optical techniques, a bunch arrival time measurement as well as an electron bunch length measurement can be implemented.

The infrastructure for this optical reference will be foreseen since the beginning of the design. Space will be reserved in the photocathode laser room as well as tubes for the fibers to be blown in later.

A large-scale timing distribution system based on short pulse fiber lasers has been developed at DESY for the XFEL Project. Many of the DESY developments will be given to industry for mass production, which enables to buy well designed products needed for an optical synchronization.

8.3 Integrated Control System

No significant R&D effort is foreseen for the development and integration of the Control Systems. These will be assembled with commercially-available components around a proven three-tier model (see Figure 8.1), building in enough scalability to demonstrate that the model is suitable for larger installations. One of the existing Integrated Control Systems that are in use at larger research facilities (see References [5–8]) will be selected and integrated, based on the availability of common layers and drivers to access all hardware in the apparatus as well as ease of programming integration and access, a long life/maintainability expectancy and a high level of community involvement. Special care will be taken to retrofit the chosen ICS system with a database back-end with no single point of failure, providing distributed operation and pervasive caching, possibly (and ideally) based on the object storage model. Ethernet over optical and copper media will be preferred as the data transfer protocol. Proprietary protocols will be avoided wherever reasonable and converted at the edge of local buses otherwise.

8.3.1 Safety-related controls

The only subsystem that will not be integrated in the ICS (except for read-only asynchronous status reporting), is the safety system, in charge of triggering mitigation actions to protect people, the environment and all facility equipment (access management, beam permit logic, environmental and hazard monitors). Dedicated (commercial) hardware, with no time-shared or volatile programming components, linked by a separate, dedicated interconnect to avoid congestion will be employed for these functions.

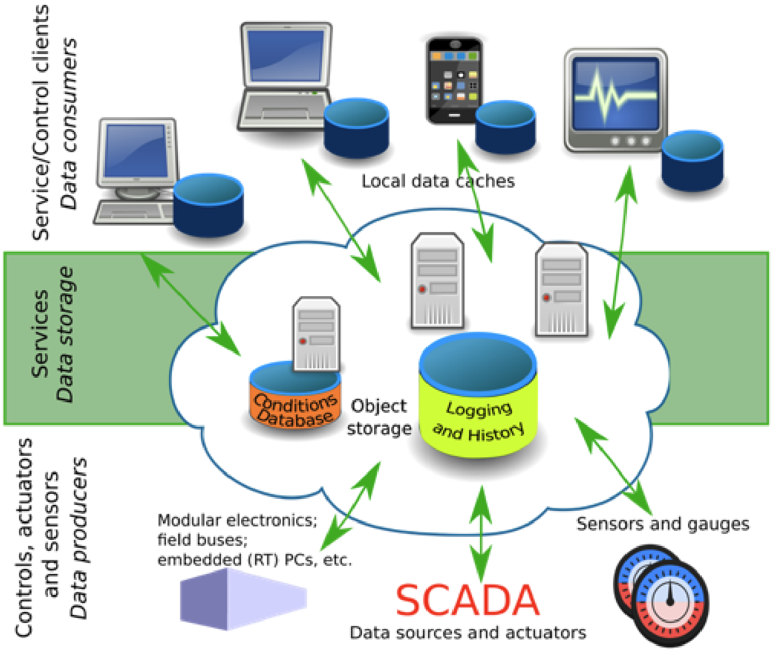

Figure 8.1: Three-tier Integrated Control System (ICS). Each element in the system is able to produce, consume and share data

Bibliography

[1] J.W. Kim et al. "An integrated femtosecond timing distribution system for XFELs". In: *Proceedings of the 10th European Particle Accelerator Conference, EPAC 2006*. 2006, pp. 2744–2746.

[2] S. Schulz et al. "Femtosecond all-optical synchronization of an X-ray free-electron laser". In: *Nature communications* 6.1 (2015), pp. 1–11.

[3] S.G. Hunziker. "Influence of environment changes on libera sync 3 long-term stability". In: *Proceedings of FEL2015, Daejeon, Korea*. 2015.

[4] J. Serrano et al. *The white rabbit project*. `https://cds.cern.ch/record/1743073/`. 2013.

[5] `https://epics.anl.gov/`.

[6] A. Götz et al. "The TANGO control system". In: *ICFA Beam Dynamics Newsletter* 47 (2008), pp. 66–80.

[7] L. Catani et al. "Introducing a new paradigm for accelerators and large experimental apparatus control systems". In: *Physical Review Special Topics-Accelerators and Beams* 15.11 (2012), p. 112804.

[8] G. Grygiel, O. Hensler, and K. Rehlich. "DOOCS: a Distributed Object Oriented Control system on PC's and workstations". In: *PCaPAC conference*. 1996.

9. Cryogenics

9.1 Overview and constraints

The cryogenic plant of the BriXSinO complex will integrate the central LASA cryogenic plant in order to support:

- controlled cool-down and warm-up of the two BriXSinO superconducting cavities cryomodules from room temperature or from an intermediate parking temperature stable stand-by cryogenic configurations at an intermediate temperature for the time windows in between cold run, specifically designed to minimize the mechanical stress and vacuum and cryogenic systems due to thermal cycling while optimizing cryogens consumption.
- sufficient cooling capacity with adequate margins at design temperature ranges to enable robust operation of all BriXSinO cryogenic components. The lowest end of such ranges being the superconducting resonators whose operating temperature is 2.0 K, achieved by evaporative cooling in boiling superfluid helium II at a saturated vapor pressure of 32 mbar.

A BriXSinO cryogenic distribution sub-system will take care of forwarding and returning the required cryogenic fluid lines, helium and nitrogen, from and to the LASA central plant through insulated transfer lines with minimal heat-loss.

In the framework of the major renewal of LASA cryogenic plant started in 2018, the proposed new LASA helium liquefier/refrigerator (not included in the scope of work of this project) is expected to provide, possibly through a cryogenic switchbox, the 5.5 K, 3 bar saturated fluid (SHe) feed and to receive the returning cold gas lines while the LASA helium gas recovery plant is expected to receive warm recovered gas lines for compression, storage, purification and liquefaction.

A schematic overview of the technical interfaces between BriXSinO and LASA cryogenic plants are shown in Figure 9.1.

9.2 Superconducting cavity cryomodules

As described in Chapters 3 and 4, the BriXSinO facility is going to host a folded, push-and-pull Energy Recovery linac (ERL) capable of circulating up to 5 mA beam current up to 45 MeV and still operate superconducting (SC) radio-frequency (RF) resonators with any appreciable beam-

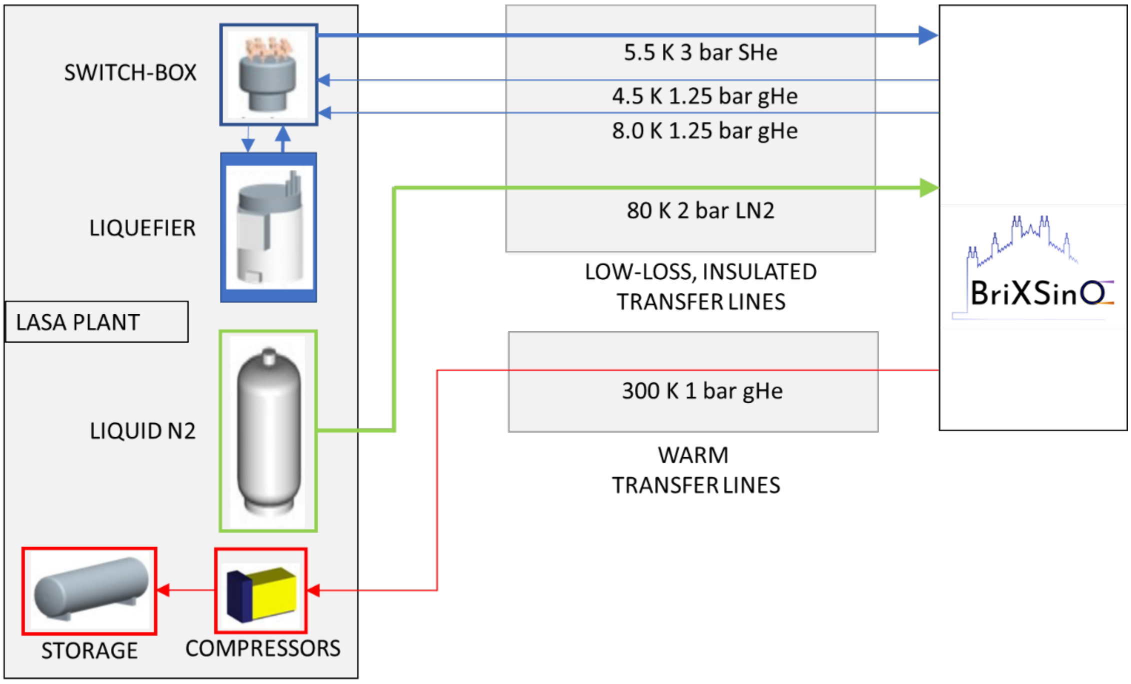

Figure 9.1: Schematic representation of technical interfaces between BriXSinO and LASA cryogenic plants.

loading. As explained, the CBETA experiment for a demonstrator ERL in Cornell (US) and the bERLinPro project being built in Helmholtz Zenter Berlin (Germany) have been identified as the most significant technical references for BriXSinO cavity and cryomodule packages design. Published data in respective design reports [1, 2] and subsequent publications [3, 4] have been hereby used as a reference for the following estimation of cryogenic heat-loads.

Two superconducting cryomodules are foreseen for BriXSinO:

- An Injector SC Booster (ISB) module, a full beam-loading cryomodule boosting the beam up to 10 MeV for the injection in the energy-recovered linac. It hosts three 1.3 GHz, 2-cells SC cavities with double power coupler operating at 2.0 K. In between each cavity there is a ferrite, coaxial, actively cooled HOM absorber.
- A ERL SC Module (ESM) designed for zero beam-loading operations in Energy-Recovery mode, it hosts three 1.3 GHz, 7-cells SC cavities operating at 2.0 K and featuring coaxial HOM absorbers as the injector module. As a baseline, this module will raise the beam energy to about 45 MeV and subsequently dump-it back down to 5 MeV adsorbing its energy back according to the folded in ERL scheme.

In the search for optimized and homogeneous solutions, BriXSinO cryomodules will largely share the cryogenic backbone technical design, schematically depicted in Figure 9.2 taking the linac module cold-string as a reference. It features:

- Superconducting cavity working point at 2.0 K, 32 mbar, with is associated supply line.
- Lower thermal intercept at about 4.5 K for power coupler cold part thermalization and for beam-pipe intercepts used to limit conduction heat transfer between cavities and HOM absorbers.
- Higher thermal intercept at about 80 K for thermal shielding and adsorption of HOM generated heat load in the ferrite absorbers.
- Modified TTF III type coupler for 10 kW kW CW RF power, two penetrations for each cavity in the injector module while one only for linac module.
- External feed-box, one for each cryomodule, hosting Joule-Thomson valve with dedicated

heat-exchanger for the 2.0 K feed, inner buffer pots and cryogens level controls.

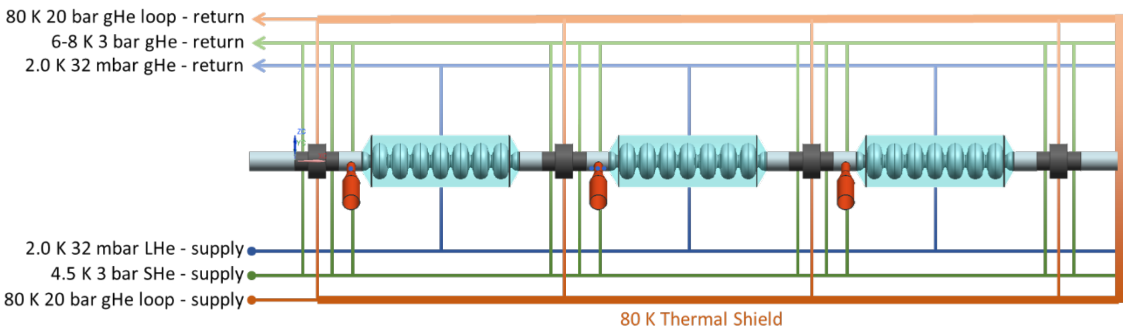

Figure 9.2: Schematic cryogenic loops scheme for BriXSinO cryomodules, in particular the ESM cold-string is taken as reference.

9.3 Cryogenic heat-loads

A first-order evaluation of BriXSinO expected cryogenic requirements is here reported through the calculation of thermal loads for the machine at its nominal working point. The numerical evaluations shown are based on published data about actually measured (preferred where possible) or simulated results. A detailed study of thermal loads at intercepts will be carried-out at a later stage with a more mature status of modules design, also including an evaluation of non-modules heat-loads as those coming from feedboxes, bypasses, transfer lines and central cold-box.

At the 2.0 K temperature level the dynamic loads given by the cavity losses are by far the largest contribution while static losses are generally leading on the loads at 4.5 K and 80 K thermal intercepts with the notable exception of the HOM absorbers heat load. Concerning power dissipated, P_{diss}, in superconducting cavities the expected resulting thermal loads can be computed for both types of structures from the cavity parameters in Chapter 4 according to the formula:

$$P_{\mathrm{diss}} = \frac{(E_{\mathrm{acc}} L_{\mathrm{acc}})^2}{\frac{R}{Q} Q_0} \tag{9.1}$$

and from the values resumed in the following Table 9.1.

Table 9.1: Electromagnetic parameters for BriXSinO SC cavities.

	ISB 2-cells cavities	**ESM 7-cells cavities**
Accelerating gradient - E_{acc} (MV/m)	7.5	16.5
Active length - L_{acc} (m)	0.218	0.810
R/Q (Ω)	222	774
Q_0	2×10^{10}	2×10^{10}
Dissipated power, per cavity (W)	0.6	11.5
Total cavity heat-load at 2.0 K (W)	**2**	**35**

For what concerns HOM loads, as a reference the average monopole HOM power dissipated per cavity can be (as detailed in Chapter 4) theoretically as high as 30 W and this power is going to be dissipated as heat within the ferrite rings thermalized at the intermediate temperature of 80 K through pressurized helium gas as a coolant medium that in turns exchange heat to liquid nitrogen coolant in a central, external cold-box [5]. HOM loss power is intrinsically strongly dynamic and dependent from the actual beam profile, beam-line geometry and alignment tolerances, an accurate estimation is therefore extremely difficult and measured values might be significantly lower (almost two orders of magnitudes) than above estimated calculated losses.

Table 9.2 finally resumes the expected overall cryogenic heat-loads scenario for the two BriXSinO cryomodules.

Table 9.2: Expected cryogenic heat-loads for the two BriXSinO linacs.

Intercepts	**ISB**		**ESM**		**Total static**	**Total**	**Total w/ margins**
	Static	**Dynamic**	**Static**	**Dynamic**			
	W	W	W	W	W	**W**	W
2.0 K	5	4	5	36	10	**50**	57
4.5 K	48	12	43	6	91	**109**	138
80 K	136	240	128	210	264	**714**	838

Aside from net values (without any safety margin applied) a tentative assessment for safety margins application is also presented. Inspiration comes from the similar analysis conducted for LCLS-II Design Report [6] where a final factor of 1.3 for static heat load and a factor of 1.1 for dynamic loads has been used to address uncertainties. These multipliers are taken on the best-estimate totals of static and dynamic heat, respectively.

9.4 BriXSinO cryogenic plant scheme

Starting from evaluated heat loads, the overall workload of the BriXSinO facility onto the hosting LASA central cryogenic plant can be assessed through a set of assumptions for the BriXSinO cryogenic plant layout, for instance:

- a main low-loss, insulated, cryogenic transfer line will (TL) transport all cold helium and nitrogen streams as in Figure 9.1, this line will feature active cooling by the same transported LN2 and is targeted to a state-of-the-art 0.2 W/m heat leakage performance toward the colder saturated helium stream (SHe).
- A dedicated, external liquid helium dewar of large capacity (e.g. 3000 l or higher) serving as a buffer and installed in close proximity of the BriXSinO hall.
- For the heat load generated at sub-atmospheric pressure within the sub-cooled helium volume the preferential choice is to avoid a cold-compressor stage in favor of a room-temperature pumping system with a throughput matching the expected mass-flow exiting the Joule-Thomson valve and its heat-exchanger. These pumping skids shall be installed in close proximity of the BriXSinO hall and their processed helium gas will be returned to central LASA plant for re-liquefaction.
- All other thermal loads pertinent to 4.5 K intercept are handled directly by the LASA liquefier to be run in refrigerator mode, thus in a closed loop that allows cold exhaust gas flows to return to the machine through a dedicated low-loss cryogenic transfer line at a temperature not higher than 8 K.
- A BriXSinO central coldbox will be installed in the closest proximity and on the same floor level of the linacs bunker and it will feature:
  - Bi-phasic helium reservoir serving a phase separator for the saturated flow as well as to cool this flow down to 4.5 K before be forwarded to cryomodules.

- Bi-phasic helium level control during machine runs through the external liquid helium storage dewar in order to equalize an imbalance between peak thermal load at the modules and available mass-flow from the LASA liquefier / refrigerator. During machine stops the cold-box can be configured to provide refilling of the storage dewar.
- Generation of pressurized gas closed loop to serve 80 K thermal intercept.
- Liquid nitrogen internal reservoir with heat-exchanger to cool-down pressurized helium gas flow of 80 K thermal intercepts.
- All the required hardware, including dedicated heat-exchangers to liquid nitrogen, to handle all the machine transients. These scenarios will include pre-cooling and cool-down (with cool-down rate at SC transition defined by cavity treatment recipe and up to 3 K/min), warm-up and a long-term stand-by mode to be set in between runs to keep linacs at a "parking"”" temperature defined to be safe to vacuum fittings and SC cavities and minimize the number of thermal cycles to those strictly needed for maintenance.

- A feedbox for each module will be installed in direct proximity of each linac vessel inside the bunker and will feature Joule-Thomson valve, heat-exchanger and the needed piping and controls to regulate 4.5 K and 2.0 K flows and levels.
- A low-loss transfer line will connect the coldbox to the modules feedboxes through bunker walls.

As a result, a potential technical layout of the BriXSinO cryogenic plant is schematically represented in Figure 9.3:

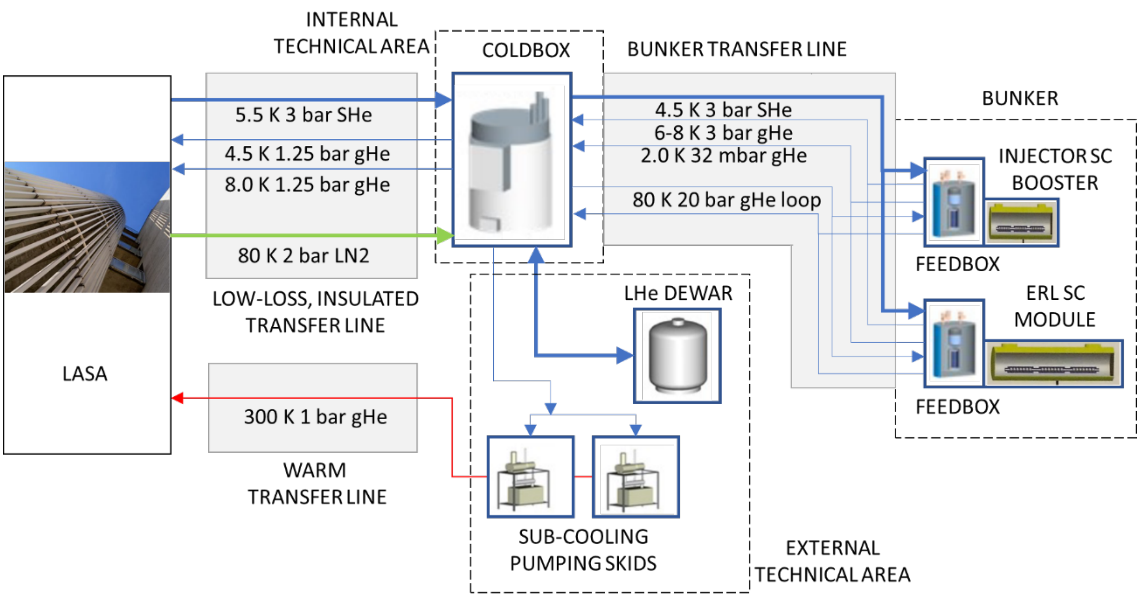

Figure 9.3: Schematic layout of the BriXSinO cryogenic plant.

9.5 BriXSinO operational workload for the LASA plant

Additional numerical evaluations of cryogenic requirements of the BriXSinO plant are resumed in the following Tables 9.3 and 9.4 and are based on the above showed layout and expected heat-loads for the two lower temperature circuits residing on liquid helium coolant only. For these evaluations, the Joule-Thomson valve isoenthalpic expansion efficiency has been set to 0.8 and additional 20 W load at 4.5 K intercept has been included as well to address power budget required by central cold-box itself and main transfer line to LASA plant, estimated to extend up to 50 m in length.

Table 9.3: Expected cryogenic requirements for the BriXSinO 2 K circuits.

<table>
<tr><td rowspan="6">2.0 K</td><td>Heat load
with
TL budget</td><td>4.5 K, 3 bar
SHe JT inlet
mass flow,
JT eff. 80%</td><td>Sub-cooling
RT pumps
throughput,
JT eff. 80%</td><td>Equivalent
LHe liq. rate
in open loop</td></tr>
<tr><td>W</td><td>g/s</td><td>$\mathrm{N\,m^3/h}$</td><td>l/h</td></tr>
<tr><td colspan="4">Static loads only, RF and beam OFF</td></tr>
<tr><td>10</td><td>0.6</td><td>310</td><td>16</td></tr>
<tr><td colspan="4">Peak loads with margins</td></tr>
<tr><td>57</td><td>3.2</td><td>1780</td><td>91</td></tr>
</table>

Expected helium flow through the sub-cooling pumping systems that withstands the 2.0 K and 32 mbar thermal sets safely in the range of commercially available pumping skids. These setups are generally realized as a two-levels, stand-alone shelf hosting a medium sized Roots pump backed by rotary primary pumps, two of such skids could easily provide 2000 to 3000 $\mathrm{N\,m^3/h}$ total throughput that could cover the requirements with margins.

Table 9.4: Expected cryogenic requirements for the BriXSinO 4.5 K circuits.

<table>
<tr><td rowspan="6">4.5 K</td><td>Heat load
with
TL budget</td><td>4.5 K, 1.25 bar
4 K to 8 K
LHe mass flow,</td></tr>
<tr><td>W</td><td>g/s</td></tr>
<tr><td colspan="2">Static loads only, RF and beam OFF</td></tr>
<tr><td>111</td><td>2.6</td></tr>
<tr><td colspan="2">Peak loads with margins</td></tr>
<tr><td>158</td><td>3.8</td></tr>
</table>

To properly frame cryogenic requirements estimated for BriXSinO, the plot in the following Figure 9.4 compares the BriXSinO values along its performance range (as in Tables 9.3 and 9.4) with figures of merit of potentially commercially available liquefier/refrigerator machines of different indicative sizes. For these machines the plot reports the potential working area underlying between pure liquefaction rate and maximum refrigeration power if used in a closed loop.

If the BriXSinO estimated range up to its peak load lies within the working area of the central LASA liquefier / refrigerator the two linacs can be run indefinitely and autonomously, without depleting the liquid helium buffer dewar. This scenario applies for instance to the machine already proposed as the potential new liquefier/refrigerator for LASA, that is close to the "size #3" machine in the plot of Figure 9.4.

Whenever instead an unbalancing exists between actual liquefier / refrigerator performances and BriXSinO requirements it could be considered that, as a rule-of-thumb, each 10 l/h missing on liquefaction rate (y-axis on the plot of Figure 9.4) as well as each 6 W missing on refrigeration power at 4.5 K (x-axis, same plot) require, independently, additional 8 l/h liquid helium feed from the buffer dewar to the central cold-box. In the cryogenic configuration here assumed the availability of this additional liquid helium feed, determined by the dewar actual capacity, will therefore set the maximum technical time extent of a BriXSinO cold-run.

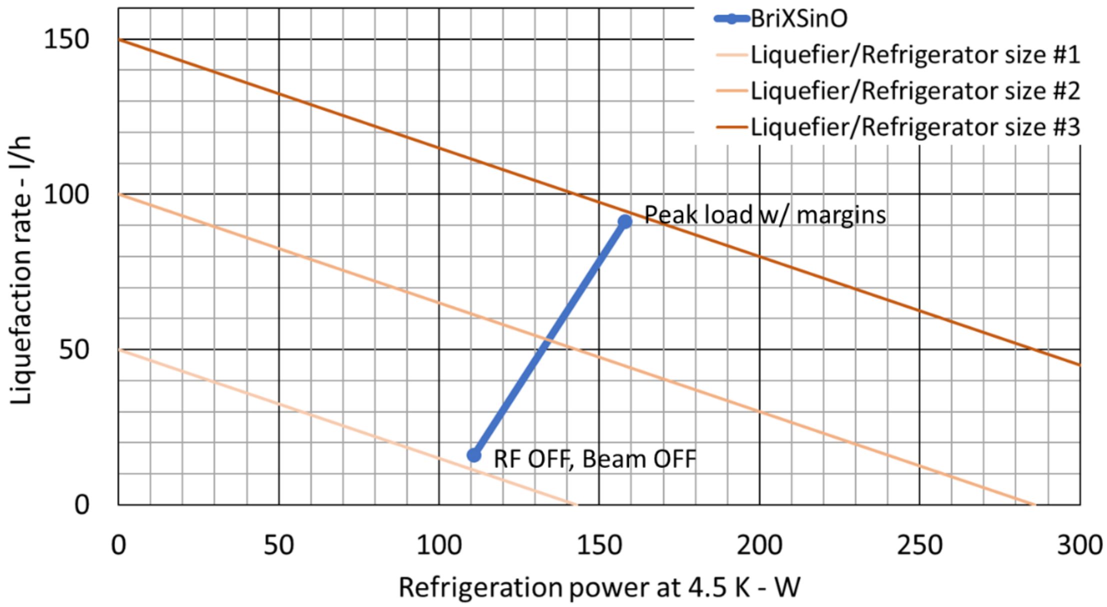

Figure 9.4: BriXSinO expected requirements range against three indicative refrigerators potentially commercially available.

As a reference, typical capacity for large dewars with installations size compatible with the BriXSinO at LASA scenario could span from 3000 l (one already in use at the LASA experimental hall) to 10000 l. This storage dewar should be routinely filled.

BriXSinO is expected to make use of the LASA centrally stored liquid nitrogen to be transferred through the main cryogenic transfer line used for all helium feeds. Peak consumption from the estimated thermal load at the 80 K intercept with margins applied results in about 18 l/h, a value subjected to an intrinsic large uncertainty due to the evaluation of HOM dynamic loads that are the larger contributing elements. In addition to this, liquefiers typically require about 0.7 liters of liquid nitrogen per liter of liquid helium produced when pre-cooling is used and this could introduce for the BriXSinO case an additional liquid nitrogen consumption of about 65 l/h. Even assuming, conservatively, the total expected peak consumption margins included the currently existing liquid nitrogen storage dewar of 10000 l capacity (regularly filled by external companies) would therefore allow for a week long machine run at nominal specifications.

Additional details about the civil engineering related to the BriXSinO cryogenic plant and about the possible positioning of key items around the BriXSinO hall at LASA site are reported in Chapter 14.

Bibliography

[1] G. Hoffstaetter, D. Trbojevic, and C. Mayes. *CBETA Design Report*. Tech. rep. Brookhaven National Lab.(BNL), Upton, NY (United States), 2017.

[2] B. Kuske et al. *Conceptual Design Report BERLinPro*. Tech. rep. Tech. rep. Berlin, Germany: Helmholtz-Zentrum Berlin für Materialien und . . ., 2012.

[3] D. Trbojevic. *CBETA-Cornell University Brookhaven National Laboratory electron energy recovery test accelerator*. Tech. rep. Brookhaven National Lab.(BNL), Upton, NY (United States), 2017.

[4] W. Anders et al. "Cryogenic system for B ERL inPro". In: *AIP Conference Proceedings*. Vol. 1573. 1. American Institute of Physics. 2014, pp. 207–214.

[5] R. Eichhorn et al. "Cornell's HOM Beamline Absorbers". In: *Proc. of the 2013 Intern. Part. Acc. Conf., Shanghai, China*. Vol. 2441. 2013.

[6] J. Galayda et al. *LCLS-II final design report*. Tech. rep. Technical Report. LCLSII-1.1-DR-0251-R0 (SLAC, 2015), 2015.

10. Magnets

10.1 General Remarks

The BriXSinO layout reported in Figure 10.1 (already shown at the end of the first chapter) shows how BriXSinO, from the magnetic point of view, is characterized by two main beam energy regions, a low energy one (about 4.5 – 10 MeV) related to the injector and a higher energy one related to the arc (22 - 45 MeV). In true, it must be considered also a third energy value for the two-pass two-way acceleration mode (paragraph "BriXSinO General Layout", Chapter 2), the beam passing backward into the main linac (ERL zone) can be accelerated at a maximum energy of about 85 MeV. BriXSinO needs magnetic optics and dedicated transport lines capable to manage these energies, that altogether do not represent any issues, i.e., the required magnets are standard and with a relatively low field.

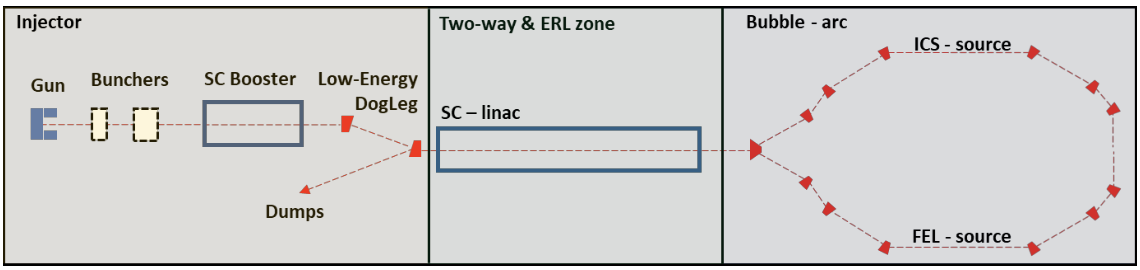

Figure 10.1: BriXSinO general layout. It is divided in tree main zone: the injection one up to the low-energy dogleg exit, the ERL Main Linac that hosts the SC linac that can be operated in the two-pass two-way acceleration mode or ERL mode and the recirculating loop, that hosts the light source and bring backs the beam to the two-way zone.

From beam dynamics (BD) studies reported in Chapter 2, all the magnets will be based on normal conducting technologies and will be powered by direct current (DC) power supplies.

All dipoles and quadrupoles will be made of solid steel yokes with accurately machined pole faces designed to maximize the field quality, according to the BD requirements, and by oxygen free copper coil. All the magnet coils will be air-cooled except for solenoids and for the high energy dump dipoles. In Table 10.1 are summarized the BriXSinO optics, reporting the quantity for each device and its main requirements that come from the BD simulations (Chapter 2), as the magnetic length and the maximum field (or gradient for quadrupoles).

Table 10.1: BriXSinO optics.

Typology	Gradient or Max. Field	Magnetic Length (m)	Quantity
The Injector (4 - 10 MeV)			
Solenoid	0.17 T		5
Dipole	0.2 T	0.2	2
Quadrupole	3.5 T/m	0.08	6
The Arc (22 - 45 MeV)			
Y Dipole	0.23 T	0.35	1
Dipole	0.23 T	0.35	12
Quadrupole	12 T/m	0.10	52
Low Energy Dump (4 - 10 MeV)			
Dipole	0.2 T	0.2	2
Quadrupole	3.5 T/m	0.08	6
High Energy Dump (22 - 45 MeV)			
Dipole	0.5 T	0.2	2
Quadrupole	6.3 T	0.08	6

In following paragraphs there is a short description for each different kind of magnet, grouped for different energy regions: the injector, the arc and the dumps. As already stressed BriXSinO does not need custom optics indeed all the devices can be found on the market. Below, for every different typology we present one example read at catalogue. The only device not at catalogue is the solenoid that has been engineered internally.

10.2 The injector optics

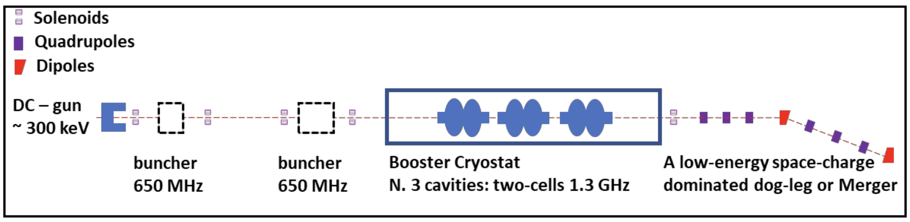

Figure 10.2: Injector blocks schema sketch: the DC-gun, the two sub harmonic bunchers, the cryostat booster carrying three two-cells cavity and the low energy dogleg. The different length of the two bunchers is because of the different phase velocity.

Low energy injector optics and their positions are sketched in Figure 10.2. In particular this region will work into the 4 - 10 MeV energy range, using four solenoids (typically used at low energies), two dipoles and six quadrupoles. The solenoids are mainly used for the emittance compensation and to control the beam envelope at very low energy (0.2 – 1 MeV), there is only one solenoid after the cryostat at higher energies (4 - 10 MeV). The six quadrupoles and the two dipoles are dedicated to the dogleg, its beam matching, and its dispersion closure.

10.2.1 The solenoid

This device has been characterized internally, performing different axial symmetric simulations with Poisson Superfish 2D FEA software [1]. A sketch of the solenoid section is shown in Figure 10.3 while main parameters are listed in Table 10.2.

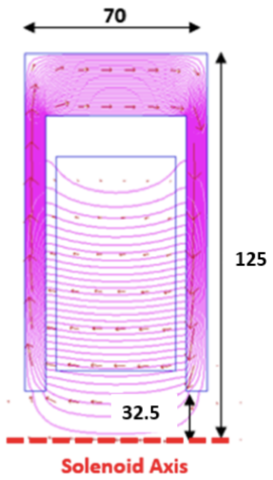

Figure 10.3: Cross section of the AC1 solenoid. Dimensions are in mm.

Table 10.2: The solenoid main parameters.

B_{max}	1700 G
Yoke Material	Low Carbon Steel
Integrated Field	11.96 T mm
Good Field Radius	10 mm
Integrated Field Quality	3×10^{-5}
COIL SPECIFICATIONS	
Number of Turns	88
Conductor dimension	5×5 / bore 3 mm
ELECTRICAL INTERFACE	
Nominal Current	110 A
Nominal Voltage	5 V
Inductance	2 mH
Resistance	42 mΩ
WATER COOLING	
Water Flow Rate	0.95 l/min
Temperature drop	8 °C
Pressure drop	1.76 bar

10.2.2 The low energy dipoles

The BD requirement for this devices, as reported above in Table 10.1, is a maximum field of about 0.2 T with a magnetic length of 0.2 m, requirements that can be found on the market, for example the EMD-01-177-630 model produced by Radiabeam Technologies is perfect for our scopes. it is shown in Figure 10.4 where are reported also the main data.

EMD-01-177-630

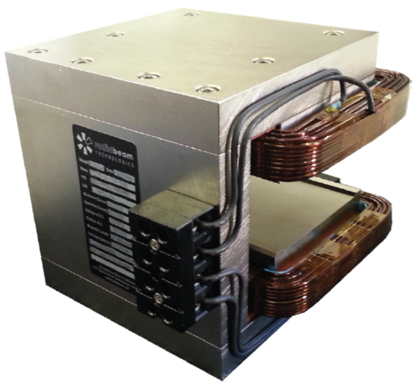

Integrated field..................... 4,000 G·cm
Field strength....................... 200 G
Magnetic length................... 19.8 cm

Current................................ 5.55 A
Voltage................................ 2.3 V
Power.................................. 13 W
Calibration........................... 680 G·cm/A
Number of turns................... 72

Gap .... 4.5 cm
Pole length.......................... 16 cm
Maximum length.................. 21 cm
Height .... 16.7 cm
Width .... 18.4 cm
Weight................................. 28 kG

The EMD-01-177-630 dipole is a compact C-frame dipole with excellent linearity. It has excellent field quality despite it's large gap-to-length ratio, making it suitable for low-energy and small emittance beams.

MAGNETIZATION

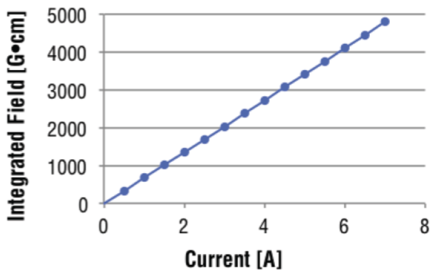

LONGITUDINAL PROFILE (I = 5.55 A)

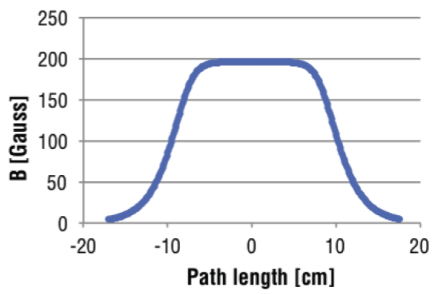

Figure 10.4: The EMD-01-177-630 Radiabeam Technologies dipole and relative data.

10.2.3 The injector's quadrupoles

These quadrupoles, in total a number of six, with a maximum gradient of 3.5 T/m and magnetic length of 8 cm are standard magnets for low energy electron beam lines easily available on the market; e.g., the EMQR-01-158-240 model from Radiabeam Technologies; in Figure 10.5 is reported and image together with the main technical data.

EMQR-01-158-240

The EMQR-01-158-240's small footprint makes it ideal for photoinjector beamlines where space is at a premium. With a 1.58 in (4.0 cm) bore, it is well matched to our 1.6 cell photoinjector.

FEATURES SHOWN

- Small footprint
- Seperable design for beam tube installation
- Kinematic stand

Integrated gradient	0.28 T
Gradient	3.46 T/m
Magnetic length	7.98 cm
Current	6.21 A
Voltage	2.5 V
Power	16 W
Calibration	0.043 T/A
Number of turns per coil	96
Bore	ø4.0 cm
Yoke length	6.1 cm
Pole length	6.1 cm
Maximum length	9.1 cm
Transverse size	ø17 cm
Weight	9.5 kg

MAGNETIZATION

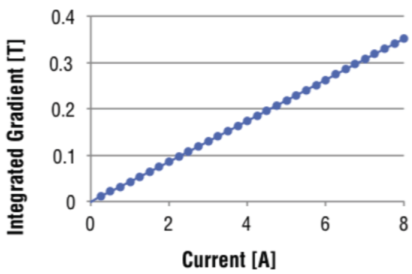

LONGITUDINAL PROFILE (I = 6.2 A)

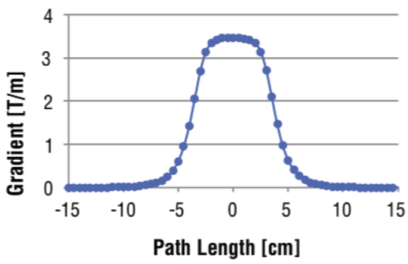

RELATED PRODUCTS

Our 6.3 T/m EMQR-02-158-240 is also available.

Figure 10.5: The EMQR-01-158-240 quadrupole model from Radiabeam Technologies and relative data.

10.3 The arc optics

Regarding the arc, based on 7 DBA (Double Bend Achromat), it is composed by 52 quadrupoles (see Figure 10.6, in red and in blu), 12 dipoles + 1 "two ways" or "Y" dipole 30° bending (in green, Figure 10.6). In Figure 10.6 in orang are also shown the Free Electron Laser undulators for the THz radiation production. Below are presented example, found on the market, of magnets ad hoc for the BriXSinO arc BD requirements.

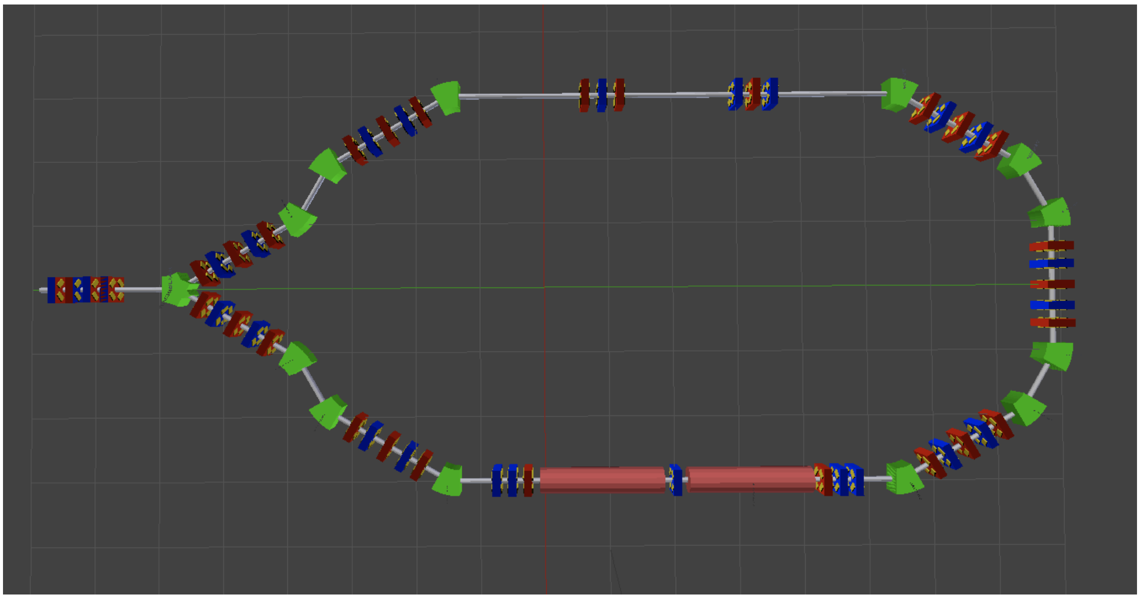

Figure 10.6: BriXSinO layout. Dipoles are green, quadrupoles are blue and red, undulator is orange.

10.3.1 Dipoles

This dipoles working with a maximum beam energy of 45 MeV, do not present particular issues; how reported in Table 10.1 we considered a maximum field of 0.23 T for a magnetic length of 0.35 m; devices that are very similar to the following one: dipole EMD-01-201-787 produced by Radiabeam technologies (RBT) that is shown in Figure 10.7 together with its main technical data. This RBT dipole has a magnetic length of 31 cm with a field strength of 2000 G. In BriXSinO simulations we considered a magnetic length of 35 cm with a field of 2300 G, which is an mild affordable improvement.

The only non-standard magnet of the arc is the Y-dipole (at the entry/exit of the arc), it has the same characteristics of other arc dipoles, with tips design ad hoc to operate in the Y configuration.

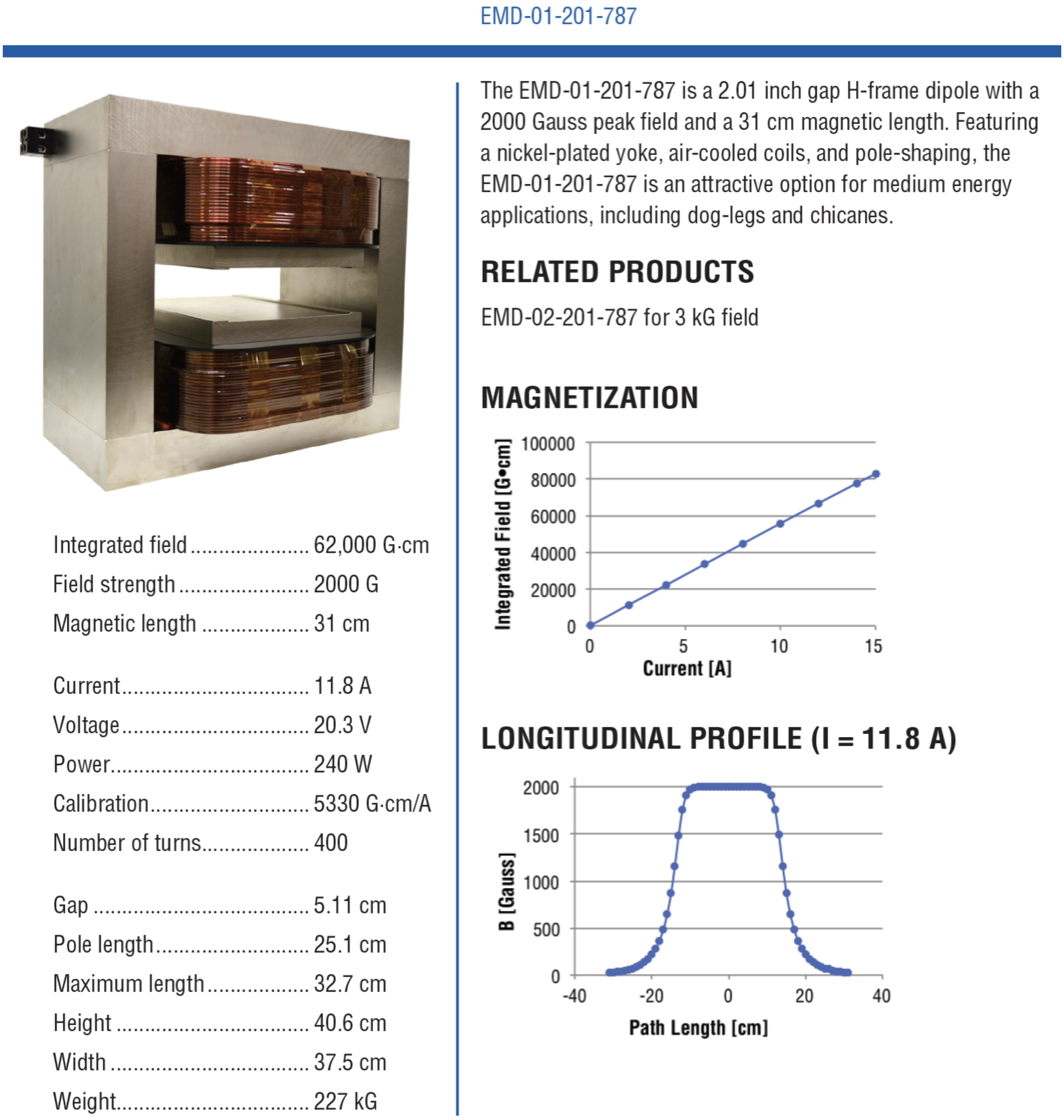
EMD-01-201-787

The EMD-01-201-787 is a 2.01 inch gap H-frame dipole with a 2000 Gauss peak field and a 31 cm magnetic length. Featuring a nickel-plated yoke, air-cooled coils, and pole-shaping, the EMD-01-201-787 is an attractive option for medium energy applications, including dog-legs and chicanes.

RELATED PRODUCTS

EMD-02-201-787 for 3 kG field

MAGNETIZATION

LONGITUDINAL PROFILE (I = 11.8 A)

Integrated field	62,000 G·cm
Field strength	2000 G
Magnetic length	31 cm
Current	11.8 A
Voltage	20.3 V
Power	240 W
Calibration	5330 G·cm/A
Number of turns	400
Gap	5.11 cm
Pole length	25.1 cm
Maximum length	32.7 cm
Height	40.6 cm
Width	37.5 cm
Weight	227 kG

Figure 10.7: A possible BriXSinO dipole, it needs to be scaled to the required field by increasing the current of about 15%.

10.3.2 Quadrupoles

The quadrupole used in the arc simulations, Section 2.1.3, again from Table 10.1, with a maximum gradient of 12 T/m and magnetic length of 10 cm can be find of the market. The maximum gradient of 10 - 12 T/m is reached in the arc matching line, while in the arc (i.e. DBAs) it is lower. In any case because these quadrupoles can be considered small devices, to standardize the project we choose to use the same quadrupoles for the arc and for its matching line.

To report a device available on the market, the Radiabeam Technologies quadrupole mod. EMQD-01-155-245 shown in Figure 10.8 with its main technical data is a good candidate.

Quadrupole

EMQD-01-155-245

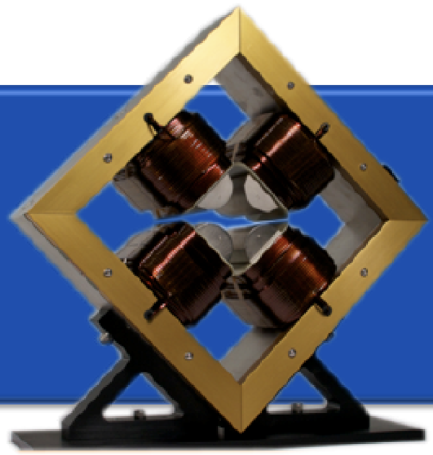

Features:
- Air-cooled
- Nickel-plated steel poles
- Aluminum wire lead protectors
- Custom colors at no extra charge
- Made in USA

Dimensions:
- 46.16 x 46.16 x 6.23 cm yoke
- 11.31 cm length
- 3.94 cm bore

Specifications:

Max. gradient	12 T/m
Magnetic length	~9.74 cm
Operating current @ specified gradient	6.3 A
Resistance per coil/quad	.49/1.96 Ω
Voltage per coil/quad	3.1/12.5 V
Number of turns	308

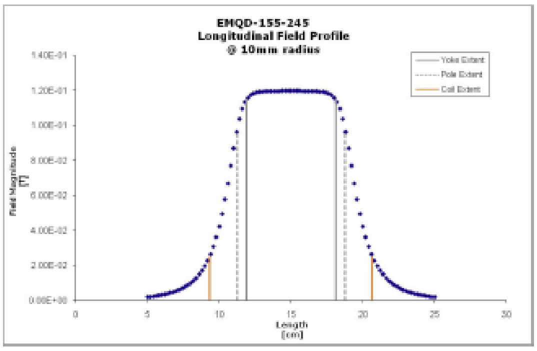

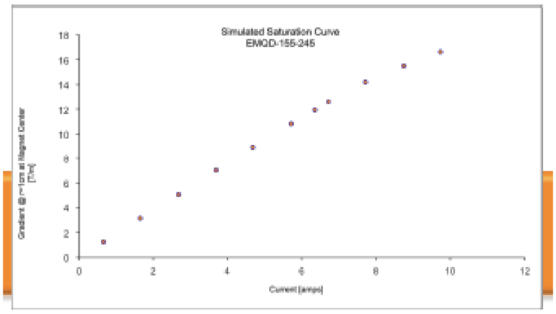

Figure 10.8: A possible arc BriXSinO quadrupole.

10.4 The dump optics

For the low energy dump, as reference, it possible to use the same magnetic devices described at the beginning of this chapter, i.e. for the BriXSinO injector, because the beam energy is exactly the same, i.e. about 4 - 10 MeV.

For the high energy dump, where it is necessary to control beams with maximum energies of about 90 MeV, it is possible to rescale dipoles from the STAR project [2] where these energies, with similar bending radius, are covered. The need is of a dipole between the one presented in Figure 10.7 (2000 G and 31 cm of magnetic length) and the STAR-Low-Energy-Line one (5000 G and 20 cm of magnetic length), again a standard device that will be customized on our request.

Concerning the high energy dump quadrupoles, we use as reference for sake of simplicity again a RBT model: EMQR-01-158-240 whose data are presented into Figure 10.9 and that is conform with our needs reported in Table 10.1.

10.5 Undulator

The undulator is foreseen to produce THz radiation. It will be split into two sections to accommodate a quadrupole in between, in order to get a better horizontal focusing.

In Figure 10.10 the produced radiation λ (λ_w, B, γ) from 45 MeV electron beam (the maximum BriXSinO beam energy) ($\gamma = 88.94$) for different undulator period λ_w and magnetic field B is shown.

The wavelength of 2.5×10^{-5} m, as reference, is shown.

As we can see the wavelength of 2.5×10^{-5} m can be achieved with a field of about 1.4 T and an undulator period of 3.5 cm and an undulator parameter $K = eB\lambda_w/2\pi m_e c = 3.7$.

By considering a lower beam energy (30 MeV) we have the following results (Figure 10.11).

As we can see in this case THz production seems to be easier because the field required spans from about 0.5 to 1.25 T according to different undulator periods. The corresponding undulator parameter spans from 3.27 for 2.8 cm undulator period to 2.87 for 3.5 cm undulator period.

The undulator will be a hybrid one (Permanent magnet + iron). Such technology is and industrial one and it is almost commercial and verified (i.e. the SPARC undulator is of the same hybrid type with λ_w=2.8 cm).

10.6 Powering

The total power needed for powering the magnets will be:

- Dipoles: 400 W $\times$ 13 = 5200 W
- Quadrupoles: 80 W $\times$ 52 = 4160 W

So, the powering of the magnets in the arc requires a total power of 9.5 kW. The magnet power consumed in the injector is mainly given by the solenoid, quadrupoles and dipoles are negligible; in total it is about 2.5 kW. The magnet power consumption into the low energy dump is few hundreds of Watts, the one of the high energy dump is mainly given by the 90 MeV dipoles that for two, rescaling from STAR-Low-Energy-Line [1], is about 2 kW. The total magnetic power will not exceed 14 kW.

Magnet/undulator procurement

The magnet type and factory cited are, of course, only indicative and does not indicate any preference.

The procurement of the magnets will follow an open tender in order to get the best performance/cost among all the producers worldwide.

Acknowledgements:
We thanks Alessandro Vannozzi (INFN-LNF) for discussions and data about the solenoid presented in this chapter.

EMQR-02-158-240

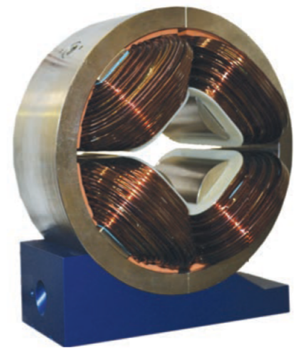

Integrated gradient	0.51 T
Gradient	6.3 T/m
Magnetic length	8.0 cm
Current	6.15 A
Voltage	5.5 V
Power	34 W
Calibration	0.083 T/A
Number of turns per coil	173
Bore	ø4.0 cm
Yoke length	6.1 cm
Pole length	6.1 cm
Maximum length	12.9 cm
Transverse size	ø17 cm
Weight	14.5 kg

RELATED PRODUCTS

Our 3.4 T/m **EMQR-01-158-240** is also available.

The EMQR-02-158-240 is a higher-gradient version of our EMQR-01-158-240 quadrupole. With nearly twice the gradient, this quadrupole packs a lot of field into a small package.

Its small footprint makes it ideal for photoinjector beamlines where space is at a premium. With a 1.58 in (4.0 cm) bore, it is well matched to our 1.6 cell photoinjector.

MAGNETIZATION

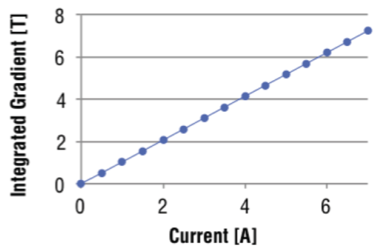

LONGITUDINAL PROFILE (I = 6.15 A)

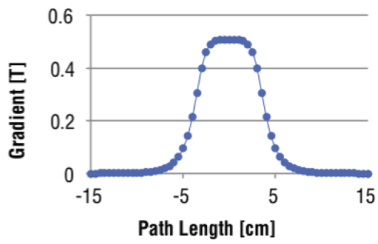

Figure 10.9: Data and image of a quadrupole produced by Radiabeam Technologies that can be use as reference quadrupole for the BriXSinO’s high energy dump transport line.

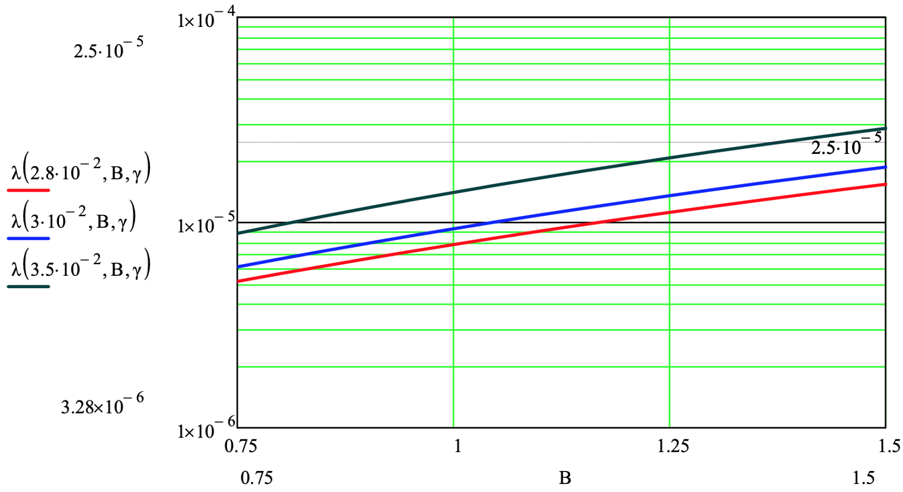

Figure 10.10: Possible radiation production vs. undulator field by a 45 MeV electron beam for different undulator periods.

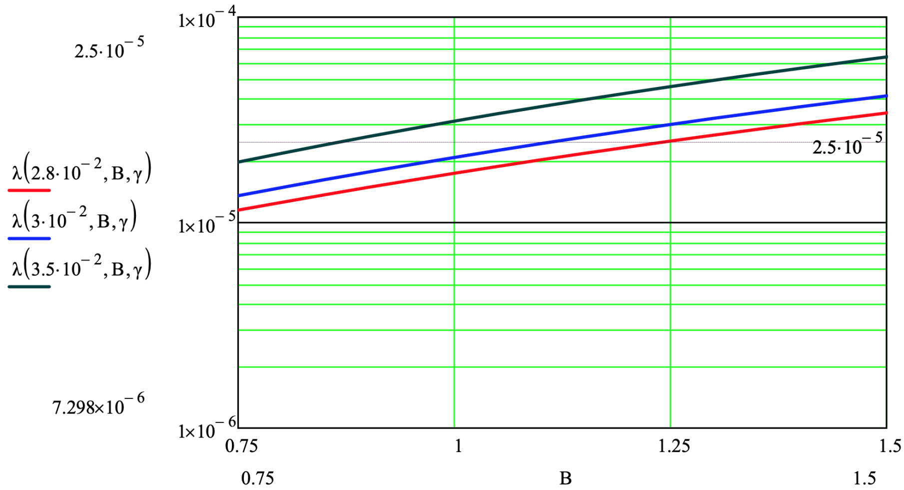

Figure 10.11: Possible radiation production vs. undulator field by a 30 MeV electron beam for different undulator periods.

Bibliography

[1] *Reference manual for the POISSON/SUPERFISH Group of Codes*. eng. Los Alamos National Laboratory, 1987.

[2] A. Bacci et al. "STAR HE-Linac Complete Detailed Design Report". In: *arXiv preprint arXiv:2109.10351* (2021).

11. Vacuum system, chambers

The BriXSinO vacuum system consists of several systems, either independent or interconnected, as the beam line vacuum, the RF coupler vacuum, the cryogenic vacuum, the photon beamline vacuum, the Fabry-Pérot cavities vacuum, etc. The beam line vacuum is in its turn composed of several sub-systems interconnected through the beam transport line, each one with specific vacuum requirements, according to their functionality and working environment. Basing on these considerations, also the vacuum system has been sectorized in several subsystems. Some general principles have been anyhow followed in the design of every vacuum sub-system:

- Ultra-High-Vacuum (UHV) conditions must be achieved wherever possible so as to grant the best operation all along the beam transport line. The points where a higher gas load is expected (such as the beam dump) must be isolated from the rest of the machine.
- Due to the reduced size of the beam pipe, the structure is conductance limited so that a uniform vacuum condition has to be achieved by distributing the vacuum components (e. g. pumping units) all along the beam line.
- Being the vacuum line itself part of the beam transport system, its effect on beam operation must be minimized. For instance, wakefield beam impedance must be maintained as low as possible (transitions between beam pipe cross sections, surface smoothness, RF shielding of vacuum components).
- Particle free operations are mandatory in the installation and operation of every vacuum component so to preserve the cleanliness of beam line surface. All the accelerator vacuum systems will be oil free, so to avoid any risk for hydrocarbon contaminations.

Table 11.1 summarizes the different vacuum systems, the relative operative pressures together with some notes.

Each of these systems can be further classified depending on their localization all along the machine, their functionality, and the technical requirements.

11.1 The beam line vacuum system

It represents the volume maintained under vacuum where the electron beam will pass through, starting from the photocathode in the electron gun, passing through the injector, the cold linac

Table 11.1: The different vacuum systems of BriXSinO with operative pressures and some comments.

Description	**Pressure** (mbar)	**Particle free (ISO x)**	**Notes**
DC gun	$<10^{-10}$	Yes, ISO 5	Highest possible pumping speed
DC gun ti injector booster	$\approx 10^{-10}$	Yes, ISO 5	
Injector Booster	$\approx 10^{-10}$	Yes, ISO 4	
ERL module	$\approx 10^{-10}$	Yes, ISO 4	
Recirculating Loop	$\approx 10^{-9}$	Not required	Conductance limited
ICS	$<10^{-7}$	Yes, ISO 5	Conductance limited
Undulator	$<10^{-7}$	Not required	Conductance limited, NEG if needed
Beamlines close to cold Linac	$\approx 10^{-10}$	Yes, ISO 4	
Beam dump	10^{-7}	Not required	High gas load
RF coupler vacuum	$<10^{-9}$	Yes, ISO 4	
Insulation vacuum	$<10^{-6}$	Not required	High gas load

accelerator section, the recirculating loop, down to the beam dump. The pressure will be in the HV (High vacuum) and UHV (Ultra High vacuum) region and the vacuum must be hydrocarbon free.

1. : **DC gun**. The electron gun will require an extremely low vacuum level (UHV, $< 10^{-10}$ mbar) to ensure a long operative lifetime to photocathodes and to avoid ion back bombardment which would degrade the cathode quantum efficiency. NEG (Non Evaporable Getter) pumps used together with SIP (Sputter Ion Pump) represent the best solution for this application: they are compact, they have an extremely high pumping speed on active gases (H_2, CO, etc.) together with a reasonable pumping speed for CH_4 and noble gases. It must be then pointed out that in the last years new pumps are available on the market, such as the SAES Getters NEXTorr®(see Figure 11.1), that combines in a synergic design NEG and SIP technologies. These pumps are characterized by extreme compactness - at least one order of magnitude with respect to SIP pumps - good pumping efficiency and long lifetime. Moreover, they are already successfully used as pumping systems for the transportation of photocathodes between different laboratories, ensuring the conservation of the photoemissive properties [1].
2. : **from DC gun to Injector booster**: this section includes the sub-harmonic bunchers and, being close to the DC gun, UHV conditions must be attained in order to avoid ion back bombardment. The combined SIP-NEG SAES Getters NEXTorr®pumps can be employed.
3. **The cold linac section (injector booster and ERL cryomodule)**. It comprises the superconducting cavities and will be in UHV condition due to the cryopumping effects of the 2 K parts. Apart He, all gases have enough low equilibrium vapor pressure to be considered as pumped. Superconducting cavities are treated and assembled in ISO 4 class, as the other parts of the beamline vacuum inside the cryomodule. In order to limit the gas load coming from the warm beamline and offering pumping speed on all gases including He, SIP pumps are foreseen at the extremities of each cryomodule (see Figure 11.2) together with NEG pumps. The latter has proven to be reliable in operation with superconducting cavities: as reported in [2], no cavity performance degradation due to field emission resulted from the activation and operation of the pump. Alternatively, the combined SIP-NEG SAES Getters NEXTorr®pump can be employed.
4. **Warm beamline adjacent to cold linac**. This part includes the connections between injector booster and ERL cryomodule, between ERL cryomodule and recirculating loop, between ERL cryomodule and beam dump. In order to reduce the risk of superconducting cavities particulate contamination, the beam line adjacent to the cryomodule is considered like a superconducting cavity and must be ISO 4 compliant. Being 20 meters the particle-free

Figure 11.1: the SAES Getters NEXTorr®pump.

"length" [3], all warm beamlines must be considered as adjacent. All components (beamline, pumps, diagnostics, etc.) within this distance need an extreme cleanliness level for particles, similar to the one of the semiconductor industry (particle free, ISO 4 to ISO 5 class). Therefore, in the design, installation, operation and future maintenance of these components, one must assure that these "particle free" conditions can be fulfilled all along the lifetime of the accelerator.

5. **The recirculating loop**. Arc beamlines are usually conductance-limited structures: lumped SIP and NEG pumps with optimized distribution on the base of the beamline components will ensure the proper pumping speed to maintain the vacuum of the arc below the design value. The possibility of ion trapping, generated by the interaction of the beam with the residual gases may also be taken into account [5]. Although the phenomenon can theoretically occur, a typical threshold for the observation of ion effects on the beam is an average current of 10 mA [6]. So, in principle ion trapping is expected to be not influential in the case of BriXSinO beam operation. However, strategies of ion clearing are available, such as the installation of ion clearing electrodes at various locations on the vacuum line. For sake of a pragmatic approach to the problem, one can proceed to assume no ion trapping issues for beam operation at 5 mA but leaving room for implementing ion clearing strategies afterward.
6. **The undulators vacuum system**. Undulators vacuum chambers are long tubes with a small diameter. Typical operating pressure is in the 10^{-7} mbar scale. The usual strategy foresees a controlled surface finishing (polishing) together with SIP or combined SIP + NEG pumps at the extremities. In case of a small diameter chamber, or the need for lower pressure, the vacuum chamber could be coated with a NEG [7], if acceptable from the point of view of impedance, surface roughness and wakefield excitation. Typically, a ternary alloy (Ti, Zr and V), with an activation temperature below 200 °C is used.
7. **The Inverse Compton Source**: ICS beam line is constituted by a small tube with a small diameter with gaps needed for the interaction of electron beam with the laser pulses. So, the inner beam line vacuum is here connected with the Fabry-Pérotcavity vacuum. Therefore, the Fabry-Pérotcavity pressure must be low enough to not interfere with recirculating loop pressure requirements. As for the undulators vacuum, a combination of SIP+NEG pumps

Figure 11.2: SIP ion pumps on one extreme of a E-XFEL cryomodule [4].

can be used.

8. **The beam dump**: A high gas load is expected at the beam dump due to high adsorbed power, so the dump vacuum must be isolated from the much lower pressure of the beam line connecting to the ERL cryomodule. SIP pumps can be installed so to grant the highest possible pumping speed.

11.2 The insulating vacuum system

The cryomodules, the LHe transfer lines and distribution systems need the vacuum to reduce the heat transfer from the room temperature components, minimizing the convective heat loads to the cold mass. The operative pressure has to be in the range of 10^{-6} mbar, so to optimize the insulation characteristics of the multilayer insulation blankets. The insulating vacuum system is characterized by high gas load due to the large surfaces exposed to vacuum (tens of layers of multilayer insulation blankets, the steel cryomodule vacuum chambers, the thermal shields, tuners motors and gear boxes, etc.). In any case, as demonstrated by the experience of several labs like SNS, DESY Flash etc., there is a residual risk of having helium leaks coming from the components inside the cryomodule: He is not cryopumped by the cold surfaces, even at 2 K, and therefore the vacuum system has to compensate for the leaks. A high pumping speed and high throughput on all gases, including He, is absolutely required for the insulating vacuum system, at least during the first phase of the pumping, before the cooling of the cold parts. Hybrid turbomolecular pumps, characterized by high pumping speed on light gases and capable of high throughput are the only feasible choice. The pump has to be located close to the cryomodule so to maximize the effective pumping speed. Careful evaluation of the pump lifetime in the harsh environment close to the linac must be considered, so do not limit the machine reliability. During the operative phases, the need for high throughput pumps is reduced due to the cryopumping effects of cold parts, which are already at cryogenic temperature. Therefore, the cryomodule needs for the installation of a dedicated vacuum pump.

11.3 The RF coupler vacuum

Each cavity installed on both the injector booster and the ERL cryomodule needs a RF coupler for feeding the RF power. The warm part of the coupler needs to be pumped, both for thermal insulation

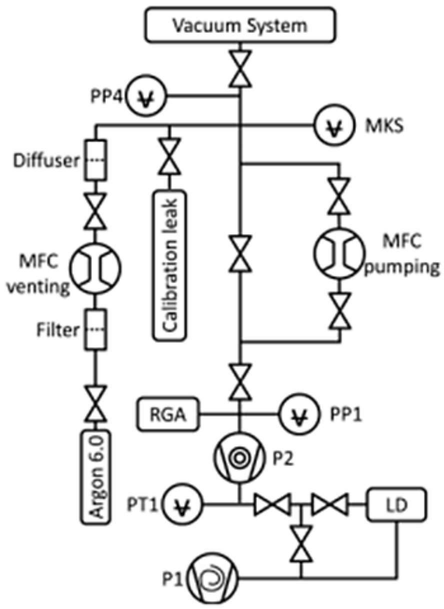

Figure 11.3: Layout of Slow pumping-slow venting system at Ettore Zanon R&I.

and for the reduction of risk of arcing. Usually, one vacuum system with several connections provides the proper pumping for all couplers. Pressure must be in the 10^{-6} mbar range, and particle free. Usually, a SIP pump is used together with a Ti sublimation pump on the coupler vacuum distribution line (see Figure 11.3).

11.4 Particle free operations

In order to avoid performance degradation, any generation of pollution of cavity inner surface must be prevented. Any activity implying the generation and transportation of micro-particulate has to be avoided within 20 m from cavity modules ("particle free length"). In this context, every pump down and venting operation must be performed with a movable slow pumping-slow venting vacuum (SPSV in the following) chart. A SPSV system grants a few l/min of maximum flow rate so to prevent the turbulent flow regime, which is known to support the transport of particles. A typical layout of a SPSV system - the one used during EXFEL cavity production [8] - is sketched in Figure 11.3. Such a compact setup is entirely based on commercially available components. The two mass flow controllers (MFC venting - MFC pumping) are gradually regulated during the cycles so as to always assure the requested mass flow conditions during the venting-pumping procedures. Typical mass flow rates of about 3 l/min can be therefore granted during pumping and 1 l/min during venting. All valves must be electrically controlled so that the SP or SV procedure can be fully automatized. Another example of a compact SPSV system can be found in [9]: such a setup, developed by DESY for FLASH and XFEL, has proven to be very reliable in avoiding any particle generation with respect to ordinary fast pumpdown systems.

11.5 Vacuum security

BriXSinO will be considered, from a vacuum point of view, as formed by different subsections. Each major component (i.e., cryomodules) will be separated from the neighbors by RF-shielded all-metal gate valves, which represents a standard for operation in CW accelerator facilities. BriXSinO vacuum system will also include a fast shutter between the ERL module and the loop. This Fast Shutter is foreseen to be activated in case of accidents in the Loop to protect the cryogenic module itself. A distributed vacuum gauge will monitor the vacuum level along with the machine, and it is thought to be implemented in the protection system of the machine. A sketch of the BriXSinO vacuum system is presented in Figure 11.4 where the major vacuum components are positioned based on the actual request for the machine operation.

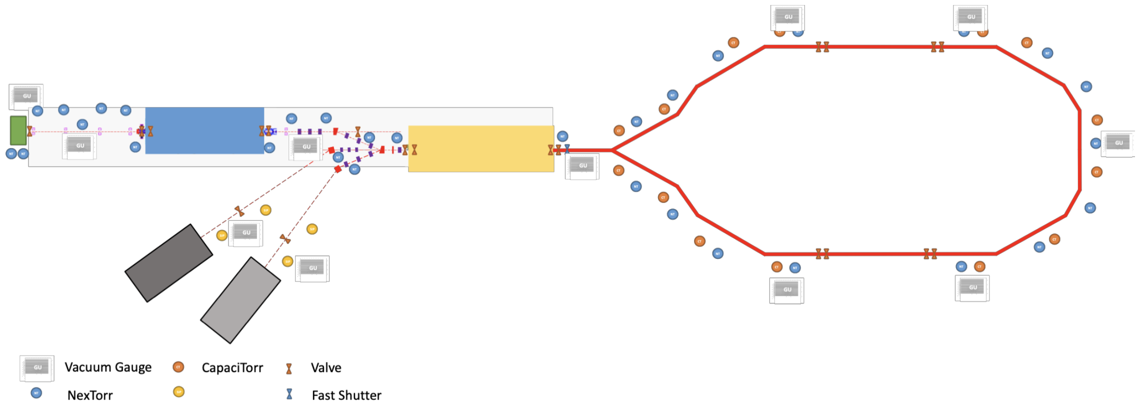

Figure 11.4: Schematic layout of the BriXSinO vacuum system. Number and position of the vacuum pumps and gauges will be defined based on the final layout of the machine.

Bibliography

[1] D. Sertore et al. “Use of non evaporable getter pumps to ensure long term performances of high quantum efficiency photocathodes”. In: *Journal of Vacuum Science & Technology A: Vacuum, Surfaces, and Films* 32.3 (2014), p. 031602.

[2] G. Ciovati et al. “Operation of a high-gradient superconducting radio-frequency cavity with a non-evaporable getter pump”. In: *Nuclear Instruments and Methods in Physics Research Section A: Accelerators, Spectrometers, Detectors and Associated Equipment* 842 (2017), pp. 92–95.

[3] J. Galayda et al. *LCLS-II final design report*. Tech. rep. Technical Report. LCLSII-1.1-DR-0251-R0 (SLAC, 2015), 2015.

[4] S. Lederer. *The European XFEL beam Vacuum System*. `https://indico.desy.de/indico/event/16256/`. 5th Workshop on the Operation of LArge Vacuum systems, Hamburg, Germany. 2017.

[5] G.H. Hoffstaetter and M. Liepe. “Ion clearing in an ERL”. In: *Nuclear Instruments and Methods in Physics Research Section A: Accelerators, Spectrometers, Detectors and Associated Equipment* 557.1 (2006), pp. 205–212.

[6] S. Full. “Ion trapping in high intensity linear accelerators”. PhD thesis. Cornell University, May 2017.

[7] T. Porcelli et al. “NEG coating deposition and characterisation of narrow-gap insertion devices and small-diameter chambers for light sources and particle accelerators”. In: *Vacuum* 138 (2017), pp. 157–164.

[8] L. Facci et al. “Quality Control And Processes Optimization For The EXFEL Superconducting Cavities Series Production At Ettore Zanon Spa”. In: *Proceedings of SRF2013, Paris, France*. 2013, p. 208.

[9] K. Zapfe and J. Wojtkiewicz. “Particle free pump down and venting of UHV vacuum systems”. In: *Proceedings of SRF2007, Beijin, China*. 2007.

12. Ancillary Plants

In this Chapter we will illustrate the general criteria adopted to define the various plant requirements necessary for the entire structure.

All the necessary plant engineering is currently planned to be positioned on the roof of the tunnel, therefore the plant work quota is +4.5 m. The planned area is about 180 square meters and will be covered with an adequate shelter.

12.1 The electrical and thermal plants

12.1.1 Electricity distribution

The estimate is that approximately 800 kW of power will be necessary for the operation of the entire structure designed for BriXSinO, so we have provided a prefabricated transformer substation of 1000 kV A. The main medium voltage power supply is derived from the current system with which the LASA is equipped. The container that will host the transformer and all its auxiliary apparatuses will be located close to the prefabricated building.

The areas of the facility to be served are easily identifiable in the various sectors that make up the structure, which can be summarized in this way;

- bunker;
- experimental area;
- underground tunnel;
- ground floor tunnel;
- prefabricated ground floor;
- prefabricated first floor;
- plant area (which obviously turns out to be the one with the greatest absorption of electricity);

The powering of the various areas can be carried out in different ways, both from inside the structure and from the outside, since it is not possible to cross the area of the shaft using walkways or any other device that will represent an obstacle.

The positioning of the various distribution panels will be provided in such a way as not to hinder any movement of material during the maintenance work of the equipment and each single area will be considered autonomous. These panels will in any case be connected, through their components, to the supervision system that the structure will be equipped with.

A series of auxiliary panels will in any case be installed in each operating area for any temporary power supply needs, the panels in question will all have the double voltage 400 V and 230 V with adequate protection, but they will be connected in series between of them protected branch by branch by the framework of the area they belong to.

The lighting of the work areas will always be achieved through suitable luminaires and the lighting level will always be guaranteed during working hours; beyond these times, a minimum level of lighting will always be guaranteed in order to highlight unforeseen events.

A system for electrical grounding will be installed. This system will exploit the massive metal structure of the reinforced concrete. The bunker and the other areas where the machine equipment will be located will be provided with a direct connection with the grounding system.

12.1.2 Ventilation systems

The whole complex will be equipped with three ventilation systems. An air exchange of 2 vol/h has been foreseen, we have not foreseen any recovery of the air except for the bunker.

For the ventilation of the bunker there is a dedicated delivery and exhaust system made with two different machines, one of 4,100 cm/h for the delivery and one of 4,500 cm/h for the exhaust in order to maintain a slight depression inside the bunker. The exhaust machine will be directly connected to the chimney for expulsion.

The second system will be provided for the ventilation of the service areas at the bunker and for the experimental area; no air recovery is envisaged here, but only an overpressurized environments.

Another system is intended for the upper floor of the prefabricated building.

Each of the ventilation systems will be equipped with its own instrumentation for the correct regulation of its operation and each machine will have a programmable logic suitable for the purpose.

The inlet and outlet, in the case of bunker ventilation, will be equipped with fire valves that will divide the various zones, the valves as well as their own sensors will also be managed by the fire detection control unit

12.1.3 Production of hot and cold for ambient conditioning

To produce the heat and the cooling necessary for the management of the complex we will proceed as follows. Heat will be generated by using a heat pump. Cooling is provided by an air cooler that includes a heat exchanger for heat recovery. In this way during the production of the cooling for the needs of the machine and its equipment, 90% of the heat produced is expected to be recovered at a temperature of 45 °C. The heating batteries of the various ventilation machines were dimensioned based on this temperature and with a temperature difference of 5 °C. If it is not necessary to use heat, the machine will dispose of it in the air.

For greater stability of the temperatures necessary for the correct functioning of the cooling system, the system will be provided with two tanks, one for the delivery and the second for the recovery; we did not consider it valid to use an inertial type tank.

12.1.4 Water cooling system for the machine

The planned system is suitable for disposing of about 400 kW of heat; to do this there is a chiller as described above. The circuits identified will be two, the first for demineralized water and a second with softened water. There are therefore two exchangers that will feed the respective circuits.

All the water needed to fill the various circuits will be treated in order to eliminate limestone and other metals that are always present as much as possible. The demineralization system will always be made with resins but will be distributed on a series of "cylinders" in order to improve the maintenance and replacement of the resins.

The entire cooling system will be managed not only by a series of pumps, each with its own reserve, but also by a series of industrial-type instruments that will be connected to programmable logic. To this purpose the instrumentation will have a 4 - 20 mA current connection. We foresee the possibility to realize the various components of the plant in general in the workshop and to be able only to assemble the various parts in a short time; for this reason we are studying assemblies that do not exceed the transportable dimensions of 2.5 m wide by 12 m of length.

12.1.5 Lighting system

We will install a lighting system consisting of LED tubes powered by busbars. The position of the busbars will be studied based on the position of the various elements during the crossing of the different sections in order to avoid as much as possible interference. Also in this case each single busbar will be powered separately.

Emergency lighting will be present in an adequate way since all the rooms are not only underground, but without natural lighting. Therefore, in addition to the normal lights necessary to comply with safety regulations, there will be lights with adequate pictograms to indicate the various paths and fluorescent strips to indicate the safety paths.

Adequate lighting has also been provided for the external area, the area is bordering on parking lots and internal roads in any case not adequately supervised.

12.1.6 Access control

LASA is already equipped with its own access control system; therefore all the doors giving access to the new installation will be controlled with the extension of the previous system which, being a proximity system, we believe gives excellent guarantees.

Access to the various areas of the experiment will be allowed only to authorized personnel who must be adequately trained and informed about the possible risks present in the structure.

12.1.7 Fire detection

The whole structure will be protected against the possible occurrence of fire principles through a capillary distribution of detectors that will be properly positioned after an adequate design according to the type of material present and the trigger possibilities.

We do not foresee an automatic extinguishing system, but a series of wheeled and portable fire extinguishers are expected to be positioned after careful study.

The foreseen control unit will also be able to intervene on the ventilation system and will be able to de-energize the magnets that will keep the various access areas open when the machine is off.

12.1.8 Video surveillance system

The envisaged system is divided into two parts, one for the control of the portion outside the experiment and a second for the control of the internal areas.

We believe that perimeter control is important for the location of the structure, in an area that is always very busy both day and night due to the presence of a hospital. Obviously, the presence of cameras must be considered a deterrent in a highly frequented area, where overcoming the protection barriers could be easy.

The cameras positioned within the entire system are designed with a dual purpose, the first to support the various stages of installation and the second to visually check compliance with the rules of conduct when the machine is running.

12.1.9 Management of the technical part

For the management of the technical part, therefore of what is described above, we consider the installation of a supervision system that can include both the SCADA for plant management and all the protocols deriving from the other systems that are intended to install.

We believe that all the cooling parts, the transformer cabin, the bunker door, and all the electrotechnical parts of the system can be integrated into a SCADA, while for the other functions, with adequate measures, everything can be integrated into a single system as now developed for large residential and office complexes.

13. Radio-Protection

13.1 Introduction

BriXSinO aims at developing at INFN LASA laboratory a test-facility that would enable addressing the physics and technology challenges posed by the ERL generation, hoping to make in a short-to-mid term scenario a significant advance in the National and INFN contest.

The layout of BriXSinO is divided in tree main zones: the injection zone extends up to the low-energy dogleg exit (max. 10 MeV) , the two-way (or ERL zone) hosting the SC linac that can be operated in the two-pass two-way acceleration mode or ERL mode (max. 80 MeV) , and the recirculating loop, hosting two large experimental areas (with electron beam energy up to max. 45 MeV) where very high flux radiation beams (in THz spectral range and in X-Ray) are made available to medical applications and applied research in general and bring backs the beam to the two-way zone.

Due to the potential radiation hazard posed by the beam power, the facility will be located underground, so to exploit the ground on top of the bunker roof as additional shielding. The basic shielding concepts so far adopted will be presented and discussed in this Chapter.

The ERL principle has two advantages in comparison with a standard linac:

a) The energy of the electrons reaching the main beam dump is below the threshold energy of nuclear reactions with photons from the bremsstrahlung, so the dump line and the main beam dump (and its cooling water) cannot be activated.

b) Electron losses in the recirculator are limited to the RF power supply of the linac module, in our case to 10 kW. If the losses are higher, the acceleration process immediately stops, because the accelerating energy is no longer available.

13.2 Shielding outlines

The BriXSinO layout has been extensively discussed in the previous chapters. Using the beam parameters listed above, the shielding has been defined in terms of size, positioning and materials to be used. The criterium adopted has been inspired by the maximum precaution and to the redundancy of the technical choices. In addition, we are also sure to guarantee all possible degrees of freedom in the event of future modifications to the machine or new needs.

High-energy electron accelerators are complex devices containing many components. All facilities contain the same basic systems:

- Accelerators structures
- RF power components
- Vacuum system
- Magnetic system associated with steering and focusing the beam
- Water-cooling
- Etc...

Prompt radiation and radioactivity induced by particle nuclear interaction in beam line elements and shielding structures represents the main radiation hazard of electron accelerators.

The accelerator's design parameters are of crucial importance in the determination of the nature and magnitude of radiation source.

13.3 Shielding Design Criteria

The shielding design criteria have been base on the text of the Italian legislation (D.Lgs. 101/20); according to European Directives as well as the recent ICRP recommendations (ICRP 103). According previous documents the individual limits are 20 mSv/year for radiation workers, and 1 mSv/year for the members of the public.

Moreover the definitions of controlled and supervised areas are useful as guidelines. A controlled area is every area where 3/10 of the limits recommended for radiation worker may be exceeded. A supervised area is one area where the overcoming of 1/10 of the previous limit may occur.

Considering the dose levels normally found around accelerators, the thickness of the shielding was calculated maintaining the doses, within the areas outside the shield and frequented by the staff, at 1 mSv/year and at 0.1 mSv/year in the other areas.

A shifting from these values could at most change the radiation classification of some areas.

In normal working condition the dose rate outside shielding should not exceed a fraction of μSv/year (about 0.02 μSv/year for 6000 h/y of operation).

13.3.1 Source Term

For shielding evaluation purposes, three components of radiation field which are produced when an electron beam, with an energy less than hundred MeV hits both a vacuum chamber wall or a thick target have to be considered.

Bremsstrahlung

Prompt photon fields produced by Bremsstrahlung constitute the most important radiation hazard from electron machines with thin shielding. Bremsstrahlung yield is very forward peaked, and increasingly so with increasing energy. The following equation describes this behavior:

$$\theta_{1/2} = 100/E_0, \tag{13.1}$$

where $\theta_{1/2}$ is the angle in degrees at which the intensity drops to one half of that at 0°, and E_0 is the energy of the initial electrons in MeV. In order to evacuate the shield thickness a "thick target", usually a target of sufficient thickness to maximize bremsstrahlung production, was considered. Photon yield from a thick target as a function of angle consists of two components: a sharply varying forward component, described in equation written above, and a mildly varying wide-angle component. Forward (or zero-degree) bremsstrahlung contains the most energetic and penetrating photons, while bremsstrahlung at wide angles is much softer.

The source term (per unit beam power) for bremsstrahlung at 90° is independent of energy.

Neutrons

Photons have larger nuclear cross-sections than electrons, so neutrons and other particles resulting from inelastic nuclear reactions are produced by the bremsstrahlung radiation. Neutrons from photonuclear reactions are outnumbered by orders of magnitude by electrons and photons that form the electromagnetic shower. However, some of these neutrons constitute the most penetrating component determining factor for radiation fields behind thick shielding.

Giant resonance production

The giant resonance production can be seen in two steps:

1. the excitation of the nucleus by photon absorption;
2. the subsequent de-excitation by neutron emission, where memory of the original photon direction has been lost.

The cross-section has large maximum around 20-23 MeV for light nuclei (mass number A$\leq$40) and 13-18 MeV for heavier nuclei.

The angular yield of giant resonance neutrons is nearly isotropic.

The giant resonance is the dominant process of photo-neutron production at electron accelerators at any electron energy.

Pseudo-deuteron production

At photon energies beyond the giant resonance, the photon is more likely to interact with a neutron-proton pair rather than with all nucleons collectively. This mechanism is important in the energy interval of 30 to $\sim$300 MeV, contributing to the high-energy end of the giant resonance spectrum. Because the cross-section is an order of magnitude lower than giant resonance, with the added weighting of bremsstrahlung spectra, this process never dominates.

13.3.2 BriXSinO shielding preliminary calculations

The bulk shielding for the accelerator enclosures has been calculated using the following expression

$$\sum_i \dot{H}_i = \sum_i \frac{s_i}{r^2} f_i e^{-\frac{d}{\lambda_i}}, \tag{13.2}$$

where $\sum_i \dot{H}_i$ is the ambient dose equivalent rate summed over all components, s_i is the source term in, r is the distance of interest, d is the bulk shielding thickness, λ_i is the attenuation length of the i$^{\text{th}}$ radiation component, f_i is conversion coefficients for use in radiological protection against external radiation for the corresponding radiation component (i$^{\text{th}}$ component)

The calculation has been performed at the maximum energy and current in the scenario of 1% beam loss on a thick copper target, operating therefore within the worst-case scenario and with the maximum redundancy, as previously stated.

The gas bremsstrahlung is produced by the interaction of the electron beam with residual low-pressure gas molecules in the vacuum pipe. Bremsstrahlung on residual gas is one of the main cause of beam loss in a storage ring and may represent a radiation hazard at synchrotron radiation facilities. This type of radiation has been thoroughly investigated at circular storage rings, where the beam current is much more intense. It is mainly in the straight section that a radiation problem could arise.

The accelerator will be located inside an underground bunker, because the bremsstrahlung in the forward direction is three orders of magnitude higher than in the transversal direction. In the transversal direction the dose rate of the bremsstrahlung is similar to the neutron radiation inside the accelerator hall. Outside the thick vertical shielding the high energy part of the neutron radiation dominates the dose rate.

13.3.3 Preliminary layout

The floor of the accelerator hall is positioned at −3.5 m, the vertical shielding consists of 1.4 m ordinary concrete and 3.0 m soil.

Three side walls of the accelerator hall are made of ordinary concrete. The two short side walls have a thickness of 80 cm each, and one long side wall has a thickness of 100 cm. The second long side wall is made of concrete with a thicknesses of 1.5 m (upstream of the linac module) and 1.3 m (downstream of the linac module). This wall shields the rooms next to the accelerator hall (so called "gallery") and the walkway to the stair case, the elevator and the lifting hole. Under the walkway and under the accelerator hall is a cable duct. The "gallery" is used for technical installations, e.g. liquid He supply, that should be close to the machine, and elements of the technical infrastructure like air and water cooling and air exchange systems.

Beam dumps

For the BriXSinO project a couple of beam dumps are planned to be installed: a first one at the end of the injector (for the first acceleration tests and for the foreseen electron radiobiological line) and a second one after the double acceleration process. The low energy dump may be moved (or duplicated) to be used after the ERL process.

Refer to Table 1.2, 1.3 and 1.4 in Chapter 1 for a detailed description of beam characteristics at these sites.

The layout of beam dumps as well as the size and shape of shielding materials has been defined. Integration of radio-protection instrumentation with the access control system will be provided.

The highest goal of all beam dump systems must be a long term, faultless, safe and reliable operation, taking into account the power absorbed.

Thus, every layout decision on the dump should be taken under the hypothetical assumption that the dump cannot be exchanged and must survive the whole lifetime of the facility. Anyway, this does not at all mean to omit the exchange possibility.

The most critical design issues were to minimize the hazardous effects of radiation, both prompt and long term, and to obtain a robust thermo mechanical design. In order to project an effective and reliable dump is necessary to take into account the following items:

- Capability to withstand the parameters of the incoming beam
- Absorption efficiency
- Lifetime
- Compactness
- Simple and Reliable Fabrication and installation Methods
- Induced Radioactivity and Radiation Shielding
- Safe dump exchange possibility
- Vacuum and cleanliness requirements
- Water cooling system
- Heating, Material Selection.

An electromagnetic shower may be characterized by

- Radiation lengths X_0
- Moliere radius X_M
- Critical Energy E_C

The geometry of an electron dump, usually consists of a cylindrical core in a low Z material (Aluminum or Graphite) of number of radiation lengths X_0 and Moliere radius X_M able to absorb the electromagnetic shower produced by a very powerful beam.

A dump must be surrounded by a sandwich of material as shown in Figure 13.1.

The high Z material is used to reduce the energy of high energy neutrons through the reaction (n,xn), and then absorbed the in a low Z shield. An additional high Z material will be used for the absorption of both photons from neutron capture and muons, if produced.

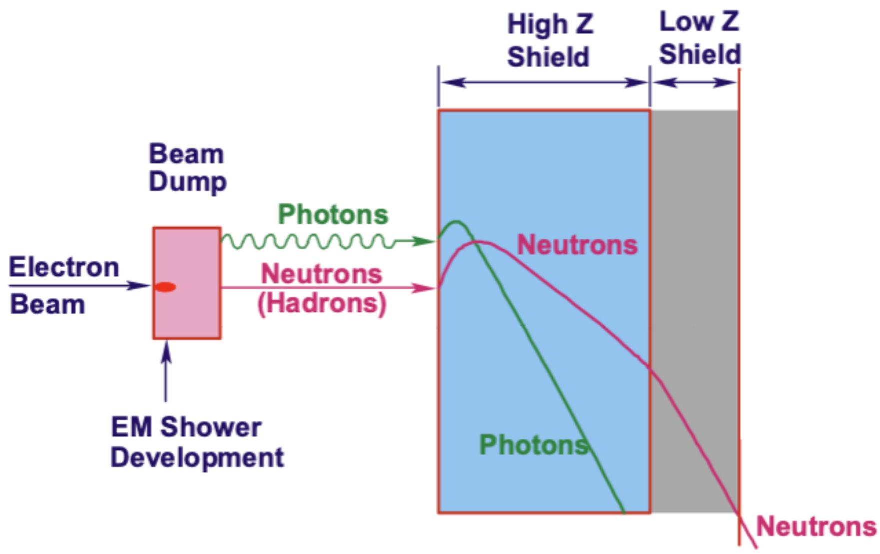

Figure 13.1: Typical shield behind high energy beam dump.

13.4 The operational radiation safety program

The purpose of the operational safety system program is to avoid life-threatening exposure and/or to minimize inadvertent, but potentially significant, exposure to personnel. A personnel protection system can be considered as divided into two main parts: an access control system and a radiation alarm system.

The access control system is intended to prevent any unauthorized or accidental entry into radiation areas.

The access control system is composed by physical barriers (doors, shields, hutches), signs, closed circuit TV, flashing lights, audible warning devices, including associated interlock system, and a body of administrative procedures that define conditions where entry is safe. The radiation alarm system includes radiation monitors, which measure radiation field directly giving an interlock signal when the alarm level is reached.

13.5 Interlock design and feature

The objective of a safety interlock is to prevent injury or damage from radiation. To achieve this goal the interlock must operate with a high degree of reliability. All components should be of high grade for dependability, long life and radiation resistant. All circuits and component must be fail safe (relay technology preferably).

To reduce the likelihood of accidental damage or deliberate tampering all cables must run in separate conduits and all logic equipment must be mounted in locked racks.

Two independent chains of interlocks must be foreseen, each interlock consisting of two micro switches in series and each micro switches consisting of two contacts.

Emergency-off buttons must be clearly visible in the darkness and readily accessible.

The reset of emergency-off buttons must be done locally.

Emergency exit mechanisms must be provided at all doors.

Warning lights must be flashing and audible warning must be given inside radiation areas before the accelerator is turned on.

Before starting the accelerator a radiation area search must be initiated by the activation of a "search start" button. "Search confirmation" buttons mounted along the search path must also be provided. A "Search complete" button at the exit point must also be set.

Restarting of the accelerator must be avoided if the search is not performed in the right order or if time expires.

The interlock system must prevent beams from being turned on until the audible and visual warning cycle has ended.

Any violation of the radiation areas must cause the interlocks system to render the area safe.

Restarting must be impossible before a new search. Procedures to control and keep account of access to accelerator vaults or tunnels must be implemented.

14. The Site and the Infrastructure Systems

BriXSinO will be hosted by the Laboratorio Acceleratori e Superconduttività Applicata (LASA) located in Segrate, a town of the surrounding belt of Milano in the North-East direction with respect to the center of the city. See the map in Figure 14.1, the stars indicates the LASA location.

The land where the LASA is located, along with the existing buildings, belongs to the Università degli Studi di Milano and is presently occupied by the Istituto Nazionale di Fisica Nucleare (INFN) and hosts several research activities connected with the construction and the operation of particles accelerators. With the development of advanced technologies for superconductivity, cryogenics and the productions of high intensity DC and RF electromagnetic fields, the laboratory has built unique competences that allowed contributing with innovative components to large international accelerator projects for high energy and applied physics. This strong background makes LASA an ideal site for the construction of an innovative research accelerator facility such as BriXSinO.

The aerial picture, Figure 14.2 shows the LASA laboratory in its present form, which consists of two major buildings, one mostly occupied by offices and small laboratories and another one where the largest research facilities are placed. BriXSinO will be built over a portion of the presently free land, indicated in red in the picture.

The infrastructure is articulated along two arms. The longest one is the underground bunker in which the Energy Recovery Linear accelerator (ERL), the Compton interaction zone and the undulator will be located, together with the laboratories that will house the experimental stations. The shorter arm, on the other hand, is the one corresponding to the external prefabricated structure where the control room, the offices and the access shaft to the bunker and the underground experimental laboratories will be found. See the picture below.

14.1 The underground building

The next picture shows the underground building in more detail. The accelerator is schematically shown along with its two SC modules and the recirculator. The concrete walls surrounding the accelerator will have a thickness determined by the radioprotection constraints.

For the underground construction of the entire complex, provisional works are required that can allow the existing structures to be consolidated before excavation. The consolidation works are expected to reach a depth of about 8 m. From geodiagnostic surveys we have ascertained that

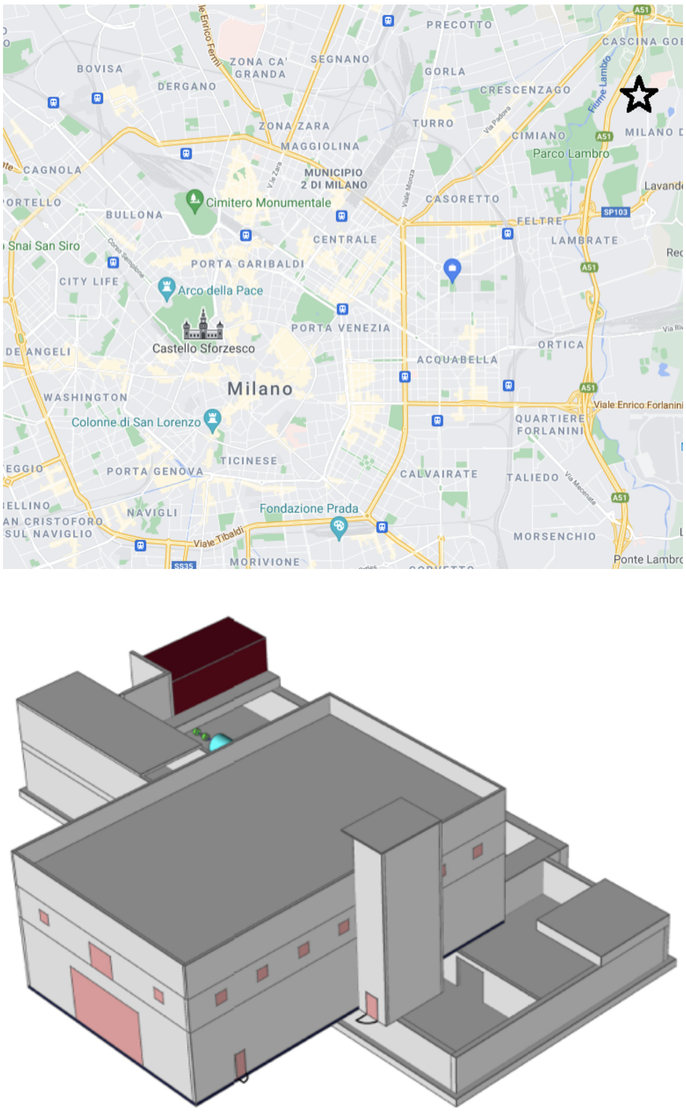

Figure 14.1: LASA location.

the aquifer is currently located at a depth of about 10 m from our ground level. Therefore the underground water should not represent a relevant issue since the floor of the bunker will be at a depth of 5 m below the ground level.

The underground structure must provide for external insulation to contain dispersions and optimal protection against water infiltrations. Particular attention will be paid to the protection of the area above the bunker for which an earth filling is foreseen, in which case a rainwater drainage system will have to be provided by discharging the water in a dedicated area.

Access to the bunker will be via stairs and elevators located in the building above ground. Inside this building there will also be a bridge crane for the transfer of the instrumentation to the lower level. After being descended to the level of the bunker there will be a large room used as a temporary storage warehouse for instrumentation. From this first room it will be possible to access the bunker in which the accelerator will be located and the area where the experimental measurement stations will be housed.

A concrete sliding door is provided to access the bunker. The opening and closing operations of the bunker door will take place mechanically through a movement system. The type of door seal

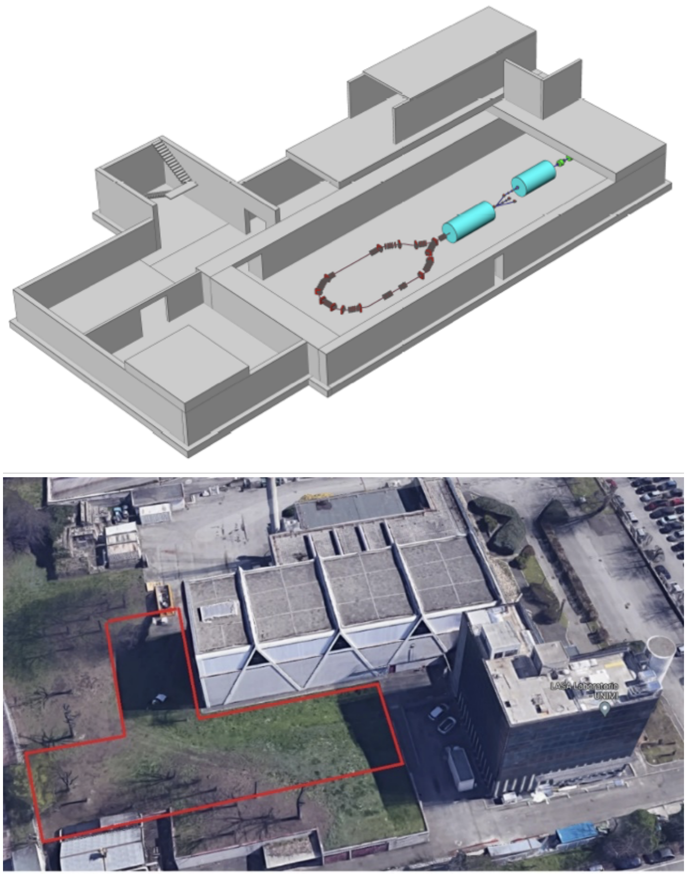

Figure 14.2: LASA Aerial picture.

will also be defined in the executive design phase of the entire structure. This door will be sealed to ensure the depression in the environment of the machine.

The experimental area will be separated from the accelerator bunker by a wall of adequate thickness in which there will be holes through which the X-Rays and the THz radiation produced by BriXSinO will reach the users experimental equipment.

In addition to the main access door to the bunker, an emergency exit will also be built on the opposite side. Leaving this side, along a metal staircase, it will be possible to directly reach the outside of the complex. There will also be a service tunnel on this side of the bunker (not shown in the figure).

On the other long side of the bunker there will be the main service tunnel inside which some of the ancillary accelerator devices (RF and cryogenics) will be placed. The dimensions of the bunker are such as to allow the handling of these devices during the installation of the machine and for maintenance operations.

The currently planned dimensions of the bunker are 40 m long and 14.5 m wide with an internal height of 3.5 m. The dimensions of the area dedicated to the experiments are 14 m by 14 m, always with a height of 3.5 m. Facing the experimental room there is a space of 14 m by 8.5 m usable as a warehouse, bearing in mind that the arrival of service systems could be expected in this area. The shaft to access the bunker is planned to have a length of 16.5 m and a width of 7 m.

To access the lower lever it is necessary to go down a flight of stairs and no type of apparatus has been foreseen that can allow the descent and/or ascent of people in a mechanical way due to lack of space.

There will be also two tunnels, one above the other, for housing the ancillary equipments for the correct operation of the facility. As a general rule the radiofrequency equipment and part of the cryogenics will be located at the bunker floor whereas the remaining part of the cryogenics on the upper floor. All the plant engineering necessary for the experiment and for the operation of the entire complex will be provided above the plant tunnel, protected by an adequate metal cover.

14.2 The buildings above ground

Along with the underground leve there will be two other major building sanding above ground. The first is a prefabricated building on two floors designed to allow correct handling of the materials to be moved in the pit. The second, right on the side of the main warehouse of the LASA existing building, for housing part of the equipment necessary for the operation of the machine and, on its top, the systems necessary for the operation of the entire complex.

The prefabricated building roof is made in such a way that a single girder bridge crane with a capacity of 6 tons can operate inside. In the upper floor it will be located the control room and also an additional space for equipment storage will be available. The height of the first floor of the prefabricated building is 6.5 m while the upper part is 3 m, the roof of the structure will still be walkable.

Next to it, a parallelepiped will rise which will house the access with a staircase, an elevator and a plant compartment that will directly access the underground level in front of the room dedicated to the experimental area.

15. Cost Evaluation and Risks

In this Chapter, a summary of the project cost is given, the basic schedule from start of construction until end of commissioning is discussed and the resulting budget profile over all phases of the project is described. Risk analysis is also illustrated.

Total project cost

All costs beginning from the project preparation up to the commissioning phase (i.e. prior to the start of operation) have to be summed up in order to determine the total project cost (TPC). There will be a period of about 3 years during which an overlap of construction/acquisition and commissioning, on one side, and operation in R&D and test-mode, on the other side, will occur.

The contributions to the TPC, summarized in Table 15.1, are:

- The project construction costs in the proper sense, due to the acquisition and/or development of main instrumentation parts as described in the previous chapters.
- The cost for commissioning the facility with beams.
- An additional personnel cost (which are not included in the TPC) covering allowances for personnel moving to work at LASA.
- The cost for personnel overheads related to management and support.

Note that recurrent costs during the construction phase (electricity, water and Helium) are not included in the TPC since it has been assumed that they will be covered by the LASA operation budget free of charge to the BriXSinO project. The same applies to the cryogenic plant.

The costs related to a dedicated building have been evaluated but they are not included in the TPC, leaving this as a possible option compared to others that involve different reconfigurations of the LASA laboratory.

Table 15.1 summarizes the costs foreseen (on the price basis of the year 2021).

As part of the construction cost evaluation, every item in the budget list is estimated within an expected lowest and highest price range based on the current knowledge about the component or system. Using these price ranges, a statistical probability distribution of the project construction cost can be derived. The estimated prices were chosen such that the estimated construction cost is in the centre of this probability distribution, i.e. at 50% probability.

Using the present structure of the project comprising 11 work packages, a breakdown of the construction costs are shown in Figure 15.1.

Table 15.1: Contributions to the total project cost.

Project preparation (before formal approval)	0.4 M€
Project construction	9.3 M€
Collaborations/Travels	0.9 M€
Personnel overhead	0.3 M€
Total construction cost	**10.9 M€**
Machine commissioning (ERL operation)	0.2 M€
Experimental areas	2.9 M€
Machine commissioning (experimental areas)	0.3 M€
Total project cost	**14.3 M€**
Research Grants	0.5 M€
Dedicated building	~8 M€

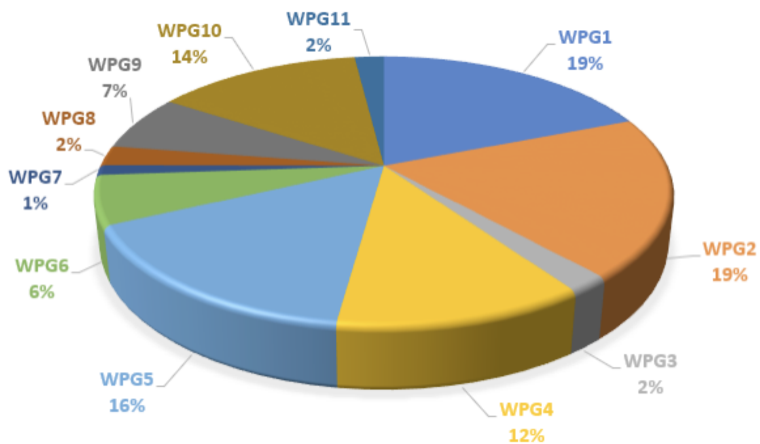

Figure 15.1: Breakdown of the total project costs.

The relation between the work package groups and the chapters in this report is shown in Table 15.2.

Table 15.2: Relation between the work package groups and the chapters in this report.

Work Package Group	Chp. 3	Chp. 4	Chp. 5	Chp. 8	Chp. 9	Chp. 10	Chp. 11	Chp. 12	Chp. 13	Chp. 6	Chp. 7	Chp. 21
WPG1- The injector	X											
WPG2 – The ERL Main SC-Linac and Cryogenics		X			X							
WPG3 – The laser subsystem			X									
WPG4 – Beam Diagnostics – Controls - Timing				X								
WPG5 - Magnets						X						
WPG6 - Vacuum							X					
WPG7 – Ancillary Plants								X				
WPG8 -Radio-Protection									X			
WPG9 - Compton Source										X		
WPG10 – THz Free Electron laser											X	
WPG11 -Application of Electron Beams on Target												X

Risk Analysis

BriXSinO aims at developing at INFN LASA laboratory a test-facility enabling the development of the physics and technology challenges posed by the ERL generation, in order to make in a short-to mid term scenario a significant advance in the National and INFN contest.

This goal will be indubitably fully achieved in the foreseen time schedule of the program. The presence of Italy as a well established partner in the European framework will be guaranteed and a solid experience will be achieved at INFN on this innovative and energetically sustainable technology.

The project members have developed a research risk management strategy to maximize the likelihood of meeting project objectives. This strategy involves identifying key areas of risk in the research, monitoring risk during the execution of the project and planning and implementing contingency plans to restrict impact of high risk tasks.

A particular element in this strategy is the close relationship that we will pursue with other worldwide laboratories already involved in this frame of research to gather our common efforts and to rationalize resources.

Our strategy may be summarized in the following:

1. We will define a detailed risk assessment of all the tasks and contingency plans within the project and from this an overall assessment of the critical points of risk. The main issues are listed in Table 15.3. Needless to say, the PI and the Project Team will be at any time available to interact with any external review process/committee that the host institutions and the sponsors will appoint to monitor the scientific, technical and operational advancement of the project.
2. During project evolution, the initial meeting will give a precise description of risk assessment factors and it will also quantify decision criteria for the technical progress. Subsequent project meetings (Steering Board monthly scheduled meetings) will consider particular risk elements forthcoming and finalize the analysis and workarounds identified by the working team to consider the full impact of the contingency plans on the project.
3. The key information used to conduct risk management during the execution of the project will be the monitoring of milestones and deliverables as well as close communication with corresponding groups involved in identifying high risk aspects at points in time.

Table 15.3: Risks assessment and mitigation.

Description of risk	**Subsystems involved and time schedule**	**Foreseen risk mitigation measures**
Organization: the coordination activities of each subsystem working group should be guaranteed	All, always	A co-leadership has been foreseen in each experimental subsystem working group
Organization: the coordination activity of PI should be guaranteed	All, always	A steering board (composed of the subsystems working group leaders) has been foreseen to coordinate all the activities and to take general decisions. In case the PI is not in condition to operate the Steering board will drive the project for the time necessary with the same prerogative of the PI

Table 15.3: Risk assessment and mitigation (continued).

Description of risk	Subsystems involved and time schedule	Foreseen risk mitigation measures
Technical: DC Gun performances	DC Gun Subsystem, 2022-2024	The design and the technological challenges related to the DC Gun are one of the major areas of risk in the project. We faced these aspects starting the analysis as soon as we could (during the TDR phase) and signing a joint development program with the people of the JLAB laboratory involved since few years in design, construction and operation of these devices. Regular monthly scheduled meetings are already in progress
Technical: photocathode performances at very high repetition rates	Photocathode Subsystem, 2022-2024	Photocathodes constitute one of the more relevant area of expertise in our group. People working on this subsystem are well recognized in the worldwide scenario as pioneers and still act as a reference in providing these components for a lot of laboratories
Technical: Injector booster and ERL module	Injector and main linac subsystems, 2022-2025	The people involved in these subsystems have more than 20 years' experience in designing, constructing, and testing SC cavities for several worldwide laboratories. Should any problem arise during the design phase we will investigate the establishment of a collaboration with laboratories involved in CW SC cavities

We will use collaborative groupware software environments which will act as a centralized project information resource accessible from anywhere. Tasks, deliverables, and technical issues will be tracked as well as notification of critical project events and milestones.

16. Time Schedule (Detailed Tech. Design, Acquisition, Install., Commiss.)

At the time of completing this document, the project preparation has advanced to a state which, from the point of view of project planning and technical readiness, allows the construction phase to begin right after project approval and fund allocation. In order to put the schedule on a realistic absolute time scale, it is assumed that the official start of project construction will be defined as the time T0 and it is assumed to be within January 2023.

A description of the fully detailed scheduling for all technical components and sub- systems of the facility, including complex inter-relations between them, is beyond the scope of this report and will be the main focus of the project team right in the initial phase of the project construction. In the following, a simplified overview of how the project will proceed from start of construction to beginning of operation is illustrated.

Its outcomes as well as its development embeds a small amount of uncertainty mostly since the project encapsulates few elements that are even beyond the current state-of-the-art in their area and given that the budget time profile has to be discussed.

A key assumption behind the timing presented in this document is that the new LASA central helium liquefier/refrigerator that, despite being fundamental to sustain BriXSinO operations, is not in the scope of work of this project, will be made available by 2024.

Most significant milestones with corresponding dates are resumed in the following Table 16.1 while a possible time layout of major activities is presented in Figure 16.1 as Gantt chart.

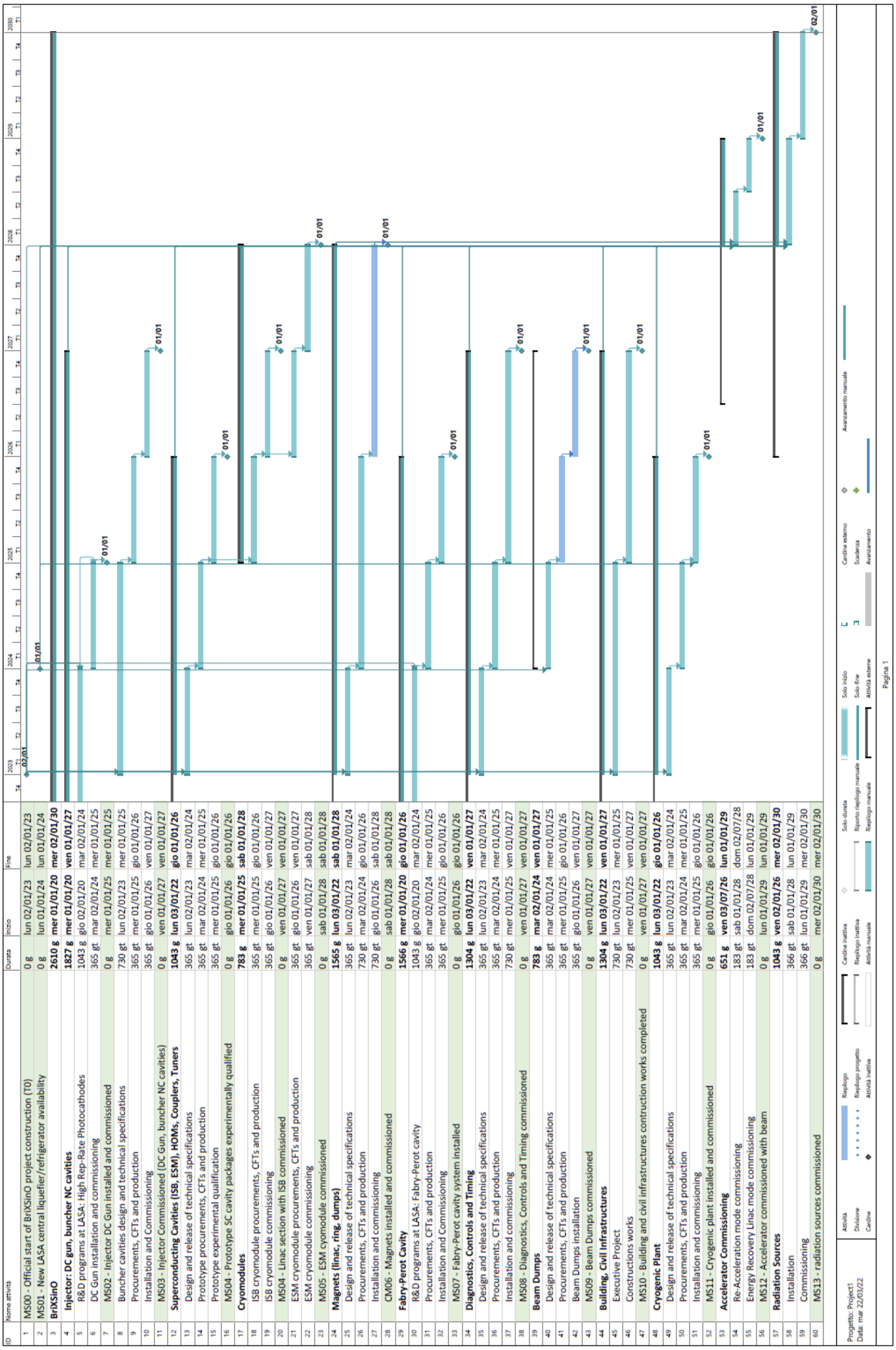

Figure 16.1: Proposal for BriXSinO timeplan.

Table 16.1: Most significant BriXSinO milestones throughout the duration of the project.

Milestone, activity	**By year**
Conclusion of R&D programs at LASA (high-rep rate photocathodes and FP cavity)	T_0+1
Design and release of technical specifications for SC cavities prototypes (ISB, ESM)	T_0+1
Building and civil infrastructures construction works start	T_0+2
Injector DC gun installed and commissioned	T_0+2
Prototype SC cavity packages experimentally qualified	T_0+3
Cryogenic plant installed and commissioned	T_0+3
Diagnostics, controls and timing commissioned	T_0+4
Injector commissioned (DC Gun, buncher NC cavities)	T_0+4
Linac section, with ISB, commissioned	T_0+4
Building and civil infrastructures construction works completed	T_0+4
Fabry-Perot cavity system installed	T_0+4
Magnets installed and commissioned	T_0+5
ESM cryomodule commissioned	T_0+5
Radiation sources installed	T_0+6
Accelerator commissioned with beam	T_0+6
Radiation sources commissioned	T_0+7

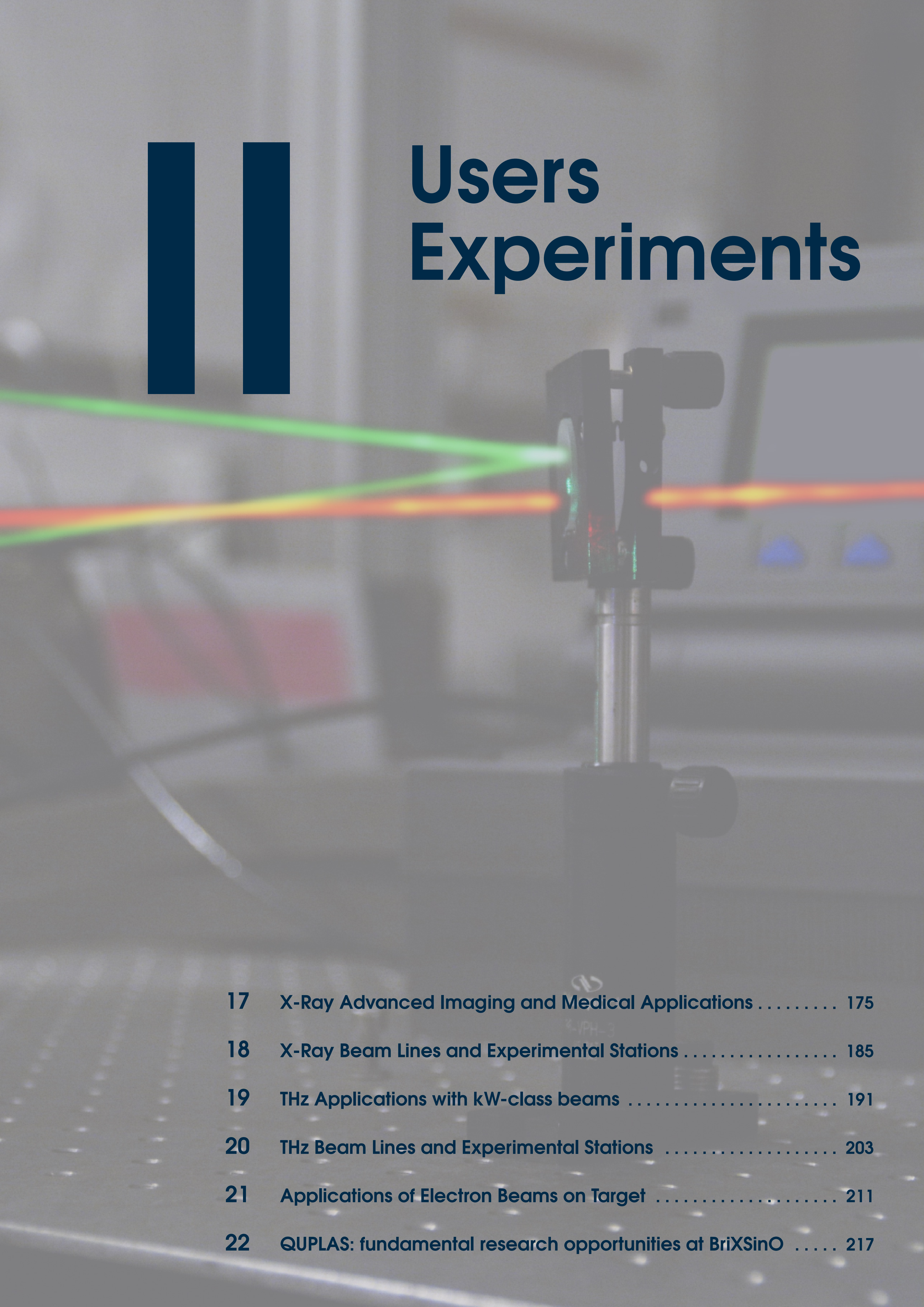

II Users Experiments

17 X-Ray Advanced Imaging and Medical Applications 175

18 X-Ray Beam Lines and Experimental Stations 185

19 THz Applications with kW-class beams 191

20 THz Beam Lines and Experimental Stations 203

21 Applications of Electron Beams on Target 211

22 QUPLAS: fundamental research opportunities at BriXSinO 217

17. X-Ray Advanced Imaging and Medical Applications

Monochromatic X-Ray sources are an important asset for research and diagnostic in many fields, such as physics, medicine, biology, cultural heritage and materials science. The number and relevance of the scientific results from experiments carried out at synchrotron and X-FEL facilities each year demonstrate the fundamental role of this powerful tool as a probe in a vast range of research fields.

Synchrotron Radiation (SR) is the gold-standard for any application requiring high-brilliance monochromatic X-Rays, especially in the energy range below 100 keV. The size and cost of SR facilities demand a national or international effort for their realization and operation and despite the effort of the scientific community, a table-top source providing a beam with synchrotron-like features, is not yet available. To bridge the gap between SR facilities and laboratory-based X-Ray sources, inverse Compton scattering has been emerging as a more compact alternative to produce high-brightness X-Ray beams. In fact, the electron energy required to obtain X-Rays in the 10–100 keV energy range with an ICS source (10–100 MeV) is about two orders of magnitude less than the energy necessary by using a typical synchrotron insertion device (1–10 GeV). Also, Synchrotron radiation divergence can be asymmetrical and quite large in the horizontal direction, but due to the relativistic nature of the emission it is always limited to tens-hundreds of microradians along the vertical direction, while the symmetry of the collimated X-ray beam from ICS sources permits to obtain a large two-dimensional irradiation field within a distance shorter (by at least one order of magnitude) than those typically achievable at synchrotron beamlines. This feature is fundamental in most X-Ray imaging applications, where the broadness and uniformity of the irradiation field allow single-shot imaging, thus avoiding scanning that requires translation of the patient/sample and the detector. This simplifies the implementation of the acquisition and prevents the generation of motion artifacts.

The technology required to realize high-performance inverse Compton sources has been rapidly growing over the last decade, with an effective ongoing transition from research-oriented and demonstrative machines towards actual user facilities. Several research institutions and laboratories worldwide are operating or developing facilities based on inverse Compton scattering (ICS). In Europe, two user facilities are currently under commissioning: STAR (University of Calabria, Cosenza, Italy) [1] and ThomX (LAL, Orsay, France) [2]. Another facility is operational since 2015 at Technical University of Munich, Germany: the Munich Compact Light Source (MuCLS) [3].

BriXSinO will provide an X-Ray beam with average energy tunable in the range 9-37 keV, a relative bandwidth $\Delta E/E$ = 1-10% and intensities between 10^9-10^{11} Photons/s. These unique characteristics, together with a small source size (<50 µm) will enable a wide range of applications. Furthermore, a unique feature of the BriXSinO source will be the possibility to perform a fast switching between two energies without changing the working point of the machine, namely the electron energy, which might be a time-consuming operation. This unprecedented dual-color mode [4] enables a broad variety of diagnostic techniques not available with ICS sources currently operating, such as dual-energy or K-edge subtraction imaging.

In the following, a selection of some of the most promising applications will be described. These represents the scientific goals that could be pursued in a first round of experiments.

17.1 Monochromatic high-resolution X-Ray imaging system

One of the most straightforward application taking advantage of BriXSinO X-Ray beam characteristics is absorption radiography, either for 2D projection radiography or 3D computed tomography (CT).

The small focal spot and the intensity of the emission within a moderate divergence make this kind of source optimal for high-resolution X-Ray imaging. A cone-beam micro-CT system could be implemented by coupling a servo-controlled motorized rotatory stage with a high-resolution X-Ray imaging detector. The achievable spatial resolution, depending on the geometry of the setup, magnification and size of the field of view, will range from few microns for millimetric samples up to hundreds of microns for sample's size of the order of 10 cm.

The monochromaticity of the beam allows the user to select the best energy for each specific imaging task, in order to maximize the contrast of the details of interests. Moreover, a monochromatic beam represents a significant advantage in tomographic imaging, so to avoid beam hardening effect and allowing the measurement of absolute Hounsfield Units, which is not possible with polychromatic X-Ray beams.

Furthermore, this imaging system, combined with the dual-energy mode and phase detection techniques will enable many innovative X-Ray diagnostic techniques, as described in the following.

17.2 2D and 3D Breast Imaging

Mammography is a specialized X-Ray imaging technique for the detection of tumors of the female breast (for review of the development, see [5]) with demands on a high image quality, in particular in terms of contrast and spatial resolution. Mammography is a soft tissue imaging technique. In the absence of K-edges, tissue contrast decreases with increasing X-Ray photon energy, the mammography is performed with low-energy X-Rays. Conventional medical X-Ray tubes emit a broad Bremsstrahlung-spectrum with anode-characteristic emission lines superimposed. In soft tissue imaging, the low-energy X-Rays do not contribute to contrast but increase the radiation dose because all photons are absorbed. On the other side, the high-energy photons are almost exclusively scattered and thus decrease image quality. Optimal would be the possibility to have monochromatic energies for mammography in the range 17 and 25 keV. This is exactly the characteristic of BriXSinO source. Studies with phantoms, contrast media, and biologic specimens reveal that the contrast in the case of monochromatic X-Rays is considerably higher as achieved with polychromatic radiation. The same considerations also apply to the case of the new 3D technologies dedicated to the breast (Digital Breast Tomosinthesys and Breast Computed Tomography).

The monoenergetic beams produced by the BriXSinO source will be an invaluable tool for the investigation of mammographic imaging and of the new proposed 3D imaging technologies of the

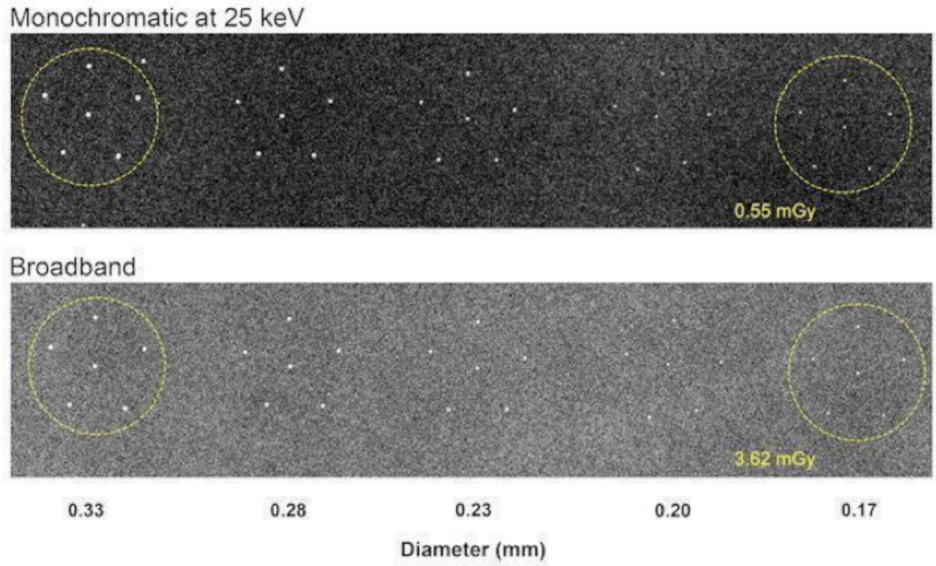

Figure 17.1: Images of microcalcifications embedded at the top of a 4.1 cm thick breast phantom acquired at a radiation dose of 0.55 mGy (top) compared with imaging obtained with a broadband mammography system at 3.62 mGy (bottom). Image courtesy of Eric Silver, PhD.

breast, such as Digital Breast Tomosynthesys and Breast Computed Tomography. The study of these techniques will happen in an ideal experimental environment with the opportunity to evaluate the imaging performance of the use of this type of source in this field, to evaluate and tune the spectra adopted in the clinical scanners in order to optimize the patient dose and the image quality of the traditional imaging systems, as well as for the investigation of the limits of the new proposed techniques.

Moreover, the beam at the BriXSinO line will permit the test and the development of a new category of physical phantoms for testing X-Ray breast imaging technology both in attenuation and phase-contrast imaging. These applications concern the experimental analysis of the materials and phantoms of new generation, produced with innovative techniques of additional manufacturing. Hence, this can permit generating phantoms with characteristics similar to real breast, based on the knowledge of the 3D structure of the organ, on the possibility of developing new breast models and on the knowledge of the properties of the multitude of the allowed materials, such as the attenuation coefficients. This last characteristic, of difficult analysis with conventional X-Ray tubes, will be easily measured by the BriXSinO monoenergetic beam. The beam will also permit to evaluate manufacturing processes by means of high resolution analysis of the produced phantoms performed via 3D images acquired at the beamline. Finally, innovative detectors, such as photon counting detectors, will have the possibility of being tested by means of reliable X-Ray beams in the appropriate energy range of interest.

17.3 Photon Counting pixel detector characterization

Photon counting X-Ray imaging detectors have been developed in the last two decades for medical imaging applications, mainly as a spin-off of microelectronic, semiconductor sensor and interconnect technologies initially developed for high-energy physics experiments [6, 7]. They have been proposed and tested also for X-Ray mammography and breast CT. Such detectors are either linear arrays or matrix arrays (2D pixel detectors) of semiconductor detector cells, operated in photoconductive or in junction (p-n, Schottky) mode.

During the X-Ray exposure, each photon depositing an energy above the equivalent noise threshold (typically, several keV) in the detector is counted by the readout analog-digital electronics of the cell, so that at the end of the exposure time the digital counter associated with each detector cell contains the number of detected photons during the exposure. When more than a counter is present in the cell readout and processing circuitry, and corresponding different energy thresholds are set in the multiple-threshold discrimination, then each counter contains, after the exposure, the number of photons depositing in that detector element an equivalent energy corresponding to the given preset energy bin. Such photon counting detectors having energy sensitivity capability permit the acquisition of so-called spectral (or "color") X-Ray images, i.e. multiple images in different energy intervals of the photon energy spectrum transmitted by the tissue irradiated with a (polychromatic) X-Ray beam. When combined with mammographic technology this spectral imaging allows a better discrimination of tissue components, and also a reduction of the radiation dose without degradation of the image quality. The addition of the spectroscopic information adds to the spatial information of bare photon-counting detectors, and this permits a better strategy for energy-weighted X-Ray spectral imaging. In this procedure, instead of giving an equal "weight" to all photon hits in the pixel, a different weight is assigned to each detected photon. It has been shown that in such an energy weighting technique, the maximum image SNR is a function of the weighting strategy, with the weights being dependent on the photon energy E, i.e. on the spectrum of the incident beam.

The use of a monochromatic source such as that of BriXSinO will allow for a precise energy characterization of the detector response in order to be able to optimize it according to the application.

17.4 Dual-energy and K-edge subtraction imaging

Conventional X-Ray detection in radiography involves an integration of the spectrum of X-Rays, weighted by the detector energy response. This results in a measurement carrying an information about the integral energy of the radiation transmitted by the irradiated sample, which is adequate for most of the conventional radiography applications.

Dual- or multi-color imaging methods, within the so-called spectral imaging methods, make use of an information or measure regarding the energy distribution of the X-Ray photons exiting the sample/patient. Currently, several solutions are being pursued to obtain spectral information by using traditional X-Ray tubes [8]. Results are promising, and some of these technologies have been also implemented for clinical routine. Nonetheless, the results of these approaches are not optimal due to overlap of the polychromatic spectra, a limited flexibility in the choice of energy distribution, additional scatter if two sources irradiate the object simultaneously or poor energy-resolution with photon-counting detectors [6, 9].

The use of a monochromatic source with tunable energy is a solution to many of these challenges. Indeed, it allows to effectively implement multi-color imaging techniques by using multiple radiographies acquired by a conventional energy-integrating X-Ray imaging detector. Multiple monochromatic beams at different energies can be used for material separation or tissue characterization, these techniques are particularly efficient if coupled to tomographic 3D imaging [10]. In the case of BriXSinO, it would be possible to acquire images of small samples such as for in-vitro, ex-vivo investigations or for small animal imaging with the monochromatic imaging system previously described. This is particularly interesting for tissue characterization of sub-structures as an alternative to the conventional histological sectioning (microtomy), which results in structural destruction or deformation. In fact, X-Ray computed microtomography (conventionally used for determining the structure of hard calcified tissues such as bone) can also be used to image the 3D morphology of intact non-calcified tissues by using multi-energy techniques for material decomposition [11].

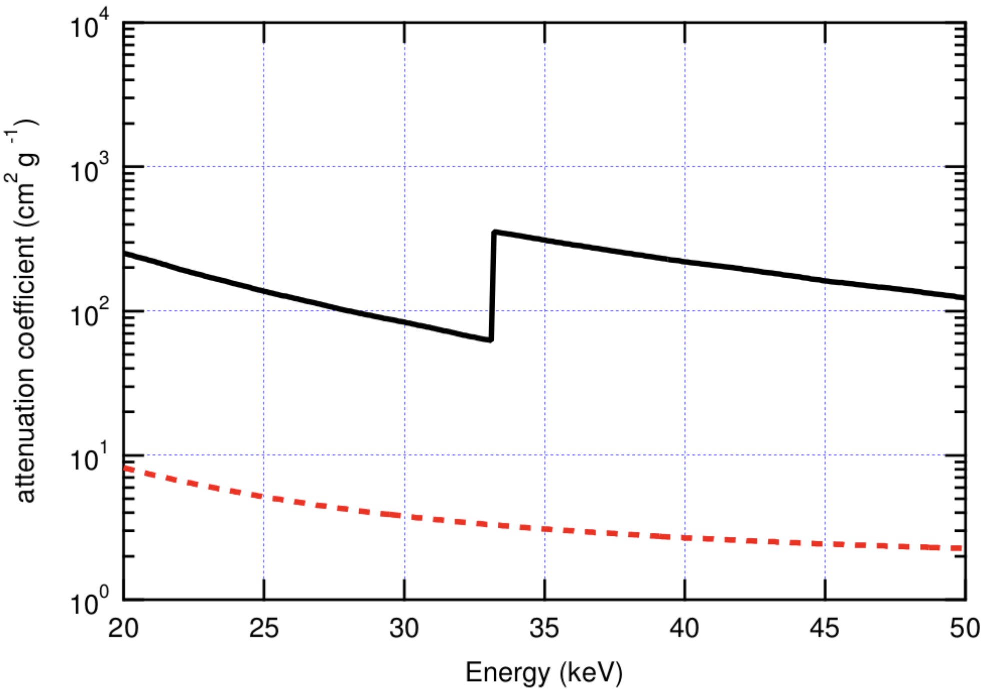

Figure 17.2: Linear attenuation coefficient μ/ρ as a function of photon energy for iodine (solid black) and soft tissue (dashed red).

A unique feature of BriXSinO will be the possibility of a dual-color modality, which is currently not available with ICS sources in operation or foreseen in the next future. One of the most straightforward and effective application of dual-energy is K-edge digital subtraction (KES) imaging, which can be used for contrast enhancement by the administration of a suitable contrast medium. In radiography, very often details of interest are difficult to detect because their attenuation matches the one of the surrounding tissues. KES takes advantage of the sharp increase (K-edge) of the absorption coefficient versus X-Ray energy of a suitable element, which can be used as a contrast agent injected in the tissues to be visualized.

This technique is based on the acquisition of two images at energies bracketing the K-edge of the element, ideally with monochromatic X-Ray beams. By combining these images, it is possible to produce hybrid images in which the contrast of relevant structures is preserved, while unwanted masking contrast is largely removed. Many applications of KES with monochromatic beams have been proved to be effective by using synchrotron radiation. A recent review concerning the application of KES techniques to bio-medical imaging can be found in Thomlinson et al. [12]. This article concludes by suggesting that with the advent of new X-Ray sources, such as compact Compton sources, KES imaging research and potential clinical applications will continue to be important areas of biomedical research.

To date, no operative ICS source allows for a fast switch between different energy levels. Nonetheless, some experiments and proof of principles have been carried out. Experiments on X-Ray imaging with ICS sources involving K-edge contrast medium have been reported, such as imaging with (quasi-)monochromatic beam at an energy above K-edge [13–16] or subtraction imaging implemented by using a K-edge filtration method with a single quasi-monochromatic beam [17]. A study concerning the image quality obtainable with K-edge subtraction in coronary angiography with ICS X-Ray beams was recently performed, and the Rose model was used to evaluate the detail detectability of a specific phantom [18]. Other recent simulations were carried out for studies on KES imaging with ICS sources for mammography and angiography applications

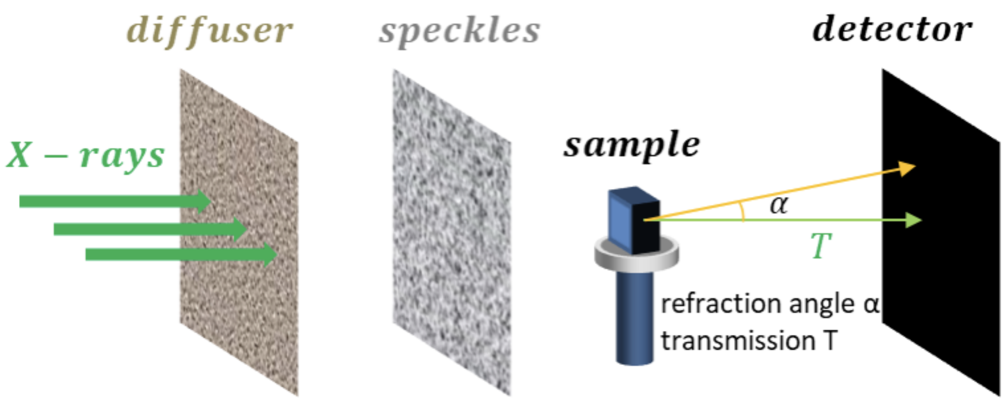

Figure 17.3: Schematic of an X-Ray speckle imaging experiment.

[19, 20]. A recent review of spectral imaging applications with ICS sources can be found in Kulpe et al [21] which proved the potential of this kind of sources for the implementation of these innovative techniques..

K-edge imaging with iodinated contrast medium is not limited to angiography, i.e., injection and perfusion in blood for the visualization of blood vessels. Innovative cationic contrast media with affinity to cartilage structures have been demonstrated to be very promising for osteoarticular imaging [22, 23]. As mentioned before, this is particularly interesting for tissue characterization of in-vitro or ex-vivo samples as an alternative to the conventional histological sectioning, by using micro-CT to image the 3D morphology of intact samples with contrast agent for tissue separation enhancement [24].

BriXSinO X-Ray beam characteristics of monochromaticity, intensity and bi-dimensional irradiation field, coupled with the unprecedented foreseen dual-energy configuration, will enable a further advance in the study and test of these innovative techniques for biomedical imaging.

17.5 Speckle-based Phase Contrast Imaging

The large coherence areas of the ICS source of BriXSinO allow to perform speckle-based phase contrast imaging (SPCI). This advanced X-Ray imaging method improve the study of specimens for biological, biomedical and pre-clinical applications as well as for materials science by characterizing small density differences and revealing the density distribution and the inner structure of the samples. The local reconstruction of both the real and imaginary part of the complex refractive index of the specimen is performed by tracking the lateral displacement of the speckle emerging from the sample and by measuring the overall intensity reduction, respectively. This multimodal approach enables local mapping of the complex refractive index of the specimen under investigation. Furthermore, by quantifying the reduction of the speckle contrast, the so-called dark-field images of the sample are assessed [25–27], which deliver valuable complementary information on the small-scale structures [28].

Speckle-based phase contrast imaging with polychromatic X-Rays has been demonstrated, thus allowing to exploit the full bandwidth of the BriXSinO source (photon flux $\approx 10^9$ - 10^{11} Photons/s) for high sensitive speckle tracking and beam tracking phase contrast imaging [29, 30] as well as for unified modulated pattern analysis methods with near field speckles [30].

The implementation of SPCI does not require sophisticated X-Rays optics or precise alignments which is fundamental for compact experimental realizations. A sketch of a typical experimental setup is shown in Figure 17.3.

Here the ICS X-Raybeam illuminates a static diffuser, and the resulting speckles are collected by a 2D sensor. When the sample under investigation is inserted in the photon beam path, the speckles are modulated in position, average intensity and local contrast. Such modulations allow to retrieve the complex refractive index of the sample and the dark-field images of the micrometric structures responsible of the scattering of the X-Rays at ultra-low angles. A 3D tomographic reconstruction of the sample is obtained by rotating the sample and by combining the 2D patterns with dedicated algorithms.

17.6 Small-angle X-Ray scattering

In addition to imaging, the characteristics of the BriXSinO X-Ray beam can be used for the implementation of material characterization techniques routinely used at synchrotron facilities. Amongst these, the analysis of coherently scattered X-Rays is a well-established tool for the characterization of materials. In fact, the spatial distribution and intensity of the peaks in the scattering pattern carries the information about the material structure. There are two main possible regimes of coherent scattering analysis: wide X-Ray scattering (WAXS) and small angle X-Ray scattering (SAXS). The former allows to look at the atomic-scale structures, while the latter allows to assess the supra-molecular structures and the large-scale arrangement (10–1000 nm) of the material. It is well established that coherent scatter-based techniques can be used to carry out material identification with higher signal-to-noise ratios than using X-Ray absorption techniques [31].

These techniques are used in a variety of applications, spanning from materials science to homeland security. For biomedical applications, several authors demonstrated that healthy and diseased tissues feature very different scattering patterns. Therefore, it is possible to take advantage of these differences to discriminate and assess the composition of a tissue sample. As an example, the changes in collagen structure when cancer invades connective tissues cause large differences in the SAXS intensity, which may be used to identify diseased samples [32]. Finally, experimental data can be used to extract molecular form factors, which are useful for tissue modeling in Monte Carlo simulations [33].

The intense, tunable and monochromatic X-Ray beams provided by BriXSinO are very well suited to implement the described scattering techniques in an effective way. In particular, a quasi-monochromatic beam with a mean energy of few tens of keV (i.e., 30 keV) and a bandwidth of few percent (i.e., 3%) could be paired with an imaging photon counting detector for performing ex-vivo characterization of biospecimens, drugs or explosives.

17.7 Non-destructive Testing for Cultural Heritage and industrial samples

Non-destructive diagnostics of Cultural Heritage by using intense monochromatic beams is well established and widely applied by using synchrotron radiation, both for samples 2D and 3D imaging (radiography, microtomography, phase-contrast imaging, ...) and material characterization (XAS, XRF, SAXS, ...) [34–36].

All the techniques described in the previous sections, from advanced X-Ray imaging to material discrimination, can be effectively translated for non-destructive testing of industrial or Cultural Heritage samples. The availability of energy-tunable, monochromatic X-Ray beams produced in compact sources of moderate cost and limited space requirements, such as BriXSinO, represents a unique opportunity for the application of this techniques. First, an easier access to an in-situ facility is important for a direct benefit of the local community of users. Moreover, the demonstration of the efficacy of ICS sources for advanced NDT, typically available only with synchrotron light, is a step forward in bridging the gap between table-top X-Ray sources and the large synchrotron facilities. Furthermore, in comparison to the X-Ray beams available at synchrotron facilities, the peculiar characteristics of BriXSinO radiation, namely the dual-energy mode and a large symmetrical divergence, make this source unique and enable experiments even beyond what is already possible with synchrotron radiation.

Bibliography

[1] L. Faillace et al. "Status of compact inverse Compton sources in Italy: BriXS and STAR". In: *Advances in Laboratory-based X-Ray Sources, Optics, and Applications VII*. Vol. 11110. International Society for Optics and Photonics. 2019.

[2] K. Dupraz et al. "The ThomX ICS source". In: *Physics Open* 5 (2020), p. 100051.

[3] B. Günther et al. "The versatile X-ray beamline of the Munich Compact Light Source: design, instrumentation and applications". In: *Journal of Synchrotron Radiation* 27.5 (2020).

[4] I. Drebot, V. Petrillo, and L. Serafini. "Two-colour X-gamma ray inverse Compton back-scattering source". In: *EPL (Europhysics Letters)* 120.1 (2017), p. 14002.

[5] J. Law. "The development of mammography". In: *Physics in Medicine & Biology* 51.13 (2006), R155.

[6] M.J. Willemink et al. "Photon-counting CT: technical principles and clinical prospects". In: *Radiology* 289.2 (2018), pp. 293–312.

[7] K. Taguchi and J.S. Iwanczyk. "Vision 20/20: Single photon counting x-ray detectors in medical imaging". In: *Medical physics* 40.10 (2013), p. 100901.

[8] A. Brahme. *Comprehensive biomedical physics*. Chap. 2, pp. 155-156. Elsevier, 2014.

[9] M. Åslund et al. "Detectors for the future of X-ray imaging". In: *Radiation protection dosimetry* 139.1-3 (2010), pp. 327–333.

[10] C.H. McCollough et al. "Dual-and multi-energy CT: principles, technical approaches, and clinical applications". In: *Radiology* 276.3 (2015), pp. 637–653.

[11] V.S.K. Yokhana et al. "Soft-tissue differentiation and bone densitometry via energy-discriminating X-ray microCT". In: *Optics Express* 25.23 (2017), pp. 29328–29341.

[12] W. Thomlinson et al. "K-edge subtraction synchrotron X-ray imaging in bio-medical research". In: *Physica Medica* 49 (2018), pp. 58–76.

[13] K. Yamada et al. "A trial for fine and low-dose imaging of biological specimens using quasi-monochromatic laser-Compton X-rays". In: *Nuclear Instruments and Methods in Physics Research Section A: Accelerators, Spectrometers, Detectors and Associated Equipment* 608.1 (2009), S7–S10.

[14] F. Carroll. "Tunable, monochromatic X-rays: An enabling technology for molecular/cellular imaging and therapy". In: *Journal of cellular biochemistry* 90.3 (2003), pp. 502–508.

[15] E. Eggl et al. "Mono-energy coronary angiography with a compact synchrotron source". In: *Scientific Reports* 7.1 (2017), pp. 1–7.

[16] R. Kuroda et al. "K-edge imaging with quasi-monochromatic LCS X-ray source on the basis of S-band compact electron linac". In: *Nuclear Instruments and Methods in Physics Research Section B: Beam Interactions with Materials and Atoms* 331 (2014), pp. 257–260.

[17] S. Kulpe et al. "K-edge subtraction imaging for coronary angiography with a compact synchrotron X-ray source". In: *PLoS One* 13.12 (2018), e0208446.

[18] G. Paternò et al. "Inverse Compton radiation: a novel x-ray source for K-edge subtraction angiography?" In: *Physics in Medicine & Biology* 64.18 (2019), p. 185002.

[19] G. Paternò et al. "Dual-Energy X-ray Medical Imaging with Inverse Compton Sources: A Simulation Study". In: *Crystals* 10.9 (2020), p. 834.

[20] T. Reutershan et al. “Numerical evaluation of high-energy, laser-Compton x-ray sources for contrast enhancement and dose reduction in clinical imaging via gadolinium-based K-edge subtraction”. In: *Applied Optics* 61.6 (2022), pp. C162–C178.

[21] S. Kulpe et al. “Spectroscopic imaging at compact inverse Compton X-ray sources”. In: *Physica Medica* 79 (2020), pp. 137–144.

[22] R.C. Stewart et al. “Contrast-enhanced CT with a high-affinity cationic contrast agent for imaging ex vivo bovine, intact ex vivo rabbit, and in vivo rabbit cartilage”. In: *Radiology* 266.1 (2013), pp. 141–150.

[23] A.E.A. Saukko et al. “Simultaneous quantitation of cationic and non-ionic contrast agents in articular cartilage using synchrotron microCT imaging”. In: *Scientific reports* 9.1 (2019), pp. 1–9.

[24] S. de Bournonville, S. Vangrunderbeeck, and G. Kerckhofs. “Contrast-enhanced microCT for virtual 3D anatomical pathology of biological tissues: a literature review”. In: *Contrast media & molecular imaging* 2019 (2019).

[25] I. Zanette et al. “Speckle-based x-ray phase-contrast and dark-field imaging with a laboratory source”. In: *Physical review letters* 112.25 (2014), p. 253903.

[26] H. Wang, Y. Kashyap, and K. Sawhney. “Hard-X-ray directional dark-field imaging using the speckle scanning technique”. In: *Physical review letters* 114.10 (2015), p. 103901.

[27] H. Wang, Y. Kashyap, and K. Sawhney. “Quantitative X-ray dark-field and phase tomography using single directional speckle scanning technique”. In: *Applied Physics Letters* 108.12 (2016), p. 124102.

[28] M. Siano, B. Paroli, and M.A.C. Potenza. “Heterodyne Near Field Speckles: from laser light to X-rays”. In: *Advances in Physics: X* 6.1 (2021), p. 1891001.

[29] F.A. Vittoria, M. Endrizzi, and A. Olivo. “Retrieving the ultrasmall-angle X-ray scattering signal with polychromatic radiation in speckle-tracking and beam-tracking phase-contrast imaging”. In: *Physical Review Applied* 7.3 (2017), p. 034024.

[30] M.C. Zdora et al. “X-ray phase imaging with the unified modulated pattern analysis of near-field speckles at a laboratory source”. In: *Applied optics* 59.8 (2020), pp. 2270–2275.

[31] C. Giannini et al. “X-ray diffraction: a powerful technique for the multiple-length-scale structural analysis of nanomaterials”. In: *Crystals* 6.8 (2016), p. 87.

[32] M. Fernández et al. “Small-angle x-ray scattering studies of human breast tissue samples”. In: *Physics in Medicine & Biology* 47.4 (2002), p. 577.

[33] G. Paternò et al. “Geant4 implementation of inter-atomic interference effect in small-angle coherent X-ray scattering for materials of medical interest”. In: *Physica Medica* 51 (2018), pp. 64–70.

[34] L. Bertrand et al. “Cultural heritage and archaeology materials studied by synchrotron spectroscopy and imaging”. In: *Applied Physics A* 106.2 (2012), pp. 377–396.

[35] F. Albertin, G. Margaritondo, and F. Kaplan. “Ancient administrative handwritten documents: virtual x-ray reading”. In: (2016). URL: `http://infoscience.epfl.ch/record/228383`.

[36] S.C. Mayo, A.W. Stevenson, and S.W. Wilkins. “In-line phase-contrast X-ray imaging and tomography for materials science”. In: *Materials* 5.5 (2012), pp. 937–965.

18. X-Ray Beam Lines and Experimental Stations

An X-Ray beamline equipped with a set of instruments and detectors is fundamental during all the phases of BriXSinO source, from commissioning to optimization and operation as user-oriented beamline. There is a set of beam line elements that are common to any user requirement and should be part of the X-Ray beamline. In Figure 18.1 an outline of the main components is reported, which includes:

1. beam stopper;
2. pre-collimation;
3. luminometer;
4. filtration,
5. collimation;
6. beam intensity monitor.

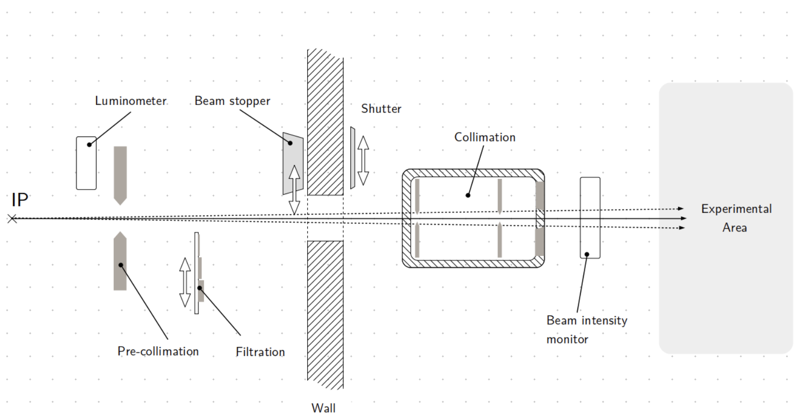

Figure 18.1: Sketch of the main components of the X-Ray beamline for BriXSinO ICS.

18.1 Beam stopper and beam shutter

The main role of this two elements is to stop the X-Ray beam from propagating to the experimental area, but the specific task and the technological implementation is slightly different for the two.

The beam stopper separates the accelerator bunker from the experimental area. For this reason if activities are foreseen in the experimental area while the electron beam is not shut down, radio-protection must be insured and the beam stopper design must be done accordingly. This implies that the attenuation requirements will be quite demanding, resulting in a bulky and possibly massive device that does not allow a fast position switching. Even if no access is foreseen, so radioprotection requirements might be relaxed, some kind of beam stopper should be implemented to protect the experimental area instrumentation from undesired exposure to radiation during machine operation, tuning or commissioning.

The X-Ray beam shutter instead is intended only to quickly switch on/off the X-Rays during experiments, without acting on the laser-electron interaction setup. Considering that some applications might require an accurate, repeatable and short exposure time of irradiation (e.g. hundreds of ms) this shutter should be controlled by a fast actuator mechanics with a reliable operation principle. Many commercial solution are available off-the-shelf from manufacturers like Vincent Associates (NY,US) and Huber (Rimsting, Germany) or could be developed in-house for custom specifications (as in the case of [1]).

18.2 Luminometer and beam intensity monitor

The luminometer and the beam intensity monitor are required get an information on the intensity of radiation emission. The output is similar but the scope and implementation is slightly different between the two.

The luminometer is the device devoted to monitor the collision alignment and synchronization by measuring the photon yield. Having a prompt measurement of the emission intensity is a crucial point during the user experiments operation, as well as in the commissioning and collision optimization phase, to monitor the stability of the photon beam. This kind of detector should not interfere with the primary beam delivered to the users. A possible solution is to place it on the X-Ray beam halo before the collimation system, so that the primary beam is not intercepted by the detector [2, 3]. To obtain a fast signal, which might be required for a closed loop feedback for collision alignment, solid state detection, such as diamond, have been proven to be effective in similar configurations [2, 4]. To obtain also information on the overlap of the colliding beams a system equipped with an imager was also proven to be effective [3].

While the luminometer is aimed at checking the interaction status, for a fast feedback, a beam intensity monitor is required to measure continuously the photon flux reaching the experimental area (after filtration and collimation). This is crucial for many experiments, such as imaging, when a normalization of the exposure is required for each acquisition. For this reason this monitor should be placed downstream all the devices which affect the beam intensity and distribution such as shutter, collimator, filters etc. A common and reliable solution used as a beam monitor is a gas ionization chamber (e.g. free-air, parallel plates), which does not affect the primary beam when the X-Ray transport beamline is in air [5–8].

18.3 Filtration

In order to modulate the flux of the X-Ray beam without acting on the collision parameters a set of filters to attenuate the photon flux should be available on the beamline. A typical solution adopted at synchrotron facilities is to use aluminum filtration. It can be a combination of suitable foils with different thicknesses that can be put on/off axis, or as a single wedge-shaped block mounted on a linear stage, in which the effective thickness is determined by the transverse position.

Also, some applications might require custom filtrations, e.g. K-edge of specific materials; for this reason, a few empty slots allowing to mount occasional filters should be included.

18.4 Collimation

As described in detail in the Chapter 6, the energy of the backscattered photons from the IP depends on scattering angle. It is maximum in the backscattered direction and decreases as the angle increases. This makes possible to adjust the energy bandwidth by selecting the angular divergence of the beam. The smaller the selected divergence, the narrower will be the resulting bandwidth. In order to tune the bandwidth in the entire energy range of BriXSinO, the angular selection of the beam must be continuously adjustable between about 1 and 10 mrad.

The task of the collimation system is to absorb the photons emitted at angles larger than the selected divergence. It will consists in a series of continuously adjustable apertures, or diaphragms, carefully designed and positioned to avoid scattering effects and degradation of the energy distribution and angular spread of the collimated beam. In the energy range of interest, few mm's of any high-Z material are sufficient for a 100% attenuation.

18.5 X-Ray transport to the experimental area

The distance between the IP and the experimental area will be around 10 m and the experimental area will be around 15 m-long, resulting in a distance of experiments ranging between about 10 and 25 m. If a free propagation in air is considered for the X-Ray transport line to the experimental area, the attenuation of air might be not negligible, as shown in Figure 18.2 where the transmission of helium gas or air is plotted as a function of the distance.

The most straightforward solution to avoid absorption and scatter by air would be to transport the X-Ray in vacuum (no ultra-high vacuum required, just air evacuation $\approx$ mbar) . However, different experiments may require different length of X-Ray propagation, and solid steel vacuum pipe are not easily adaptable in length. For this reason, bags of modular length filled with helium gas could be a viable solution, especially for very low-energy (<10 keV) experiments (e.g., as used in [9]).

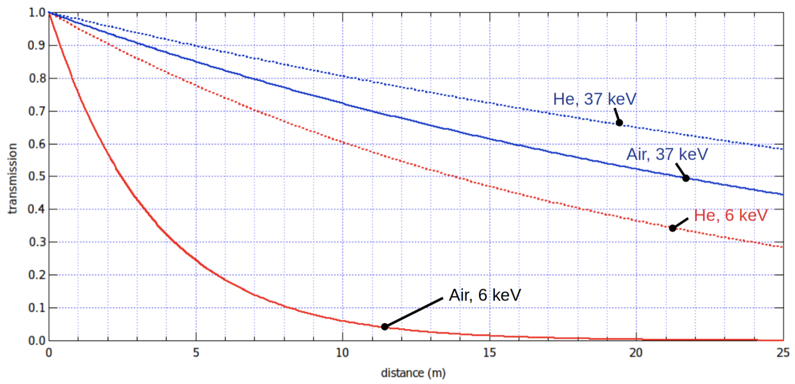

Figure 18.2: Plot of Helium gas and dry air transmission as a function of distance for 6 keV and 37 keV monochromatic photons energies.

18.6 Experimental stations

The inverse Compton source is aimed at providing bright, high repetition rate and tunable X-Rays. The 30 µm radiation source generates coherent areas a few micrometers wide at the entrance of the experimental hall (≈10 meters from the interaction point) thus making the ICS source fully compliant with coherent imaging requirements. The peculiar properties of the ICS source will be measured with dedicated experimental stations to

- Characterize the fundamental properties (expected) of the X-Ray beam.
- Monitor the source properties during the machine operation and optimization of the source parameters.
- Support the electron beam size diagnostics with precise non-destructive transverse beam size measurements.
- Support the users with accurate X-Ray beam parameters measured in-line in the actual working conditions.

Two experimental stations **EXPS1** and **EXPS2** will be installed in the experimental area at about 13 meters and 15 meters from the interaction point, respectively, as shown in Figure 18.3. The stations will be realized with a compact design (2 meters long and 1 meter wide).

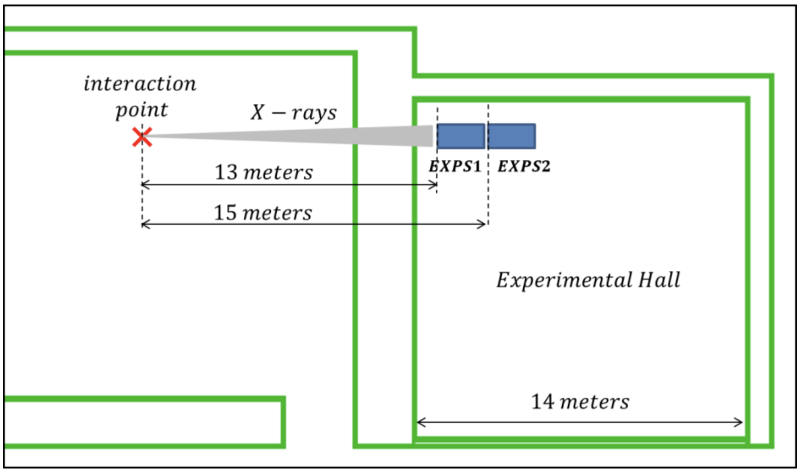

Figure 18.3: View of the experimental hall with the stations EXPS1 and EXPS2.

EXPS1 will be equipped with calibrated diffraction wires for Quantitative Inline Phase Contrast Imaging [10] (QIPCI) and for Fresnel Diffraction Interferometry [11] (FDI). Wires with diameter in the micrometric range will be made of high density materials such as tungsten for FDI [11] or low density polymeric materials such as polyethylene terephthalate, polymethymethacrylate and Nylon for QIPCI [10]. Calibrated silica nanoparticles will be used for 2D transverse coherence mapping with the Heterodyne Near Field Scattering (HNFS) technique [12–14], which provides resolutions in the micrometric range compatible with the expected coherence areas [15]. EXPS1 will additionally provide quasi-real-time monitoring of the coherence properties of the radiation for phase contrast imaging applications, enabling to assess the stability or degradation of parameters over time.

EXPS2 will be equipped with a beam profile monitor consisting of a low-noise high-resolution cooled digital camera coupled to a high resolution crystal type scintillators such as LuAG:Ce or YAG:Ce to efficiently convert the 9 - 37 keV photon energy into visible light.

A peculiar property of the ICS source is the dependence between the photon energy and the emission angle. This make possible a photon energy tuning extended from 9 keV to 37 keV with relative bandwidth (rms) in the range 1 - 10% . A solid state scanning spectrometer with tens mm^2 detection area will be installed in the EXPS2 station to measure the radiation spectrum and spectral profile (angular dependence) of the ICS source. The spectrometer will be based on Silicon or Cd-Te crystals with conversion efficiencies over 80%, in the entire range of the ICS spectrum, and resolutions of hundreds of eV.

The distance between EXPS1 and EXPS2 can be modified in order to work in both Fresnel and Fraunhofer regions of the samples.

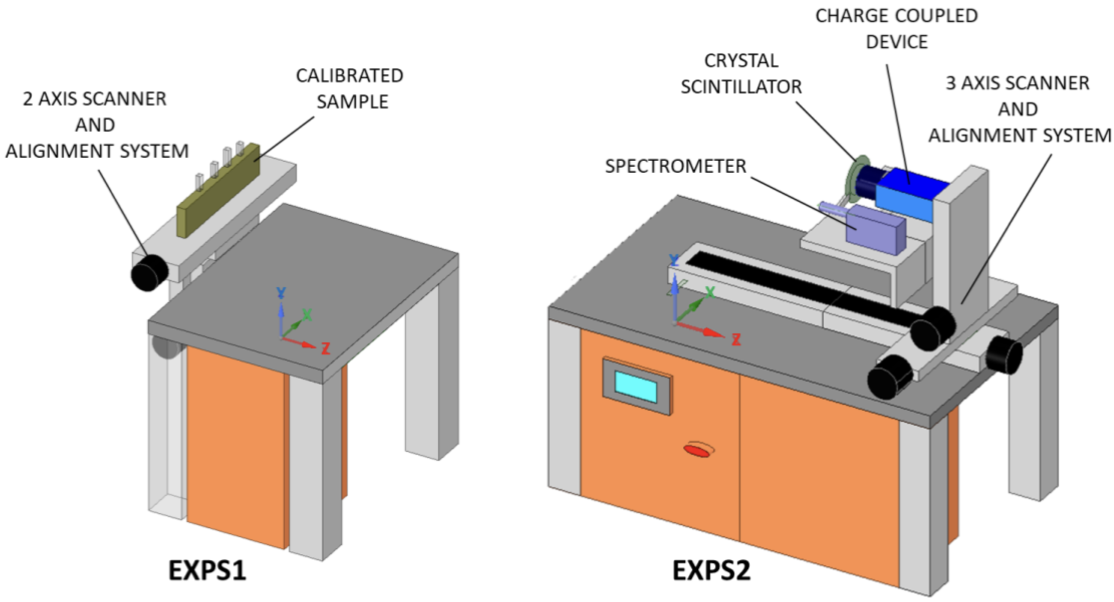

Figure 18.4: Concept design of the experimental stations EXPS1 and EXPS2.

A sketch of the experimental stations is shown in Figure 18.4. An automated motorized system installed on EXPS1 will provide precise alignment of the samples in the X-Y plane, while on EXPS2 the CCD and the spectrometer will be mounted on a three-axis scanner (X-Y-Z) and alignment system. The control of the experimental stations will be completely integrated with the central control unit of BriXSinO.

Bibliography

[1] Y. Oku et al. “Development of a Rotating X-ray Shutter for Coronary Angiography Using Synchrotron Radiation”. In: *Journal of synchrotron radiation* 5.2 (1998), pp. 123–127.

[2] T. Williams et al. “Novel applications and future perspectives of a fast diamond gamma ray detector”. In: *Nuclear Instruments and Methods in Physics Research Section A: Accelerators, Spectrometers, Detectors and Associated Equipment* 845 (2017), pp. 199–202.

[3] B. Günther et al. “Device for source position stabilization and beam parameter monitoring at inverse Compton X-ray sources”. In: *Journal of synchrotron radiation* 26.5 (2019), pp. 1546–1553.

[4] M. Antonelli et al. “Bunch by Bunch X-Ray Beam Position and Intensity Monitoring Using a Single Crystal Diamond Detector”. In: *Astroparticle, Particle, Space Physics and Detectors for Physics Applications*. World Scientific, 2012, pp. 817–821.

[5] L.I. Hua-Peng et al. “Devices for high precision x-ray beam intensity monitoring on BSRF”. In: *arXiv preprint arXiv:1512.09197* (2015).

[6] J.C. Crosbie et al. “Reference dosimetry at the Australian Synchrotron’s imaging and medical beamline using free-air ionization chamber measurements and theoretical predictions of air kerma rate and half value layer”. In: *Medical physics* 40.6Part1 (2013), p. 062103.

[7] S.N. Ahmed et al. “High-precision ionization chamber for relative intensity monitoring of synchrotron radiation”. In: *Nuclear Instruments and Methods in Physics Research Section A: Accelerators, Spectrometers, Detectors and Associated Equipment* 449.1-2 (2000), pp. 248–253.

[8] J.E. Lye et al. “Absolute dosimetry on a dynamically scanned sample for synchrotron radiotherapy using graphite calorimetry and ionization chambers”. In: *Physics in Medicine & Biology* 61.11 (2016), p. 4201.

[9] R.L. Owen, J. Juanhuix, and M. Fuchs. “Current advances in synchrotron radiation instrumentation for MX experiments”. In: *Archives of biochemistry and biophysics* 602 (2016), pp. 21–31.

[10] P. Oliva et al. “Quantitative evaluation of single-shot inline phase contrast imaging using an inverse compton x-ray source”. In: *Applied Physics Letters* 97.13 (2010), p. 134104.

[11] V. Kohn, I. Snigireva, and A. Snigirev. “Direct measurement of transverse coherence length of hard x rays from interference fringes”. In: *Physical review letters* 85.13 (2000), p. 2745.

[12] M.D. Alaimo et al. “Probing the transverse coherence of an undulator x-ray beam using brownian particles”. In: *Physical review letters* 103.19 (2009), p. 194805.

[13] M.D. Alaimo et al. “Mapping the transverse coherence of the self amplified spontaneous emission of a free-electron laser with the heterodyne speckle method”. In: *Optics express* 22.24 (2014), pp. 30013–30023.

[14] S. Mazzoni et al. “Progress on transverse beam profile measurement using the Heterodyne Near Field Speckles method at ALBA”. In: *International Beam Instrumentation Conference*. JACoW. 2019, pp. 538–541.

[15] M. Siano et al. “Electron Beam Size Measurements Using the Heterodyne Near Field Speckles at ALBA”. In: *IBIC 2019*. JACoW. 2019, pp. 1–4.

19. THz Applications with kW-class beams

19.1 Introduction

THz radiation, i.e the electromagnetic radiation in a frequency interval from 0.3 to 30 THz (1 mm – 10 μm wavelength), has been consolidating over the last decades as the next frontier in science and technology. Basic research and technological developments in advanced sensing and imaging in the THz band has remained unexplored till few years ago due to the lack of sources, detectors and optical components versus the relatively well-developed science and technology in the microwave and optical frequencies. For this reason, researchers used to refer to this problem as "the THz gap". Though relevant steps forward to advanced components and systems have been taken in the frequency interval from 0.3 to 10 THz, i.e. from 1 mm down to 30 μm wavelength, few or nothing has been done in the interval from 10 to 30 THz, i.e. for wavelengths down to 10 μm. The latter bandwidth represents, in a sense, a sort of a "THz sub-gap".

Due to their unique features, such as low photon energy, good penetrability, and excellent capability for spectral analysis [1, 2], LT-waves have drawn a great deal of interest for a wide variety of optoelectronic, sensing, and imaging applications both in fundamental research and in industrial sectors [3–5]: biological imaging, nondestructive testing (NDT), security scanning, and process control to next-generation wireless communication systems [6–8].

In order to push forward THz technologies for all the above-mentioned and other applications, two main issues should be addressed:

- developing optical components and methods for sensitive and accurate detection of phase and polarization of light;
- extending generation, manipulation and detection capabilities to the frequency interval from 10 to 30 THz, so to fill the "gap inside the THz gap".

Considering the large extension of this wavelength range, we subdivide it into three sub-domains:

- the long-wavelength side of the Far-IR, customarily referred to as the THz wavelength range $\sim$ 100 - 300 μm (or $\sim$ 1 - 3 THz) will be mentioned as Long wavelength T-waves or LT-waves;
- the wavelength range $\sim$ 20 - 100 μm (or $\sim$ 3 - 15 THz), corresponding to the Reststrahlen

band of III-V materials, henceforth mentioned as Medium T-waves or MT-waves;

- the wavelength range *sim* 10 - 20 μm (or $\sim$ 15 - 30 THz), corresponding to the Reststrahlen band of wide bandgap materials (SiC, diamond, III-nitrides), henceforth mentioned as Short T-waves or ST-waves.

Many novel technologies have been developed in the T-Waves domain since the first pulsed THz Time-Domain Spectroscopic (TDS) system has been invented more than 30 years ago. Electromagnetic waves in this domain appear now less elusive than in the past, including Terahertz Diffractive Optical Elements (DOEs) [9]. Medium T-waves and Short T-waves have received little attention thus far, despite being a wavelength range of potential interest for remote morphological characterization of objects – including medical imaging – as well as for explosives detection [10] chemical and biological spectroscopy [11, 12], astrophysics applications [13–15]. Many applications in NDT require imaging techniques. Methods such as X-Ray or ultrasonic testing employing detector arrays generate images in or close to real time. Differently, conventional THz TDS systems use short pulses of broadband THz radiation to generate highly precise spectroscopic information for the sample at single point. Compared with other far-infrared spectroscopic techniques, THz-TDS with coherent detection has tremendous advantages in terms of high sensitivity, pure polarization and direct measurement of both real and imaginary parts of the dielectric function. Typical THz-TDS systems have a frequency bandwidth between 0.1 and 5 THz, a spectral resolution of 10 GHz, an acquisition time under one minute and a dynamic range in electric field detection of 10^5 – 10^6 [2]. A THz-TDS system with a nonlinear crystal as the emitter and a InGaAs/InAlAs photoconductive antenna as the detector has been demonstrated to have a frequency coverage up to 8 THz with a center frequency at 1.44 THz [16]. A broader bandwidth enables a more accurate material identification ability. However, broadband THz-TDS schemes with over 6 THz bandwidth are usually very expensive and difficult to operate, thus hindering their practical applications.

The possibility to exploit the unique features of the THz-FEL TerRa@BriXSinO, a source with a narrow bandwidth, high power (up to 10^3 W, on average), with tunability over a wide frequency range in the Medium to Short Wavelength region from 6 THz up to 30 THz ($\sim$ 10 - 50 μm), with a peak of efficiency between 10 and 25 μm, will give us the possibility to achieve the following goals:

1. expanding THz imaging methods to the yet unexplored frequency range from 6 THz up to 30 THz, with applications to medical imaging, molecular spectroscopy and remote mesoscopic morphological characterization of materials;
2. providing full extended images based on interferometric systems, which encode phase into intensity and are based on microbolometer arrays detectors; wherever possible, results will be compared with THz-TDS system based on coherent two-dimensional electro-optic imaging;
3. selecting information and improving sensitivity of imaging methods introducing explicit control on both wavefront shape and polarization of the THz probe beam;
4. simultaneously developing a complete toolbox for handling wavefront shape and polarization state of the THz probe beam, both in the input preparation and output detection stages.

In the THz-FEL TerRa@BriXSinO, the possibility of combining THz and X-Ray radiation pulses allows for several significant works across a wide range of subject areas by using pump-probe layouts at X-Ray FEL facilities. As an example, the time dynamics of different complex atomic and molecular systems can be experimentally investigated. BriXSinO project, therefore, is expected to pave the way to novel research opportunities for the run of high field two-color THz spectroscopy measurements or X-Ray pump/THz probe experiments. As a further option, the THz source can be easily coupled to a pump laser synchronized with the oscillator, with a delivery station having photon energies in the three main bands, NIR, VIS and UV, installed in a dedicated area.

In the following sections, we will describe in detail a collection of applications we have planned to build up.

19.2 Imaging for photoelastic processes in biomedicine

Imaging using intense THz sources can be applied in many processes involving the photoelastic effect [17–19]. The effect can be essentially described in terms of a permanent or transient birefringence induced in the material by the action of some internal/external force. All dielectric media in principle can show photoelasticity, but besides the study of the fundamental physics of this effect, it is predominantly used as a tool for studying and experimentally mapping the forces/stresses applied into a given material. This is particularly important and useful around discontinuities in the material, where those forces are strong and the material can have weak points (critical stress points), and in general for irregular geometries, where calculations can be cumbersome and less reliable. Naturally, the material under investigation must be, at least partially, transparent to visible light, and indeed this technique has been applied successfully for many years on studying relaxations/deformations dynamics in glasses and plastics [20, 21].

In the case of a material which is not transparent to visible wavelengths, one immediate solution can be found by changing the wavelength itself. This is not always easy or straightforward as it may seem, because one should match the very high technological level which has been reached on visible light (both in terms of sources, manipulation, and detectors). THz waves seem particularly interesting in this context, especially when powerful sources such as BriXSinO will be developed. The photoelastic effect requires a crossed polarizers configuration. Only a small portion of light, whose polarization has been affected by the material birefringence, will be transmitted, and therefore strong sources (and sensitive detectors) are key to make the experiment practically possible [22]. One intrinsic feature of the THz wave is its high transmittivity through optically opaque materials, making it a suitable radiation range to investigate the internal properties of these materials [23]. Today, the research field of THz photoelasticity is rapidly growing, but still relatively unexplored. The proven ability of THz radiation to distinguish between different kinds of human bone tissue could be extremely beneficial in order to study the osteointegration process in real conditions [24]. One interesting application of TerRa@BriXSinO is to implement in the facility a THz photoelastic setup, with the aim of studying dental implants in animal (and, in a future, human) bones. The implants can be studied at first on dead animals (no osteointegration), then in dead animals which have been implanted a given time before death (study of the osteointegration process as a function of time). Finally, they can be measured in-vivo, which is a crucial step in order to achieve the possibility to study real human implants.

19.3 Hybrid approaches using X-Ray and metamaterial research for sensing in biology

X-Ray studies reveal THz-induced, nonthermal changes in the structure of crystallized proteins, where the excitations of large molecules are associated with THz and FIR radiations. Small Angle X-Ray Scattering (SAXS) using a THz transparent 3D printed microfluidic cell was first presented by Schewa et al.[25]. Using a microfluidic cell for the experiments, authors combined SAXS with an external THz field to determine the collective vibrational modes. Even if the authors have successfully demonstrated the main concept, the idea halted because of the lack of high field and more broadband THz sources. TerRa@BriXSinO can be the solution. Furthermore, the availability of such intense pulses in the THz frequency region will enable strong field–matter interactions and investigation of a wide range of scientific phenomena. Potential research topics include THz field-induced lattice distortion, molecular alignment, resonant and non-resonant control, as well as transient bandgap dynamics. Multidimensional spectroscopic characterization of a complex target material is challenging. Coherent diffractive imaging using synchronized THz pump and extreme-ultraviolet or X-Rayprobe pulses offers a number of exciting and promising solutions for time-resolved imaging with a nanometer-scale spatial structure of a variety of intense field–matter interactions, including molecular vibrations and rotations, and spin precession [26].

Photonic metamaterials represent another relevant research area, where tailored micro-structured subwavelength building blocks allow the light manipulation and the development of unconventional electro optical properties such as unnatural, metal level refractive index, zero reflection, perfect absorption and enhanced nonlinear phenomena [27].

One of the most promising future perspectives for THz science and technology is focused on developing fast, label-free, and cost-effective sensing applications for bacteriology and virology research and analysis. The main challenge, in this direction, is the limited sensitivity, due to the THz wavelength being far larger than cells/viruses size (a typical bacterial cell is on the order of $\sim \lambda/100$ with respect to THz range). To address this problem, suitable metamaterials have been engineered to amplify the coupling in-between living matter and THz radiation [28, 29]. The latter approach is limited by the degradation of the quality factor of the intrinsic resonances characterizing the exploited metamaterial, due to the THz absorption of the infiltrated aqueous fluid. The TerRa@BriXSinO source, thanks to its high intensity and tunability features, enables to provide TDS-complementary technique for research on bio-systems (where water absorbance becomes a major problem) and sensing applications where metamaterial-based THz devices are involved.

19.4 Hyperspectral Imaging and THz thermometry

We intend to develop an innovative method that combines hyperspectral imaging with THz thermometry, i.e. the so-called Teramometry [30]. Teramometry offers several advantages over the standard thermography:

1. it is independent of the thermal background (providing a higher S/N ratio);
2. it offers the possibility to obtain, in the future, additional spectroscopic information;
3. it enables to penetrate certain materials such as clothes and bandages.

The activity will be first based on a standard Time Domain Spectrometer (TDS) exploiting Photoconductive Antennas (PCAs). After calibration and optimization, THz thermometry will be implemented by using TerRa@BriXSinO source to achieve high spatial resolution with improved signal-to-noise ratio and advanced temperature sensitivity.

The general scheme of the opto-mechanical setup based on PCAs is shown in Figure 19.1. The system consists of femtosecond laser driven photoconductive antennas (PCAs) for both emission and detection in the THz domain. The sample will be placed on a temperature-controlled cell with high stability (0.1 °C or better). The system includes a high intensity IR laser arm (blue arrows in Figure 19.1) that can be adjusted to the desired power rates, allowing to conduct optical pump-THz probe experiments. This arm will be used first to locally heat the target phantom for thermal calibration, and then eventually replaced by a portable laser diode.

Standard calibration curve method is widely used to estimate the quantity of interest. An example of a standard THz calibration curve is shown in Figure 19.2(c) and (d). The developed system will allow to gain know-how on THz thermometry calibration and applications, and to conduct the preliminary measurements on various samples to validate the concept.

As THz-based temperature calibration requires thermal stability over a wide range of temperatures, glass cells with built-in heating elements for calibration will be used in transmission mode and metallic resistive heaters for the calibration in reflection mode. A calibration map from a large surface area will be produced to eliminate heat transfer related uncertainties. Ultra-fast raster scanning will enable us to visualize the local temperature maps of the target multilayer media (i) to reveal a 3D deviation of the local-thermal effects within the media and (ii) to investigate the thermal diffusion across the surface locally pumped by the high energy IR laser beam. As a final goal, we will be combining the spectral data acquired from the hyperspectral images with the 3D thermal maps of the system.

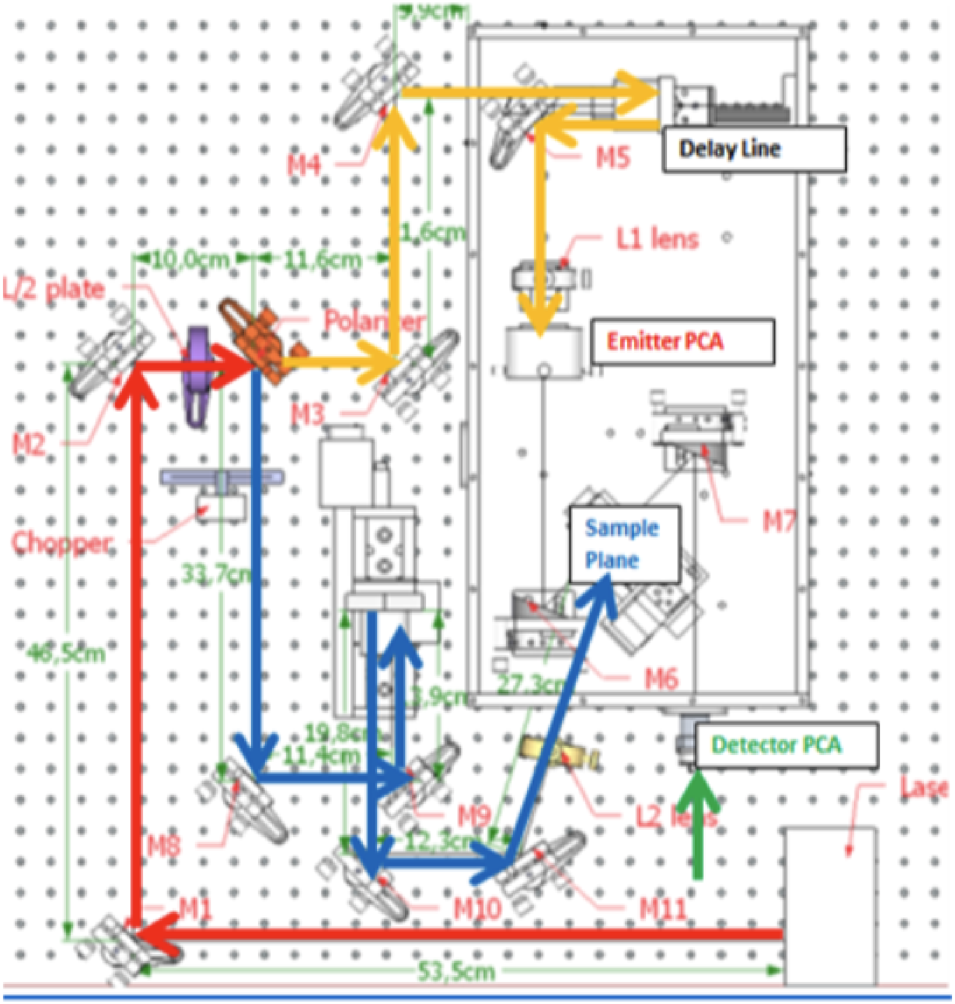

Figure 19.1: Optical layout of the THz spectrometer in pump-probe configuration. The IR laser excitation arm is shown using a red arrow.

Once the system is optimized, the setup will be moved to the beam line of TerRa@BriXSinO and implemented to achieve a better temperature sensitivity and spectral resolution, by the combination of the high intensity THz source and a high-sensitivity THz camera.

19.5 Geometric phase based shearography for stress tests on composite structures and surface profilometry

A composite material consists of two or more materials with different physical and chemical properties, in order to create a novel material suitable for very specific jobs, such as, for instance, materials having mind-boggling properties suitable for spacecrafts. In general, composite materials, such as glass-fiber-reinforced materials, carbon-fiber-reinforced materials and honeycomb structures, consist of multilayered structures. Separation between layers could occur through an internal defect in one of them (delamination). Moreover, their mechanical properties could be reduced by false adhesion, wrinkle, crack, impact damage, etc. causing serious consequences. Therefore, non-destructive testing (NDT) methods, such as shearometry, play an important role in this technology sector [31]. In the present project, based on the narrow bandwidth and high peak-power of TerRa@BriXSinO, we propose to develop shearography in the THz domain. We ambitiously aim at enhancing ordinary shearography by exploiting wavefront structured input probe beams. To date,

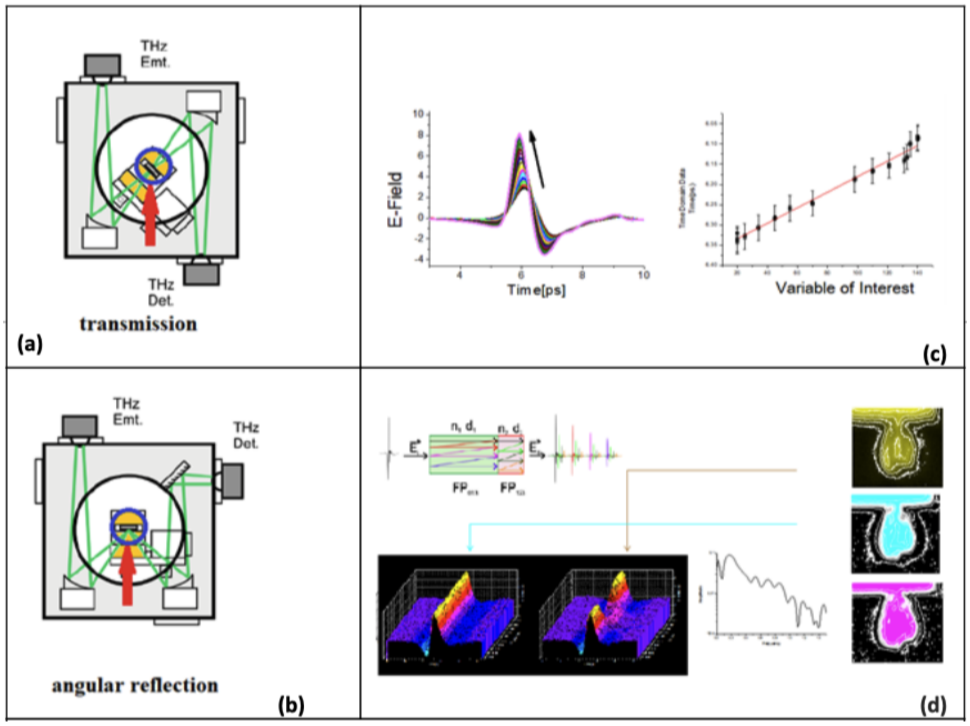

Figure 19.2: Details of the spectroscopy and imaging area (sample chamber) in (a) transmission and (b) reflection geometries. The IR-Laser excitation arm is shown with red arrows. The heating elements (blue circles) are attached on the computer-controlled X-Y stages (yellow). (c) An example of a standard THz calibration curve is shown, where the time dependent electric field deviation (time shift and/or intensity) under controlled variation of an external effect (variable of interest) is plotted to be used for calibration. (d) Hyperspectral images acquired on leaf structures revealing differences in the composing materials within the surface area of the structure. Hyper spectral information acquired from diverse subsections are presented in 3D plots, maps acquired from different spectral zone of interest (different frequencies) are shown with green, turquoise and magenta colors consecutively.

structured input beams have not been proposed yet in Optics. We ambitiously aim at reimporting this technique from T-waves back to visible radiation. To this purpose, we have planned to build a Geometric Phase Shearing Interferometer (GPSI) as a part of a platform consisting of optical tools aimed at measuring, with high sensitivity and in real time, both the wavefront and polarization of the THz radiation pulses transmitted or reflected by tested materials. The platform is described in detail in Chapter 20 and it is based on Geometric Phase Optical Elements (GPOEs) and is therefore dubbed Geometric Phase Enhanced Short T-waves platform or GESR. We are confirmed that the GPSI is unvaluable to unveil, with high reliability, the possible issues in composite structures [32]. Any further detail about the method will be provided in the next chapter.

19.6 THz Hyper-Raman spectroscopy with twisted light for chiral agents' detection

Very recently, some of us have demonstrated a new nonlinear technique in the THz domain which combines near-infrared optical pulses and intense sub-ps broadband THz pulses to generate a THz-optical four wave mixing in the investigated material [33]. We have named this effect coherent 'THz Hyper-Raman' (THYR) and a schematic representation of the technique is provided in Figure 19.3(a), (b) and (c). The reason for this name will be clarified henceforth.

Standard hyper-Raman spectroscopy is a modified version of the Raman technique where the scattered light displays a frequency spectrum with components that are close to the double frequency or second harmonic generated (SHG) signal of the fundamental laser frequency ωL. These components are the Stokes (anti-Stokes) frequencies $\omega_{s;a}$. The energy conservation law for the hyper-Raman effect can be written as $\omega_{s;a} = 2\hbar\omega_L \mp \hbar\Omega$ where Ω is a low-energy excitation of the material under investigation. Importantly hyper-Raman spectroscopy may provide information on low- energy modes that are suppressed in Raman spectra because of its symmetry selection rules. A second advantage is that detecting the signal close to the $2\omega_L$ frequency allows a more effective rejection of the extremely intense radiation at ω_L. The intense THz pulses generated by TerRa@BBriXSinO source are expected to impulsively excite the material low-energy modes and then mix with the visible light so to generate a stimulated hyper-Raman signal, in the same way as in the THYR effect, where the THz wave at ω_T may directly couple to the Ω of the material, thus enhancing the THYR signal when $\omega_T = \Omega$ (Figure 19.3(c)). In THYR, the THz photon at ω_T mixes with the two photons of the visible pulse at ω_L and generates new spectral components at lower (Stokes) and higher (anti-Stokes) frequencies as compared to the SHG central frequency $2\omega_L$. In crystalline quartz, in Ref. [33], the THYR signal has been shown to carry information on a large variety of low-energy excitations, including polaritons and phonons far from the Γ-point, usually not observable with standard optical techniques.

We notice that, in general, Raman spectroscopy is a powerful technique, being extensively used in different fields including chemical and biological analysis [34]. Additionally, when interacting with chiral molecules, the Raman signal exhibit a slight dependence on the handedness of a circularly polarized pumping beam. This effect is known as Raman Optical Activity (ROA) [35]. Since most biomolecules are chiral, ROA has been extensively applied for sensing structure, conformations, and functionalities of chiral biomolecules [36, 37]. An additional advantage of ROA is its persistence in aqueous solutions, and therefore invaluable to investigate [38].

Since most biomolecules are chiral, ROA has been extensively applied for sensing structure, conformations, and functionalities of chiral biomolecules [36, 37]. An additional advantage of ROA is its persistence in aqueous solutions, and therefore invaluable to investigate [38]. Analogously to chiral molecules, vector beams carrying an optical orbital angular momentum (OAM) per photon due to their helical phase front structure, are chiral. The interaction of vector beams with chiral molecules s expected to be enhanced. In particular, an intensity enhancement or different selection rules for the THYR and THz-SFG signals are expected when a chiral degree of freedom is added to the beams [40, 41]. These theoretical predictions open the possibility of using THYR and THz-SFG with chiral photons as advanced tools for spectroscopic and microscopic analysis of chiral biological samples in their aqueous environment.

19.7 Remote detection of inhomogeneities, form and stress birefringence in bulk materials based on GEST platform

Detecting the symmetry properties of inhomogeneous materials is of vital importance to understand their origin in fabrication processes as well as to predict the possible issues arising during their operation. Our platform enables to detect such symmetry properties by measuring the SAM and OAM locally exchanged between light and matter. SAM is specifically useful when inhomogeneous birefringent materials are envisaged or when inhomogeneities in isotropic materials have a spatial degree of correlation such that a form birefringence effect arises within the material [39]. To this purpose, we have specifically designed a Full Stokes Imaging Geometric Phase Polarimeter (FSIGPP) to be included into our GEST platform. This can be directly demonstrated in the case of artificially realized inhomogeneously polarized structures [42].

To unveil inhomogeneities in isotropic materials, OAM represents an invaluable probe: OAM, in fact, is only exchanged when rotational symmetry is broken. In addition to polarimetric (SAM)

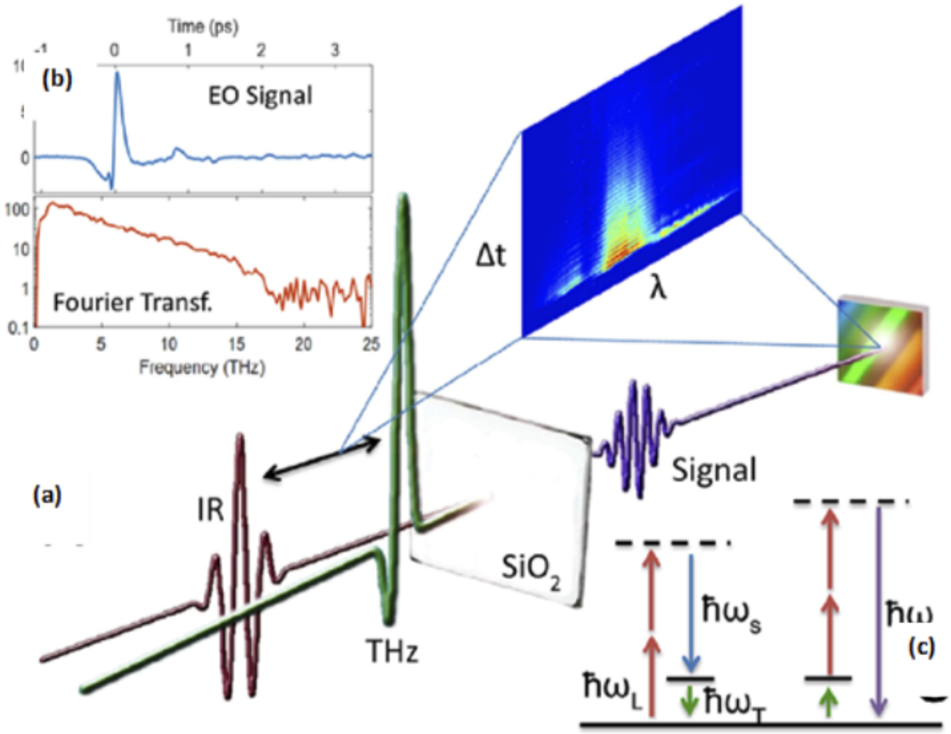

Figure 19.3: THYR Spectroscopy scheme. (a) Intense THz pulses (green curve) are sent to the sample together with IR pulses at 800 nm wavelength (red curve) at adjustable delay Δt. After removal of the fundamental IR light (not shown), the THYR signal (violet curve) is decomposed spectrally by a reflection grating, and its spectral components intensity is measured as a function of both Δt and λ. (b) THz pulse measured by Electro-Optic Sampling technique in time-domain (upper panel, light blue curve) and its correspondent Fourier transform (lower panel, red curve). (c) Photon energy diagram of the THYR effect (Ref. [39]).

measurements performed via FSIGPP, therefore, we will perform also OAM measurements exploiting a Polarizing Sagnac Interferometer with Dove prism (PSID) included in GEST. The PSID enables, in one shot, without passing through the measurement of the entire OAM spectrum coefficients, to obtain the amount of the symmetry breaking occurring in the studied material. This is, in fact, quantified by the overall mean L_z and variance ΔL_z of the OAM exchanged between light and matter. Of course, in this case, we have to prepare the probe beam in a non-zero average OAM state. The Geometric Phase Beam Shaper (GPBS) – described in Chapter 20 – has been designed to this purpose.

Bibliography

[1] J.F. Federici et al. “THz imaging and sensing for security applications—explosives, weapons and drugs”. In: *Semiconductor Science and Technology* 20.7 (2005), S266.

[2] B. Ferguson and X.C. Zhang. “Materials for terahertz science and technology”. In: *Nature materials* 1.1 (2002), pp. 26–33.

[3] X.C. Zhang and J. Xu. *Introduction to THz wave photonics*. Vol. 29. Springer, 2010.

[4] Y.H. Tao, A.J. Fitzgerald, and V.P. Wallace. “Non-contact, non-destructive testing in various industrial sectors with terahertz technology”. In: *Sensors* 20.3 (2020), p. 712.

[5] A. Redo-Sanchez and X.C. Zhang. “Terahertz science and technology trends”. In: *IEEE Journal of Selected topics in quantum electronics* 14.2 (2008), pp. 260–269.

[6] R. Piesiewicz et al. “Short-range ultra-broadband terahertz communications: Concepts and perspectives”. In: *IEEE Antennas and Propagation Magazine* 49.6 (2007), pp. 24–39.

[7] A. Hirata, M. Harada, and T. Nagatsuma. “120-GHz wireless link using photonic techniques for generation, modulation, and emission of millimeter-wave signals”. In: *Journal of Lightwave Technology* 21.10 (2003), pp. 2145–2153.

[8] N. Hasegawa et al. “Remote identification of protrusions and dents on surfaces by terahertz reflectometry with spatial beam filtering and out-of-focus detection”. In: *Applied Physics Letters* 83.19 (2003), pp. 3996–3998.

[9] A. Siemion. “The Magic of Optics—An Overview of Recent Advanced Terahertz Diffractive Optical Elements”. In: *Sensors* 21.1 (2021), p. 100.

[10] M.R. Leahy-Hoppa, M.J. Fitch, and R. Osiander. “Terahertz spectroscopy techniques for explosives detection”. In: *Analytical and bioanalytical chemistry* 395.2 (2009), pp. 247–257.

[11] J.H. Son. “Terahertz electromagnetic interactions with biological matter and their applications”. In: *Journal of Applied Physics* 105.10 (2009), p. 102033.

[12] T.R. Globus et al. “Submillimeter-wave Fourier transform spectroscopy of biological macromolecules”. In: *Journal of Applied Physics* 91.9 (2002), pp. 6105–6113.

[13] S. Schlemmer. “High-resolution laboratory terahertz spectroscopy and applications to astrophysics”. In: *Frontiers and Advances in Molecular Spectroscopy*. Elsevier, 2018, pp. 471–525.

[14] D. Appadoo and R. Plathe. “THz/Far-IR Astrophysical Studies at the Australian Synchrotron”. In: *2019 44th International Conference on Infrared, Millimeter, and Terahertz Waves (IRMMW-THz)*. IEEE. 2019, pp. 1–2.

[15] P.H. Siegel. “THz instruments for space”. In: *IEEE Transactions on Antennas and Propagation* 55.11 (2007), pp. 2957–2965.

[16] Y. Zhang et al. “A broadband THz-TDS system based on DSTMS emitter and LTG InGaAs/InAlAs photoconductive antenna detector”. In: *Scientific reports* 6.1 (2016), pp. 1–6.

[17] P.S. Stefanova et al. “Tensile Stress Measurements with Photoelastic Scattering at THz Frequencies”. In: *2020 45th International Conference on Infrared, Millimeter, and Terahertz Waves (IRMMW-THz)*. IEEE. 2020, pp. 1–2.

[18] S. Ebara et al. "Highly sensitive birefringence measurement in THz frequency region and its application to stress measurement". In: *2007 Joint 32nd International Conference on Infrared and Millimeter Waves and the 15th International Conference on Terahertz Electronics*. IEEE. 2007, pp. 666–667.

[19] Q. Chen et al. "Electro-optic transceivers for terahertz-wave applications". In: *JOSA B* 18.6 (2001), pp. 823–831.

[20] A.Y. Yi et al. "Residual stresses in glass after molding and its influence on optical properties". In: *Procedia Engineering* 19 (2011), pp. 402–406.

[21] P. Schemmel, G. Diederich, and A.J. Moore. "Direct stress optic coefficients for YTZP ceramic and PTFE at GHz frequencies". In: *Optics express* 24.8 (2016), pp. 8110–8119.

[22] K. Wiesauer and C. Jördens. "Recent advances in birefringence studies at THz frequencies". In: *Journal of Infrared, Millimeter, and Terahertz Waves* 34.11 (2013), pp. 663–681.

[23] Z. Wang et al. "Determination of plane stress state using terahertz time-domain spectroscopy". In: *Scientific reports* 6.1 (2016), pp. 1–6.

[24] A.S. Nikoghosyan et al. "Optical properties of human jawbone and human bone substitute Cerabone® in the terahertz range". In: *Journal of Contemporary Physics (Armenian Academy of Sciences)* 51.3 (2016), pp. 256–264.

[25] S. Schewa et al. "A THz transparent 3D printed microfluidic cell for small angle x-ray scattering". In: *Review of Scientific Instruments* 91.8 (2020), p. 084101.

[26] X.C. Zhang, A. Shkurinov, and Y. Zhang. "Extreme terahertz science". In: *Nature Photonics* 11.1 (2017), pp. 16–18.

[27] C.M. Soukoulis and M. Wegener. "Past achievements and future challenges in the development of three-dimensional photonic metamaterials". In: *Nature photonics* 5.9 (2011), pp. 523–530.

[28] G.P. Papari, C. Koral, and A. Andreone. "Sensing biological fluids using Resonating Surface Plasmon Polaritons in the THz range". In: *2019 Thirteenth International Congress on Artificial Materials for Novel Wave Phenomena (Metamaterials)*. IEEE. 2019, pp. X–293.

[29] G.P. Papari, C. Koral, and A. Andreone. "Encoded-enhancement of THZ metasurface figure of merit for label-free sensing". In: *Sensors* 19.11 (2019), p. 2544.

[30] R. Naccache et al. "Terahertz thermometry: Combining hyperspectral imaging and temperature mapping at terahertz frequencies". In: *Laser & Photonics Reviews* 11.5 (2017), p. 1600342.

[31] Q. Zhao et al. "Digital shearography for NDT: phase measurement technique and recent developments". In: *Applied Sciences* 8.12 (2018), p. 2662.

[32] L.A. Alemán-Castaneda et al. "Shearing interferometry via geometric phase". In: *Optica* 6.4 (2019), pp. 396–399.

[33] A. Rubano et al. "Terahertz hyper-Raman time-domain spectroscopy". In: *ACS Photonics* 6.6 (2019), pp. 1515–1523.

[34] R.L. McCreery. *Raman spectroscopy for chemical analysis*. Vol. 225. John Wiley & Sons, 2005.

[35] S. Ostovar, L.D. Barron, and E.W. Mutter S.T. Blanch. "Chapter 6 - Raman Optical Activity". In: *Chiral Analysis (Second Edition)*. Ed. by Prasad L. Polavarapu. Second Edition. Elsevier, 2018, pp. 249–291. ISBN: 978-0-444-64027-7. DOI: `https://doi.org/10.1016/B978-0-444-64027-7.00006-9`. URL: `https://www.sciencedirect.com/science/article/pii/B9780444640277000069`.

[36] V. Parchaňsky, J. Kapitán, and P. Bouř. “Inspecting chiral molecules by Raman optical activity spectroscopy”. In: *RSC Advances* 4.100 (2014), pp. 57125–57136.

[37] L.D. Barron. “The development of biomolecular Raman optical activity spectroscopy”. In: *Biomedical Spectroscopy and Imaging* 4.3 (2015), pp. 223–253.

[38] L.A. Nafie. *Vibrational optical activity: Principles and applications*. John Wiley & Sons, 2011.

[39] M. Born and E. Wolf. *Principles of optics: electromagnetic theory of propagation, interference and diffraction of light*. Elsevier, 1999.

[40] K.A. Forbes. “Raman optical activity using twisted photons”. In: *Physical review letters* 122.10 (2019), p. 103201.

[41] K.A. Forbes. “Nonlinear chiral molecular photonics using twisted light: hyper-Rayleigh and hyper-Raman optical activity”. In: *Journal of Optics* 22.9 (2020), p. 095401.

[42] P. Darvehi et al. “Increasing the topological diversity of light with modulated Poincaré beams”. In: *Journal of Optics* 23.5 (2021), p. 054002.

20. THz Beam Lines and Experimental Stations

20.1 Introduction

In this proposal, we present the layout of a complex extendable optical platform designed for multiple integrated analyses of materials and devices in the Short Wavelengths Terahertz domain. Its purpose is the practical realization of the applications described in detail in Chapter 19, i.e. to perform hyperspectral analyses, test dielectric and, above all, morphologic properties of material objects over a variable lateral scale ranging from hundreds down to few tens of micrometers and a variable depth scale from few nanometers up to few tenths of micrometers. The THz-FEL TerRa@BriXSinO source will provide the latter platform a narrow bandwidth, high power - up to 10^3 W, on average - with tunability over a wide frequency range in Short Wavelengths THz region from 6 THz up to 30 THz ($\sim$ 10 - 50 µm), with a peak of efficiency between 10 and 25 µm. The setup includes high performance optical components based on Spatially Varying Axis Plate (SVAP) concept [1, 2]. Such components are based on Pancharatnam-Berry or Geometric Phase. They will be designed and tailored specifically for TerRa@BriXSinO source, in order to allow for efficient management of light polarization as well as wavefront structuring and sensing. Importantly, a high-power source is imperative in building complex layouts including a host of optical components with many interposed free-space layers, especially in view of the non-negligible absorption at $\lambda \geq$ 15 µm ($\nu \leq$ 20 THz), mainly due to CO_2 and water vapor. Considering the prominent role played by Geometric Phase in the development of the platform, we have baptized the system Geometric Phase Enhanced Short wavelength Terahertz, or GEST[1], platform.

In Section 20.2, a short effective view about Geometric Phase Optical Elements (GPOEs) is provided, in order to explain their potentialities for tackling the challenges of this research activity. In this way, the prominent role of GPOEs in building the GEST platform will be clarified. In Section 20.3, the platform layout is described in any detail.

20.2 Geometric Phase Optical Elements

Geometric Phase Optical Elements (GPOEs) or Pancharatnam-Berry Phase elements are of vital importance for GEST. A comprehensive description of basic related concepts can be found in Ref.

[1]Here the footnote

[3]. Nevertheless, we here briefly describe the method we have planned to exploit for designing a fabricating such components in the framework of the present project. The simplest possible design of a GPOE is a Spatially Varying optic Axis birefringent half-wave Plate (SVAP), so that the above-mentioned geometric phase in the transverse directions and results into a reshaped optical wavefront. When the input light is circularly polarized, only phase effects will arise. The output will be also circularly polarized with opposite handedness. The resulting optical phase component has a uniform thickness, but arbitrarily large phase differences can be anyway induced across the plate. Opposite handedness of the input circularly polarized light induces opposite phase retardations across the plate, and the wavefront outputs come to be reciprocally “conjugate”. The working principle of the device is illustrated pictorially in Figure 20.1. Liquid crystals are particularly well-suited for making SVAPs, as they are birefringent and their optic axis distribution can be easily controlled with patterned surface treatments or external fields. More importantly the overall retardation δ of a SVAP can be continuously changed between 0 and 2π by applying a weak (~ 1 - 2 V rms voltage) external AC electric field. Ideal substrate material is diamond Type IIA. A recently proposed material more suitable for this task is the poly(3,4-ethylenedioxythiophene) polystyrene sulfonate (PEDOT:PSS) [4].

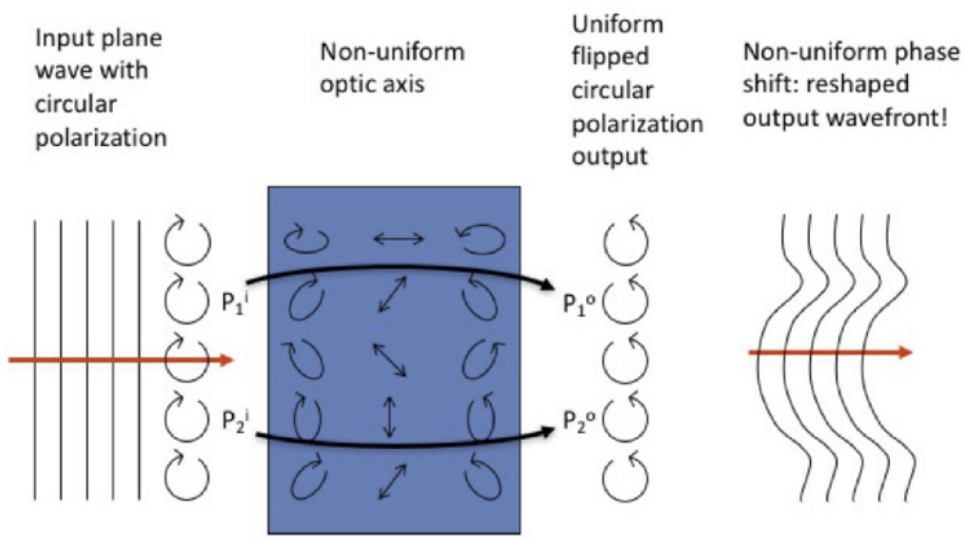

Figure 20.1: Working principle of a GPOE. A GPOE can be made as a birefringent medium with a uniform half-wave birefringent retardation but an optic axis that is space-variant in the transverse plane. An input circularly-polarized plane wave passing through the medium will be transformed into the opposite-handed circular polarization uniformly across the plate. The two optical rays will acquire a relative geometric phase difference given by half the solid angle subtended by these two meridians [3].

20.3 Design of the optical layout of GEST platform

The designed layout for GEST platform is sketched in Figure 20.2(a) and (b). TerRa@BriXSinO provides a linearly polarized pulsed wave in the frequency range between 6 THz ($\lambda = 50\,\mu$m) and 30 THz ($\lambda = 10\,\mu$m) with an output power on the order of 1 kW. The output beam has a divergence of 4.5 mrad. If necessary, to improve the quality of the output TEM_{00} mode, the beam has been focused and re-collimated by means of two confocal biconvex diamond (Type IIA) lenses, L_1 and L_2, with focal lengths respectively $f_1 = 25$ mm and $f_2 = 50$ mm. The aperture diameter should be at least on the order of $2f_1\lambda/\pi w_0$. Depending on the test type, polarization state and wavefront shape can be easily modified through the versatile electro-optical system represented by Module for Geometric Phase Beam Shaping (GPBS). It includes several liquid crystals-based electro-optically driven homogeneous retardation waveplates and SVAPs. The latter have suitably shaped optic axis distributions that can be tailored to sculpt the wavefront or the polarization transverse distribution as required [1, 2]. The modules for polarization and wavefront analyses will be described in greater detail in Section 20.3.2, 20.3.3 and 20.3.4. The sample is then inserted. Depending on the sample material and/or the test type, transmitted or reflected light is analyzed (Figure 20.2(b)).

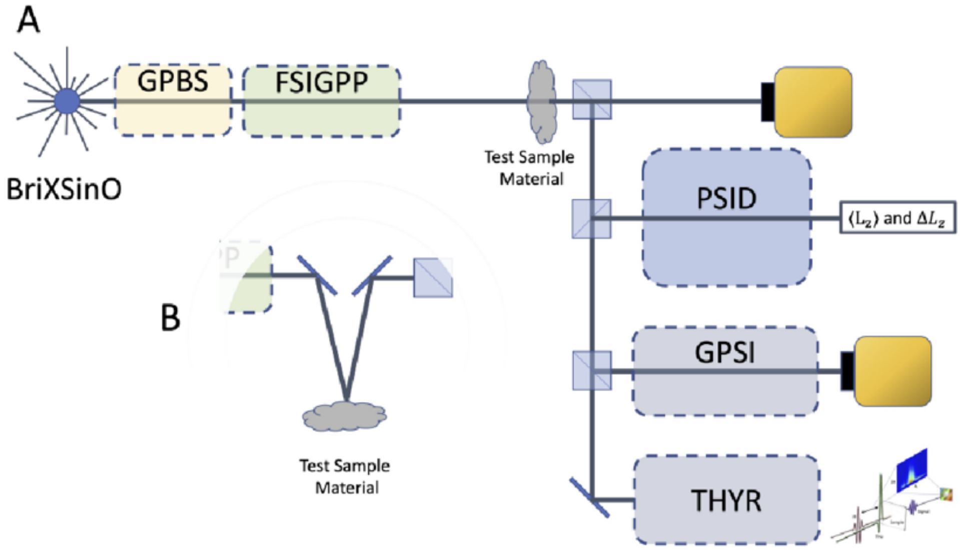

Figure 20.2: Block diagram sketch of the platform GEST. TerRa@BriXSinO is source is supposed. GPBS is the Geometric Phase-based Beam Shaper; FSIGPP, Full-Stokes Imaging Geometric Phase Polarimeter; PSID, Polarized Sagnac Interferometer; GPSI, Geometric Phase Shearing Interferometer; THYR, TeraHertz Hyper-Raman spectroscopy system. A microbolometric camera array is planned to be used as image detector. Inset (b) represents the option for reflection measurements.

In order to perform combined polarization and wavefront analyses, the GEST platform includes an electro- optically driven Full-Stokes Imaging Geometric Phase Polarimeter (FSIGPP), that we have specifically designed for the platform. Such device consists of a wiregrid polarizer and six liquid-crystal retardation wave plates, that can be electrically tuned independently from each other (SUAP or Spatially Uniform Axis Plates). In this way, any desired retardation can be achieved, and any required polarization component can be selected for subsequent wavefront analysis. Two 50:50 beam splitters, BS_1 and BS_2 and the mirror M, are cascaded to generate three replicas of the output beam from the polarimeter to be injected in the following systems for subsequent intensity measurements and wavefront analyses:

- direct output from the polarimeter (FSIGPP) for pure polarization analysis and measurement of the Spin Angular Momentum (SAM) transferred from light to matter and vice versa;
- Sagnac Polarizing Interferometer containing a Dove prism (PSID), delivering the mean and variance of the Orbital Angular Momentum (OAM) transferred from light to matter and vice versa;
- Geometric Phase-based Shearing Interferometer (GPSI), delivering the phase derivative of the input wavefront with respect to multiple coordinates depending on the shearing core device and the wavefront shape impinging on the sample, for optical devices aberrometry and for surface profilometry.
- Twisted Light Terahertz Hyper-Raman (THYR) Spectroscopy in both frequency and time

domains can be implemented by exploiting FSIGPP to prepare wavefront and polarization of the pump/probe beams used to generate and detect a THz-optical four wave mixing in the investigated material.

Imaging for photoelastic processes (IPP) in biomedicine, Hyperspectral imaging and THz thermometry (THM), and THYR spectroscopy technique have been illustrated in detail in Chap. 19 They are all represented by the bottom right block in Fig. 2 (a). Here we remark that, in THYR, the frequencies of the generated signal correspond to a large variety of material excitations, such as Γ-point phonons, polaritons, and phonons out of the *Gamma*-point, which can be usually observed only by neutron scattering techniques. Twisted light adds a further degree of freedom to the technique and enables to investigate chiral molecular agents, which have high relevance in Biology and Medicine.

Some detection stages in this layout include a high-performance camera, such as a NEC IRV-T0831 uncooled microbolometer array (320×240 pixels, 23.5 µm pixel size). Microbolometers are originally designed for thermal imaging at the long wavelength infrared (LWIR) region at 7 - 14 µm, but they are known to retain sensitivity at THz frequencies and have been effectively used for THz beam profiling and imaging at longer wavelengths (14 - 300 µm) [5].

In the GEST platform, the Pancharatnam-Berry or Geometric Phase underpins the operation principle not only of optical components and devices deployed all over the optical layout, but also of entire building blocks, such as the preparation stage of both polarization and wavefront of the beam irradiating the sample, as well as the detection stage of polarization and, of course, the GPSI. At present, Geometric-Phase based optical devices and systems are not available on the market and we will fabricate them in the Photonics Lab of the Department of Physics “E. Pancini” at University of Naples “Federico II”. The design and fabrication of liquid crystal-based SVAPs for ST-waves are extremely challenging and require a fairly cunning strategy to be realized in practice.

20.3.1 Test beam preparation: setting the polarization and the wavefront of the beam output from future TerRa@BriXSinO source

TerRa@BriXSinO generates an output beam linearly polarized in the vertical direction with contrast ratio that can reach values of the order of 10.000:1, in the transverse fundamental gaussian mode TEM_{00} with waist $w_0 = 5$ mm. The polarization state can be homogeneously changed at will by using a couple of electrically tunable liquid crystal- based retardation waveplates with uniform optic axis distribution or Spatially Uniform Axis Plates (SUAPs), fabricated in our Photonics Lab in Naples (Figure 20.3(a)). The axis of the first SUAP is oriented at 45° with respect to the linear polarization direction of TerRa@BriXSinO output. Its retardation δ_1 can be tuned to any value between 0 and 2π with resolution of $\approx 10^{-2}\pi$. The second waveplate retardation is set to an appropriate value $\delta_2 = \pi/2$ for Half-Wave Plate (HWP) operation and the axis can be rotated in order to set at will the orientation of the polarization ellipse. SUAPs fabricated in our lab take advantage against ordinary retardation waveplates tunability: the retardation δ_1 or δ_2, as explained in Section 20.3.4, can be changed to perfectly match the peak wavelength of the laser pulse by changing the amplitude of the AC voltage signal applied to the SUAP.

In order to impart the beam a transversely inhomogeneous polarization, a suitably designed SVAP is required [2], as shown in Figure 20.3(b). In generating vector beams, SVAPs are by far more efficient than interferometric devices: they are easy to use, compact and, above all, when operated as Quarter-Wave Plates (QWPs), the polarization distribution is coincident with the optic axis distribution. To reshape the wavefront while maintaining the polarization uniform and preserving input power, a suitably designed SVAP is again required, but the input polarization has to be preliminarily converted from linear into circular by means of a 45° oriented SUAP with retardation $\delta = \pi/2$ [1]. Most probably, q-plates are the most well-known examples of such devices [6].

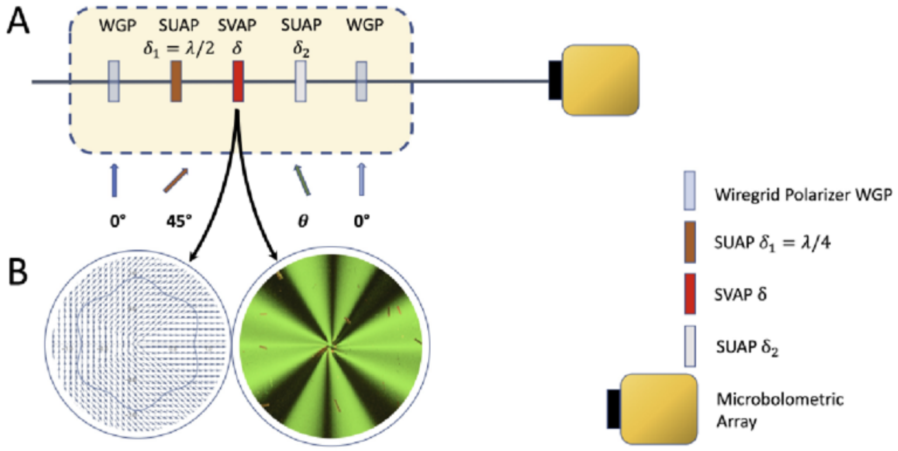

Figure 20.3: Internal optical layout of GPBS included in GEST. (a) General scheme of the preparation stage and bolometric camera. (b) Optic axis pattern of a wavefront reshaping SVAP (on the left) and polarizing microscope image of the corresponding real SVAP sandwiched between crossed polarizers (on the right).

20.3.2 Polarization detection stage

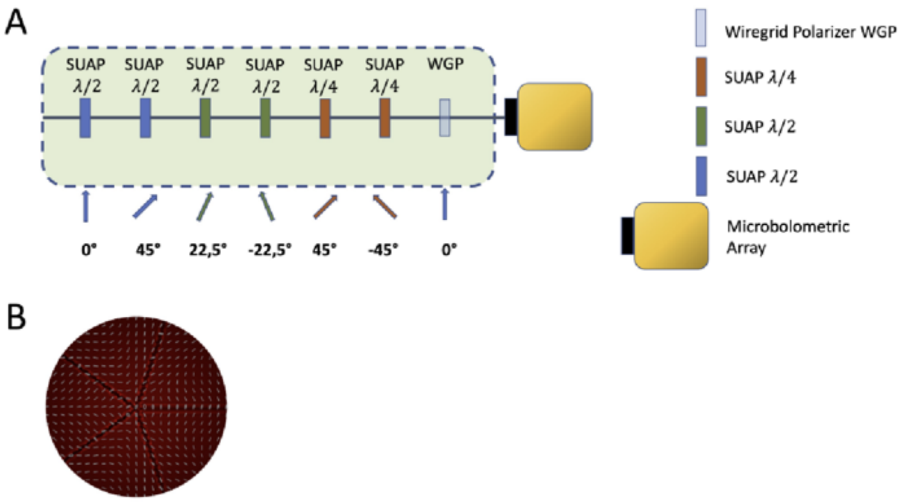

Figure 20.4: Internal optical layout of FSIGPP included in GEST and polarigram of an inhomogeneous birefringent liquid-crystal film. (a) Each SUAP can be switched on and off independently of the others and has its axis orientation fixed. (b) The local optic axis distribution can be displayed based on FSIGPP technology [2].

Beyond the test sample, a geometric phase-based polarimeter is posed. It consists of six SUAPs and a wire-grid polarizer (WGP) model P03 from InfraSpecs (Figure 20.4(a)). WGP is a high contrast Far-Infrared and Mid-Infrared substrate-free wire-grid polarizer P03, with extinction ratio 10.000:1. All the SUAPs, as well as the WGP, are mounted on stepper-motor-driven rotary tables having angular resolution 0.02°. Combined with the NEC IRV-T0831 microbolometric camera, our system enables full-Stokes imaging - hence the name of the subsystem, Full-Stokes Imaging Geometric Phase Polarimeter (FSIGPP). The polarization inhomogeneity map of the light transmitted or reflected by an object (Figure 20.4(b)) can be reconstructed with a resolution depending on the specifications of the camera and the magnification of the optical system adopted to locally scan the sample. The magnification system consists of an infinity-corrected microscope objective (reflective objective LMM-UVV by Thorlabs) with a predetermined magnification ratio mounted on a stepper-motor-drive XYZ translation stage for both transverse and longitudinal scanning. Full-Stokes parameters measurements through a single SUAP is allowed thanks to the possibility to set the retardation δ for both HWP and QWP operation all over the wavelength range of interest. Such a stage serves as polarization detector as well as polarization selector for subsequent wavefront analysis.

20.3.3 Polarizing Sagnac Interferometer with Dove prism (PSID)

In a polarizing Sagnac interferometer (Figure 20.5) two replicas of the input beam propagate in two opposite directions along the same planar path (common-path interferometer) and are linearly polarized along mutually orthogonal directions. A Dove prism whose basis is tilted out of the interferometer plane by an angle α is inserted into the path and provides a rotational shift of the two replicas around their own axes by an angle 2α. The phase delay between the beams leaving the interferometer is adjusted to $\pi/2$ or 2π through a SUAP with the optic axis aligned along one of the PSID axis. A second SUAP with $\delta = \pi$ and the optic axis at 45° to the PSID axes is used to make the output beams interfere and, finally, a balanced polarizing homodyne detector is used to provide the contrast ratio between the two output ports. By this method, the mean and variance of the Orbital Angular Momentum (OAM) transferred between light and sample can be directly measured without passing through the determination of its full spectral distribution [7].

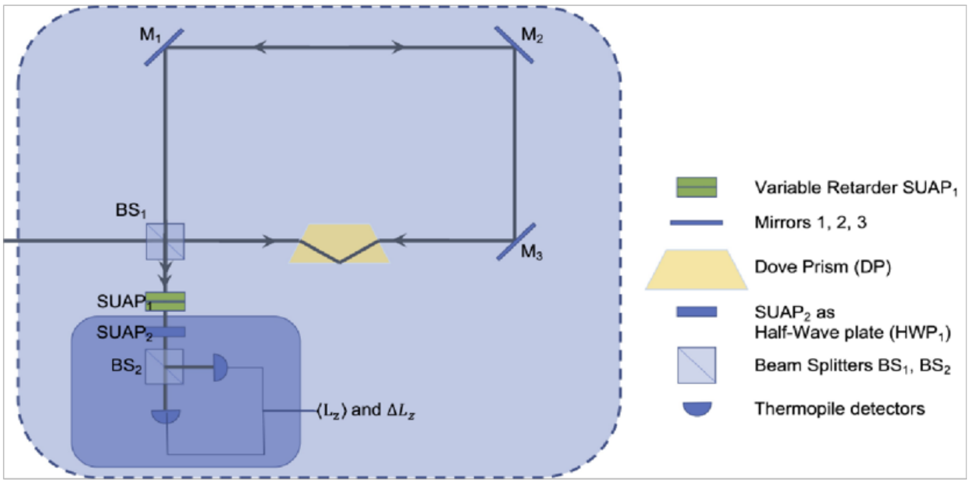

Figure 20.5: Internal optical layout of PSID included in GEST. BS_1 is the input/output port of the polarizing Sagnac interferometer (PSID) whose path is closed by mirrors M_1, M_2 and M_3. PSID contains a Dove prism used to rotate the two counter-propagating beams with respect to each other. At the output of the PSID, a $SUAP_1$ compensator is used to adjust the relative phase-shift δ. The last stage is a balanced polarizing homodyne detector, with the axes rotated by 45° with respect to the PSID axes through the $SUAP_2$ operated as a half waveplate half-waveplate [7].

20.3.4 Geometric Phase-based Shearing Interferometer (GPSI)

A shearing interferometer is a common-path interferometer delivering the derivative of the optical phase with respect to a given coordinate. The derivative is performed by generating two replicas of the input beam, so that they are slightly shifted with respect to each other along the given coordinate and making them interfere with opposite phases. This method enables to reconstruct wavefronts without resorting to any reference wave. We have included into our platform a Geometric Phase-based Shearing Interferometer (GPSI) (Figure 20.6(a)), which has been fully developed in our

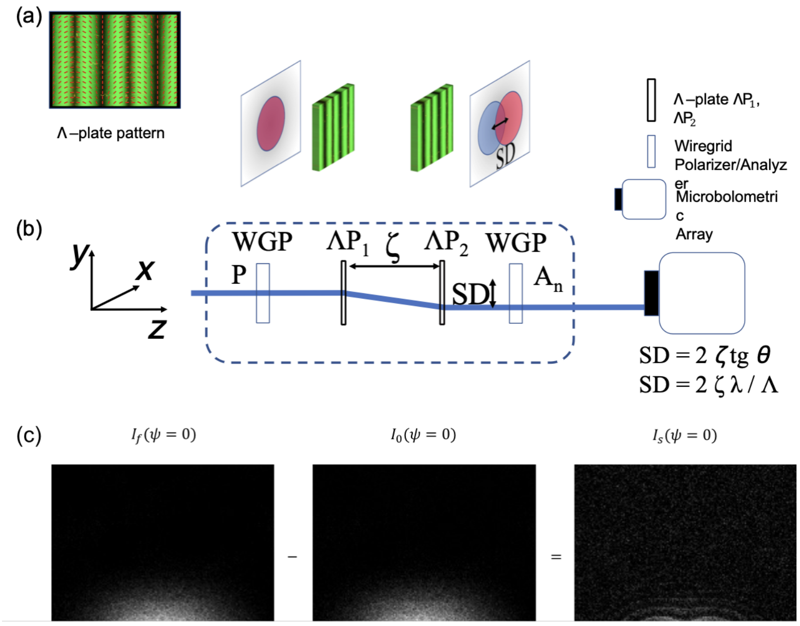

Figure 20.6: Internal optical layout of GPSI included in GEST and simulated shearograms for NDT of a dent deformation over a metal surface enabled by the GPSI included in GEST platform. The inset (a) shows the fast-axis distribution of a Λ -plates superposed to the plate's experimental fringe pattern. The spatial period Λ corresponds to a fast axis rotation of π. (b) A linear polarizer P, positioned between the source and the SVAPs, provides the two replicas of the input wavefront as a superposition of two circularly polarized states with opposite handedness. Two identical Λ-plates with separation ζ introduce a controlled shear between these replicas, and an analyzer A selects the polarization component used for studying their interference. (c) $I_f(\Psi = 0)$ represents the intensity pattern acquired for about a dent over a test surface; $I_0(\Psi = 0)$ represents the intensity pattern acquired for the flat non-deformed surface; $I_s(\Psi = 0)$ represents the derivative of the dent-deformed surface.

Photonics Lab in Naples and represents the most advanced delivery of shearing interferometry technology [8].

The key elements are two identical parallel SVAPS, performing the shearing by imparting different geometric phases on the two circular polarization components of a linearly polarized incident wavefront. (Figure 20.6(b)). These two SVAPs (Λ-plates) are separated by the distance ζ and introduce a controlled lateral Shear Distance (SD) between the replicas. A Λ-plate is a SVAP in which the fast axis rotates in the transverse plane along the horizontal direction, say x, so that the rotation angle Θ of the optic axis increases or decreases linearly with x from 0 to π over a distance Λ, representing the spatial period of the plate axis distribution. As a result, a Λ-plate deflects light of wavelength λ and circular polarization $C_{\pm}$ by an angle $\pm \arctan(\lambda/\Lambda)$ (Figure 20.6(b)).

The scheme of the optical layout for the lateral GPSI is shown in Figure 20.6(a). The shearing distance SD depends on both Λ and the distance ζ between the plates and it can be continuously. The input beam replicas are made to interfere through an output linear analyzer providing a speckle pattern, or speckle interferogram, recorded by the NEC IRV-T0831 camera and then computer stored.

Bibliography

[1] B. Piccirillo, E. Piedipalumbo, and E. Santamato. “Geometric-Phase Waveplates for Free-Form Dark Hollow Beams”. In: *Frontiers in Physics* 8 (2020), p. 94.

[2] P. Darvehi et al. “Increasing the topological diversity of light with modulated Poincaré beams”. In: *Journal of Optics* 23.5 (2021), p. 054002.

[3] B. Piccirillo et al. “Flat polarization-controlled cylindrical lens based on the Pancharatnam–Berry geometric phase”. In: *European Journal of Physics* 38.3 (2017), p. 034007.

[4] J. Li et al. “Study of conductive polymer PEDOT: PSS for infrared thermal detection”. In: *Optical Materials Express* 9.11 (2019), pp. 4474–4482.

[5] D. Jang et al. “Spectral characterization of a microbolometer focal plane array at terahertz frequencies”. In: *IEEE Transactions on Terahertz Science and Technology* 9.2 (2019), pp. 150–154.

[6] B. Piccirillo et al. “The orbital angular momentum of light: genesis and evolution of the concept and of the associated photonic technology”. In: *La Rivista del Nuovo Cimento* 36.11 (2013), pp. 501–554.

[7] B. Piccirillo et al. “Directly measuring mean and variance of infinite-spectrum observables such as the photon orbital angular momentum”. In: *Nature Communications* 6.1 (2015), pp. 1–7.

[8] L.A. Alemán-Castaneda et al. “Shearing interferometry via geometric phase”. In: *Optica* 6.4 (2019), pp. 396–399.

21. Applications of Electron Beams on Target

21.1 Introduction

The BriXSinO project aims at developing at INFN LASA laboratory in Segrate (Milan) a test-facility that would enable addressing the physics and technology challenges posed by the ERL generation, hoping to make in a short-to-midterm scenario a significant advance in the National and INFN contest.

The structure of the facility may be considered divided into 3 main sections: an injector, a SC accelerating stage and the recirculating arc which hosts 2 experimental stations for radiation generation.

Table 21.1 reports the main parameters of the electron beam at the exit of the injector where an experimental area, devoted to fixed target experiments and medical applications.

Table 21.1: Electron beam parameters for fixed target experiments

Energy (MeV)	< 10
Bunch charge (pC)	25 - 50
Repetition rate (MHz for CW operation)	< 92.86
Average Current (mA)	2.5 - 5
Beam power @ dump (kW)	< 50

The electron source is a photocathode DC gun driven by laser pulses train of 22 ps length and with a repetition rate that may be continuously controlled from low values up to 92.86 MHz with the possibility to super-impose a temporal structure with periods of no beam. This source will feed a buncher and a first SC booster to increase the energy up to nearly 10 MeV. The enormous flexibility of the time structure along with the high values of the bunch charge play the relevant role in the proposal we are discussing.

21.2 Low energy electrons in Therapy

Radiotherapy (RT) is an essential contributor for cancer cure, but a substantial proportion of cancers are multi-resistant, especially to RT, defining an unmet clinical need for more effective and better tolerated forms of RT.

Delivering high curative radiation doses to tumors depends on the ability to spare normal tissues from the harmful effects of ionizing radiation. Over the last century, both fractionation and precise volume optimization appeared as the most powerful tools to increase both normal tissue tolerance and the differential effect between normal tissues and tumors. However, based on some pre-clinical rationale FLASH-radiotherapy (FLASH- RT) is strongly emerging in the last years as a third factor able to markedly improve the normal tissue tolerance, called the FLASH effect. This method delivers the radiation dose almost instantaneously in milliseconds (ms) which is thought to induce a massive oxygen consumption and a transient protective hypoxia in normal tissue as opposed to conventional RT delivering the same dose in minutes.

A first patient has been treated in 2019 at the Lausanne University Hospital for a CD30+ T-cell cutaneous lymphoma. A 5.6 MeV electron beam has been used from a prototype linac specifically engineered for accelerating electrons in the FLASH mode.

However, understanding the mechanisms underlying the FLASH effect still requires a period of extensive biological experimentation. This must be able to address all aspects of the phenomenon, from the understanding of the basic effects to the dependence on the peculiarities of the possible beams of particles or radiation that can be used. In this context, the experimental activity must be articulated to exploit all the possibilities offered by dedicated accelerators or in any case available to generate the necessary fields.

The unique opportunity to have up to 1.5×10^{15} electrons in a 100 ms period (the one recognized of interest for FLAH) and the possibility to modulate the intensity to study the dynamic of the involved biological reactions must be regarded as very promising tool and may play a relevant role in this scenario and would encourage radio biological studies at the LASA facility.

21.3 Ultrahigh dose rate X-Ray generation

In the FLASH scenario above discussed, preclinical laboratory research predominantly employs kV X-Rays. In contrast to electron beam, kV X-Ray dose distribution has minimal lateral spread indicative of local energy deposition, although the steep dose gradient with depth would be undesirable for thick medium. For FLASH research, dose deposition and biological damage from X-Rays, as with electrons, stem from relatively uniform low LET events, and avoid the confounding factors of variable LET associated with light and heavy charged particle irradiations. The possibility to enclose a kV irradiation system within a self-shielded cabinet is arguably the most attractive feature, which renders the modality as a staple laboratory instrument for preclinical radiation research [1, 2].

It would be ideal to extend the capabilities of current cabinet X-Ray irradiators to support FLASH irradiation of small animals. To meet such a goal the first order specifications of the cabinet system would provide radiation that (a) penetrates a 20 mm thick medium (equivalent to a mouse thickness) to achieve an adequate uniform depth dose ($\pm 5\%$) over 10 mm, (b) delivers an absolute dose up to 50 Gy at ultrahigh dose rates of 40–200 Gy/s in the irradiated volume, and (c) irradiates a 30 mm $\times$ 15 mm field.

At present, X-Ray sources are based on a design that foresees a stationary anode technology. A recent study showed that commercially available 160 kVp sources with stationary anode can produce X-Rays at the ultrahigh dose rates of 100–150 Gy/s at the tube exit window. The dose rates, however, decreased rapidly below 20 Gy/s within a few millimeter distances from the exit window, which made them unsuitable for a research plan that cover the filed from radiobiology up to small laboratory animals.

It seems a matter of fact that X-Ray sources based on stationary anode technology cannot be suitable for FLASH aimed experimental setup. At the same time the availability of high capacity radiographic and fluoroscopy X-Ray sources and the possibility to use high current electron beams from dedicated or modified or ERL-focused electron linacs has opened the panorama to study sophisticated design based on rotating anode along with the research for new material schemes and geometry.

Monte-Carlo simulations and experimental tests on radiation processing facility using a 10 kW Linac has been carried out in the past years and the most valuable results so far obtained shows that using a high-power electron beam on a suitable composite target may produce X-Rays with an overall conversion efficiency of the order of 15% and an average energy of the order of 1 MeV.

The possibilities offered by a beam as the one delivered from the first stage of the BriXSinO facility suggested to promote a research proposal for the design of an innovative anode for an irradiation facility devoted to FLASH based experiments.

21.4 A proposal for a dedicated experimental area

Taking in consideration all the possibilities offered by the know how that is available within the frame of the BriXSinO collaboration and the experience gained from most of us in the field of the application of particle beams and radiation in the therapy area, we considered specific research in the FLASH-based environment.

The research will be articulated over 3 different steps:

- study of the setup for high charge electron bunches radiobiological applications.
- Study of a suitable geometrical, mechanical and thermal configuration of the new anode design for ultra-high rate bremsstrahlung production.
- Preliminary test using available electron beams on a small scaled prototype.

The deliverable from these activities will consist of detailed studies involving the following arguments:

- new frontiers on electron beams irradiation setup based on medium energy, high current electron beams with a highly modulated temporal profile.
- Detailed thermal and dosimetry scenario for an advanced multi-material anode with high efficiency cooling schemes. The anode will fit both within the scope of a FLASH-based irradiator setup and for radiation processing of food products and sterilization of medical items.
- Experimental tests using suitable and available electron beams.

Picture 21.1 reports a tentative layout for the experimental station.

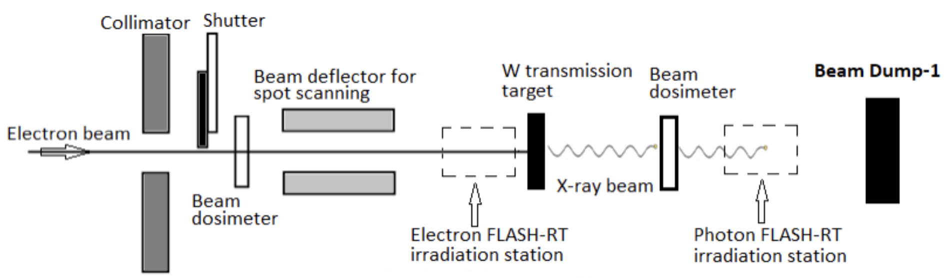

Figure 21.1: Layout of the experimental station at the end of the injector.

A very careful preliminary analysis of the possible solutions about the multi-material anode materials to be investigated and the geometry involved has been so far carried out using simulation tools already available both at LASA and at the Napoli unit and taking as an inspiration some papers available in the literature [3, 4].

Monte Carlo simulations are ongoing to determine the photon spectrum, the flux and the heat load of the target, whose temperature must be lower than critical thresholds. These aspects will be studied via Geant4 MC simulations, which will permit to calculate the generated spectrum and fluence given the characteristics of the BriXSinO electron beam. In addition, the energy deposition in the target material will be scored and input to Ansys software tool for investigating the thermal behavior of the target. We are investigating appropriate target configuration and material.

For the proposal of the activities and as a preliminary contribution to the research, a simplified scheme has been studied to prove the feasibility of the project.

The scheme of the simulation setup for investigating the heat load of the target for bremsstrahlung X-Ray production with <MeV electron beam is shown in Figure 21.2

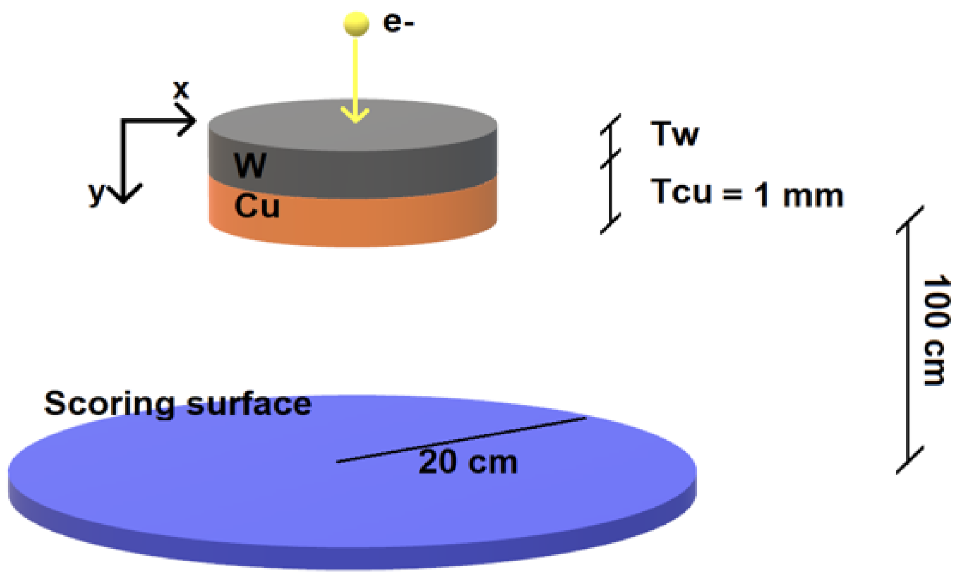

Figure 21.2: Scheme of the simulation setup for heat load studies.

The tungsten target (of variable thickness in the simulation geometry) is thermally backed by a copper layer. The W/Cu discs have a diameter of 1 cm. The W and Cu layers are 1 mm thick.

The scoring surface, for the electrons and X-Ray spectra calculation is circular with a radius of 20 cm and placed at 100 cm from the downer surface of the Cu layer.

A coronal slice of the scored energy deposit map in the W/Cu materials is shown in Figure 21.3.

Figure 21.3: Coronal slice of the energy deposit in the W/Cu materials.

The result of a simulation for MV photons losses due to an electron beam of 10 MeV slowing down in a W target and the scored X-Ray spectra are reported in Figure 21.4.

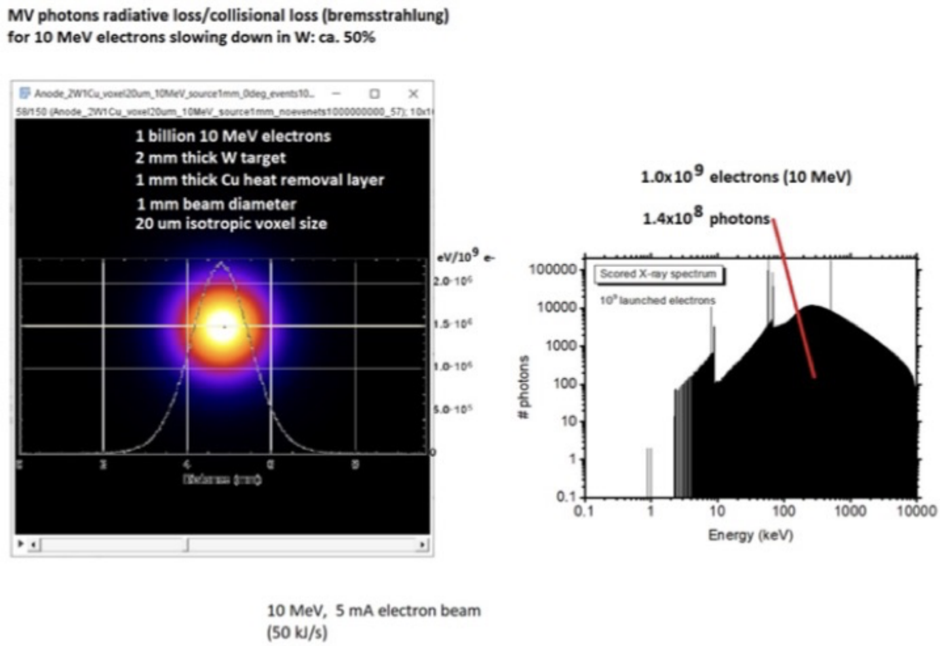

Figure 21.4: Radiative losses vs. collisional losses in a 2 mm thick W target and related X-Ray spectra.

A remarkable result that arises from these very preliminary studies is the one related to the estimated air kerma rate in the geometry described in the first picture. A value up to 38 Gy/s has been obtained over a 40 cm diameter field at a 100 cm distance, as reported in Figure 21.5. Such a result may be considered a suitable starting point to investigate further the possibilities offered by the development of dedicated anode to be coupled with high current medium energy linacs.

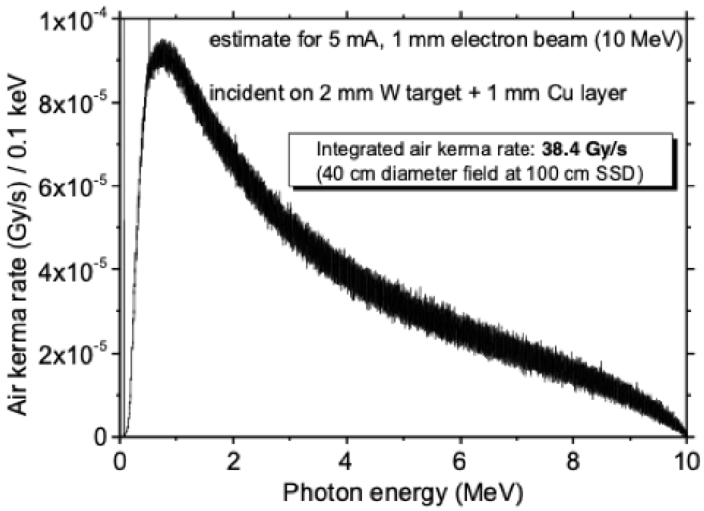

Figure 21.5: Air kerma rate over photon energy.

Bibliography

[1] M. Rezaee, I. Iordachita, and J.W. Wong. "Ultrahigh dose-rate (FLASH) x-ray irradiator for pre-clinical laboratory research". In: *Physics in Medicine & Biology* 66.9 (2021), p. 095006.

[2] S.M. Lee. "Compact anode design with the heat capacity performance in rotating anode x-ray tube for digital radiography". In: *Applied Science and Convergence Technology* 24.5 (2015), pp. 136–141.

[3] V.C. Petwal et al. "Bremsstrahlung Converter for High Power Eb Radiation Processing Facility". In: *Radiat. Phys. Chem* (2007), pp. 767–769.

[4] J. Wang et al. "Thermal limits on MV x-ray production by bremsstrahlung targets in the context of novel linear accelerators". In: *Medical physics* 44.12 (2017), pp. 6610–6620.

22. QUPLAS: fundamental research opportunities at BriXSinO

22.1 (QUantum interferometry and gravitation with Positrons and LASers)

QUPLAS is a line of research (and a series of experiments) dedicated to the study of fundamental laws in Modern Physics - mainly the CPT symmetry and the Weak Equivalence Principle - two cornerstones of Quantum Field Gauge Theory and General Relativity.

This research line makes use of leptonic Antimatter at low energy, namely the anti-electron (positron, e^+) and the e^+e^- bound system, Positronium (Ps). QUPLAS is part of the LEA (Low Energy Antimatter) initiative of the Committee III of Infn and features the groups of Como (Politecnico di Milano and Infn), Milano (Università degli Studi di Milano and Infn), Brescia (Università di Brescia and Infn Pavia). Modena-Reggio (Università di Modena-Reggio and Infn Bologna) and Firenze (Università and Infn Firenze). The current main location of the experiment is the L-NESS Laboratory of the Politecnico di Milano in Como.

22.2 Introduction

QUPLAS was proposed in 2015, with the initial goal of opening the field of Quantum Interferometry with Antimatter [1]. The idea was based upon using the positron beam of the L-NESS Laboratory of the Politecnico in Como, coupled to an interferometer and followed by a high resolution nuclear detector.

The available positron beam at L-NESS comes from a radioactive (positron emitting) ^{22}Na source, followed by a Tungsten foil moderator (W [100], 1 µm thick) and an electrostatic accelerator. The accelerator uses the positrons emitted by the Tungsten surface ($\sim$3 eV) and reaches a maximum positron energy of 20 keV. The intensity of the beam is of about 6×10^4 particles/s maximum in a spot of about 2 mm (FWHM).

The QUPLAS beam quality was studied and improved, in order to reach the coherence requirements needed for interferometry. The specific Talbot-Lau interferometric configuration was selected to the goal [2] and the interferometer itself was built and tested in the following years.

The choice of nuclear emulsion as the detector to be used in the first phase of QUPLAS was dictated by the need of very high spatial resolution in the integration of an interference pattern. In addition, this was a natural choice, given the previous experience of the QUPLAS group at CERN (in the AEGIS experiment) when we demonstrated the capability of resolving antiproton impact points at the micron scale resolution [3]. The same performance was reached in the case of positron detection in QUPLAS [4].

After this preparation period, QUPLAS took its first data taking test [5], whose success paved the way for the first measurements, executed during 2018 with the goal of establishing Quantum Interferometry with positron, a milestone that was called QUPLAS-0. In fact, in a series of interferometric measurements executed during several months in 2018, we were able to demonstrate Quantum Interferometry with positrons [6].

QUPLAS-0 was therefore the first demonstration of Antimatter Quantum Interferometry, with the additional interest that the experiment was executed in "single particle mode". For these reasons, QUPLAS was included among the "Top 10 Breakthrough" experiments of the year in 2019 by the Physics World magazine.

22.3 Towards Positronium Quantum Interferometry

After the QUPLAS-0 milestone, the experimental activity has been divided in two main routes:

- Exploitation of the QUPLAS-0 strategy to perform more quantum mechanical experiments with single positrons (with the ^{22}Na positron source).
- Study of positronium (Ps) interferometry to test the fundamental physical laws, with special attention to the matter-antimatter gravitational symmetry law.

In this text we will concentrate on the second research line, which is the main QUPLAS development, and which would greatly benefit from an increase of statistics – such as the use of a LINAC accelerator (to produce positrons as a secondary beam) instead of the ^{22}Na source.

In fact during the years from 2019 to 2022, new techniques have been developed by our group precisely in the direction of this important step: the realization of a Positronium (Ps) beam suitable for interferometrical studies [7–10].

Positronium a neutral particle with a symmetric matter-antimatter content and therefore it appears particularly suitable for experiments both on CPT and on its gravitational properties (Weak Equivalence Principle - WEP tests). Our strategy to reach this goal is based on three key elements:

1. A LINAC accelerator source, in order to significantly increase the statistics with respect to the maximum that can be reached with ^{22}Na sources (no more than 10^5 positrons/s). For this specific item, the possibility of integrating QUPLAS in the BriXSinO setup could be a critical improvement, of at least three orders of magnitude in statistics, according to very preliminary estimates.
2. The realization of a well collimated Ps beam to be obtained through the intermediate Ps$^-$ ion (the bound $e^-e^+e^-$ state). Once the Ps ion is produced, it will be electrostatically focused, and a subsequent photodetachment laser pulse will turn it into the neutral Ps, still keeping most of the good collimation properties of the previous stage.
3. The interferometric stage, to be performed by exploiting the relation linking the phase of the Ps wave function at the end of the interferometer with the gravitational acceleration $\Delta\phi = k_{\text{eff}} g T^2$ (where T is the propagation time in the interferometer k_{eff} the transferred wave vector). The interferometer will be based on laser gratings to exploit the $n = 2$ and $n = 3$ Ps states and will be a Large Momentum Transfer (LMT) Mach-Zehnder interferometer operating in single photon pulses transitions.

22.4 QUPLAS and BriXSinO: the positron beam

The coherence requirement of an interferometric experiment call for a very demanding positron beam quality and stability, difficult to obtain with the usual technique of radioactive ^{22}Na sources.

For these reasons, the possibility of using the injection stage of BriXSinO as the primary beam for QUPLAS seems very attractive, thanks to its high beam brightness, phase space quality and very high beam stability.

This technique, already suggested for a similar goal, by the GBAR experiment at CERN [11], would allow higher statistics and a superior quality for the primary positron beam, used to produce the Ps ion in the conversion target. The requirements for QUPLAS are of an electron beam energy of about 8 MeV and a high intensity and quality as the one proposed by BriXSinO.

The final positron beam requirements for QUPLAS propose an intensity of 10^{10} positrons/s, submillimeter spot and an angular divergence of less than 100 µrad, based on estimates of the optimal BriXSinO characteristics. A positron beam with these characteristics would be the world's brightest antimatter beam, that would fit well with the positrons generated by LINAC with electrons up to $sim 10$ MeV and intensities on the order of the milliampere.

22.5 Conclusion

The main QUPLAS research line consists in the development of a medium-term strategy to obtain a Ps beam of intensity and quality as to be able to perform Quantum Interferometry and to address fundamental physical topics. The achievement of this ambitious goals will require three important steps to be undertaken, as listed in the above. One of these steps is the use of a LINAC, such as possibly the one in the injector stage of BriXSinO, to significantly increase the quality and the statistics of the beam.

Bibliography

[1] S. Sala et al. “Matter-wave interferometry: towards antimatter interferometers”. In: *Journal of Physics B: Atomic, Molecular and Optical Physics* 48.19 (2015), p. 195002.

[2] S. Sala, M. Giammarchi, and S. Olivares. “Asymmetric Talbot-Lau interferometry for inertial sensing”. In: *Physical Review A* 94.3 (2016), p. 033625.

[3] S. Aghion et al. “A moiré deflectometer for antimatter”. In: *Nature communications* 5.1 (2014), pp. 1–6.

[4] S. Aghion et al. “Detection of low energy antimatter with emulsions”. In: *Journal of instrumentation* 11.06 (2016), P06017.

[5] S. Aghion et al. “Nuclear emulsions for the detection of micrometric-scale fringe patterns: An application to positron interferometry”. In: *Journal of Instrumentation* 13.05 (2018), P05013.

[6] S. Sala et al. “First demonstration of antimatter wave interferometry”. In: *Science advances* 5.5 (2019), eaav7610.

[7] A. Ariga et al. “The QUPLAS experimental apparatus for antimatter interferometry”. In: *Nuclear Instruments and Methods in Physics Research Section A: Accelerators, Spectrometers, Detectors and Associated Equipment* 951 (2020), p. 163019.

[8] L. Anzi et al. “Sensitivity of emulsion detectors to low energy positrons”. In: *Journal of instrumentation* 15.03 (2020), P03027.

[9] G. Vinelli et al. “Real-time monitoring of a positron beam using a microchannel plate in single-particle mode”. In: *Journal of Instrumentation* 15.11 (2020), P11030.

[10] E. Pasino et al. “An interferometric method for particle mass measurements”. In: *Symmetry* 13.7 (2021), p. 1232.

[11] M. Charlton et al. “Positron production using a 9 MeV electron linac for the GBAR experiment”. In: *Nuclear Instruments and Methods in Physics Research Section A: Accelerators, Spectrometers, Detectors and Associated Equipment* 985 (2021), p. 164657.

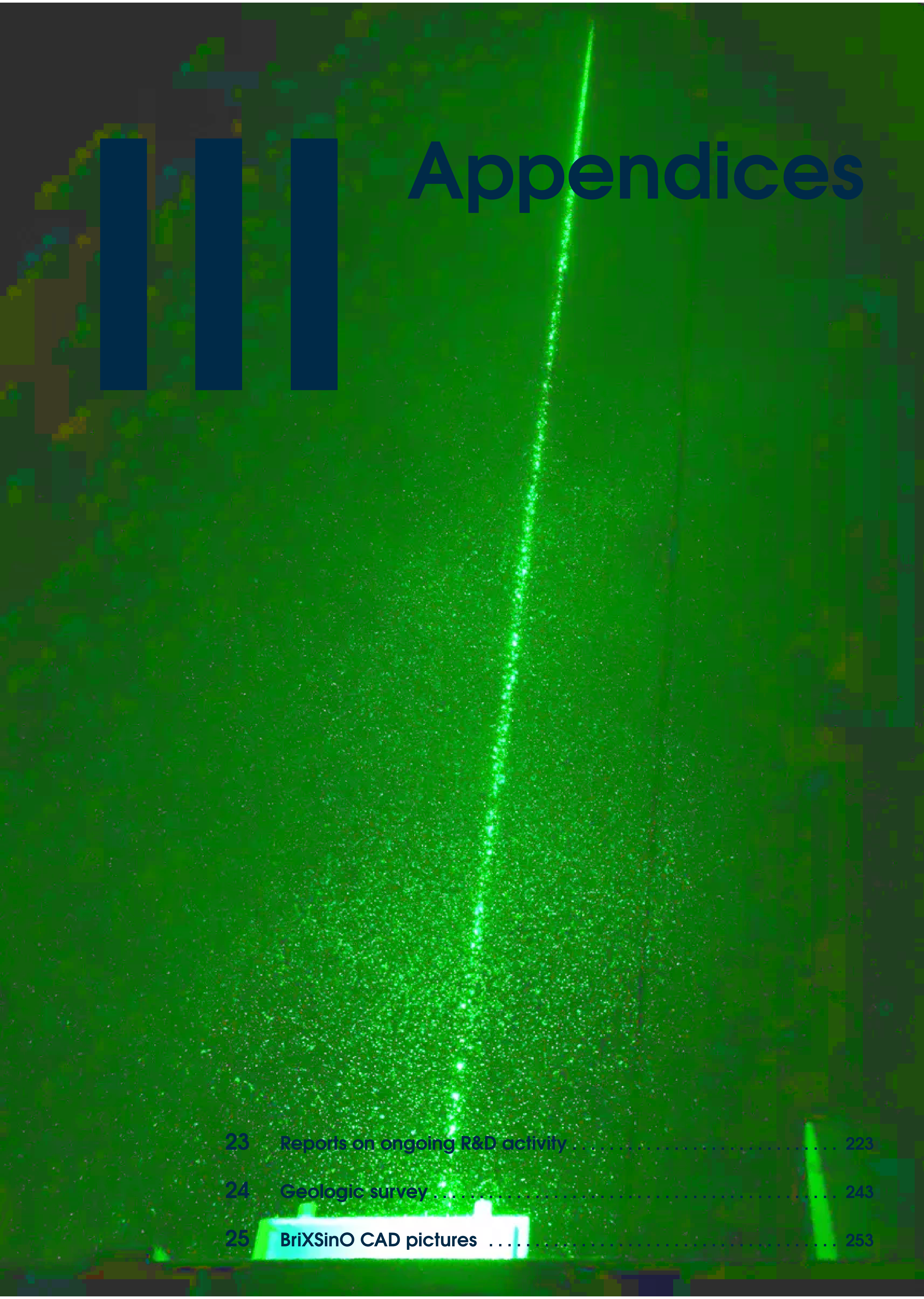

III Appendices

23 Reports on ongoing R&D activity 223

24 Geologic survey 243

25 BriXSinO CAD pictures 253

23. Reports on ongoing R&D activity

23.1 The purpose of the R&D program

The purpose of the R&D program is two-fold and, on the laser system, consists in defining and testing all the components for the BriXSinO project, while on the photocathode side is mainly to prove the possibility of using Cs_2Te photocathode at 100 MHz repetition rate and high average current (mAs scale).

The three main objectives of the R&D program on laser are the high Finesse Fabry-Pérot (FP) optical cavity, the amplification system and the lines for the RF-Guns (harmonic + temporal and spatial shaping + spatial stabilization). The goal of the photocathode activity is the characterization of Cs_2Te photocathodes in term of quantum efficiency (QE) and operative lifetime when used at the high repetition rate of 100 MHz as foreseen for BriXSinO (the so-called photocathode stress test).

These activities will be carried out in parallel in two optical laboratories to save time. The amplifier is not needed to test the structure and the stabilization of the cavity, as no high power operation is required to test the patterns for the temporal and spatial shaping.

23.2 Laser System

23.2.1 State of art and current knowledge

At the moment we have tested the Yb-fiber laser oscillator, the active stabilization of the FP-cavities, and the shift of the foci and the stages of amplification. Furthermore, we are currently testing the line for a DC Gun.

Below are reported the measurements carried out until now and the next steps already planned.

Oscillator

The laser oscillator tested, equal to that will be used in the final system, is a commercial mode-locked Yb-laser model Orange from the Menlo Company. The light is centered at the wavelength of 1035 nm with a spectral width of 13 nm while the repetition frequency of the pulses is about 93 MHz. The oscillator, besides an internal amplification system that guarantees an output of about 10 W, holds several actuators that can be driven from the outside.

The following table summarizes the actuators present in the oscillator, with their dynamics and ranges.

Table 23.1: Expected cryogenic requirements for the BriXSinO 2 K circuits.

	f_{rep}			CEO	
	Mirror motor	**Piezo**	**EOM**	**β-Prisms**	**Pump**
Dynamic range	Large (mm)	Medium (µm)	Low (nm)	Large (100 MHz)	Medium 20 MHz
Bandwidth	1 Hz	10 kHz	1-10 MHz	1 Hz	100 Hz

Mirror motor

In Figure 23.1 is displayed the measured repetition rate of the Menlo oscillator in function of the step position of the mirror motor.

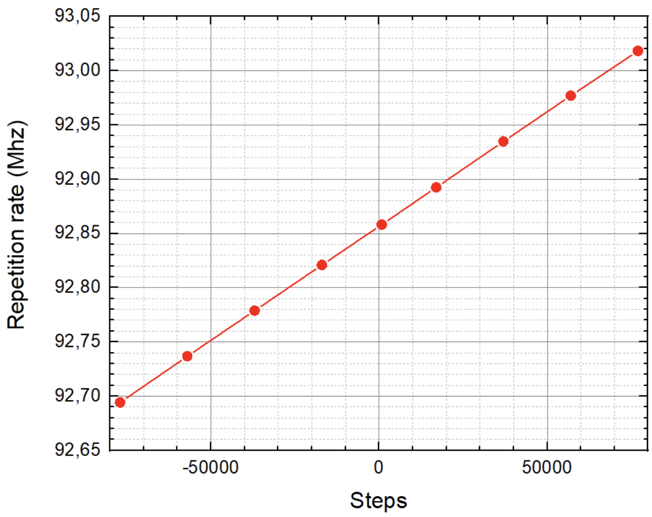

Figure 23.1: Measured repetition rate as function of the motor step position.

The repetition rate range is 92.696 – 93.020 MHz (> 0.3 MHz). The motor step precision is 80 nm which correspond to a variation in the repetition rate of about 2 Hz.

Piezo

The piezo works at voltages ranging from 0-150 V, providing a total round trip length change of about 2.8 µm. The dynamic range, within which the repetition rate can be changed, is > 80 Hz with a bandwidth of 16 kHz. The stabilization of the repetition rate through the piezo was tested in the laboratory. As shown in Figure 23.2, a radio-frequency generator acted as an external reference while a homemade stabilizer drove the voltage on the piezo.

The power spectral density, extrapolated from the stabilizer error signal, is characterized by a peak structure at low frequency. Such contribution on time jitter is completely negligible (16 as). About the high-frequency range, the company Menlo declares an integrated noise up to 1 MHz of about 100 fs. Since the piezo bandwidth is 16 kHz, we can conclude that even with our stabilizer we would have a maximum jitter noise of 100 fs.

The following actuators are employed instead to correct laser CEP and thus improve the coupling with the FP cavities.

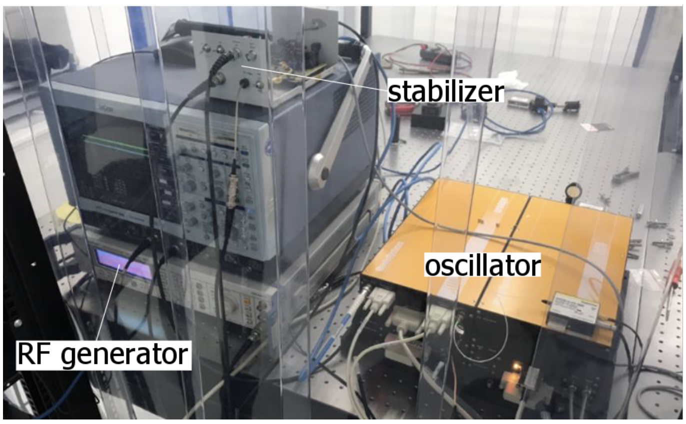

Figure 23.2: Setup of the repetition rate stabilization system.

β-Prisms

A couple of glass prisms with different reflexive indexes provide to change the phase velocity of the laser, keeping the group velocity constant. In this way, the repetition rate does not undergo substantial variation while acting on the CEP. We measure that the maximum variation, for a full CEP range (several times 2π), is minor of 70 Hz for a repetition rate of 92.857 MHz.

Pump current

Operating on the pump current is possible to change the temperature of the active material, driving the CEO of the laser. The Menlo has an input for the controlling of the pump current at ± 10 V. The bandwidth is several hundred Hz while the maximum CEO variation measured, in the ± 10 V range, is about 10 MHz.

Amplification system

As discussed in Chapter 5, the laser system will need two amplification systems: one for the cavities and one for the photocathodes. We currently already have the components for both the pre-amplifier and the high-power amplification (up to 100 W) necessary for the Fabry-Pérot cavities. The scheme of the amplification system for the cavities is displayed in Figure 23.3.

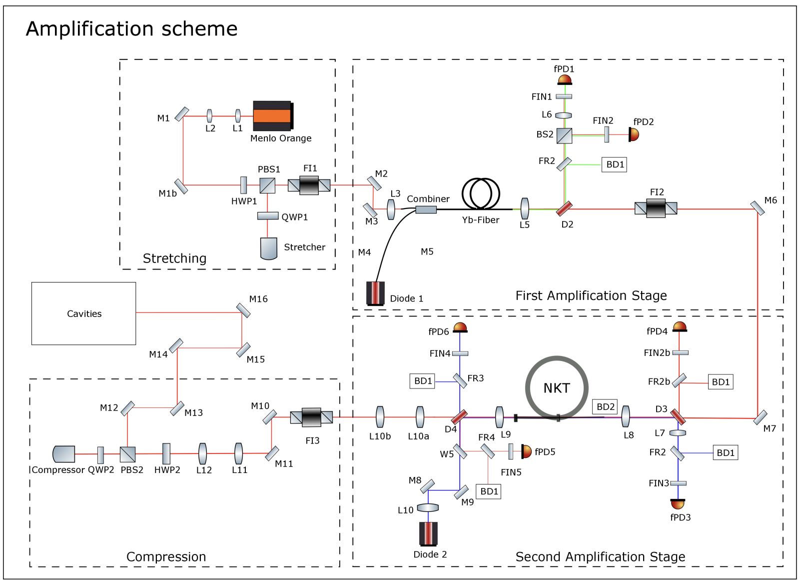

Figure 23.3: Amplification system scheme.

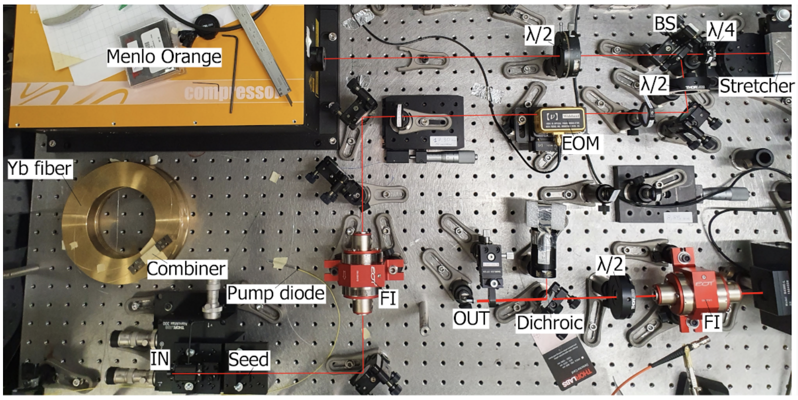

Figure 23.4: Pre-amplifier system assemble in laboratory.

In Figure 23.4 is shown the pre-amplifier system build in our laboratory: the signal is stretched in time and then coupled to a 4-meter long double-cladding Yb-doped fiber (Yb1200-10/125 DC-PM).

At the start and the end of the fiber there are Faraday isolators (FIs) to avoid selflashing phenomena and to protect the oscillator from dangerous reflections. The chosen FIs are the PAVOS from Eltro-Optics Technology, EOT Company. The pre-amplifier is pumped forward by a 976 nm Photontec (M976) laser diode, which supplies a maximum power of 60 W. Both pump light and seed pulses are coupled to the fiber thanks to a Pump Combiner from AFR Company.

In Figure 23.5 are displayed the measurements made on this system

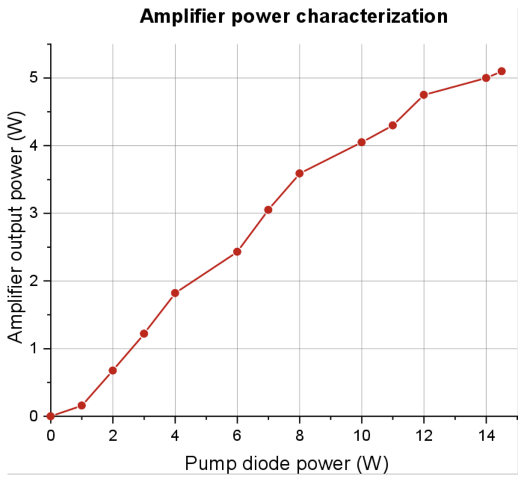

Figure 23.5: Pre-amplifier stage output power plotted versus the pump power.

On the same optical table, we assembled the high-power amplifier which is composed of a commercial fiber module aeroGAIN-BASE-1.2, Yb-doped, from NKT company pumped with 976 nm diode. As displayed in Figure 23.6 left, the module is cooled by continuous water flow supplied by a chiller. The pump laser, which can reach a power of 200 W, is kept at a constant temperature by a homemade dissipation system. Moreover, the diode current is maintained stable thanks to a driver assembled in the laboratory. Right of Figure 23.6 shows the amplifier on the table: the seed comes from the pre-amplifier and it is pumped in the backward configuration.

The NKT company does not guarantee a good functioning of the module for pump powers higher than 100 W even if the fiber can handle it. Currently, the module has been tested up to 60 W of amplified seed and the next step will be to test the cavities with this input power.

Fabry-Pérot cavities

The two FP cavity are stabilized to respect the external laser exploiting the so-called Pound – Drever – Hall (PDH) technique. Each cavity is equipped with its own servo system that read the error signals and control the actuators. Currently in the laboratory we have two cavities which feedback systems are homemade, as shown in Figure 23.7. The cavities have both the geometry and the Finesse of the final system. The nominal Finesse, measured with a novel technique [1], is about 5000, so it can get 200-300 kW with an input signal of about 100 W. Currently the cavity has been tested with the preamplifier only at a maximum input power of 4.5 W, obtaining a cavity power of about 11.5 kW.

We have evaluated the spectral noise of the cavities by means of power spectral density of the error signal.

In Figure 23.8 is displayed the power spectral density of the one cavity and its sigma, for an input signal of about 10 mW. The Finesse of the cavity, measured by amplitude modulation, is 5110 while the relative fluctuations of the transmitted are of the order of 2.2%.

Dual color and focus shift

As discussed in Chapter 6, the peculiarity of the BriXSinO ICS source will be producing a dual-color X-Ray. This task is assigned to two FP cavities oriented differently with respect to the electron beam.

The two cavities have been built in our laboratory with the design scheme presented in Figure 23.9. The switch between the two energies can be made by swapping the interaction laser. The innovative technique proposed for our source involves rotating the curved mirrors by two opposite angles to translate the optical plane vertically [2]. This technique allows us to shift the focus of the cavity by about 120 μm in 50 ms while keeping the cavity stabilized. Figure 23.9 also shows the scheme used to measure the focus displacement: a pellicle beam splitter (BS) is placed near the cavity focus and, with a lens system, the image of it is displayed to a CCD.

Our results are presented in Figure 23.10: on left is shown the image of the focus before and after the move. On the right, the variation of the transmission during the movement.

Currently the limit of the maximum displacement is due solely to the dynamics of the piezo-electric.

The next sections are about the RF-Guns line actually in development at the LASA laboratory.

RF-Gun Line

In Figure 23.11 is shown the process chain for the treatment of impulses before reaching the photocathode. Starting from the IR light at 1035 nm, the 4th harmonic (258.75 nm) is generated to obtain pluses suitable for the photoemission process. Subsequently, the pulses undergo an intensity profile shaping both in temporal and spatial domain. A fundamental point that will be tested in this R&D phase will be the variation of the repetition rate through the Pockels cell. Below are shown

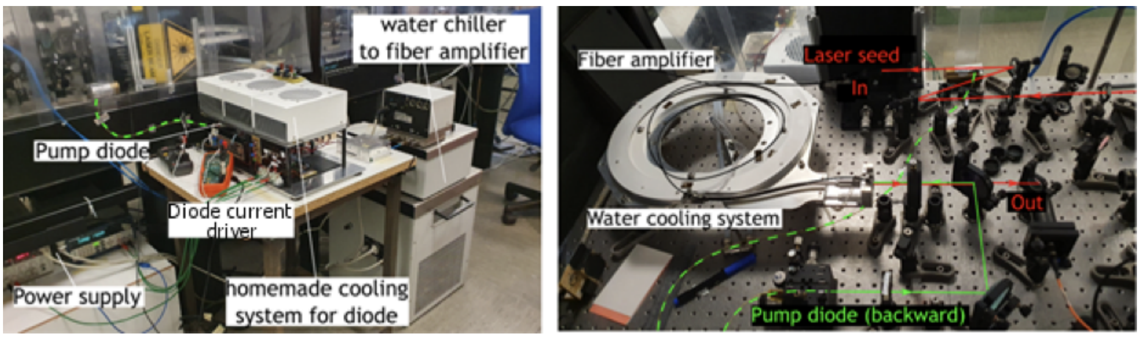

Figure 23.6: High-power amplifier stage with homemade cooled system.

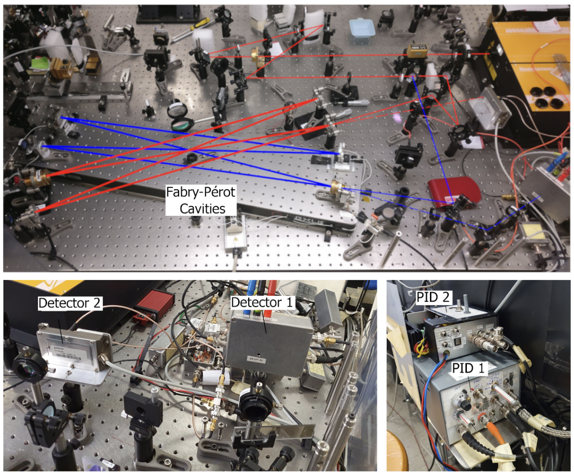

Figure 23.7: Optical cavities with their active stabilization system.

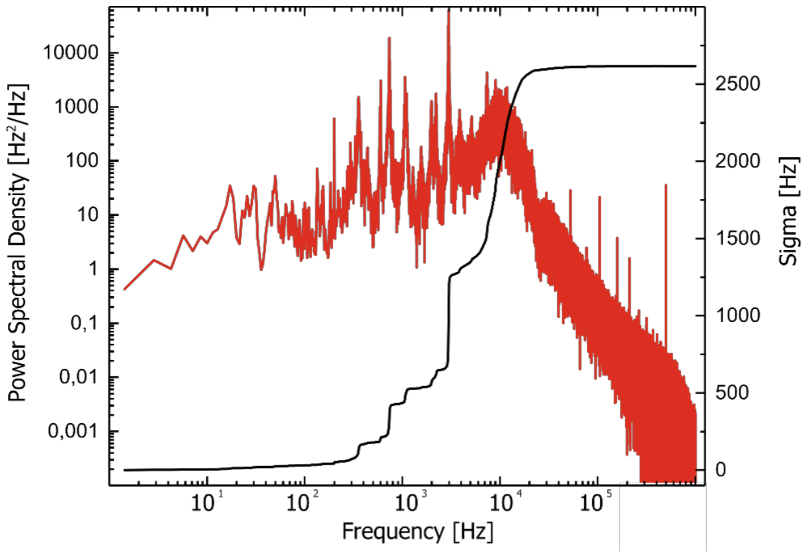

Figure 23.8: Power spectral density of the optical cavity.

the simulations for the generation of 4th harmonic, for the temporal shaping and the proposed technique for the repetition rate.

Current development: Harmonic Generation and Temporal Shaping

At the moment we have realized, at the INFN laboratory of LASA, the line for the generation of the second and fourth harmonic, the temporal shaping system and the cross-correlator for the characterization of the impulses (Figure 23.12).

The 4th harmonic at 258.75 nm is generated via two consecutive second harmonic (SH) stages of the original beam laser wavelength (1035 nm). The first SH generation (SHG, 517.5 nm) is performed by an LBO crystal. The second SHG exploits a BBO crystal. The maximum efficiency for the SHG, assuming a 5 mm long LBO, is to keep the crystal at 180.5 °C temperature. The system is tested up to 10 W of first harmonic (1035 nm) reaching a power of 3.1 W in second harmonic (517.5 nm).

The phase condition for the 4th harmonic, on the other hand, is achievable in the critical phase-matching rotating the axes of the crystal to the incident beam. In this configuration, however, the beam experience a walk-off process. Moreover, due to the different group dispersion of the 2nd and

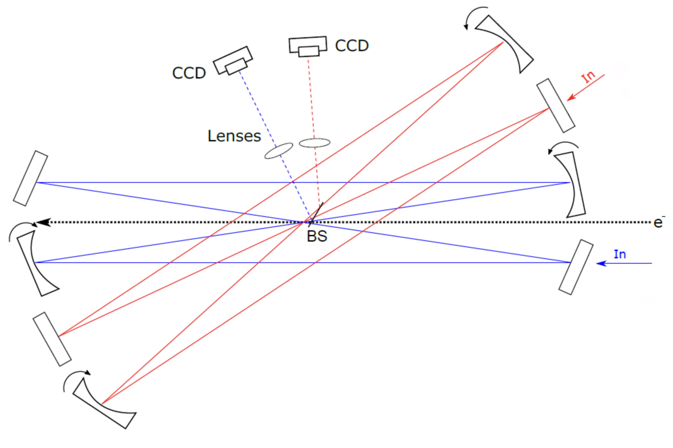

Figure 23.9: Scheme of the imaging system for cavity foci.

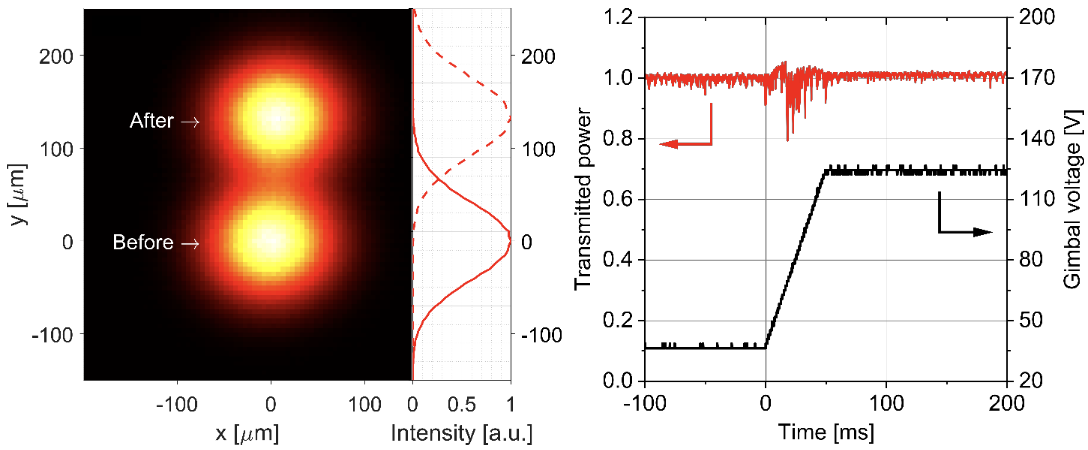

Figure 23.10: Left: imaging of the focus before and after the shift. Right: signal transmitted by the cavity during the shift.

4th harmonic inside the BBO crystal, the latter slips on the first giving rise to a long slope before the peak getting a time length of about 3 ps. In order to minimize the walk-off, we generate the 4th harmonic using three BBO crystal 1.5 mm long, aligned with opposite optical axes so that the effect is compensated.

The shape of the 4th harmonic peak is important for the spatial shaper system present in the photocathode chain. In our tests, starting with 3.1 W in the second harmonic, we have generated about 600 mW of the 4th harmonic. Such power would allow obtaining a current of 1 mA (10 pC) with quantum efficiency (QE) of 1% or 10 mA (100 pC) with QE of 10%. However, losses due to spatial and temporal shaping will reduced the 4th harmonic power to about 400 mW, still enough for the generation of a 5 mA electron beam.

About the temporal shaping, different techniques are reported in the literature used to control the temporal profile of laser pulses, such as passive pulse stacking technique. A temporal shaper based on a set of birefringent crystals looks suitable for our project, since it is simple, flexible, and very stable. In our system we employed a set of three α-BBO to get 8 replicas of the initial pulse. The starting crystal is 13 mm long to obtain a 22 ps pulse duration. The temporal profile of the pulses is acquiring throw a cross-correlation with the first harmonic, as visible in Figure 23.12 left. Such cross-correlation between the 1st and 4th harmonic generates the 3rd harmonic (345 nm). This signal, suitably filtered, guarantees a low background noise which would not be achieved with

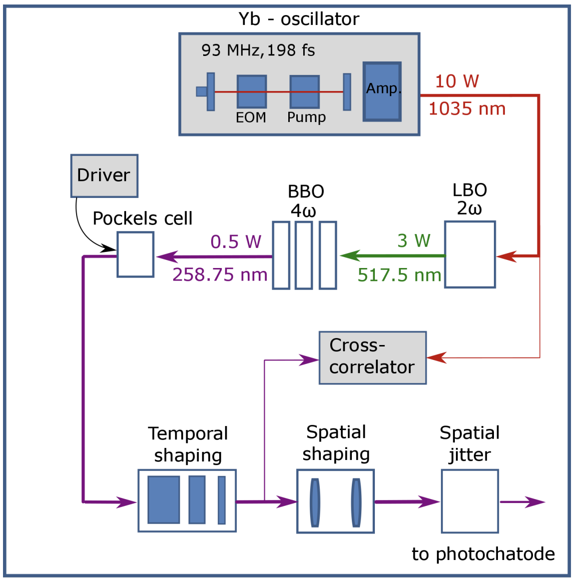

Figure 23.11: Diagram of the optical table for the treatment of the pulses arriving at the photocathode.

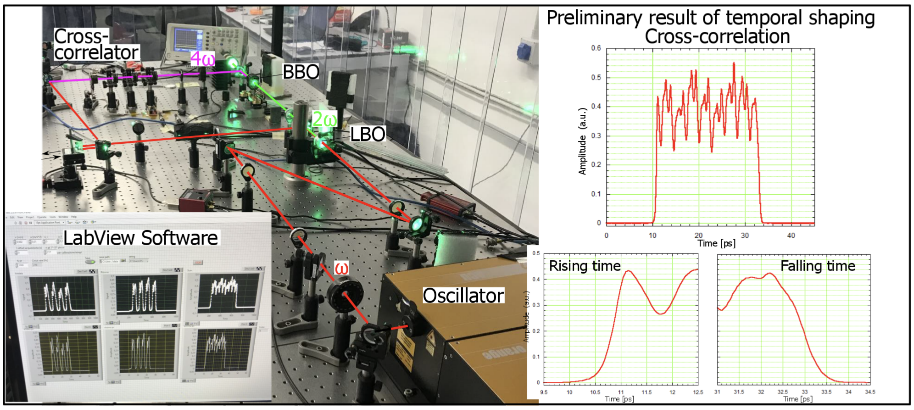

Figure 23.12: Laser line for the test of photocathodes currently realized in the laboratory and preliminary measurements of temporal shaping.

a correlation between the 2nd and the 4th. The results are displayed in Figure 23.12 right. The visible ripple is due to the pulse shape of the fourth harmonic and we are currently working on it. Furthermore, it depends on the time length of the starting pulse. It is important to highlight that in the final setup the starting impulse will have a length of about 1.7 ps instead of the 200 fs of our preliminary measurements, guaranteeing a ripple after spatial shaping of less than 10%.

Power gradual increase

As mentioned above, the line to the photocathode requires a system that controls the repetition rate of the pulses. This task is assigned to a Pockel cell, driven by a modulator.

The Pockels cell is a BBO-Pockels cell from Eksma Optics Company, with a clear aperture diameter of 3.5 mm and a half-wave voltage of 1.5 kV.

The repetition rate, and consequently the power of the beam, will be increased according to two different regimes: the first works up to 1 MHz, the second instead to reach the operating frequency. In the range of kHz, one pulse at a time will be selected from the starting train at 93 MHz, as shown in Figure 23.13 left. With this procedure, with a BBO-Pockels Cell, it is possible to bring the repetition rate up to 1 MHz. To go further it will be necessary to lengthen the wave arriving at the Pockels cell to select more pulse at a time. In this regime, the train of pulses that will arrive at the photocathode will therefore have holes and clusters as displayed in Figure 23.13 right.

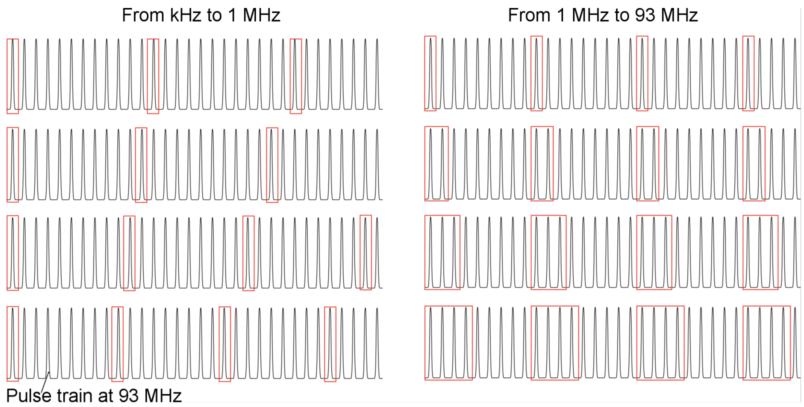

Figure 23.13: Impulse selection representation via BBO-Pockels Cell.

This pulse structure should not affect the energy recovery process. The response time of the latter, calculated as the RF period (10^{-9} s) multiplied to the Q-loaded (10^7), is in the order of milliseconds. This means that the system does not notice the addition of one pulse at a time, as shown in Figure 23.13 right, since it will integrate the average incoming power over longer times.

Layout of the final system

In the following are reported the drawings of the final table with the two Fabry-Pérotcavities, in the UHV chamber.

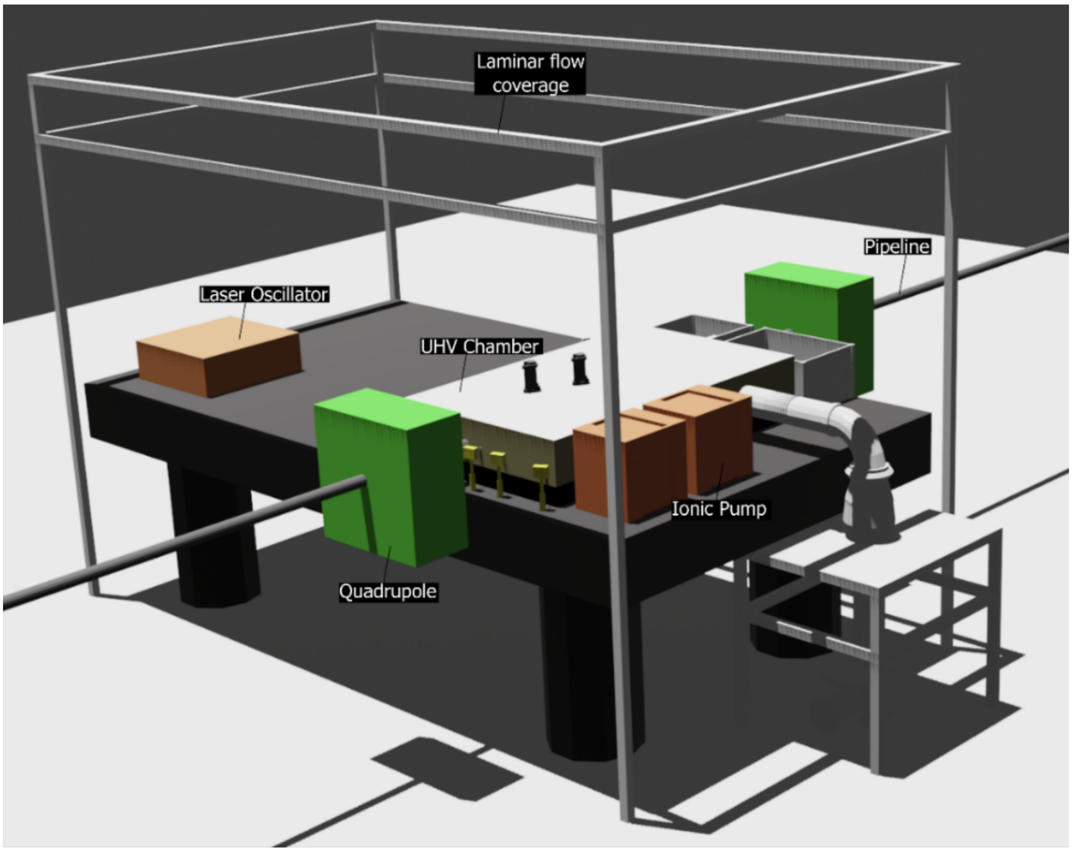

Figure 23.14: 3D model of the optical table in the final configuration, view 1

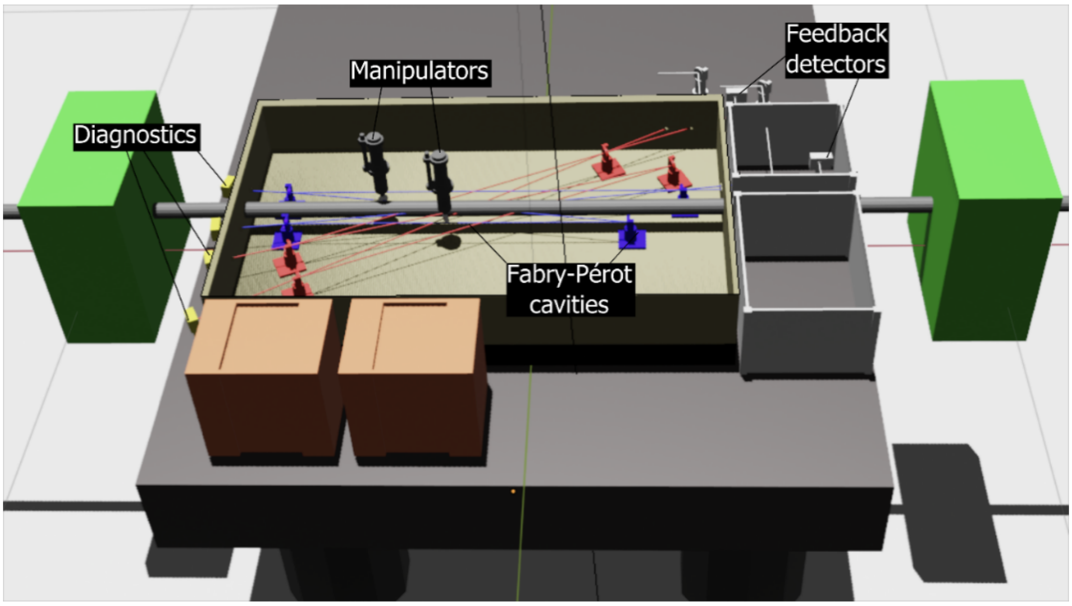

Figure 23.15: 3D model of the optical table in the final configuration, view 2

23.3 The photocathode stress test

The test bench for testing Cs_2Te photocathodes at 100 MHz laser repetition rate is under installation at INFN LASA. This high repetition operation mode is foreseen to be the base operation mode of BriXSinO and qualification of the Cs_2Te photocathodes is a key component. At this regime, it is important to demonstrate the availability of photocathodes able to sustain this impressive rate of emission as well as drive lasers able to operate up to these frequencies and able to provide nWs per pulse with proper transverse and longitudinal shaping to reduce beam emittance. It is in this context that our test bench will operate to stress photocathodes and to show that they can cope with such challenging conditions.

23.3.1 Test bench layout

The main components of the test bench at INFN LASA are:

- a DC gun to sustain 100 kV with a dedicated UHV beamline with diagnostic insertions.
- High voltage and high power components, in particular a 150 kV (at 3 mA) power supply.
- Different photoemissive materials produced in the photocathode laboratory at LASA.
- A high repetition rate laser able to provide different pulse energies as well as different repetition rates.

Figure 23.16 shows a schematic view of the set-up under installation at INFN LASA.

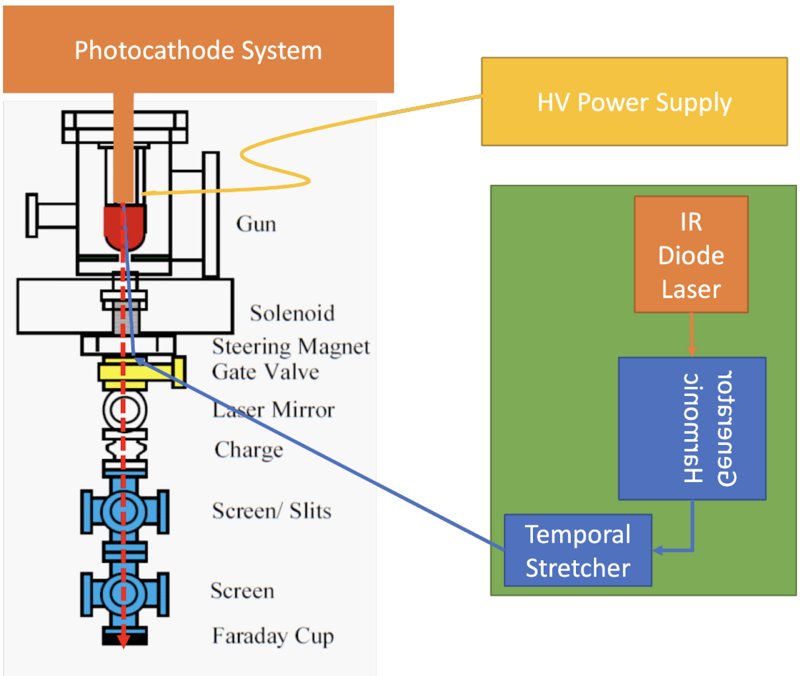

Figure 23.16: Sketch of the test bench at LASA.

In Figure 23.17 it is shown the photo of the laser laboratory after the assembly of some components. On the right the DC Gun, on the bottom the photocathode transfer system. The two optical tables for the laser system and for the Fabry-Pérot optical cavity have been already positioned in their final location.

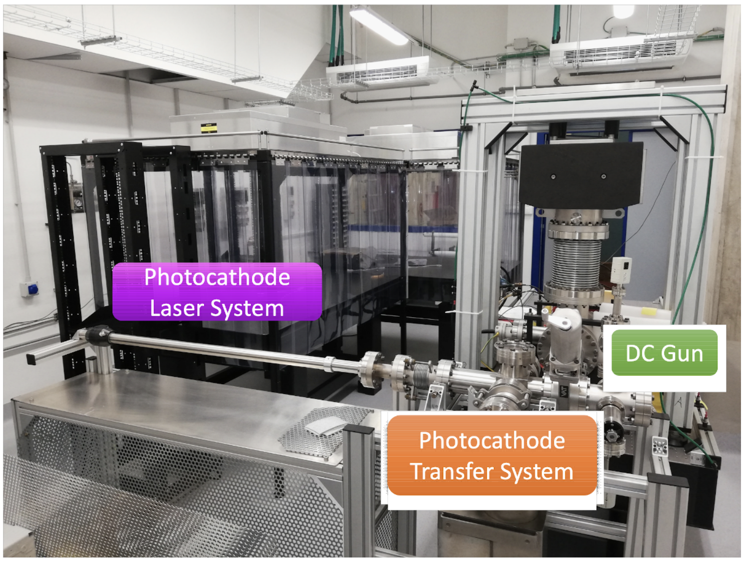

Figure 23.17: Actual status of the laser lab at LASA.

23.3.2 DC Gun Structure

The DC "gun" uses a pseudo parallel–plate geometry with a removable photocathode, followed by a solenoid to focus the electrons, and a short beamline (0.4 m long) with various diagnostics. All the elements stay on top of an optical table.

The DC high voltage extractor itself is based on a CERN design, modified to accommodate our cathode substrates and to increase the accelerating gradient while maintaining fixed the peak surface fields [3]. This has been achieved by designing the curvature around the extraction hole with an elliptical shape. The same concept has been used to design the cathode region. This modification has reduced by 6% the Kilpratick limit thus allowing an increase in the maximum accelerating gradient while keeping constant the gap voltage. The nominal maximum voltage is 100 kV across a gap of 8 mm. The insertion of the photoemissive cathode in the proper position into the DC gun is realized by a manipulator. Finally, a load–lock unit is used to load and un-load cathodes from the storage photocathode suitcase. In Figure 23.18 and 23.19 the HV DC gun and load-lock system and details during the assembly phase are shown.

23.3.3 High voltage elements

A special designed Heinzinger negative HV power supply (model HNCS) will be used to polarize the cathode. It can deliver up to 150 kV @ 3 mA and is completely remotely controlled.

A two meters cable (80 pF capacitance) connects the power supply to the gun. A 1 MΩ resistance in series to the cable is used to limit the accumulate energy. Preliminary tests using higher resistance value (30 MΩ) do not show any significant improvement.

Increasing the applied voltage with respect to the de-sign value of 100 kV would allow to improve the performances of the test bench in term of extractable charge as well as in term of beam dynamic performance.

23.3.4 Photocathodes (LASA photocathode laboratory)

INFN LASA has a long-standing expertise on growing and characterization of different photocathode materials sensitive either to UV (Cs_2Te) or to visible light (KCsSb, NaKCsSb, etc.) [4, 5]. We started in the 90s and since then we delivered about 150 Cs_2Te photocathodes employed both in high brightness guns and in user facilities (FLASH and PITZ at DESY, FAST at FNAL, APEX at

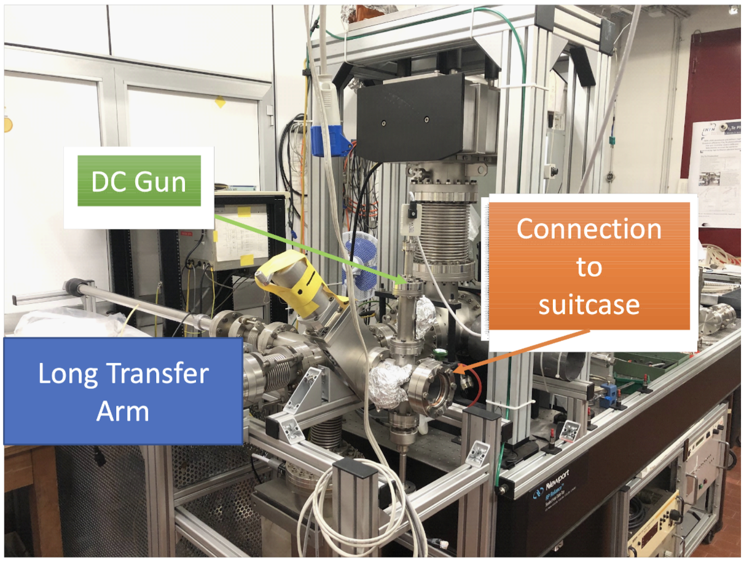

Figure 23.18: Overview of the HV DC gun and of the load-lock system installed in the Laser Laboratory at LASA.

LBNL, LCLS-II injector commissioning phase at SLAC). Moreover, the Mo plug substrate used for the film deposition has become a standard (namely "INFN plug") since it can be used in all different sites. The success of our photocathodes is related mainly to their stability and uniformity in term of Quantum Efficiency (QE), low dark current, long operative lifetime increased from the initial few months to few years [6]. These results have been obtained improving the diagnostics during and after the film deposition, obtaining a better control of all parameters to reach a stable and reproducible recipe and better conditioning of the RF guns. A key issue is the vacuum quality of the system, important during the deposition process but also during the storage and transport of photocathodes to the labs and user facilities (base pressure of the preparation chamber and of the transport box strictly in the 10^{-10} mbar range). These cathodes have been tested in pulsed machine demonstrating a long operative lifetime but also in CW RF gun at 1 MHz (as APEX) showing a lifetime estimated in about 17 days [7]. In Figure 23.20 and 23.21 photos of the LASA production systems and of the transport box are shown.

23.3.5 The Laser System

Details have been already described in previous section dedicated to the R&D on lasers. Figure 23.22 reports the QE working point we will use for the cathode stress test, based on a typical spectral response of a Cs_2Te photocathode.

Based on the laser parameters, the working area of our Stress Test Experiment is shown in Figure 23.23 where two QE values are reported along with the corresponding current or charge emitted from the photocathode.

23.3.6 Beam dynamics

Beam dynamics simulations have been performed using code ASTRA [8] and considering both 50 pC and 100 pC extracted bunch charges for a 50 fs flat-top laser time (rise times = 1 ps). The main goal of this study was to investigate the electron bunch size at 0.4 m and its dependence from the laser spot size at the photocathode.

Preliminary simulation results are reported in Figure 23.24 where a laser spot size at the cathode of 400 µm gives very similar results for both charges of 50 pC and 100 pC.

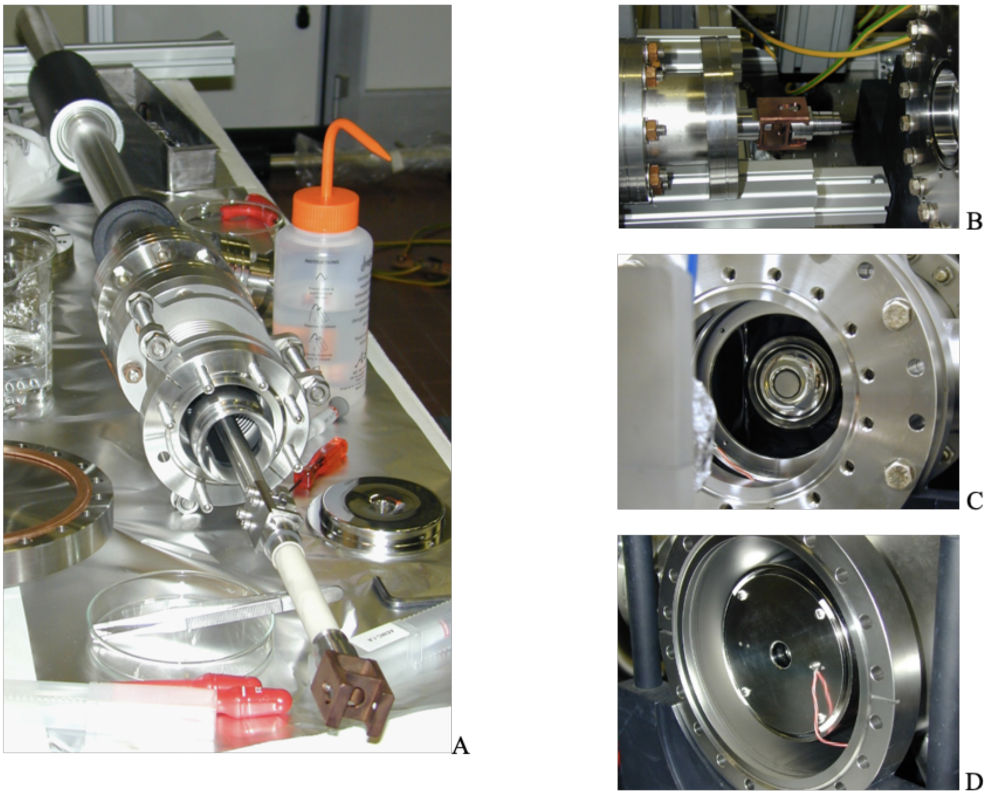

Figure 23.19: Details of the system during its assembly. A: the insulated pincer and the manipulator used to insert the cathode in the gun back-plane; B: detail of the cathode on the pincer; C: the cathode after its insertion in the DC gun; D: the grounded anode.

23.3.7 Expected performances

The charge extraction mechanism in the DC gun, strongly depends on the emission regime determined by the length of the bunch w.r.t. longitudinal dimension of the accelerating gap.

In the long bunch regime, Child-Langmuir law limits the maximum extractable current density (in case of a parallel plane configuration) according to:

$$I_{\text{Child}} = 2.34 \times 10^3 \frac{\Delta V^{\frac{2}{3}}}{d^2} \left[\frac{\text{A}}{\text{cm}^2}\right], \tag{23.1}$$

where ΔV is measured in MV and d in cm. Considering the nominal voltage of 100 kV, the maximum current density achievable is 116 A/cm^2 that can be increase up to 212 A/cm^2 if we reach the 150 kV available from the power supply. Assuming a laser spot size of 0.4 mm, the corresponding current at nominal voltage is 500 mA.

In the short bunch regime, the charge extraction is approximated by a charge sheet. The maximum charge density is, in this case, given by:

$$\sigma = \frac{E}{\varepsilon_0}, \tag{23.2}$$

where E is the electric field at the cathode and ε_0 is the vacuum dielectric constant. Assuming a gap distance of 8 mm, at the nominal voltage the corresponding electric field is 12.5 MV/m and the corresponding charge density is 11 nC/cm^2. For the same spot size as before, the charge per bunch extractable is 56 pC that, at 100 MHz, corresponds to an average current of 5.6 mA.

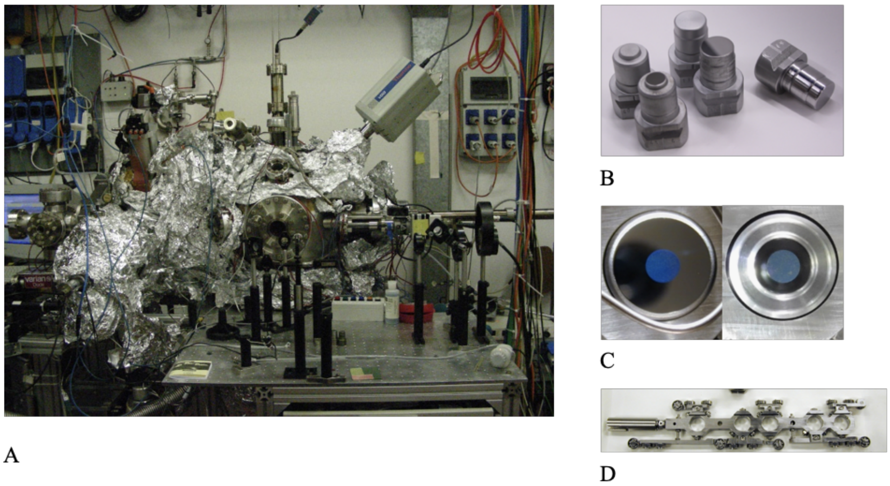

Figure 23.20: The LASA production systems. A: the preparation chamber and the optical line used during the deposition process; B: the INFN Mo plugs; C: Cs_2Te films; D: the cathode holder (carrier).

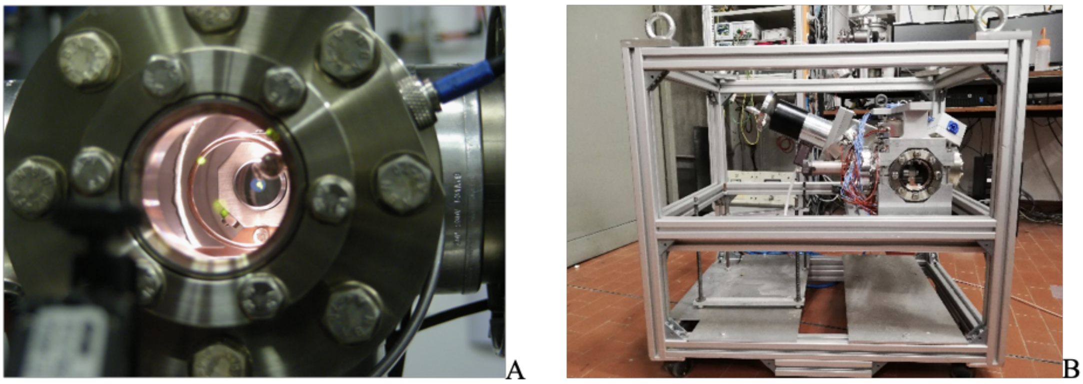

Figure 23.21: The LASA transport box (suitcase), used for the diagnostic and for the transport of the photocathodes to the different facilities. A: Cs_2Te photocathode in the transport box (UV viewport); B: the transport box (suitcase) ready for the delivery.

In case of our DC gun and pulse length, we are in the transition region between the two regimes. Already a 20 ps of the laser pulse translates into 6 mm spatial laser pulse length that is clearly comparable to the voltage gap of our DC gun. Study this transition region is a further opportunity given by the operation of the DC gun.

23.4 First results with HOMEN

A first set of preliminary simulations of a single 7 cells cavity and beam has been performed with HOMEN. In the following we present a preview of the results. We have simulated the interaction of the fundamental mode TM_{010} with a series of consecutive bunches injected on accelerating crest. In Figure 23.25 the result of the passage on the cavity axis of 100 bunches spaced in time about 10.8 ns each can be observed.

The stored energy in the cavity fundamental mode decreases of few hundreds of nJ during the bunch acceleration as a result of the energy exchange (the 3$^{\text{rd}}$ term in Equation (2.4)), note that $\tau_{\text{cav}_i} \approx 5$ ns. Then, the energy is restored by the power provided by the RF source that has to be

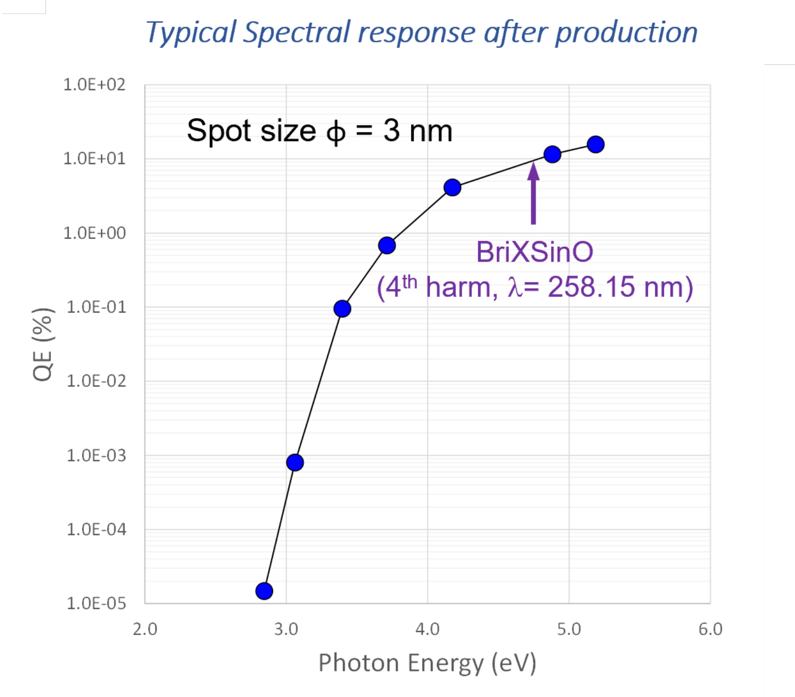

Figure 23.22: Typical spectral response of a Cs_2Te photocathode.

carefully tuned considering the power dissipation on the cavity walls (in this preliminary simulation campaign) and energy exchanged with the bunches. The stability of the stored energy in the cavities involves the stability of the energy of the electron bunches at the exit is shown in the bottom frame of Figure 23.25 with the red line.

After testing the behavior of the system with the fundamental mode we considered the first strongly resonant monopole HOM in the cavity (ν = 2437.268 MHz), represented by the second spike in Figure 2.13.

The simulations reported below were performed in "pure wake" mode, this means that the fundamental mode was turned off in order to observe only the phenomenon of excitation of the HOM and the effect this has on the energy of the bunch at the output of the cavity.

To properly evaluate the effect of HOMs, it is necessary to provide an estimation of the value of the loss factor parameter k_{loss} introduced in the Section 2.2.

The first available estimates indicate that the integral value of this parameter considering resonant modes relative to the longitudinal impedance up to the frequency of 30 GHz is about 3.5 V/pC for one module (as described in the previous section). For the simulated frequency, i.e. ν = 2437.268 MHz, first estimates indicate a value of the loss factor around 0.9 V/pC. In order to have a first estimation of the expected effects that would take place in a single cavity, we chose to simulate the resonant mode employing 3 different values of the k_{loss}, n: 0.5, 0.9 and 2.0 V/pC and further the very high value of 4.0 V/pC to over-estimate the integral effect of the loss factor The values of 0.5 and 2.0 can be considered as example values associated to other modes still under investigation.

In Figure 23.26 we show the energy accumulated in the HOM over the time. The runs were performed by simulating the passage of 3 million consecutive bunches.

The energy gain and its dissipation reach an equilibrium after the characteristic time $t_{ch,n} = Q_n/\nu_n$, in our specific case $t_{ch,n} \simeq 13.045$ ms. The bottom frame in Figure 23.26 shows the bunch energy distribution at the cavity exit. Its characteristic shape is due to a small oscillation of the energy in the cavity caused by the injection phase instability and its amplitude is $\propto \sqrt{U_n}$ (a closer

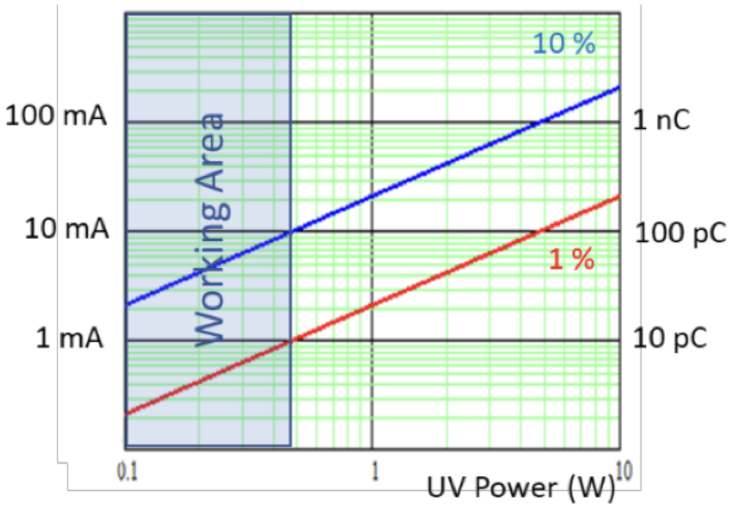

Figure 23.23: Expected performance for the Photocathode Stress Test with respect to different QEs values.

look to this effect is shown in Figure 23.27).

In conclusion, these entirely preliminary estimates lead us to conclude that the first resonant mode (green in Figure 23.26) leads to an accumulation of ~400 μJ in the cavity, resulting in an energy fluctuation at the cavity exit of a few tens of keV. We expect that a variation of this magnitude will not introduce major effects on the quality of the radiation produced by either

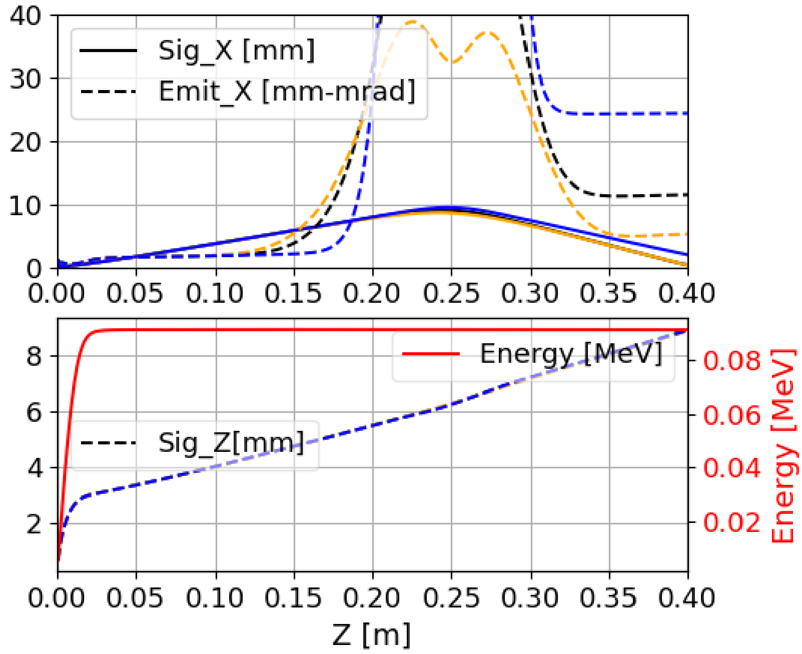

Figure 23.24: The upper plot shows beam emittances (dashed lines) and envelops (solid lines) for three different solenoid maps ($B_{z\,\text{peak}} \approx 300$ G). In yellow the longer fringing fields, in black short fringing field, in blue a quasi hard edges fringing field. The lower plot shows the energy gain (in red) and the bunch lengthening (dashed blue) common values for the three maps cases.

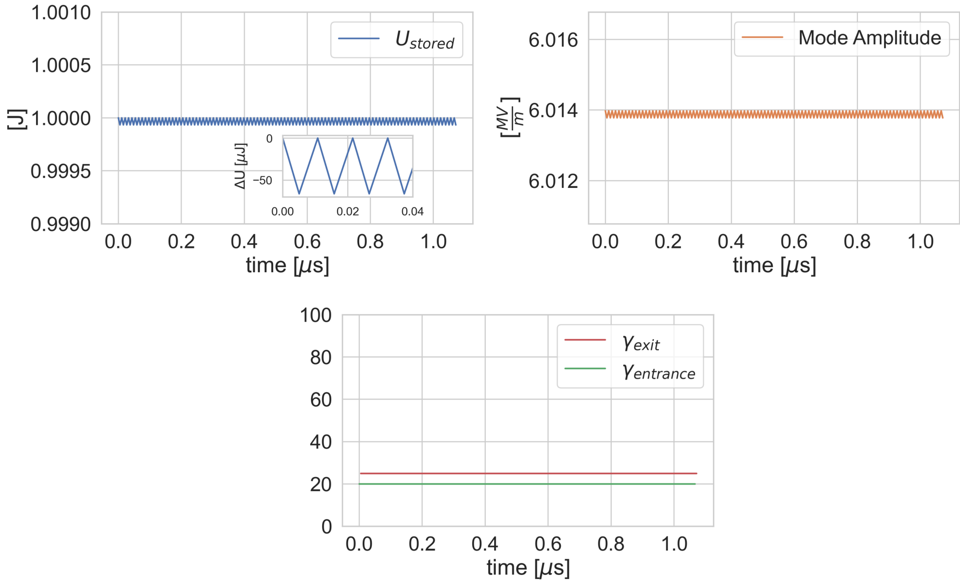

Figure 23.25: Behavior of the cavity and beam system considering the accelerating mode only, in the case of 100 bunches. Top graphs: the stored energy variation and mode amplitude in the cavity, in the frame a zoom of the energy losses due to the first 4 bunches. Bottom graph: trend of the beam energy at the entrance and at the exit of the module.

BriXSinO light sources.

Future estimates will take into account the coupling of 3 appropriately spaced consecutive modules and the dynamics of counter-propagating beams in cavities considering the complex BriXSinO arc beam dynamics.

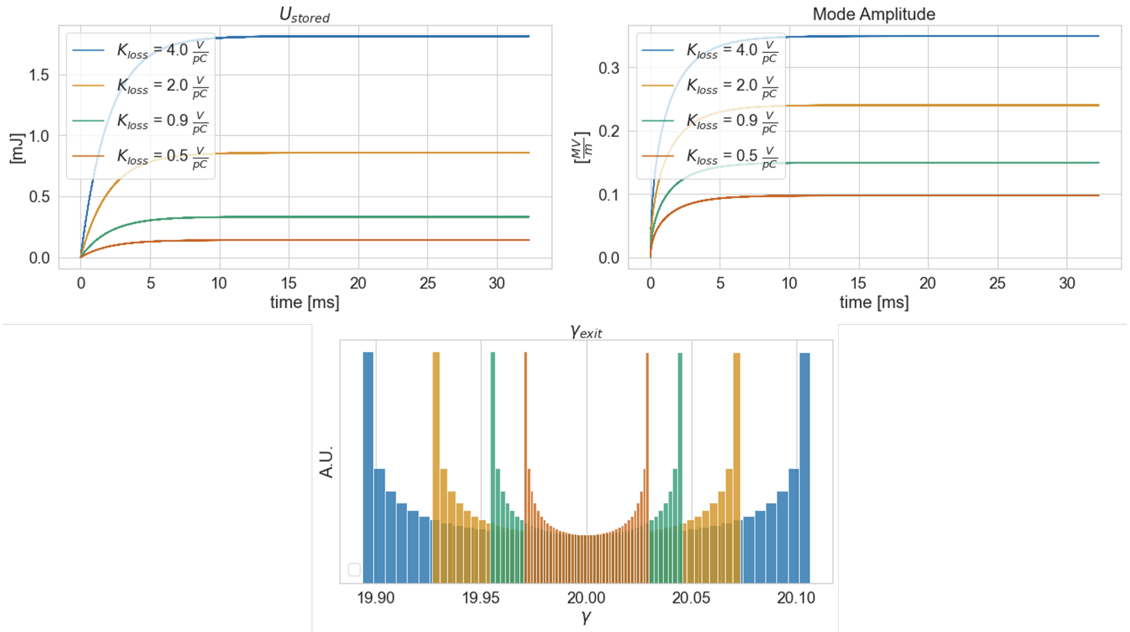

Figure 23.26: Behavior of the cavity and beam system considering the first resonant monopole HOM in "pure wake" mode. Top graphs: the stored energy variation and mode amplitude in the cavity. Bottom graph: the bunch energy distribution at the cavity output.

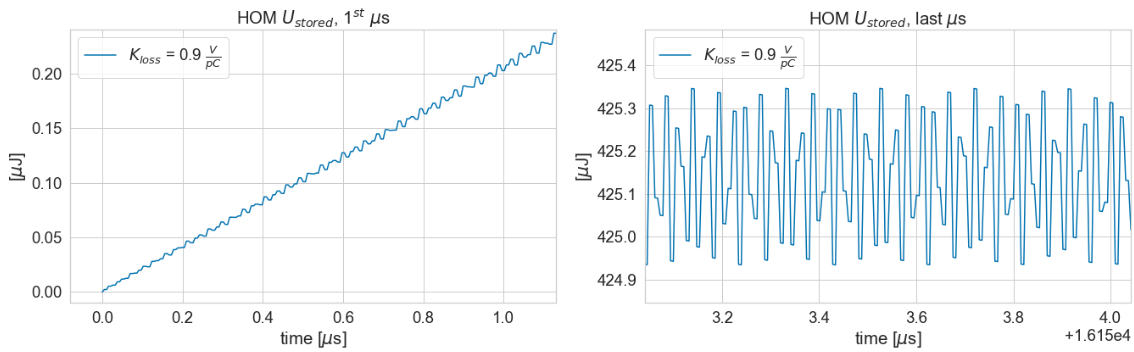

Figure 23.27: Oscillation of the energy stored in the studied HOM during a 1.5 million bunches simulation (16 ms long). Left: initial gain of the stored energy in the mode during the first µs. Right: energy fluctuation around a stable average value after the t_{ch}.

Bibliography

[1] G. Galzerano et al. "Accurate Measurement of Optical Resonator Finesse". In: *IEEE Transactions on Instrumentation and Measurement* 69.11 (2020), pp. 9119–9123.

[2] E. Suerra et al. "A new method for spatial mode shifting of stabilized optical cavities for the generation of dual-color X-Ray". In: *Nuclear Instruments and Methods in Physics Research Section A: Accelerators, Spectrometers, Detectors and Associated Equipment* 1019 (2021), p. 165852.

[3] G. Travish et al. "A High Voltage Extractor with Photocathodes". In: *Proceedings of the 6th European Particle Accelerator Conference (EPAC'98) D*. Vol. 5. 1998, p. 1133.

[4] C. Pagani et al. "LASA Cs_2Te Photocathodes: The Electron Source for XFELs". In: *Congress of the Department of Physics*. Springer. 2017, pp. 281–292.

[5] L. Monaco et al. "Growing and Characterization of Cs_2Te Photocatodes with Different Thicknesses at INFN LASA". In: *Proc. FEL'19* (Hamburg, Germany). International Free Electron Laser Conference 39. JACoW Publishing, Geneva, Switzerland, 2019, pp. 297–300. DOI: `10.18429/JACoW-FEL2019-WEA04`.

[6] S. Schreiber et al. "Update on the Lifetime of Cs_2Te Photocathodes Operated at FLASH". In: *Proc. of International Free Electron Laser Conference (FEL'17), Santa Fe, NM, USA, August 20-25, 2017* (Santa Fe, NM, USA). International Free Electron Laser Conference 38. JACoW, 2018, pp. 415–418. DOI: `https://doi.org/10.18429/JACoW-FEL2017-WEP003`.

[7] D. Filippetto, H. Qian, and F. Sannibale. "Cesium telluride cathodes for the next generation of high-average current high-brightness photoinjectors". In: *Applied Physics Letters* 107.4 (2015), p. 042104.

[8] K. Flöttmann et al. *ASTRA: A space charge tracking algorithm*. 2011.

24. Geologic survey

This appendix shows the results of the geoseismic surveys that have been commissioned to a specialized company. The report is in Italian and here we summarize the most relevant results.

Several different tests have been carried out:

- Coring.
- SPT (Standard Penetration Test) in the hole.
- DPSH (Dynamic Probing Super Heavy).
- Seismic spreading.

The most relevant results described in the report are the following:

1. The depth of the aquifer stands at -9.92 m from ground level (measurement performed on 06/05/2021 in the micropiezometer installed in the S1 survey hole). This depth value is very comforting as it is much greater than the depth of the excavations to be carried out for the construction of the BriXSinO bunker.
2. The stratigraphy shows a first layer of fill up to an average depth of -1.50 m from the surface. Below there is a loamy-sandy horizon not very consistent followed by sandy-gravelly and gravelly-sandy horizons from medium to well thickened.
3. The seismic survey performed made it possible to define the category of subsoil which was found to be of type "C" considering the speed V_{seq} = 323 m/s calculated in the interval from the surface at -30 m.
4. From the radar survey it can be assumed that the spurs of the foundations extend up to about 1.50 m from the walls of the existing building; in fact they were identified in the longitudinal profile (Profile 001) executed parallel to the building at a distance of about 1.00 m from it, while they were not recognized in the longitudinal profile (Profile 002) executed parallel to the building at a distance of about 2.00 m. The profiles performed (Profile 001, 004, 005, 006) show how the maximum depth reached by the spurs of the foundations is about -4.50 m from the ground floor. Also these date are of great relevance for the design of the bunker.

R 4045

ISTITUTO NAZIONALE DI FISICA NUCLEARE

- Via G. Celoria, 16 – 20133 Milano -

Report indagini eseguite

c/o

-LABORATORIO L.A.S.A.-

Via F.lli Cervi, 201 – Segrate (MI)

Settembre 2021

GEOINVEST s.r.l.

Sommario

1 INDAGINI GEOGNOSTICHE E SISMICHE ESEGUITE 3
1.1 Sondaggio a carotaggio continuo 5
1.2 Prove SPT in foro (Standard Penetration Test) 6
1.3 Prove penetrometriche dinamiche 9
2 MODELLO GEOLOGICO DEL SITO 16
3 MODELLO GEOTECNICO DEL SITO 17
4 ANALISI DEL RISCHIO SISMICO 19
4.1 RIFERIMENTI NORMATIVI NAZIONALI 19
4.2 ASPETTI NORMATIVI E METODOLOGICI REGIONALI 21
5 STRATEGIA DI PROGETTAZIONE 23
6 PERICOLOSITÀ SISMICA DI BASE DEL TERRITORIO COMUNALE 24
7 CARATTERIZZAZIONE SISMICA DEL SITO 25
8 MISURA DELLA Vs30 TRAMITE PROVE SISMICHE 27
8.1 Prova Re.Mi. 27
8.2 Prova MASW 28
8.3 Elaborazione dati 29
8.4 Analisi dei risultati 30
9 RISPOSTA SISMICA LOCALE 31

via della Conciliazione, 45/A - 29122 Piacenza Italia
telefono 0523 593622 - fax 0523 593640
www.geoinvest.it - geoinvest@geoinvest.it
PEC: geoinvest@legalmail.it

GEOINVEST s.r.l.

1 INDAGINI GEOGNOSTICHE E SISMICHE ESEGUITE

La caratterizzazione geologica e geotecnica dell'area è stata realizzata tramite prove in sito di tipo diretto (Sondaggio a carotaggio continuo, prove SPT in foro e prove penetrometriche dinamiche DPSH) e di tipo indiretto (prova MASW/Re.Mi).

Le indagini condotte sono state le seguenti:

- Esecuzione di n. 1 sondaggio a carotaggio continuo spinto fino a -15m da p.c. per la valutazione delle condizioni litostratigrafiche dei terreni superficiali con istallazione micropiezometro provvisorio per la misura puntuale del livello della falda superficiale (S1-Pz1);
- Esecuzione di n. 2 prove SPT in foro eseguite durante l'avanzamento della perforazione a -9.00 e -12.00 m da p.c.;
- Esecuzione di n. 6 prove penetrometriche dinamiche DPSH (P1-P6) spinte fino a rifiuto all'avanzamento, raggiunto alla profondità massima di -6.60m da p.c. in corrispondenza delle prove P1 eP2, per la valutazione delle caratteristiche geotecniche dei terreni superficiali;
- Esecuzione n. 1 stendimento sismico con acquisizione prove tipo Masw/Re.Mi (M1-R1) per la definizione della categoria sismica del sottosuolo in funzione della velocità Vs30.

Di seguito si riportano le indagini eseguite ubicate su foto aerea.

Fig. 1 – Ubicazione indagini geognostiche e sismiche eseguite

1.1 Sondaggio a carotaggio continuo

Per la valutazione della stratigrafia dell'area di indagine è stato realizzato nr.1 sondaggio meccanico spinto fino a 15m di profondità. Il sondaggio è stato eseguito a rotazione con carotaggio continuo dei terreni attraversati e ha le seguenti coordinate nel sistema di riferimento UTM WGS84 (zona 32N)

Longitudine Est: X = 520491.4m

Latitudine Nord: Y = 5039011.3m

Quota s.l.m: 125.00m

Per l'esecuzione del sondaggio è stata utilizzata una perforatrice idraulica con mast telescopico, corsa di 4.5m, testa traslabile e doppia morsa montata su un trattore gommato a motore diesel SAME ANTARES.

La perforazione è stata realizzata mediante l'impiego di carotiere semplice con diametro pari a 101 mm con corona con inserti in Widia. Il foro è stato rivestito lungo tutto il suo sviluppo con tubi di 127 mm diametro per evitare il franamento delle pareti.

Le carote prelevate sono state alloggiate in nr. 4 cassette catalogatrici in PVC, ciascuna delle quali munita di cinque scomparti da 1.00 metro, in modo da accogliere 5.00 metri di sondaggio. Ciascuna cassetta è stata catalogata, documentata e fotografata e posta nel luogo prescritto a disposizione della Committenza.

Le operazioni di sondaggio si sono svolte nella giornata del 6 Maggio 2021. Al termine dei lavori nel foro è stato installato un micropiezometro provvisorio per la misura puntuale del livello della falda superficiale.

Nel foro di sondaggio sono state eseguite nr. 2 Prove SPT con campionatore Raymond alle seguenti profondità: -9.00m, -12.00m.

1.2 Prove SPT in foro (Standard Penetration Test)

Le prove SPT in foro (come prescrive la procedura ISSMFE, 1988) sono state realizzate con un dispositivo di percussione costituito da:

- Testa di battuta in acciaio avvitata alle aste;
- Maglio d'acciaio di 63.5Kg;
- Dispositivo di guida e sganciamento automatico del maglio in grado di assicurare una corsa a caduta libera di 0.76m

La prova d'infissione, previa pulizia del foro dai detriti di perforazione, consiste nel far penetrare un campionatore Raymond dotato di punta conica con dimensione standardizzate, per tre tratti successivi di 15cm registrando ogni volta il n. colpi necessario (N1, N2, N3).

Con il primo tratto, detto di avviamento, s'intende superare la zona di terreno rimaneggiata in fase di perforazione. In caso di terreno molto compatto o in presenza di inclusi lapidei, se con N1=50 colpi l'avviamento è <15cm, questo numero di colpi viene assunto come valore per l'infissione preliminare.

Se il tratto d'avviamento è stato superato, si prosegue la prova conteggiando separatamente i numeri di colpi N2 e N3 per i tratti di avanzamento da 15 a 30cm e da 30 a 45cm e la prova si ritiene conclusa. Nel caso la somma di N2 e N3 raggiunga il limite complessivo di 100 colpi, si sospende la prova annotando l'avanzamento ottenuto.

Il parametro caratteristico della prova SPT é: N2 + N3 espresso in n.colpi x 30cm di avanzamento.

Nella tabella seguente sono riportate le quote e i risultati ottenuti nelle singole prove realizzate:

Sondaggio	Profondità (m dal p.c.)	Risultato (N1, N2, N3)	Nspt (n. colpi x 30cm)
S1	-9.00	39-50 (12cm)	R
	-12.00	28-33-38	71

Segue monografia sondaggio meccanico a carotaggio continuo dei terreni eseguito (S1-Pz1).

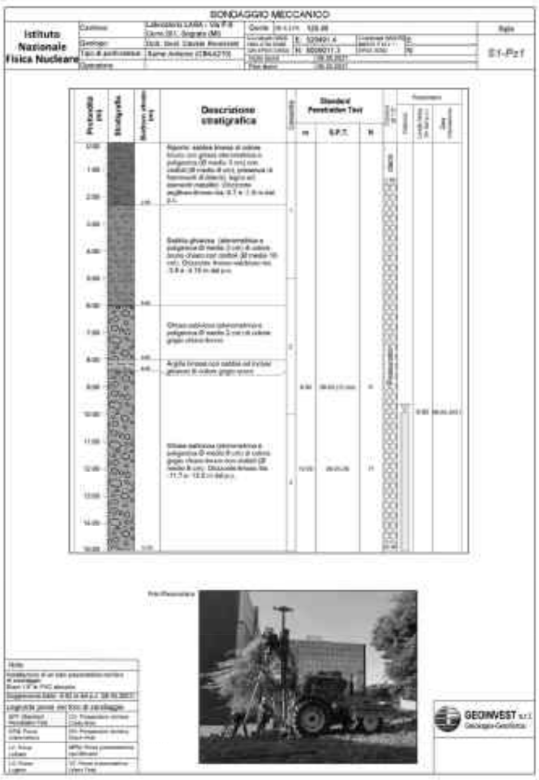

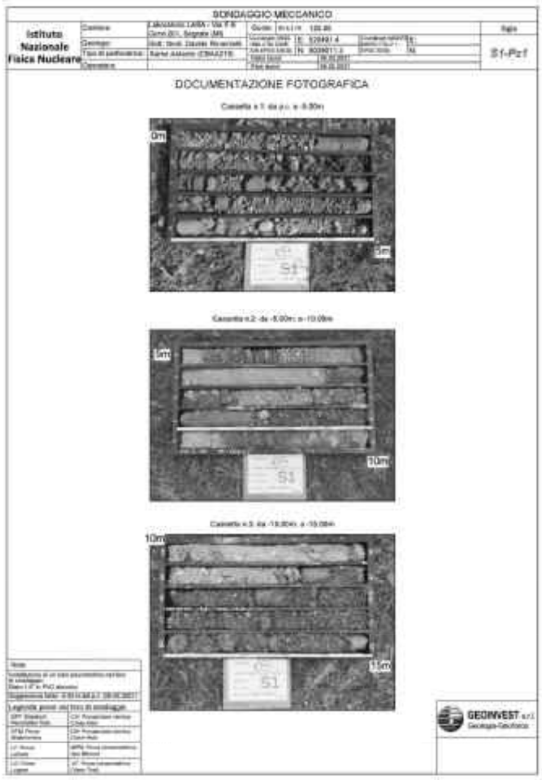

1.3 Prove penetrometriche dinamiche

La prova Standard Penetration Cone Test (SCPT) consiste nella misura della resistenza alla penetrazione di una punta conica di dimensioni standard, infissa per battitura nel terreno, per mezzo di un idoneo dispositivo di percussione.

Le informazioni ricavate sono di tipo continuo poiché le misure di resistenza alla penetrazione vengono eseguite durante tutta l'infissione a partire dal piano campagna.

Il campo di utilizzazione della prova è molto vasto potendo essere eseguita praticamente in tutti i tipi di terreno coesivo o granulare (dalle argille alle ghiaie), fornendo una valutazione qualitativa del grado di addensamento e di consistenza dei terreni attraversati.

Nell'indagine in oggetto è stato utilizzato un penetrometro dinamico superpesante DPSH "Pagani". Le principali caratteristiche sono le seguenti:

- Peso maglio 63.5 kg;
- Altezza caduta libera 75 cm
- Diametro punta 51 mm;
- Angolo apertura punta 60°
- Peso singola asta 6.3 kg

Le prove sono state spinte fino a rifiuto strumentale raggiunto alla profondità massima di -6.60 m da p.c. nei punti P1 e P2.

I risultati, ottenuti conteggiando il numero di colpi N necessario per infiggere la punta di 30cm, sono graficamente riportati di seguito.

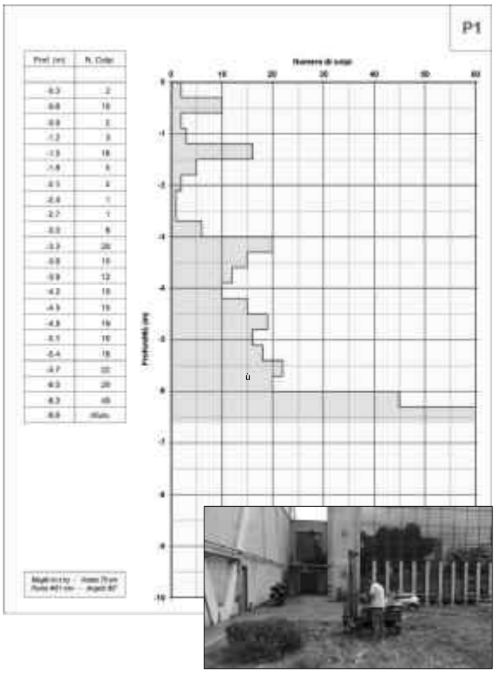

via della Conciliazione, 45/A - 29122 Piacenza Italia
telefono 0523 593622 - fax 0523 593640
www.geoinvest.it - geoinvest@geoinvest.it
PEC: geoinvest@legalmail.it

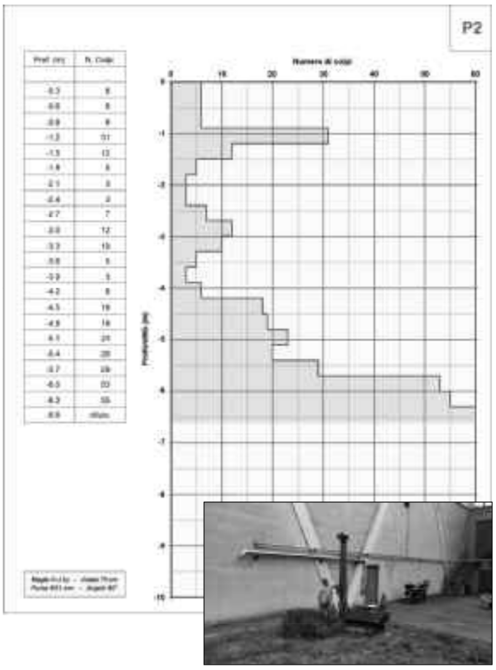

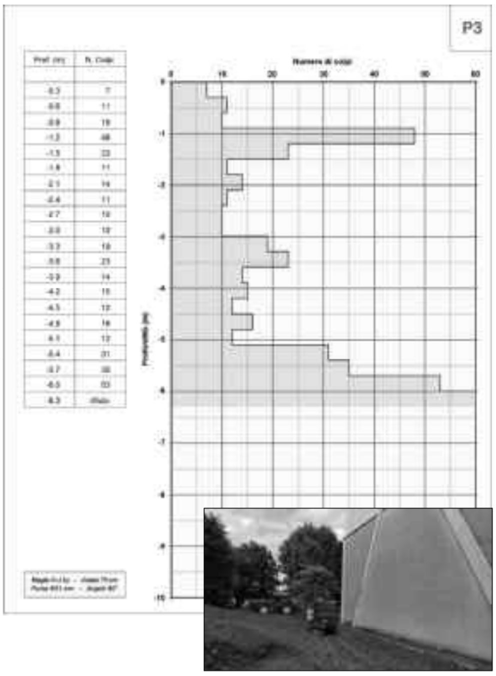

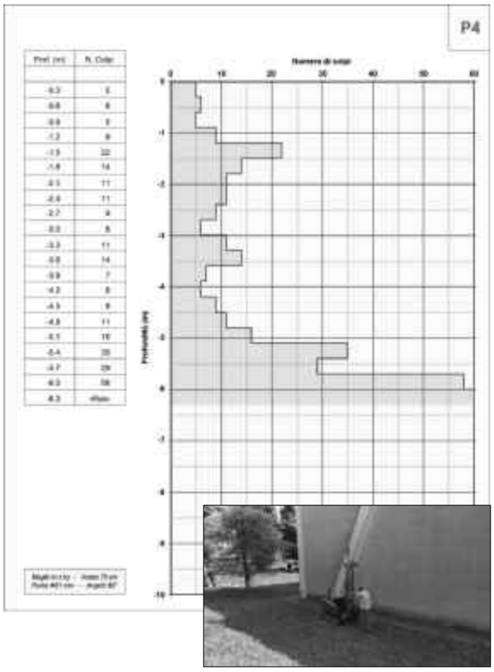

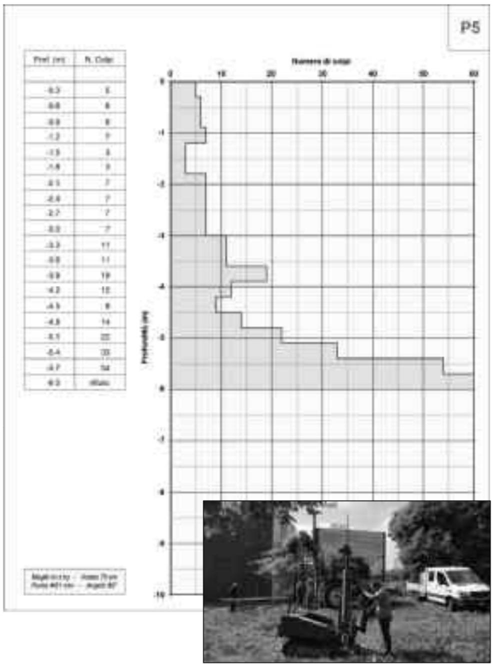

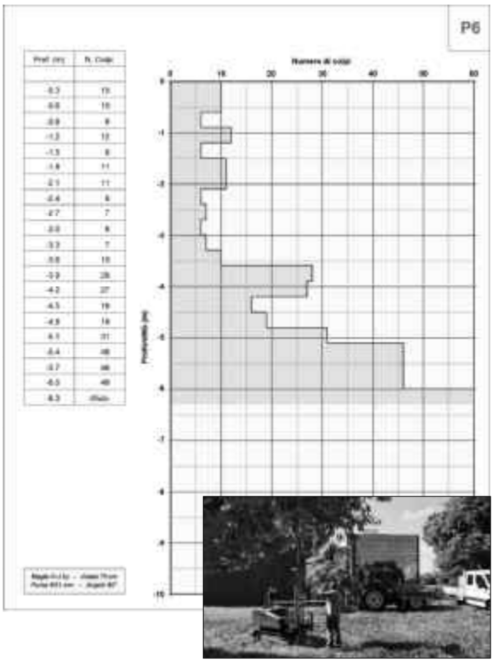

2 MODELLO GEOLOGICO DEL SITO

L'analisi dei risultati ottenuti con le indagini geognostiche condotte mediante esecuzione di n.6 prove penetrometriche dinamiche DPSH e n.1 sondaggio a carotaggio continuo S1, ha permesso di riconoscere una successione litostratigrafica del sito di intervento caratterizzata sostanzialmente da tre livelli con caratteristiche geotecniche differenti al di sotto di un primo strato di riporto (Livello R) costituito da materiale rimaneggiato di natura sabbioso limosa, di spessore variabile da 1.50 m in corrispondenza delle prove P1, P2, P3, P4, a 3.0 m in corrispondenza della prova P5.

Livello A (da -1.50 m a -3.00/-4.20 m dal p.c.)

Orizzonte superficiale che si riconosce esclusivamente in corrispondenza delle prove P1 e P2, costituito da depositi di natura prevalentemente limoso-sabbiosa, poco consistenti. Risulta caratterizzato da valori di resistenza del n.colpi x 30cm di avanzamento delle aste variabili da 1 a 12 con valore medio Nspt = 4.

Livello B (da -1.50/-4.20 m a -4.80/-6.00 m dal p.c.)

Orizzonte subsuperficiale costituito da depositi di natura prevalentemente sabbiosa ghiaiosa mediamente addensati. Si riconosce con buona continuità in tutta l'area indagata, direttamente al di sotto del livello R di riporto nelle prove P3, P4, P5, P6 e al di sotto del livello A, limoso-sabbioso, nelle prove P1 e P2.

Risulta caratterizzato da valori di resistenza del n.colpi x 30cm di avanzamento variabili da 6 a 29 con valore medio Nspt = 16.

Livello C (da -4.80/6.00 m a -15.00 m dal p.c.)

Orizzonte di fondo costituito da depositi prevalentemente ghiaioso-sabbiosi ben addensati con un intervallo argilloso-limoso tra 8.00 e 8.40 m in corrispondenza del Sondaggio S1. Le caratteristiche dell'unità verificate in profondità direttamente nelle carote di sondaggio si riscontrano con buona continuità verticale nella successione litostratigrafica fino ad almeno -15.00 dal p.c., massima profondità d'investigazione raggiunta.

Risulta caratterizzato da valori di resistenza del n.colpi x 30cm di avanzamento variabili da 29 a valori di rifiuto con valore medio Nspt = 56.

Le prove SPT in foro di sondaggio eseguite a -9.00m e -12.00m dal p.c. hanno condotto al rifiuto nel secondo tratto di avanzamento per la prova più superficiale e a un valore di Nspt = 71 per la più profonda.

3 MODELLO GEOTECNICO DEL SITO

Per la caratterizzazione geotecnica dei terreni interessati dall'intervento vengono di seguito forniti i parametri maggiormente significativi ai fini fondazionali, ottenuti empiricamente partendo dai risultati delle prove penetrometriche dinamiche e dalle prove NSPT in foro. I valori di resistenza Nscpt all'avanzamento delle prove sono stati correlati ai valori Nspt utilizzati per la determinazione dei parametri di resistenza e deformabilità secondo la relazione:

$$Nspt = Nscpt \times Cf.$$

Il valore di Cf dipende dalle caratteristiche strumentali del penetrometro utilizzato e dal tipo di litologia presente nell'area di intervento. I valori del N di colpi riportati nei diagrammi sono valori Nspt ovvero i risultati delle letture in campagna moltiplicati per Cf.

La determinazione del valore di **coesione non drenata Cu** è stata ottenuta secondo la correlazione di Sanglerat per argille limose:

$$Cu = 0.100\ Nspt\ (Kg/cm^2)$$

Il **modulo edometrico Ed** è stato determinato empiricamente secondo la seguente relazione di Stroud e Butler proposta per argille a bassa plasticità in cui:

$$Ed = 6\ Nspt\ (Kg/cm^2)$$

Per la valutazione **dell'angolo di attrito** φ in termini di sforzi efficaci è stato utilizzato il metodo diretto proposto da Peck-Hanson-Thornburn-Meyerhof (1956); la correlazione è la seguente:

$$\varphi = 27 + \left(10\ x\ \frac{Nspt_{corr}}{35}\right)$$

La stima del valore della **densità relativa Dr** è stata determinata attraverso l'equazione proposta da Skempton (1986): $Dr = \sqrt{\frac{Nspt}{60}}\ (\%)$

Mentre per le litologie incoerenti (limi sabbiosi, sabbie e ghiaie), **il modulo di deformazione elastica E** è stato determinato empiricamente secondo il metodo proposto da Schmertmann (1978): *E (kg/cmq) = 2BNSPT*

Laddove B è una costante variabile in funzione della litologia come da tabella allegata di seguito:

B	Litologia
[illegible]	sabbia fine
[illegible]	sabbia media
[illegible]	sabbia grossolana

Applicando quanto contenuto nelle Istruzioni applicative delle NTC 2018 del Cons. Sup. dei Lavori Pubblici vengono assunti quali valori caratteristici *Vk* delle terre i valori prossimi ai minimi *Vm*.

Si sottolinea che l'orizzonte superficiale di riporto, Livello R, citato al precedente capitolo, non è stato considerato nel modello geotecnico di seguito descritto.

Lo schema del modello geotecnico di sito rappresentativo del sottosuolo con i parametri determinati per ogni singolo livello con caratteristiche differenti è il seguente:

Livello A (da -1.50/-3.00 m a -3.00/-4.20 m dal p.c.) *Depositi di natura prevalentemente limosa-sabbiosa poco consistenti*	
Peso di volume γ	1.85 t/m^3
Coesione non drenata Cu	0.40 Kg/cm^2
Modulo edometrico Ed	24 Kg/cm^2
Angolo di attrito φ	28°
Densità relativa Dr	65%
Modulo elastico Es	48 Kg/cm^2
Livello B (da -1.50/-4.20 m a -4.80/-6.00 m dal p.c.) *Depositi di natura prevalentemente sabbioso-ghiaiosa mediamente addensati*	
Peso di volume γ	1.92 t/m^3
Angolo di attrito φ	30°
Densità relativa Dr	52%
Modulo elastico Es	192 Kg/cm^2
Livello C (da -4.80/-6.00 m a -15.00 m dal p.c.) *Depositi di natura prevalentemente ghiaioso sabbiosa ben addensati*	
Peso di volume γ	2.05 t/m^3
Angolo di attrito φ	33°
Densità relativa Dr	70%
Modulo elastico Es	348 Kg/cm^2

4 ANALISI DEL RISCHIO SISMICO

4.1 RIFERIMENTI NORMATIVI NAZIONALI

La pericolosità sismica è lo strumento di previsione delle azioni sismiche attese in un certo sito su base probabilistica ed è funzione delle caratteristiche di sismicità regionali e del potenziale sismogenetico delle sorgenti sismiche; la sua valutazione deriva quindi dai dati sismologici disponibili e porta alla valutazione del rischio sismico di un sito in termini di danni attesi a cose e persone come prodotto degli effetti di un evento sismico.

La pericolosità sismica valutata all'interno di un sito deve essere stimata come l'accelerazione orizzontale massima al suolo (scuotimento) in un dato periodo di tempo, definendo i requisiti progettuali antisismici per le nuove costruzioni nel sito stesso.

La mappatura della pericolosità sismica del territorio italiano ha permesso di stilare una classificazione sismica secondo le direttive promulgate dalla Presidenza del Consiglio dei Ministri il 23 marzo 2003 – Ordinanza n. 3274 "*Primi elementi in materia di criteri generali per la classificazione sismica del territorio nazionale e normative tecniche per le costruzioni in zona sismica*", con la quale sono stati approvati i "Criteri per l'individuazione delle zone sismiche – individuazione, formazione ed aggiornamento degli elenchi delle medesime zone" e le connesse norme tecniche per fondazioni e muri di sostegno, edifici e ponti attesi a cose e persone come prodotto degli effetti di un evento sismico.

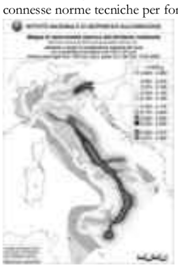

Sulla base di tale classificazione territorio comunale di Segrate ricadeva in Zona Sismica 4 - *Zona a sismicità bassa*, caratterizzata da una accelerazione massima su suolo di categoria A (Vs>800 m/s) 0.05<Ag≤ 0.15 g.

Nel 2006 sono stati approvati i "*Criteri per l'individuazione delle zone sismiche e la formazione e l'aggiornamento degli elenchi delle medesime zone*" e la Mappa di pericolosità sismica di riferimento a scala nazionale, con OPCM n. 3519, successivamente aggiornati in relazione alle modifiche apportate dalla revisione delle Norme Tecniche per le Costruzioni, emanate con D.M. 14 settembre 2005. Nella figura a lato viene riportata la mappa della pericolosità sismica come pubblicata nel sopraccitato OPCM.

Con la pubblicazione delle *Norme Tecniche per le Costruzioni* (D.M. 17 gennaio 2018) si definiscono i criteri definitivi per la classificazione sismica del territorio nazionale in recepimento del Voto n. 36 del Consiglio Superiore dei Lavori Pubblici del 27 luglio 2007 ("*Pericolosità sismica e criteri generali per la classificazione sismica del territorio nazionale*"); tali criteri prevedono la valutazione dell'azione sismica non più legata ad una zonazione sismica ma definita puntualmente al variare del sito e del periodo di ritorno considerati, in termini sia di accelerazione del suolo a_g sia di forma dello spettro di risposta.

L'Allegato A al D.M. 17 gennaio 2018 "*Norme Tecniche per le Costruzioni*" prevede che l'azione sismica venga valutata in fase di progettazione a partire da una "pericolosità sismica di base" in condizioni ideali di sito di riferimento rigido con superficie topografica orizzontale. La pericolosità sismica di un determinato sito deve essere descritta con sufficiente dettaglio sia in termini geografici che temporali, fornendo, di conseguenza i risultati del suddetto studio:

- in termini di valori di accelerazione orizzontale massima $\mathbf{a_g}$ e dei parametri che permettono di definire gli spettri di risposta ($\mathbf{F_o}$ – valore massimo del fattore di amplificazione dello spettro in accelerazione orizzontale, $\mathbf{T^*_c}$ – periodo di inizio del tratto a velocità costante dello spettro in accelerazione orizzontale);
- in corrispondenza dei punti di un reticolo di riferimento (*reticolo di riferimento*) i cui nodi non siano distanti più di 10 km;
- per diverse probabilità di superamento in 50 anni e/o diversi periodi di ritorno Tr ricadenti in un *intervallo di riferimento* compreso almeno tra 30 e 2475 anni.

Il valore di sollecitazione sismica di base a_g atteso nel territorio di Segrate così come definito nella tabella 1 allegata al D.M. 17 gennaio 2018 "*Norme tecniche per le costruzioni*" per eventi con tempo di ritorno di 475 anni e probabilità di superamento del 10% in 50 anni che ha condotto all'elaborazione della mappa di pericolosità sismica fornita dall'INGV di cui sotto, indica il range 0.050<Ag<0.075.

L'azione sismica così individuata deve essere variata in funzione delle modifiche apportate dalle condizioni sito-specifiche (caratteristiche litologiche e morfologiche); le variazioni apportate caratterizzano la **risposta sismica locale**. L'Allegato B alle citate norme fornisce le tabelle contenenti i valori dei parametri $\mathbf{a_g}$, $\mathbf{F_o}$ e $\mathbf{T^*_c}$ relativi alla pericolosità sismica su reticolo di riferimento, consultabile sul sito http://esse1.mi.ingv.it/.

4.2 ASPETTI NORMATIVI E METODOLOGICI REGIONALI

La Regione Lombardia, con D.g.r. n.14964 del 7 novembre 2003 ha recepito la classificazione dell'OPCM n.3274/03 imponendo la progettazione antisismica in zona 4 esclusivamente agli edifici strategici e per le opere infrastrutturali rilevanti (oggetto di particolare attenzione perché possono ospitare numerose persone, oppure servono alle comunicazioni e alle esigenze di base della collettività, così come individuati nel D.D.U.O. n. 19904 del 21 novembre 2003.

Con la pubblicazione sul B.U.R.L. del 19 gennaio 2006, 3° supplemento straordinario, della D.G.R. n. 8/1566 del 22 dicembre 2005 "Criteri ed indirizzi per la definizione della componente geologica, idrogeologica e sismica del Piano di Governo del Territorio, in attuazione dell'art. 57, comma 1, della Legge Regionale 11 marzo 2005 n. 12", la Regione Lombardia ha definito le linee guida e le procedure operative per la valutazione degli effetti sismici di sito a cui uniformarsi nella definizione del rischio sismico locale, successivamente aggiornate con la D.G.R. n. 8/7374 del 28 maggio 2008 "Aggiornamento dei Criteri ed indirizzi per la definizione della componente geologica, idrogeologica e sismica del Piano di Governo del Territorio, in attuazione dell'art. 57, comma 1, della Legge Regionale 11 marzo 2005 n. 12 approvati con D.G.R. 22/05 n. 8/1566" pubblicata sul B.U.R.L. del 12 giugno 2008, 2° supplemento straordinario al n° 24, a seguito delle avvenute modifiche in materia di norme tecniche sulle costruzioni (D.M. 17 gennaio 2018). Secondo le direttive regionali, l'analisi della sismicità del territorio in termini di valutazione dell'amplificazione sismica locale deve seguire le metodologie dell'Allegato 5 al D.G.R. n. 8/7374/2008, che prevedono tre diversi livelli di approfondimento in funzione della zona sismica di appartenenza (1° livello, 2° livello, 3° livello).

Tale classificazione, secondo quanto riportato al punto 1.4.3 della D.G.R. n. 8/7374/2008, definisce unicamente l'ambito di applicazione dei vari livelli di approfondimento in fase pianificatoria.

Si sottolinea comunque che, in accordo alla D.G.R. n. 8/7374/2008, su tutto il territorio comunale gli edifici il cui uso prevede affollamenti significativi, gli edifici industriali con attività pericolose per l'ambiente, le reti viarie e ferroviarie la cui interruzione provochi situazioni di emergenza e le costruzioni con funzioni pubbliche o strategiche importanti e con funzioni sociali essenziali di cui al D.D.U.O. 21 novembre 2003 n. 19904 "Approvazione elenco tipologie degli edifici e opere infrastrutturali e programma temporale delle verifiche di cui all'art. 2, commi 3 e 4 dell'ordinanza p.c.m. n. 3274 del 20 marzo 2003, in attuazione della d.g.r. n. 14964 del 7 novembre 2003" dovranno essere progettati adottando i criteri antisismici di cui al D.M. 17 gennaio 2018 "Norme tecniche per le costruzioni", definendo le azioni sismiche di progetto a mezzo di analisi di approfondimento di 3° livello, indipendentemente dalla presenza o meno di possib ili scenari di amplificazione locale.

Con *D.G.R. del 30.11.2011 - n. IX/2616* è stato effettuato l'aggiornamento dei "*Criteri ed indirizzi per la definizione della componente geologica, idrogeologica e sismica del piano di governo del territorio, in attuazione dell'art.57, comma 1, della l.r. 11 marzo 2005, n.12*", approvati con d.g.r. 22 dicembre 2005, n.8/1566 e successivamente modificati con d.g.r. 28 maggio, n. 8/7374.

Con D.G.R. del 11 luglio 2014 – n.X/2129 è stato prodotto l'aggiornamento delle zone sismiche in Regione Lombardia ai sensi del l.r. 1/2000, art.3, c.108, lett.d, in cui sono indicate le zone sismiche dei comuni compresi nella Regione Lombardia e le relative accelerazioni massime (AGMAX) presenti all'interno dei territori comunali (O.P.C.M. 3519/06 e Decreto Min. Infrastrutture 14/01/08 aggiornate con D.M. del 17 gennaio2018). La classificazione sismica inserisce il Comune di Segrate in zona sismica 3 attribuendo un valore di **Ag_{max}=0,057205g**

ELENCO DEI COMUNI CON INDICAZIONE DELLE RELATIVE ZONE SISMICHE E DELL'ACCELERAZIONE MASSIMA (AGMAX) PRESENTI ALL'INTERNO DEL TERRITORIO COMUNALE (O.P.C.M. 3519/06 E DECRETO MIN. INFRASTRUTTURE 14/01/08)

ISTAT	Provincia	Comune	Zona sismica	AgMax
[illegible]	[illegible]	[illegible]	3	[illegible]

5 STRATEGIA DI PROGETTAZIONE

Le NTC 2018 stabiliscono che le verifiche di sicurezza e prestazionali di una struttura devono essere effettuate in relazione agli stati limite di riferimento che si possono verificare durante la vita dell'opera, intesi come condizioni superate le quali l'opera non è più in grado di soddisfare le esigenze per le quali è stata progettata. In tale condizione, la definizione del periodo di riferimento relativamente alla vita dell'opera implica che, nell'ambito della definizione delle azioni di carico, da considerare nelle verifiche di sicurezza delle opere, sia ricompresa anche l'azione sismica, la cui valutazione è stata oggetto del O.P.C.M. 3274 del 20.04.2003. Il periodo di riferimento per l'azione sismica V_R risulta, quindi, dall'incrocio dei parametri: vita nominale e classe d'uso, definiti dal tipo di costruzione.

La vita nominale di progetto V_N di un'opera è convenzionalmente definita come il numero di anni nel quale è previsto che l'opera, purché soggetta alla necessaria manutenzione, mantenga specifici livelli prestazionali.

I valori minimi di VN da adottare per i diversi tipi di costruzione sono riportati nella Tab. 2.4.I. Tali valori possono essere anche impiegati per definire le azioni dipendenti dal tempo.

Tab. 2.4.I – Valori minimi della Vita nominale V_N di progetto per i diversi tipi di costruzioni

	TIPI DI COSTRUZIONI	Valori minimi di V_N (anni)
1	Costruzioni temporanee e provvisorie	10
2	Costruzioni con livelli di prestazioni ordinari	50
3	Costruzioni con livelli di prestazioni elevati	100

La vita nominale delle opere in progetto (essendo costruzioni a livello di prestazioni ordinarie di tipo 2) è di **V_N=50 anni.**

La classe d'uso è definita con riferimento alle conseguenze di una interruzione di operatività o di un eventuale collasso, le costruzioni sono suddivise in 4 classi d'uso (I, II, III, IV) a ciascuna delle quali corrisponde un coefficiente d'uso **CU** come definito nelle NTC 2018(Tab.2.4.II).

Tab. 2.4.II – Valori del coefficiente d'uso C_U

CLASSE D'USO	I	II	III	IV
COEFFICIENTE C_U	0,7	1,0	1,5	2,0

Le costruzioni in progetto rientrano nella **Classe II** *il cui uso preveda normali affollamenti senza contenuti pericolosi per l'ambiente e senza funzioni pubbliche e sociali essenziali. Industrie con attività non pericolose per l'ambiente. Ponti opere infrastrutturali reti varie non ricadenti in Classe d'uso III o in Classe d'uso IV, reti ferroviarie la cui interruzione non provochi situazioni di emergenza. Dighe il cui collasso non provochi conseguenze rilevanti.*

Secondo la Tab. 2.4.II NTC2018 a tale classe corrisponde un **Coefficiente d'uso Cu = 1.0** e conseguentemente il periodo di riferimento per l'azione sismica **V_R** risulta pari a **V_N x Cu = 50 x 1.0 =50 anni.**

6 PERICOLOSITÀ SISMICA DI BASE DEL TERRITORIO COMUNALE

Con riferimento al D.M. 17/01/08 *Norme tecniche per le costruzioni* la sismicità di base del territorio comunale di Segrate è definibile in funzione del valore assunto dall'accelerazione massima attesa su suolo rigido per eventi con tempo di ritorno di 475 anni e proba bilità di superamento del 10% in 50 anni definita nella tabella 1 allegata al citato decreto ministeriale in corrispondenza dei nodi di un reticolo di riferimento nazionale.

Le coordinate del sito esaminato sono:

WGS84: *latitudine= 45,4504296°, longitudine= 9,262255°*

ED50: *latitudine= 45,505229°, longitudine= 9,263313°*

La tabella a lato mostra le coordinate del reticolo di riferimento (ED50) e la loro distanza in metri dal sito in esame.

	ID	Latitudine [°]	Longitudine [°]	Distanza [m]
Sito 1	12039	45,509230	9,215706	3891,3
Sito 2	12040	45,511730	9,284842	1826,8
Sito 3	12262	45,461780	9,285462	5214,0
Sito 4	12261	45,458290	9,217374	6238,6

La mappa sulla sinistra inquadra territorialmente l'ubicazione dei quattro nodi del reticolo di riferimento. I parametri sismici di riferimento per i differenti stati limite ai **sensi delle NTC 2018 tenuto conto di un** periodo di riferimento per l'azione sismica Vr=50 anni, sono i seguenti:

STATO LIMITE	Tr [anni]	ag [g]	Fo	Tc* [s]
Operatività (SLO)	30	[illegible]	[illegible]	[illegible]
Danno (SLD)	50	[illegible]	[illegible]	[illegible]
Salvaguardia vita (SLV)	475	[illegible]	[illegible]	[illegible]
Prevenzione collasso (SLC)	975	[illegible]	[illegible]	[illegible]
Periodo di riferimento per l'azione sismica	50			

7 CARATTERIZZAZIONE SISMICA DEL SITO

La normativa D.M. 17.01.2018 "Norme tecniche per le costruzioni", afferma che ai fini della definizione della azione sismica di progetto (punto 3.2.2), deve essere valutata l'influenza delle condizioni litologiche e morfologiche locali sulle caratteristiche del moto del suolo in superficie, mediante studi specifici di risposta sismica locale. In alternativa, qualora le condizioni stratigrafiche e le proprietà dei terreni siano chiaramente riconducibili alle categorie definite nella Tab. 3.2.II, si può fare riferimento a un approccio semplificato che si basa sulla classificazione del sottosuolo in funzione dei valori della velocità di propagazione delle onde di taglio, V_S.

I valori di V_S sono ottenuti mediante specifiche prove oppure, con giustificata motivazione e limitatamente all'approccio semplificato, sono valutati tramite relazioni empiriche di comprovata affidabilità con i risultati di altre prove in sito, quali ad esempio le prove penetrometriche dinamiche per i terreni a grana grossa e le prove penetrometriche statiche.

La classificazione del sottosuolo si effettua in base alle condizioni stratigrafiche ed ai valori della velocità equivalente di propagazione delle onde di taglio, $V_{S,eq}$ (in m/s), definita dall'espressione:

$$V_{S,eq} = \frac{H}{\sum_{i=1}^{N} \frac{h_i}{V_{S,i}}} \qquad [3.2.1]$$

con:
h_i spessore dell'i-esimo strato;
$V_{S,i}$ velocità delle onde di taglio nell'i-esimo strato;
N numero di strati;
H profondità del substrato, definito come quella formazione costituita da roccia o terreno molto rigido, caratterizzata da V_S non inferiore a 800 m/s.

Per le fondazioni superficiali, la profondità del substrato è riferita al piano di imposta delle stesse, mentre per le fondazioni su pali è riferita alla testa dei pali. Nel caso di opere di sostegno di terreni naturali, la profondità è riferita alla testa dell'opera. Per muri di sostegno di terrapieni, la profondità è riferita al piano di imposta della fondazione.

Per depositi con profondità H del substrato superiore a 30 m, la velocità equivalente delle onde di taglio $Vs_{,eq}$ è definita dal parametro Vs_{30}, ottenuto ponendo H=30 m nella precedente espressione e considerando le proprietà degli strati di terreno fino a tale profondità.

Nel nostro caso, la classificazione è effettuata sulla base del parametro Vs_{30} determinato con la prova di acquisizione sismica di tipo MASW/Re.Mi che è risultato pari a 323 m/s per un piano di fondazione posto a piano campagna. Di seguito l'analisi di dettaglio.

Le categorie di sottosuolo che permettono l'utilizzo dell'approccio semplificato sono definite in Tab. 3.2.II.

Tab. 3.2.II – *Categorie di sottosuolo che permettono l'utilizzo dell'approccio semplificato.*

Categoria	Caratteristiche della superficie topografica
A	*Ammassi rocciosi affioranti o terreni molto rigidi caratterizzati da valori di velocità delle onde di taglio superiori a 800 m/s, eventualmente comprendenti in superficie terreni di caratteristiche meccaniche più scadenti con spessore massimo pari a 3 m.*
B	*Rocce tenere e depositi di terreni a grana grossa molto addensati o terreni a grana fina molto consistenti, caratterizzati da un miglioramento delle proprietà meccaniche con la profondità e da valori di velocità equivalente compresi tra 360 m/s e 800 m/s.*
C	*Depositi di terreni a grana grossa mediamente addensati o terreni a grana fina mediamente consistenti con profondità del substrato superiori a 30 m, caratterizzati da un miglioramento delle proprietà meccaniche con la profondità e da valori di velocità equivalente compresi tra 180 m/s e 360 m/s.*
D	*Depositi di terreni a grana grossa scarsamente addensati o di terreni a grana fina scarsamente consistenti, con profondità del substrato superiori a 30 m, caratterizzati da un miglioramento delle proprietà meccaniche con la profondità e da valori di velocità equivalente compresi tra 100 e 180 m/s.*
E	*Terreni con caratteristiche e valori di velocità equivalente riconducibili a quelle definite per le categorie C o D, con profondità del substrato non superiore a 30 m.*

Per queste cinque categorie di sottosuolo, le azioni sismiche sono definibili come descritto al § 3.2.3 delle NTC 2018.

Per qualsiasi condizione di sottosuolo non classificabile nelle categorie precedenti, è necessario predisporre specifiche analisi di risposta locale per la definizione delle azioni sismiche.

8 MISURA DELLA Vs30 TRAMITE PROVE SISMICHE

8.1 Prova Re.Mi.

Le tecniche correntemente utilizzate (Down-Hole, Cross-Hole) per la stima delle velocità delle onde di taglio per caratterizzare un sito sotto il profilo della risposta sismica, dovendo necessitare di almeno un foro di 30 m nel quale eseguire la prova, sono normalmente troppo onerose per essere impiegate come indagine di routine negli studi di microzonazione e di classificazione dei profili stratigrafici dei suoli di fondazione per progettazioni di opere non concentrate in areali ristretti. La tecnica di prospezione "Refraction Microtremor" (Re.Mi.) utilizzata capovolge il concetto comune del parametro "segnale-disturbo", per il quale tradizionalmente il primo (segnale) ha necessità di essere rilevato in condizioni favorevoli quindi in assenza o scarsità di rumore. Viceversa, in presenza di forte rumore di fondo (es. ambiente urbano), le tradizionali rilevazioni sismiche hanno sempre trovato una condizione di difficile applicazione a causa della difficoltà di discriminare il segnale dal rumore.

Con questa nuova tecnica, il disturbo o "noise" ambientale, diventa il segnale utilizzato per la caratterizzazione sismica. Sono i microtremori (rumore di fondo generato dal traffico stradale, ferroviario e comunque il rumore presente costantemente in ambito urbanizzato) a costituire la sorgente di energia utile allo scopo.

La metodologia d'indagine più applicata per la determinazione del profilo verticale di velocità delle onde di taglio Vs, è stata proposta e sperimentata da J.N.Louie del Seismological Laboratory and Dept. of Geological Sciences dell'Università del Nevada, ed è basata su due aspetti fondamentali:

- *uno pratico*, rappresentato dal fatto che alcuni sistemi di acquisizione di sismica a rifrazione (con dinamica a 24bit) sono in grado di registrare onde di superficie con frequenze fino a 2 Hz per intervalli di tempo sufficientemente lunghi (30 sec);
- *uno teorico*, sulla base del quale una semplice trasformata bidimensionale (p-f) slowness-frequency della registrazione di un rumore di fondo (microtremore) è in grado di separare le onde di Rayleigh (onde di superficie) da altri tipi di onde che compongono il sismogramma, rendendo possibile il riconoscimento delle vere velocità di fase dalle velocità apparenti.

Re.Mi. - Modalità d'intervento

L'acquisizione dei dati per la definizione della **Vs_{30}** è stata svolta tramite l'acquisizione e la registrazione del noise ambientale impiegando geofoni da 4.5 Hz ed un acquisitore digitale multicanale a 24 canali con dinamica a 24bit.

E' stato acquisito n.1 profilo sismico (come riportato in planimetria), costituito da un allineamento di n.17 geofoni equispaziati di 3.00 m. Per la prova sismica sono stati registrati oltre 15 records di lunghezza di 30 sec con campionamento ogni 2ms.

8.2 Prova MASW

Il metodo MASW è una tecnica di indagine non invasiva che si basa sulla misura delle onde superficiali fatta in corrispondenza di diversi sensori (accelerometri o geofoni) posti sulla superficie del suolo. Il contributo predominante alle onde superficiali è dato dalle onde di Rayleigh, che viaggiano con una velocità correlata alla rigidezza della porzione di terreno interessata dalla propagazione delle onde. La natura dispersiva delle onde superficiali è correlabile al fatto che onde ad alta frequenza con lunghezza d'onda corta si propagano negli strati più superficiali e quindi danno informazioni sulla parte più superficiale del suolo, invece onde a bassa frequenza si propagano negli strati più profondi e quindi interessano gli strati più profondi. Il metodo di indagine MASW si distingue in metodo attivo e metodo passivo (Zywicki, D.J.1999) o in una combinazione di entrambi.

MASW –Modalità d'intervento

Nell'indagine eseguita è stato utilizzato il metodo attivo in cui le onde superficiali vengono generate in un punto sulla superficie del suolo tramite una massa battente di 8kg, sono misurate da uno stendimento lineare di sensori, nel nostro caso n.17 geofoni con frequenza propria di 4.5Hz e spaziatura di 3.00 m, collegati ad un sismografo digitale Geode della Geometrics a 24 canali. L'energizzazione è stata realizzata a 7m e 4m di distanza sommando n.5 battute. La lunghezza delle registrazioni è stata di 1 sec con un passo di campionamento di 1ms. Il metodo attivo generalmente consente di ottenere una velocità di fase (o curva di dispersione) sperimentale apparente nel range di frequenze compreso tra 5Hz e 70Hz, quindi dà informazioni sulla parte più superficiale del suolo, nei primi 15 m-20 m, in funzione della rigidezza del suolo.

8.3 Elaborazione dati

Considerando la buona qualità degli spettri ottenuti dalle prove ReMi e MASW si è provveduto ad effettuare il "picking" delle curve di dispersione per entrambi i metodi, di seguito sono mostrate le relative immagini:

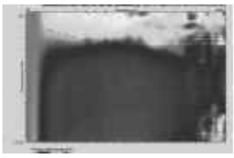

Spettro Re.Mi. e "Pick"

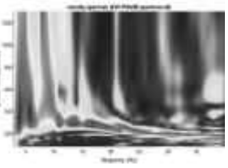

Spettro MASW e "Pick"

Da tale elaborazione è stata poi estrapolata la curva di attenuazione del segnale caratteristico; in funzione del suo andamento (curva di dispersione), attraverso una procedura di "inversione", si risale al modello stratigrafico, espresso in termini di velocità delle onde di taglio (Vs) e quindi al valore **V_{S30}**.

8.4 Analisi dei risultati

L'elaborazione dei dati acquisiti ha consentito la ricostruzione del modello stratigrafico in funzione delle velocità sismiche Vs e la determinazione del parametro **Vs30 = 323 m/s.**

Ai fini della caratterizzazione sismica del sito per la definizione delle azioni sismiche di progetto (Tab. 3.2.II, NTC 2018), la categoria del suolo di fondazione risulta di tipo "**C**" la cui definizione nella classificazione dei suoli di riferimento normativo è la seguente:

Categoria C: *Depositi di terreni a grana grossa mediamente addensati o terreni a grana fina mediamente consistenti con profondità del substrato superiori a 30 metri, caratterizzati da un graduale miglioramento delle proprietà meccaniche con la profondità e da valori di velocità equivalente compresi tra 180 e 360 m/s.*

Il modello stratigrafico in funzione delle velocità Vs con riportati il valore del parametro V_{S30} e la categoria sismica del suolo di fondazione è il seguente:

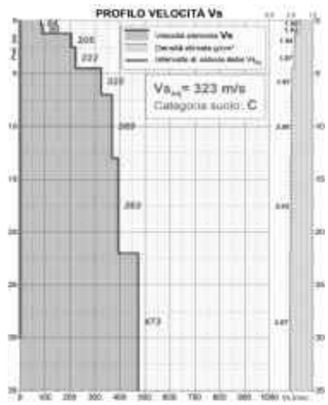

9 RISPOSTA SISMICA LOCALE

L'azione sismica "di base" viene successivamente corretta tramite la valutazione della "risposta sismica locale" una volta definita la **categoria sismica di sottosuolo** che è risultata di tipo **"C"** e le condizioni topografiche del sito, con riferimento alle NTC 2018 Tab. 3.2.III, rientranti nella "**Categoria topografica T1** *Superficie pianeggiante, pendii e rilievi isolati con inclinazione media <=15°*.

Tab. 3.2.III – *Categorie topografiche*

Categoria	Caratteristiche della superficie topografica
T1	Superficie pianeggiante, pendii e rilievi isolati con inclinazione media i ≤ 15°
T2	Pendii con inclinazione media i > 15°
T3	Rilievi con larghezza in cresta molto minore che alla base e inclinazione media 15° ≤ i ≤ 30°
T4	Rilievi con larghezza in cresta molto minore che alla base e inclinazione media i > 30°

La sintesi dei coefficienti sismici di sito da applicare ai differenti stati limite calcolata dal programma appositamente dedicato una volta definiti i parametri sismici, la categoria sismica del sottosuolo e quella topografica è la seguente:

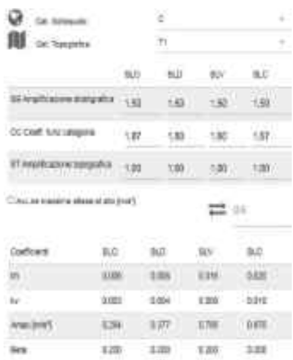

Al fine di determinare i valori del Fattore di amplificazione Fa per il confronto con i limiti di riferimento indicati dalla Regione Lombardia, sulla base del valore di V_{S30}, della categoria sismica del suolo e della successione litostratigrafica dell'area viene individuata la scheda litologica più attinente riportata nel D.G.R. n. IX/2616 del 30.11.2011.

Nel nostro caso i dati ottenuti con le indagini vengono inseriti nella scheda per litologie sabbiose.

Di seguito viene fornita la scheda con le curve di amplificazione di sito rapportate a quelle normative di riferimento.

I fattori di amplificazione di sito risultano i seguenti:

Intervallo 0.1<To<0.5 s Fa sito = **1.25** < Valore soglia = **1.85**

Intervallo 0.5<To<1.5 s Fa sito = **1.97** < Valore soglia = **2.41**

Si osserva che il valore di Fa in entrambi gli intervalli di periodo 0.1-0.5s e 0.5-1.5s è inferiore al valore di soglia corrispondente, pertanto la normativa D.G.R. n. IX/2616 del 30.11.2011 è da considerarsi SUFFICIENTE a tenere in considerazione anche i possibili effetti di amplificazione litologica del sito per litologie sabbiose.

I.N.F.N. Laboratorio L.A.S.A.

R 4045 - 33/33

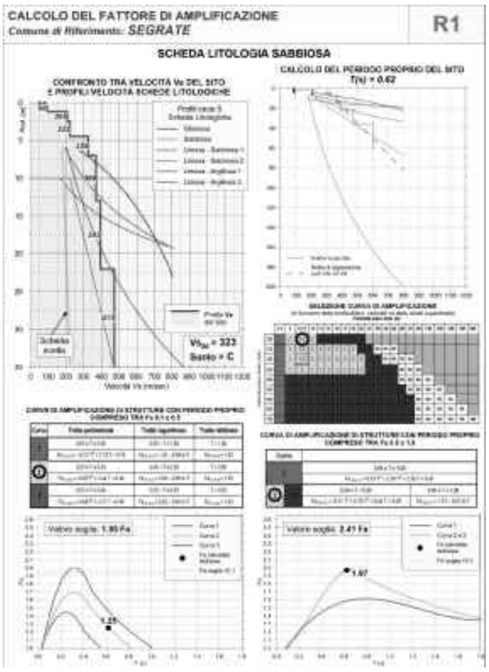

via della Conciliazione, 45/A - 29122 Piacenza Italia
telefono 0523 593622 - fax 0523 593640
www.geoinvest.it - geoinvest@geoinvest.it
PEC: geoinvest@legalmail.it

GEOINVEST s.r.l.
Geologia Geofisica

25. BriXSinO CAD pictures

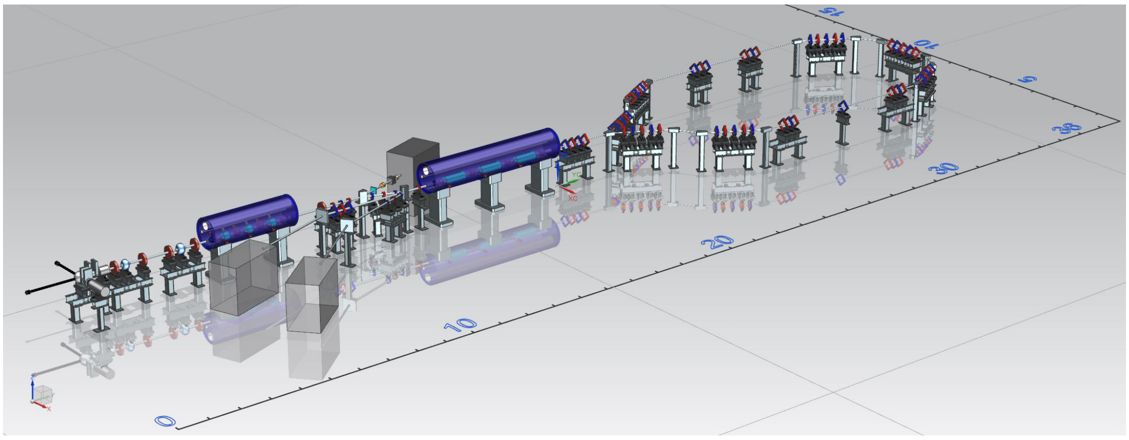

Figure 25.1: BriXSinO axonometric projection.

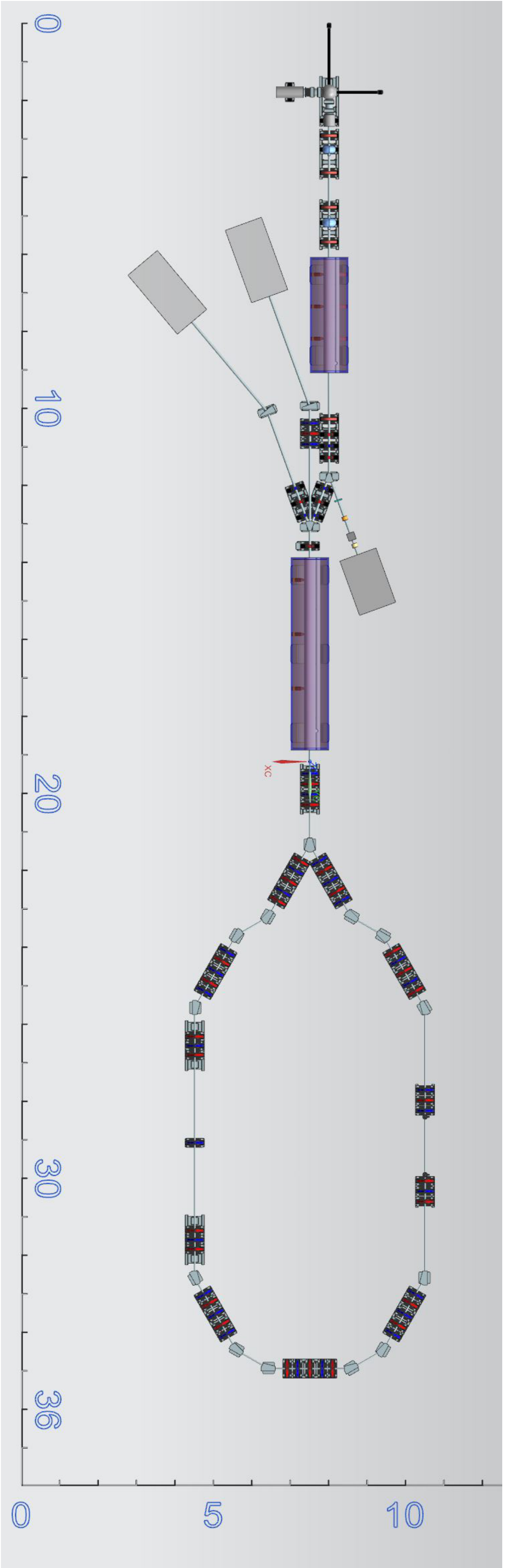

Figure 25.2: BriXSinO top view.